School of Science
Department of Applied Physics
International Centre for Radio Astronomy Research
Curtin Institute of Radio Astronomy

Applications of High-Frequency Resolution, Wide-Field VLBI: Observations of Nearby Star-Forming Galaxies & Habitable Exoplanetary Candidates

Hayden Rampadarath

This thesis is presented for the Degree of
Doctor of Philosophy
of
Curtin University

April 2014

To the best of my knowledge and belief this thesis contains no material previously published by any other person except where due acknowledgement has been made. This thesis contains no material which has been accepted for the award of any other degree or diploma in any university.

.....

HAYDEN RAMPADARATH

10th April 2014

"We shall not cease from exploration
And the end of all our exploring
Will be to arrive where we started
And know the place for the first time"

T.S. Eliot

Acknowledgements

Ever since I read *Cosmos* by Carl Sagan (which was loaned to me by a school mate) at a ripe young age of 14, its been my dream to become an Astrophysicist. However, never had I thought, while growing up in the country side of Trinidad that, I would one day be bestowed with the title of Doctor of Philosophy in Astrophysics. And now with this thesis, the dream of a 14 year old school boy has become a reality. I would, therefore, like to take the opportunity to sincerely thank all those who have supported me during this awesome journey.

Firstly, my PhD supervisors, Prof. Steven Tingay and Dr. John Morgan. Your support and constant guidance over the last 3.5 years were crucial for the eventual success of this thesis. I would like to thank both of you for allowing me the freedom to forge my own path, and to work on a couple of projects that while obscure, were very interesting. While working under you both was sometimes arduous, it was nonetheless, in the end a great pleasure to work with and learn from a couple of fantastic astrophysicists. Particular thanks to Steven for securing the postgraduate scholarship from ICRAR, so that I may comfortably pursue the PhD.

I would like to express my deepest gratitude Prof. Mauri Valtonen for giving me my first foray into the world of professional astronomy research, many years ago in Trinidad. I would not be submitting a PhD thesis in Astrophysics if not for your support and guidance during the early years of my studies.

Special thanks to Prof. Michael Garrett for introducing me to the world of VLBI and radio interferometry. My first VLBI project was with you on 90 cm VLBA in 2008, and either you were a great teacher or I am mentally unsound, since I eventually decided that VLBI is somehow wonderful and that I want to

work on it for my PhD. I will never forget your support during my time at Leiden.

A special thanks to Dr. Cormac Reynolds. I think I bothered you far more than anyone else in CIRA, including my supervisors! You are the coolest person I knew out the office and yet was one of the most intimidating persons to approach while at your desk. Still, you were always willing to answer my questions (once they weren't too ridiculous) on AGNs and general VLBI stuff. I would also like to thank Dr. Emil Lenc for showing me the early ropes on wide-field VLBI, LBA calibration and all the cool stuff with starburst galaxies. You are great and I enjoyed working with you on the NGC 253 project. To Dr. Cath Trott for not only for imparting your knowledge on statistics, but for being a wonderful person to have a little chat, that somehow always made me feel better. Special thanks to Dr. Roberto Soria, for teaching me about optical and X-ray astronomy. Your enthusiasm during the M51 project was very infectious, and I absolutely enjoyed working with you.

To the many members of CIRA academic staff, both past and present, Drs. Leith Godfrey, Megan Argo, Hayley Bignall, Natasha Hurley-Walker, James Miller-Jones, Steven Trembley, Nadia Kudryavtseva, Peter Curran, Randall Wayth and even Jean-Pierre (J-P) Macquart for all the insightful, wonderful and entertaining discussions (both academic and non-academic) over the course of my degree that have no doubt left a lasting impression.

While I had little chance to work with the engineering and technical staff, I nonetheless had a number of interesting discussions (especially with Dave Pallot, Jon Tickner, Brian Crosse, Mark Waterson, and Dave Emrich), that provided a welcomed respite from the daily grind.

What would a PhD degree be without a bunch of wonderful fellow students working, having fun and sharing the most important period of their education together? However, instead I was stuck with a bunch of like-minded "numbnuts" that preferred to suffer loudly while trying our best not to knock each other off? Yes, I am talking about you guys: Divya Palaniswamy, Tom Russell, Samuel Oronsaye, (Cmdr.) Chittawan Choeysakul, Aziz Jiwani, John Goldsmith (soon to be Dr. Goldsmith) and Dr. Jun Yi "Kevin" Koay. It was fun doing (or not doing) a PhD with you guys and I wish you all the success in the world (unless it is to take over the world)!

A special thanks to Dr. Budi Juswardy for introducing me to Chen style taiji (aka taichi) and to his taiji master Sien-Long Chong, during my PhD. Its calming effects played a huge role in keeping me sane during my PhD.

If CIRA was a well oiled machine, then the administrative staff are the oil. I

cannot thank Tina Sallis, Jennifer Talbot, Tanya Jones, Rachel Kennedy, Angela Dunleavy and the many temporary members of administrative staff enough for all they have done to keep us "eggheads" from descending into savagery.

Thibuat, Emilie, Giorgia, Nikta, Daniel H, Daniel R, Tri, Kalle and Niruj, while our time together at Leiden was foreshortened, I will always cherish those days. They were filled with great and wonderful times. I can safely say it ... guys I've finally done it!!!

To my mom and late dad, I wonder what you thought when I told you 15-16 years ago of my dreams. You were there from the start and will always be with me, your endearing love and support. Thanks and I would like you know that all your hard work and sacrifice was not in vain. Hey, Anand, do you remember those nights, lying in the yard looking up at the night sky wondering what was there? Those days played a very important role in the path I chose.

Finally and most important of all, I would like to thank my wonderful partner in life, Laura. My quest for the PhD took us from the sandy shores and blue seas of Trinidad and Tobago, to the cold (in)tolerance of the picturesque town of Leiden, to the wonderfully mad city of Manchester, and then finally Perth, a place that will forever have special place in my heart. While it was tough going, you stuck through it all and together we enjoyed the wonders of this journey. Without you this would have been dull and lifeless. Your constant support and belief in me during the many years have shone like a beacon that kept me steady on my path, especially when it all felt impossible. Now together, we face an unknown future, encouraged by the experiences of a wonderful past.

I would like to acknowledge the International Centre for Radio Astronomy Research for providing me with financial support through their postgraduate scholarship schemes. During this thesis I made full use of data from: the Australian Long Baseline Array, operated by the Australia Telescope National Facility (ATNF) of the Commonwealth Scientic and Industrial Research Organization (CSIRO) Astronomy and Space Science (CASS) Division, and by the University of Tasmania (UTas); and the European VLBI Network, which is a joint facility of European, Chinese, South African and other radio astronomy institutes funded by their national research councils. I also made use of archive data from: the Very Large Array and the Very Long Baseline Array, both operated by the National Radio Astronomy Observatory (NRAO) is a facility of the National Science Foundation operated under cooperative agreement by Associated Universities, Inc.; the Hubble Space Telescope, operated by NASA and the Space Telescope Science Institute; XMM-Newton, operated by the European Space Agency; and

Chandra X-ray telescope, operated for NASA by the Smithsonian Astrophysical Observatory. Data were also obtained through the NASA/IPAC Extragalactic Database (NED), operated by the Jet Propulsion Laboratory, California Institute of Technology, under contract with NASA, the Aladin Sky Atlas operated by CDS Strasbourg, France

I would like to thank all those who were responsible for conducting the observations on my behalf and data correlation, especially the people at Bonn (namely Dr. Alessandra Bertarini) and Dr. Olaf Wucknitz for moving my data from Bonn to Perth within reasonable time to complete this thesis. Thanks to Dr. Chris Phillips for providing the support required to successfully utilise the computing cluster, CAVE. Special thanks to Dr. Megan Argo for providing MERLIN data of M51, and Dr. Gaelle Dumas for providing VLA data of M51. This thesis made use of services from iVEC, a jointly operated venture between CSIRO, and various Western Australian universities, including Curtin University.

And to all my doubters, thank you very much because you guys have also pushed me. - Usain Bolt

Abstract

Until recently, the maximum observable field of view of Very Long Baseline Interferometric (VLBI) observations was limited, predominantly, by the ability to process large volumes of data. However, the availability of software correlators and high performance computing have provided the means to overcome these restrictions, giving rise to the technique of wide-field VLBI. This thesis reports on the application of this technique to investigate two different science cases: (1) to explore the use of VLBI for targeted searches for extra-terrestrial intelligence (SETI); (2) to investigate the compact radio source populations, supernovae, and star formation rates and the interstellar media of nearby star-forming galaxies.

Radio sources detected with VLBI will display characteristic variations as a function of time and frequency that are dependent on their locations with respect to the observing phase centre. Thus, a planet with a radio emitting civilisation, bright enough to be detected, can be identified and separated from human generated signals through VLBI observations. This idea was tested on a VLBI observation of the planetary system Gliese 581. The dataset was searched for candidate SETI signals, in both time and frequency, with amplitudes greater than five times the baseline sensitivity on all baselines. Candidate signals were selected and through the use of automated, statistical data analysis techniques were ruled out as originating from the Gliese 581 system. The results of this study place an upper limit of 7 $\mathrm{MW\,Hz^{-1}}$ on the power output of any isotropic emitter located in the Gliese 581 system, within this frequency range. While the study was unable to identify any signals originating from Gliese 581, the techniques presented are applicable to the next-generation interferometers, such as the long baselines of the Square Kilometre Array.

A multi-epoch, wide-field VLBI survey of the nearby starburst galaxy, NGC 253, is presented. The images revealed seven sources that were detected by previous radio interferometric observations of this galaxy, with no significant changes in flux density and size. The results of this survey were combined with radio data from the literature, spanning 21 years to: investigate the radio spectra and interstellar medium; determine an upper limit of 10^4 km s^{-1} on the expansion speed of the brightest supernova remnant in NGC 253; and develop a model that estimates a supernova rate of $<$0.2 yr^{-1} for the nuclear region of NGC 253, through the incorporation of an improved radio supernova peak luminosity distribution. A star formation rate of $SFR(M \geq 5M_{\odot}) < 4.9\ M_{\odot}\,\mathrm{yr}^{-1}$ was also estimated using the standard relation between supernova and star-formation rates. Our improved estimates of supernova and star-formation rates are consistent with studies at other wavelengths. The results of this study point to the possible existence of a small population of undetected supernova remnants, suggesting a low rate of radio supernova production in NGC 253.

Finally, the results of the most sensitive, highest resolution, wide-field VLBI survey of a nearby face-on star-forming galaxy is presented. Here, the Whirlpool galaxy, M51, is surveyed through the implementation of the technique of simultaneous multi-phase correlation on a single VLBI observation at 18 cm. Six radio sources were detected, two associated with M51 and four background AGNs. The VLBI observations resolve the low-luminosity Seyfert nucleus of M51 into a core-jet structure typical of AGNs. Combining the VLBI results with multiple (epoch and frequency) radio interferometry data, reveal a possible precessing of the parsec jet and a fossil radio lobe located 1.44 kpc from the Seyfert nucleus. An upper limit of the star formation rate of $SFR(M \geq 5M_{\odot}) < 0.044\ M_{\odot}\,\mathrm{yr}^{-1}$ was estimated for the inner nuclear region of M51 through the standard relations of radio emission and star formation rate. The supernova SN 2011dh was imaged 159 days after its explosion and was used to provide a more robust estimate on the light curve at 18 and 6 cm. The four background AGNs were investigated in detail through the combination of X-ray, optical and multi-wavelength radio ancillary data, revealing complex structures and properties of powerful radio galaxies.

Abbreviations, acronyms and symbols

The page number indicates where the symbol or abbreviation is first introduced.

Principal abbreviations and acronyms

VLBI	Very Long Baseline Interferometry (p.1)
DiFX	Distributed FX (p.1)
SXFC	Software XF Correlator (p.1)
JIVE	Joint Institute for VLBI in Europe (p.1)
SETI	Search for Extra-Terrestrial Intelligence (p.1)
VLBA	Very Long Baseline Array (p.3)
NRAO	National Radio Astronomy Observatory
FWHM	Full Width at Half-Maximum (p.3)
EVN	European VLBI Network (p.4)
SNR	Supernova Remnants (p.4)
NOAO	National Optical Astronomy Observatory (p.4)
AGN	Active Galactic Nuclei (p.6)
ISM	Inter-Stellar Medium (p.7)
mJIVE-20	mJy Imaging VLBA Exploration (p.7)
FIRST	Faint Images of the Radio Sky at Twenty cm (p.7)
LBA	The Australian Long Baseline Array (p.7)
ATNF	Australia Telescope National Facility (p.7)
CSIRO	Commonwealth Scientic and Industrial Research Organization (p.7)
MPIfR	Max Plank Institute for Radioastronomy (p.7)
SNe	Supernovae (p.9)
HII	Ionised Hydrogen (p.9)
VLA-A	Very Large Array in A configuration (p.10)
VLA-C	Very Large Array in C configuration (p.12)
HI	Neutral Hydrogen (p.13)

SKA	Square Kilometre Array (p.14)
LOFAR	Low Frequency Array (p.15)
VFASTR	The VLBA Fast Transit experiment (p.17)
MERLIN	Multi-Element Radio Linked Interferometer Network (p.17)
DFT	Discrete Fourier transform (p.19)
DIFMAP	Difference mapping program for synthesis imaging (p.24)
CASA	The Common Astronomy Software Applications package (p.24)
MIRIAD	A data reduction package for radio interferometry (p.24)
FWFM	Fast Wide Field Mapping (p.33)
SEFD	System Equivalent Flux Density (p.36)
AIPS	The Astronomical Image Processing System (p.36)
ATCA	Australia Telescope Compact Array (p.37)
JVLA	The Karl G. Jansky Very Large Array (p.39)
WSRT	The Westerbork Synthesis Radio Telescope (p.39)
SERENDIP	Search for Extraterrestrial Radio Emissions from Nearby Developed Intelligent Populations (p.46)
AU	Astronomical Unit (p.47)
Gl581	Gliese 581 (p.47)
RFI	Radio Frequency Interference (p.48)
Mp	Mopra radio telescope (p.51)
Pa	Parkes radio telescope (p.51)
RA	Right Ascension (p.51)
Dec	Declination (p.51)
ICRF2	The International Celestial Reference Frame (p.51)
FITS	Flexible Image Transport System (p.51)
NASA	The National Aeronautics and Space Administration (p.52)
UT	Universal Time (p.53)
INMARSAT	The International Mobile Satellite Organisation (p.56)
GSO	Geostationary Orbit (p.56)
NP	Neyman-Pearson (p.58)
RSN	Radio supernova (p.67)
ACS	Advanced Camera for Surveys (p.68)
ANGST	Nearby Galaxy Survey Treasury (p.68)
RRL	Radio-recombination line (p.69)
Ho	Hobart radio telescope (p.71)
Cd	Ceduna radio telescope (p.71)
RCP	Right circular polarisation (p.71)
LCP	Left circular polarisation (p.71)
PKS	Parkes Survey (p.71)
IF	Intermediate frequency (p.71)
USNO	United States Naval Observatory (p.73)
PA	Position angle (p.78)
RMS	Root Mean square (p.82)
Cas A	Cassiopeia A (p.89)
Ref	Reference (p.93)

NED	NASA/IPAC Extragalactic Database (p.95)
NIR	Near infrared (p.95)
SFR	Star formation rate (p.98)
FIR	Far infrared (p.99)
Ef	Effelsberg radio telescope (p.104)
Jb1	Jodrell Bank 70 m Lovell dish (p.104)
Wb	Single WSRT dish (p.104)
Mc	Medicina radio telescope (p.104)
On	Onsala 25 m radio telescope (p.104)
Sv	Svetloe radio telescope (p.104)
Zc	Zelenchukskaya radio telescope (p.104)
Bd	Badary radio telescope (p.104)
Ur	Urumqi radio telescope (p.104)
Sh	Shanghai radio telescope (p.104)
CAVE	Curtin ATNF VLBI Experiment (p.108)
LR	Likelihood ratio (p.115)
VLA-B	Very Large Array in B configuration (p.124)
VLA-D	Very Large Array in D configuration (p.124)
HST	Hubble Space Telescope (p.124)
CIAO	Chandra Interactive Analysis of Observations (p.125)
UBVRI	Ultraviolet, blue, visual, red and infrared magnitudes (p.125)
XNC	Extranulcear cloud (p.130)
CSM	Circumstellar medium (p.135)
SSA	Synchrotron self-absorption (p.135)
FR I	Fanaroff-Riley class 1 sources (p.144)
FR II	Fanaroff-Riley class 2 sources (p.144)
SDSS	Sloan Digital Sky Survey (p.146)
ASKAP	Australian Square Kilometre Pathfinder (p.156)

Symbols

λ	Observing wavelength (p.2)
$b_{\max}$	Maximum baseline (p.2)
d	Antenna Diameter (p.3)
Θ	Primary beam or full width at half-maximum of an unblocked aperture (p.3)
$M_{\odot}$	Solar Mass (p.10)
σ	Image sensitivity (p.12)
N_{civ}	Number of detectable civilisations in our Galaxy (p.13)
M_{Earth}	Earth Mass (p.14)
$\Delta\nu$	Frequency resolution (p.15)
δt	Time resolution (p.15)
$\vec{b_{\lambda}}$	Baseline vector (p.21)
τ	Time delay (p.21)
ν	Observing frequency (p.21)

$\vec{s_0}$	Direction of point source (p.21)
V_ν	Response of the interferometer (p.22)
$\vec{s}$	Direction vector of source element offset from $\vec{s_0}$ (p.23)
$d\Omega$	Solid angle of source element represented by $\vec{s}$ (p.223)
$\vec{\epsilon}$	Resulting direction vector between $\vec{s_0}$ and $\vec{s}$ (p.23)
I_ν	The source intensity distribution as observed at the location of the antennas (p.23)
c	Speed of light (p.23)
ϕ	Phase of the recorded signal arising due to τ (p.23)
Σ	Surface of the celestial sphere, equivalent to 4π steradians (p.23)
I_ν^D	Dirty image (p.24)
B	Dirty beam (p.24)
$S(u,v)$	Sampling function (p.24)
θ	Angular resolution (or fringe spacing) (p.25)
n_{pixels}	Number of pixels (p.25)
R_ν	Reduction of amplitude response due to bandwidth smearing (p.27)
I_{re}	Brightness distribution due to frequency averaging (p.27)
I_0	Brightness distribution without bandwidth smearing (p.27)
$\Delta\Theta$	Distance from phase centre (p.27)
ω_{Earth}	Angular velocity of the Earth (p.28)
ω_{vis}	the frequency of the visibilities due to ω_{Earth} (p.28)
R_t	Reduction of amplitude response due to time averaging (p.28)
Γ	Factor that is dependent on the shape of the (u, v) coverage (p.29)
T_{obs}	Total observing time (p.30)
ϕ_{e}	Phase error (p.30)
Θ_{f}	Desired field to image (p.30)
$\Delta\nu_{\text{bw}}$	Total observing bandwidth (p.30)
A	Power reception pattern of a single parabolic antenna (p.34)
f	Complex voltage distribution of the field incident upon the antenna (p.34)
F	Fourier transform of f (p.34)
J_1	The Bessel function of the first kind and first order (p.34)
Θ_{bessel}	The FWHM of J_1 (p.34)
x	Offset from the pointing centre (p.34)
Θ_{ln}	Related to Θ (p.34)
η	System efficiency factor (p.35)
$\Delta\sigma$	The theoretical noise (p.35)
N	Number of elements (or antennas) in an array (p.35)
n_{if}	Number of frequency sub-bands (p.37)
n_{pol}	Number of polarisations (p.37)
n_{ch}	Number of channels (p.37)
S/N	Signal to noise ratio (p.42)
n	Range of positive and negative integers (p.50)
e_{RA}	Positional offset in RA (p.53)
e_{Dec}	Positional offset in Dec (p.53)
H_1	The alternative hypothesis (p.58)

H_0	The null hypothesis (p.59)
$T(x)$	Test statistic related to hypothesis testing (p.59)
p	The significance level of rejecting the null hypothesis (p.60)
τ_0	free-free optical depth at 1 GHz (p.69)
S_P	Peak flux density (p.79)
S_I	Integrated flux density (p.79)
S_m	Modelled flux density (p.81)
S_r	Recovered flux density (p.81)
S_ν	Flux density at frequency ν GHz (p.82)
S_0	Flux density at 1 GHz (p.82)
α	Spectral index (p.82)
τ_ν	Free-free optical depth at ν GHz (p.82)
v	Expansion velocity (p.89)
$\beta_{\rm SN}$	Proportion of SNRs detected (p.90)
ΔF	Type II SNe peak luminosity distribution (p.91)
T_r	Time after optical peak to reach radio peak luminosity (p.91)
β	RSNe luminosity power decay with time (p.91)
χ^2	Chi-square test value (p.92)
$\rm L_{5;CasA}$	5 GHz peak luminosity ratio to Cas As (p.92)
$\rm S_5$	Peak flux density at 5 GHz (p.93)
$\rm L_5$	Peak luminosity at 5 GHz (p.93)
$\nu_{\rm SN}$	Supernova rate (p.95)
$N_{\rm field}$	Number of smaller fields (p.113)
S_m	S/N threshold (p.113)
$\sigma_{\rm SD}$	Standard deviation of Gaussian distribution (p.113)
μ	Mean of Gaussian distribution (p.113)
$N_{\rm freq}$	Frequency of occurrence (p.114)
p(H_0)	The likelihood the pixel is a noise spike (p.114)
p(H_1)	The likelihood the pixel associated with a catalogued source (p.114)
$\rm B_{maj}$	Major beamsize (p.116)
$\rm B_{min}$	Minor beamsize (p.118)
$\nu_{\rm beam}$	Reference frequency of the antenna (p.120)
$S_{\rm IMFIT}$	Flux density measured from IMFIT (p.122)
$S_{\lambda_{\rm eff}}$	Flux density at effective optical wavelength (p.125)
$\rm es^{-1}$	Electrons per second (p.125)
$\rm AB_{mag}$	The absolute flux density for a point source of 1 $\rm es^{-1}$ for a particular ACS filter (p.125)
A	Galactic foreground colour magnitude extinction (p.125)
$C_{\rm es^{-1}}$	Is the total count of $\rm es^{-1}$ (p.125)
$\rm T_B$	Brightness temperature (p.127)
$\theta_{\rm maj}$	The major deconvolved size of a radio source (p.127)
$\theta_{\rm min}$	The minor deconvolved size of a radio source (p.127)
k	The Boltzmann constant (p.127)
L_ν	Radio luminosity at frequency ν (p.132)
Λ	Expected number of random alignments (p.133)

A	Area of field (p.133)
κ	Surface density of sources (p.133)
$d_{\max}$	Distance between the two furthest sources (p.133)
$p_{\max}$	Distance joining two outer sources (p.133)
t_{age}	Supernova age (p.135)
t_0	Explosion date of supernova (p.135)
$r_{2011\text{dh}}$	Radius of SN 2011dh (p.135)
$K1$	A scaling factor related to the flux density at 5 GHz 1 day after t_0 (p.136)
τ_{opt}	Optical depth due to SSA (p.136)
$K5$	Optical depth 1 day after the explosion (p. 136)
δ	The power-law dependency of τ_{opt} on age of SN (p.136)
S_{X}	X-ray flux density (p.139)
S_{R}	Radio flux density (p.139)
N_H	Column density of neutral hydrogen atoms (p.139)
γ	Related to the spectral index (p.139)
S_{opt}	Optical flux density (p.140)
R_{mag}	Johnson-Cousins R-band magnitude (p.140)
R_{L}	Radio loudness parameter (p.141)

Contents

List of Tables

List of Figures

1 Introduction

1.1 Motivation

Science with Very Long Baseline Interferometry (VLBI) has entered a new age. The ability of software correlators (e.g. DiFX, Deller et al. 2007, 2011; and the EVN Software Correlator at JIVE, SXFC Kettenis et al. 2009) to produce data sets with spectral resolution higher than previously achieved, coupled with improved computing facilities, have allowed the VLBI astronomer to venture beyond the traditional narrow fields of view and explore the full primary beam of the instrument. This has allowed wide fields, many arcminutes in radii, to be surveyed with milli-arcsecond resolution and micro-Jansky sensitivity (e.g. Morgan et al. 2011, 2013; Middelberg et al. 2011, 2013). With the next generation of radio interferometers focussed on wide-field, high resolution and deep surveys, the application of high-spectral resolution, wide-field VLBI may serve a dual purpose: a technical pathfinder that prepares astronomers for the challenges presented by the next generation of instruments; and as a technique to work alongside these instruments, providing deep, high resolution, wide field observations.

In this thesis, I will explore two very different science applications for high-spectral resolution, wide-field VLBI. The first concerns the compact radio source populations in nearby star-forming galaxies; two prominent galaxies are studied in detail, with the aim of understanding their radio source populations to further our understanding of the host galaxies. The second concerns a pilot study aimed at exploring the potential of VLBI to search for non-natural radio emission from potentially habitable exoplanets, as part of the Search for Extra-Terrestrial Intelligence (SETI).

In the following sections I will present: the motivation for and a brief description of wide-field VLBI (Section 1.1.1); a background on star-forming galaxies

and their radio source populations (Section 1.2.1); and the quest to detect radio emission from potential habitable exoplanets (Section 1.2.2). The chapter will then end with a concise description of the subsequent chapters.

1.1.1 VLBI

VLBI is a type of interferometry used in radio astronomy, where the longest spacing between individual antennas is hundreds to thousands of kilometres. After or during a VLBI observing session, the signals from the individual antennas are sent to the correlator (Thompson, 1999), a dedicated signal processor, either by recording a digital representation of the analogue waveform incident on the antenna to computer disks, which are later shipped or, more recently, via network links in real-time (Szomoru, 2008). At the correlator the signals from pairs of antennas are aligned, corrected for various geometrical and instrumental effects, and combined coherently (typically Fourier-transformed and multiplied) to produce 4-dimensional (baseline, time, frequency, & polarisation) datasets. The datasets are then used to determine the brightness distribution of the sky at radio frequencies (e.g. Thompson 1999; Thompson et al. 2001). The primary characteristic of VLBI is very high angular resolution. The angular resolution of the interferometer is proportional to $\lambda/b_{\rm max}$, with λ being the observing wavelength and $b_{\rm max}$ the maximum projected baseline. For VLBI, the angular resolution falls in the milli-arcsecond and sub-milli-arcsecond regimes, the highest resolution currently achievable with conventional imaging techniques in astronomy.

The development of VLBI came as a result of a push towards higher angular resolution. Observations of radio sources in the 1960s produced tantalising evidence for the existence of structures with angular sizes smaller than could be resolved with connected (via cables or radio-linked) radio interferometers (Kellermann and Moran, 2001; Clark, 2003). Initially, there was a continuous discovery of unresolved compact sources with increasing baseline length of connected arrays (see Kellermann and Moran 2001, Section 2.3). Second, repeated observations of radio quasars revealed flux density variations on time-scales from days to months (Sholomitsky, 1965; Dent, 1965; Pauliny-Toth and Kellermann, 1966), suggesting linear scales of one light-year or less. If the cosmological interpretation of their redshifts was correct (which we know today to be), then the variation time-scale multiplied by the speed of light divided by the distance indicated sub-arcsecond angular sizes (Miley and Rickett, 1967). Further evidence came from the observed spectral turnover due to synchrotron self-absorption in Gigahertz-Peaked

Spectrum objects (Conway et al., 1963; Bolton et al., 1963).

However, the transition from connected interferometers to VLBI presented new technical challenges, such as: storing, transporting and correlating the data; moving to coherent but independent frequency standards; and accounting for the large delays and phase rates due to the very long baselines (please see Kellermann and Moran 2001 and Clark 2003 for detailed reviews of the technical challenges faced during the development of VLBI). Once the technical hurdles were overcome, the angular resolution of radio interferometers increased from arcminutes to milli-arcseconds, opening up the high-resolution radio Universe. VLBI observations continue to provide important information on many astrophysical processes such as: the structures around Active Galactic Nuclei (AGN), including their accretion disks, powerful relativistic jets and investigation of the intervening intergalactic medium (e.g. Ulvestad et al. 2005; Giroletti and Panessa 2009; Alexandroff et al. 2012; Panessa and Giroletti 2013; Middelberg et al. 2013); the imaging of peculiar binary stars, radio-stars and young supernovae and their remnants, both galactic and extra-galactic (e.g. Lenc and Tingay 2006; Fenech et al. 2010; Martí-Vidal et al. 2011; Bietenholz et al. 2012); spectroscopic investigation of compact maser emitting regions of various kinds in galaxies, star-forming regions and stellar envelopes (e.g. van Langevelde et al. 1992; Sanna et al. 2010; Imai et al. 2012). See the comprehensive review by Middelberg and Bach (2008) for a detailed discussion on the various scientific applications of VLBI past and present.

1.1.1.1 Wide-Field VLBI

Since the astrophysical phenomena observable with VLBI are confined to sub-arcsecond regions, many of the applications of VLBI have mainly been confined to narrow fields of view, typically a few arcseconds. However, the maximum observable field of view of a VLBI observation is given by the primary beam[1], Θ, of the individual antennas (Morgan et al., 2011). For example, the Very Long Baseline Array (VLBA) operated by the National Radio Astronomy Observatory[2], with an antenna diameter of 25 m and an observing wavelength of 20 cm, boasts a primary beam of $\Theta \sim 30'$. However, this is generally not realised as the field of view of a given VLBI dataset is limited due to time and bandwidth

[1]The primary beam is defined as the full width at half-maximum (FWHM) for an unblocked aperture as $1.22 \cdot \lambda/d$, where λ is the observing wavelength and d is the antenna diameter.

[2]The National Radio Astronomy Observatory (NRAO) is a facility of the National Science Foundation operated under cooperative agreement by Associated Universities, Inc.

smearing (Bridle and Schwab, 1999). This has historically been the result of restrictions placed on the number of output channels and integration time by hardware correlators (for example the JIVE Mark IV correlator: see Campbell 2004) and limitations placed on computer storage and processing. Nonetheless, this limiting of the observable field of view was not seen as a concern as it suited many applications of VLBI, and still does.

Early attempts at venturing beyond the typical VLBI fields, while restricted due to bandwidth and time smearing, managed to produce fantastic results. The most common approach was to correlate using the highest frequency and time resolution that was allowed by the hardware correlator, and image without further averaging. An early application led to the detection of multiple hotspots from arcsecond scale jets in the gravitational lens system 0957+561 with the European VLBI Network (EVN) (Garrett et al., 1999). Around the same time, Pedlar et al. (1999) employed this technique to observe a starburst galaxy, M82, and detected multiple supernova remnants (SNR) on VLBI scales. This seminal work led to the development of long term, wide-field VLBI monitoring campaigns to study M82 (McDonald et al., 2002; Beswick et al., 2006; Fenech et al., 2010; Gendre et al., 2013), as well as many similar galaxies such as: NGC 253 (Tingay, 2004; Lenc and Tingay, 2006); NGC 4945 (Lenc and Tingay, 2009); Arp220 (Rovilos et al., 2005; Lonsdale et al., 2006; Parra et al., 2007; Batejat et al., 2011); and Arp299 (Ulvestad, 2009; Romero-Cañizales et al., 2011; Bondi et al., 2012). Further information on starburst galaxies and VLBI is given in Section 1.2.1 and Chapter 4.

Additional methods such as reducing the baseline length and dividing the field into sub-fields for separate imaging were successful in imaging objects arcminutes from the image centre (Garrett et al., 2001, 2005; Lenc et al., 2008, for example). These methods were successfully employed by Garrett et al. (2005) to perform a 1017 arcminute^2 survey of the NOAO Bootes field at 1.4 GHz with the VLBA. Figure 1.1 illustrates the peak amplitude response at different VLBA baselines, due to bandwidth and time smearing for the Garrett et al. (2005) study. The horizontal dashed lines represents a 5% amplitude loss due to bandwidth and time smearing. However, sacrificing the longer baselines results in decreased resolution and sensitivity in these fields. Imaging multiple sources via multiple passes through the correlator can overcome this problem (Rioja et al., 1999; Garrett et al., 2005; Lenc et al., 2008), however as the number of sources increases, this becomes impractical.

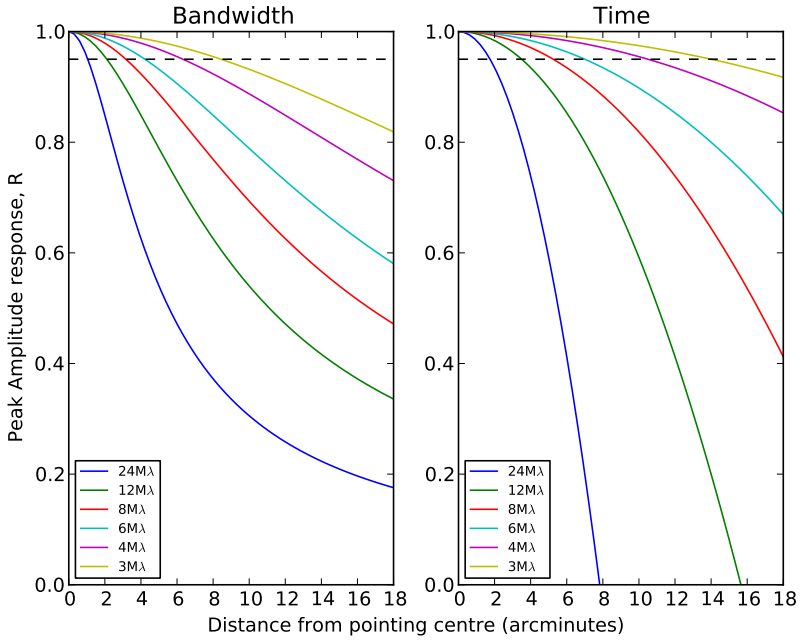

Figure 1.1: The peak amplitude response as a function of distance from the phase centre given by the equations of Bridle and Schwab (1999), for the VLBA observation of the NOAO Bootes field at 1.4 GHz by Garrett et al. (2005), with a spectral resolution of 0.06 MHz and temporal resolution of 0.5 s and the different colours represent different maximum baselines. The plot shows that with shorter baselines, it is possible to image further from the pointing centre with little loss due to bandwidth and time smearing. This was successfully employed by Garrett et al. (2005) to image radio sources up to 18 arcminutes from the pointing centre. Typically an amplitude loss of 5% due to bandwidth and time-average smearing (the dashed lines) is taken as acceptable.

1.1.1.2 Wide-Field VLBI and Software Correlators

Software correlators such as DiFX (Distributed FX[3], Deller et al. 2007, 2011), present fewer constraints on the output time and frequency resolution than traditional hardware correlators. Furthermore, software correlators have been designed to run on modern CPUs under Linux or Mac OS X, which has contributed to software correlators replacing hardware correlators as the preferred method of correlation for a number of the world's leading VLBI facilities (see Section 1.2).

While DiFX provides a number of advantages over hardware correlators (see

[3]The two fundamental operations required to correlate signals are a Fourier transform (F) and cross-multiplication (X). The order of these operations are interchangeable giving rise to the XF and FX correlators. For detailed description on the differences between the two types please see Thompson et al. (2001).

Deller et al. 2007 and Dellar and Brisken 2009 for more details), two main functionalities have allowed imaging of sources throughout the primary beam of a typical VLBI observation. First, fewer constraints on the time and spectral resolution are imposed, allowing sub-kHz and millisecond resolution in the output datasets. Early applications of this functionality allowed VLBI observations of the full nuclear region of starburst galaxies such as NGC 253 (Lenc and Tingay, 2006) and NGC 4945 (Lenc and Tingay, 2009).

Secondly, a recent addition to DiFX makes it possible to simultaneously correlate multiple phase centres within the primary beam (Deller et al., 2011), via uv-shifting (Morgan et al., 2011). Implementation of both methods during correlation can be done to target known sources or to survey an entire field to search for new sources. After the uv-shifts, the datasets are averaged in time and frequency to provide smaller, more manageable datasets, each covering a fraction of the desired field of view. Applying this mode of correlation to the Garrett et al. (2005) approach, smaller visibility datasets would be created at the positions of the 61 surveyed sources without baseline reduction and sensitivity loss, keeping the peak flux densities to within 5% of the true value and keeping the full angular resolution of the longest baselines.

Using this technique Middelberg et al. (2011) successfully imaged 67% of the primary beam with the full VLBA (i.e. up to the maximum baseline of 8611 km), with only a 5% loss due to bandwidth and time-averaging smearing. Middelberg et al. (2011) used this large field of view to observe 96 radio sources in the *Chandra* deep field South brighter than 0.1 mJy[4]; they correlated at the positions of the 96 sources and detected 20. This study was the first to successfully use DiFX to survey a very wide field using multiple phase centres with VLBI. In an attempt to further explore the survey capabilities of VLBI, Middelberg et al. (2013) observed the Lockman Hole/XMM field with multiple, overlapping pointings of the VLBA. Their survey targeted 217 known sources, of which they detected 65, thereby allowing for the first time construction of the source counts of VLBI-detected AGN. In addition to surveying well known fields, this technique allowed Morgan et al. (2013) to detect 16 background AGN within a radius of 35 arcminutes of the core of the nearby galaxy M31 with a single VLBA pointing at 18 cm. They noticed that background AGN closer to the nucleus of M31 were 3-5 times larger than those located at the edge of the galaxy's disk. They concluded that the size difference is due to scatter broadening by the ionised interstellar medium (ISM)

[4]mJy (milli-Jansky) = 10^{-3} Jy; where 1 Jy (Jansky) = $10^{-26}\,\mathrm{Wm^{-2}Hz^{-1}}$; is the standard unit of flux measurement in radio astronomy

of M31, similar to the inner disk of our Galaxy (van Langevelde et al., 1992; Lazio and Cordes, 1998).

Utilising the multiple phase centre correlation technique, Deller and Middelberg (2014) embarked on the largest 20 cm VLBI imaging campaign to date. Their project, the mJy Imaging VLBA Exploration, or mJIVE-20 makes use of filler time (i.e. short segments scheduled in bad weather and/or with a reduced number of antennas, during which no highly rated science projects can be scheduled) on the VLBA to survey sources pre-selected from the Very Large Array Faint Images of the Radio Sky at Twenty cm (FIRST) survey (Becker et al., 1995). The survey has thus far covered almost 200 $\deg^2$, with more than 20,000 sources, which was achieved through the use of the multi-phase technique to place phase centres at the locations of multiple FIRST sources within $20'$ of the beam centre per pointing. The mJIVE-20 project aims to image all FIRST sources, thereby providing the largest ever VLBI survey to date. VLBI through the capabilities of software correlators, has finally become a true large-scale survey technique.

1.2 Scope of Thesis

The work described in this thesis applies the techniques of wide-field VLBI to improve our understanding of nearby star-forming galaxies. This study is an extension of the work by McDonald et al. (2002), Tingay (2004), Lenc and Tingay (2006) and Morgan et al. (2013), and aims to understand both the compact radio source population and the ionised media in the galaxies. This thesis also investigates the suitability of VLBI for detecting radio emission from potential habitable planets as part of the Search for Extra-Terrestrial Intelligence (SETI). Both projects utilise the powerful functions of the DiFX software correlator. Each of the science applications will be discussed in more detail in the following subsections.

Two main VLBI facilities were used in this project: the Australian Long Baseline Array (LBA)[5], which comprises eight antennas of various diameters across Australia and New Zealand; and the European VLBI Network (EVN)[6] which comprises 15-20 antennas, also of various diameters located mainly in Europe,

[5]The LBA is operated by the Australia Telescope National Facility (ATNF) of the Commonwealth Scientic and Industrial Research Organization (CSIRO) Astronomy and Space Science (CASS) Division, and by the University of Tasmania (UTas)

[6]The European VLBI Network is a joint facility of European, Russian, Chinese, South African and other radio astronomy institutes funded by their national research councils

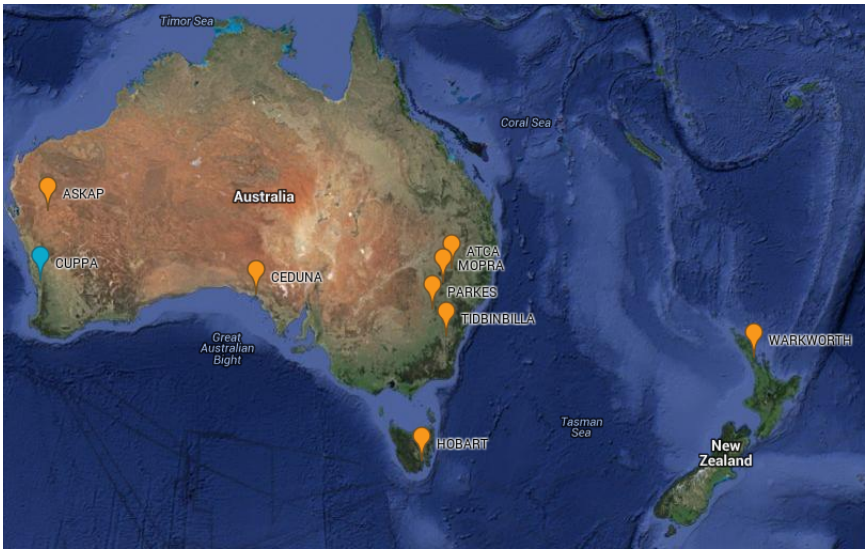

Figure 1.2: Location of the antennas that make up the Australian Long Baseline Array and the correlator, CUPPA (Curtin University Parallel Processor for Astronomy) located at Curtin University, Perth, WA. Image credits: Google maps

Russia and Asia. The locations of the main antennas and the correlators used by both arrays are displayed in Figures 1.2 and 1.3.

Since 2006 the LBA has been using DiFX as the preferred correlator, while the Max Plank Institute for Radioastronomy (MPIfR) has begun routine operation of DiFX in parallel with the EVN hardware correlator. Furthermore, the Joint Institute for VLBI in Europe (JIVE) has recently developed their own software correlator, the SXFC[7] (Kettenis et al., 2009) and has begun offering this as the preferred method for correlating EVN observations.

Two projects of this thesis (Chapters 3 & 4) made use of DiFX version 1 (Deller et al., 2007), that allows high time and frequency resolution, while the third project (Chapter 5) benefited from the DiFX version 2 (Deller et al., 2011), that incorporates full wide field functionality (i.e. both high time and frequency resolution and uv-shifting). Aside from the LBA and EVN, the VLBA operated by the NRAO has replaced its hardware correlator with DiFX and has been successfully used for wide-field VLBI (see the previous sections). However, observations from the VLBA were not used in this thesis.

[7] `http://www.jive.nl/jivewiki/doku.php?id=sfxc`

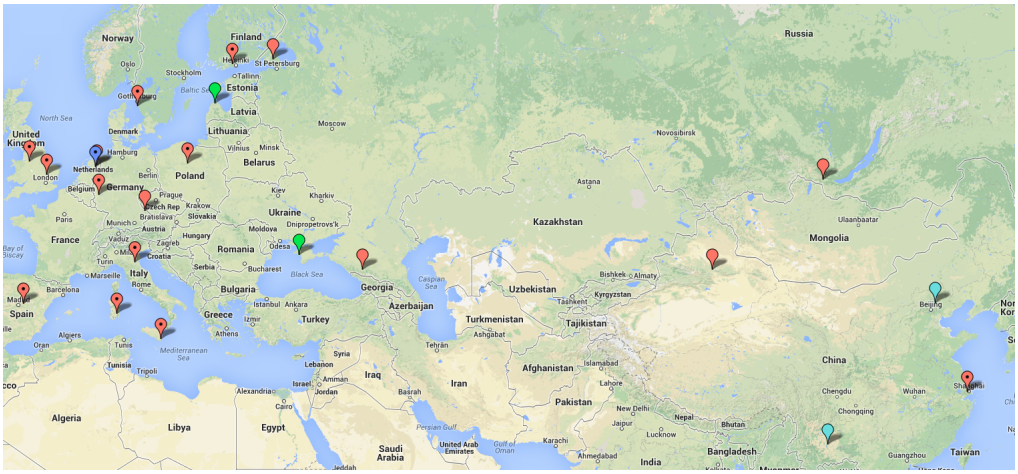

Figure 1.3: Location of the antennas commonly used in the European VLBI Network, and the correlator located at the Joint Institute for VLBI in Europe (JIVE), in the Netherlands (blue marker). Image credits: Joint Institute for VLBI in Europe and Google maps

1.2.1 Star-Forming Galaxies

Star-formation is a fundamental astrophysical process, existing in almost all galaxy types[8] and is responsible for a wide range of phenomena such as the evolution of galaxies (e.g. Somerville et al. 2001; Somerville 2008; Papovich et al. 2011), nucleosynthesis (Section 9.3, Prialnik 2000), planet formation (Section 10.3, Prialnik 2000) and the origin of life (Ehrenfreund et al., 2002). In this thesis, star-forming galaxies are defined as galaxies that are actively forming stars in the disk and/or circumnuclear regions. In these galaxies, the radio emission is not dominated by a supermassive black hole or related nuclear engine, but by synchrotron emission from Type II and Type Ib supernovae (SNe), whose remnants are thought to accelerate most of the relativistic electrons, and free-free emission from HII regions associated with gas ionised by hot, young stars (e.g. Condon 1992; McDonald et al. 2002). However, it is not uncommon for star-forming galaxies to host a low luminosity Seyfert AGN (e.g. Ford et al. 1985; Pellegrini et al. 2000; Lenc and Tingay 2009; Perez-Torres et al. 2010; Rampadarath et al. 2010; Paggi et al. 2013; Panessa and Giroletti 2013).

Star-forming galaxies can be separated into normal galaxies and starburst galaxies, where the star-formation in the latter is at least an order of magnitude greater than normal galaxies and is generally circumnuclear (Kennicutt, 1998).

[8]It was previously thought that star-formation occurs only in late type galaxies such as spiral and irregular galaxies (Kennicutt, 1998). However, recent evidence suggests that early type (E/S0) galaxies are also actively forming stars (Crocker et al., 2011).

Nonetheless, the products of the star-formation process in both types are similar; massive stars ($M > 8M_{\odot}$) that form SNe (Condon, 1992; Prialnik, 2000), and less massive stars that evolve into white dwarfs (Prialnik, 2000), which are typically found within stellar clusters (Clarke et al., 2000). These objects play an important role in galaxy evolution, via a feedback process where material is ejected back into the ISM (Efstathiou, 2000; Lagos et al., 2013). In addition, the collective energy from this process is thought to be the driving factor behind the massive super-winds found in nearby galaxies such as M82 (Ohyama et al., 2002) and NGC 253 (Boomsma et al., 2005), which can suppress star-formation (Bolatto et al., 2013).

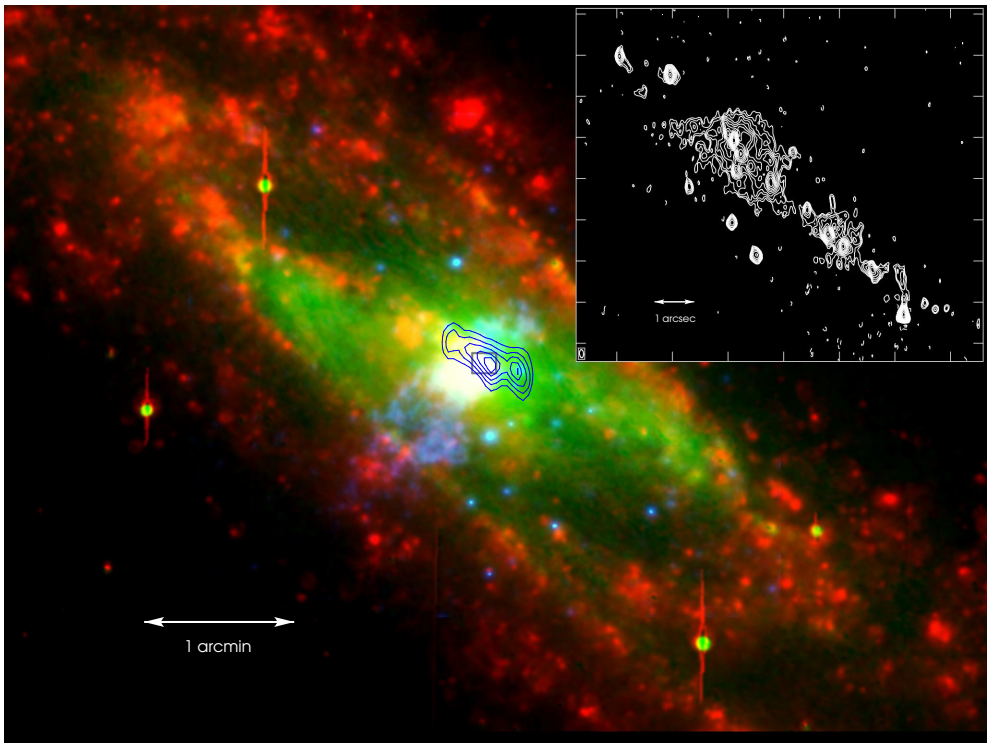

Figure 1.4: Multi wavelength view of NGC 253. The red, green and blue colours represents Hα, infrared and soft X-ray emission, respectively. The Owens Valley Radio Interferometer CO emission-line contour map of the inner 3 kpc is shown in blue with contours at 19%, 38%, 57%, 76%, and 87% of the peak. The inset shows the VLA-A configuration 2 cm image from Ulvestad and Antonucci (1997) of the central boxed region, with contours are in logarithmic intervals of $\sqrt{2}$, beginning at 0.23 mJy/beam. Image courtesy: Lenc and Tingay (2006)

The radio SNe eventually evolve into supernova remnants (SNRs) when the blast wave expands into the surrounding denser ISM (Woltjer, 1972; Ferreira and de Jager, 2008), producing the well-known shell structures observed both in our Galaxy and in nearby star-forming galaxies such as M82 and NGC 253. As these

objects evolve, the shells sweep up matter, expand and slow down to ultimately merge with the ISM (see Woltjer 1972 for a description of the stages of SNR evolution). The duration of the SNR stage depends strongly on the density of the surrounding medium and can be decades to centuries (Woltjer, 1972; Ferreira and de Jager, 2008).

While these objects are individually interesting, a population of SNe and SNRs within a galaxy can provide statistical information concerning their evolution, the surrounding ionised medium (for example optical depth), as well as provide knowledge on the star-formation history of the galaxy. Nearby galaxies, for example NGC 253 (Figure 1.4) and M51 (Figure 1.5), are ideal laboratories for studying these processes on parsec and sub-parsec scales. Additionally, since the objects local to these galaxies are essentially at the same distance, studies with the same angular resolution and sensitivity are free from selection effects (Fenech et al., 2010). While the regions of intense star-formation can be studied across the electromagnetic spectrum, the high resolution studies provided by radio interferometry reveal objects that are otherwise obscured by the high levels of gas and dust associated with star-formation (example NGC 253, Figure 1.4). Additionally, observing these regions over closely spaced multiple epochs with high sensitivity radio interferometry allows an opportunity to discover new SNRs that may be detectable for only a short period, thus providing tighter constraints on core-collapse supernova and massive star-formation rates (Lenc and Tingay, 2006). Furthermore, the disks of these galaxies, which are arcminutes in size, provide an opportunity to detect a population of background AGN with wide-field VLBI, which can be used to probe the ionised medium of the foreground galaxy (e.g. Morgan et al. 2013).

In this thesis, the high angular resolution of VLBI arrays, in conjunction with the wide-field capabilities of DiFX, are used to observe and monitor two nearby (distance $\leq$10 Mpc) star-forming galaxies. The galaxies chosen for this study are: the southern edge-on starburst galaxy NGC 253 (Figure 1.4); and the Whirlpool galaxy (M51, NGC 5194) which is a grand-design spiral galaxy, with a face-on orientation (Figure 1.5).

The difference in orientation of M51 and NGC 253, means that the amount of ionised matter the compact radio sources are seen through in each case is different. Sources within NGC 253 would have a higher chance of being seen through higher density compared to sources within M51. Thus, high resolution radio observations of sources within and behind (e.g. background AGNs) edge-on galaxies such as NGC 253, may be affected by higher optical depths and even

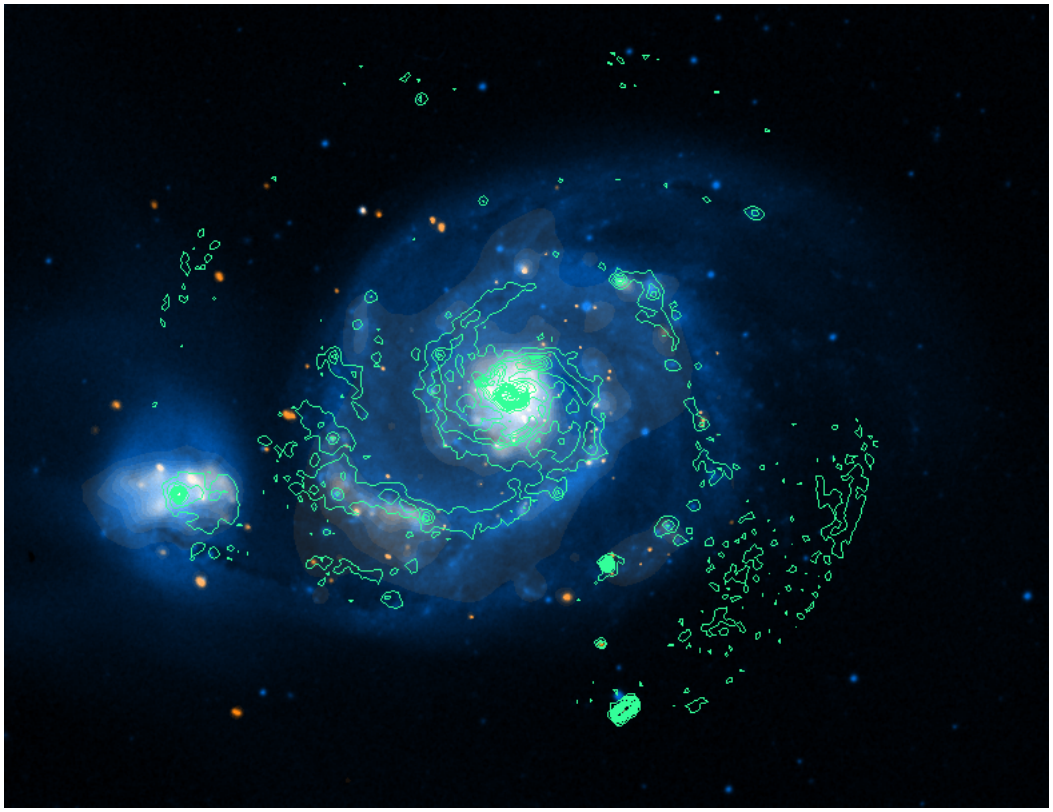

Figure 1.5: Multi-wavelength composite image of the Whirlpool galaxy, M51. The blue and red colours indicates optical 610 nm image from the Palomar/Caltech Digitized Sky Survey (courtesy Aladin sky server) and *Chandra* soft X-rays (courtesy R. Soria) respectively. The green contours are VLA-C configuration 6 cm archive data, in intervals of $3n\sigma$, where $n = \{1, 3, 5, 7, ...\}$, and $\sigma = 18.9$ μJy/beam.

greater scattering than face-on galaxies.

Aside from their orientation, both galaxies differ by their star-formation and the dominant radio emission mechanism. In NGC 253, the star-formation is concentrated within the nuclear region, possibly arising from a tidal disruption (Davidge, 2011), that resulted in the radio emission within this region being dominated by SNRs (see Chapter 4). Through the use of multi-epoch, multi-wavelength radio data from the literature, spanning decades, Chapter 4 presents a model that aims to provide tighter constraints on the core-collapse SN and massive star-formation rates of this galaxy, that is free from contamination by AGN activity or other forms of radio emission. This type of study is important as it provides an independent measure that can be used to determine the validity of other measurements.

In M51, which is currently undergoing a merger with a smaller companion

galaxy, NGC 5195, the star-formation is distributed mainly in the spiral-arms with a slight increase in star-formation rate nearer to NGC 5195 (Kaleida and Scowen, 2010). Furthermore, its nuclear region is dominated by a low-luminosity Seyfert galaxy with a bipolar jet (see Chapter 5) that is apparently not associated with the general galactic star-formation. In Chapter 5, the full disk of M51 is surveyed using the high sensitivity of the EVN to provide the deepest, highest resolution, wide-field radio survey of a nearby face-on star-forming galaxy. The VLBI data are compared to multi-wavelength archive data from X-ray, optical and radio instruments, to help in understanding the nature of the radio source population of M51 and estimate the supernova and high mass star-formation rate of the nuclear region.

1.2.2 Searching for Radio Emission from Potential Habitable Exoplanets

In the 1950s and 1960s, radio astronomy was a new field. Grote Reber had not long before made the first map of the radio sky and with the development of radio astronomy technologies, astronomers soon realised that the radio universe was teeming with new and exotic natural wonders. At this time a few individuals began to wonder about the possibility of using the radio telescopes to detect signals from technically advanced civilizations from beyond our Solar System. This recognition produced three key events, that led to the creation of an entirely new scientific field.

First, in 1959, Giuseppe Cocconi and Philip Morrison published a seminal paper in Nature with the controversial title "Searching for Interstellar Communications" (Cocconi and Morrison, 1959). In it they proposed that radio telescopes had become sufficiently sensitive to detect radio transmissions that might be broadcast by civilisations orbiting other stars. They proposed that the signal could be transmitted at the 21 cm (1420 MHz) HI line, since being the most common element in the universe, it should be known to every observer and seen as a standard universal frequency.

At around the same time Frank Drake began *Project Ozma*, the first survey dedicated to search for extra-terrestrial intelligence (SETI) (Drake, 1961). By using a 26 m dish, Drake monitored two nearby Sun-like stars, for six hours per day between April and July 1960 at the 21 cm line, with no success.

The third key event could be considered the formulation of the famous Drake

Equation in 1961[9], that aims at estimating $N_{\rm civ}$, the number of detectable civilisations in our galaxy. However, this equation is far from able to provide an actual approximation to $N_{\rm civ}$, due to the simplistic nature of the algebraic expression and because most of the parameters are difficult to estimate. A more direct approach at estimating $N_{\rm civ}$ would be to monitor all known habitable planets for the evidence of life.

At the time of these events, it was unknown whether planets existed (though strongly suspected) around other stars, much less habitable ones. Today, due to advances in astronomical techniques and instrumentation, ∼900 exoplanets have been found orbiting ∼600 stars, with more than 3,000 candidates yet to be confirmed from the *Kepler* space mission[10]. The high percentage of stars with planets has led Cassan et al. (2012) to the conclusion that stars in our Galaxy are orbited by planets as a rule not an exception.

Moreover, there are a number of observing programs (past, present and future), both ground and space based, dedicated to detect exoplanets that lie within their host star's habitable zone. The habitable zone is defined as the circumstellar region in which a terrestrial mass planet ($0.1M_{\rm Earth} \leq M \leq 10M_{\rm Earth}$), with favourable atmospheric conditions, can sustain liquid water on its surface (Hart, 1978; Kasting et al., 1993; Kopparapu, 2013), and thus possibly sustain life as we know. To date, 20 exoplanets have been discovered to be potentially habitable[11], and 62 additional candidates from the *Kepler* space mission (Gaidos, 2013). Additionally, it is estimated that the frequency of Earth-like planets in the habitable zone of M-dwarf stars lies between 48% to 61% (Kopparapu, 2013), indicating that the potential of finding habitable planets may be higher than reported. Thus, Earth may not be as unique as was always thought. In fact, it is possible that these potentially habitable planets may harbour life, and, while the probability is low they may eventually develop radio emitting technologies, these planets would nonetheless provide viable targets for current and future SETI programs, with the next generation of radio telescopes such as the Square Kilometre Array (SKA, Carilli and Rawlings 2004).

Figure 1.6 shows the minimum detectable flux density at 1.4 GHz for a few of the world's leading radio facilities, including the future SKA. The figure also shows the expected flux densities for a number of radio emitters as a function of distance in light years (Tarter, 2004). The proposed SKA is a factor of two

[9]The Drake Equation Revisited, Astrobiology Magazine. 29 September 2003.

[10]NASA exoplanet archive: `http://exoplanetarchive.ipac.caltech.edu/`

[11]`http://phl.upr.edu/projects/habitable-exoplanets-catalog`

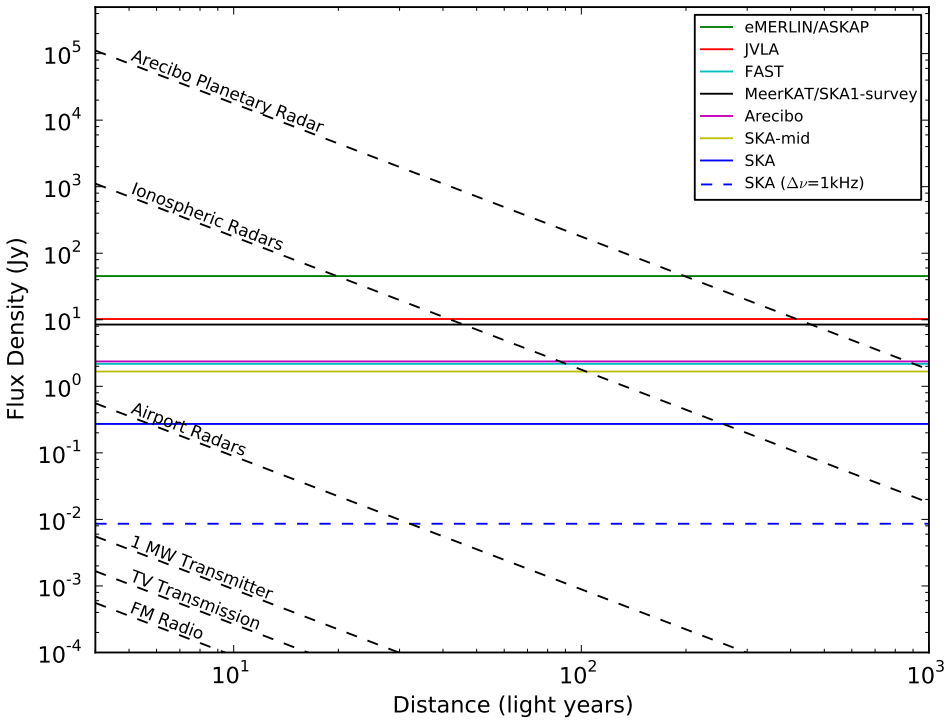

Figure 1.6: Plot showing the minimum flux density detectable, at 1.4 GHz, for a number of radio frequency emitters (from Tarter 2004), as a function of distance in light years. Included are the 1.4 GHz sensitivity (1σ) for a number of current and future radio facilities, assuming a frequency resolution, $\Delta\nu = 1$ Hz and integration time, $\delta t = 1$ s. The sensitivity for the SKA was taken from Dewdney et al. (2009), while the other facilities were obtained from the SKA1 baseline design (Dewdney et al., 2013, Table 1). Included are the sensitivity for the SKA with $\Delta\nu = 1$ kHz.

more sensitive than all current and future radio facilities. It is notable that with an increased bandwidth, it may be possible to detect even fainter, but broader band, transmissions with the SKA.

The search for extra-terrestrial intelligence is listed as part of the *Cradle of Life* key science project for the SKA (Carilli and Rawlings, 2004), and currently the SKA pathfinder, the Low Frequency Array (LOFAR)[12], has begun to search for low frequency radio signals from civilisations on planets orbiting nearby stars. In this thesis, the idea of SETI with the SKA is taken further with the design and

[12] `http://www.astron.nl/about-astron/press-public/news/lofar-opens-low-frequency-universe-and-starts-new-seti-search/lofar-o`.
Prof. M. Garrett was recently awarded the IBM Faculty Award for this pioneering work. See `http://www.ibm.com/news/be/en/2013/09/17/j078203h20140f36.htmlfordetails`.

implementation of a proof-of-concept VLBI SETI experiment. The use of VLBI as a test-bed for the techniques required for SETI with the SKA is strongly motivated by the possibility of the addition of long baselines to the SKA (Dewdney et al., 2009; Lobanov, 2012; Godfrey et al., 2012). Thus allowing efficient discrimination of artificial signals originating from potentially habitable planets from the radio emission of their host star and terrestrial sources.

The capabilities of the SKA place it as the next leading radio astronomical facility, not only in sensitivity, but field of view, survey speed and frequency agility. In the words of Cocconi and Morrison *"The probability of success is difficult to estimate; but if we never search, the chance of success is zero"*. Thus, it would be worthwhile to use this instrument to search for an answer to the question that has puzzled humankind for many years.

1.3 Thesis Outline

In Chapter 2, the development of a framework for wide-field VLBI will be presented. First, the fundamentals of aperture synthesis are introduced, followed by the special challenges associated with imaging wide-fields with VLBI, including methods of overcoming these challenges e.g. through the capabilities of the DiFX software correlator. A practical guide to preparing and imaging wide-field VLBI observations is discussed and the chapter will end with a brief description of non-imaging applications of high frequency resolution, wide-field VLBI to SETI.

Chapter 3 will present a proof-of-concept study, aimed at investigating the use of VLBI for targeted SETI. The chapter will begin with a brief discussion of SETI, including the various parameter space and search strategies. This is then followed by a discussion of the advantages of using VLBI for SETI and the description of the technique developed in this thesis. The application of the technique to a test field is then described, including the target, observations and the results. The chapter is then concluded with discussions emphasising the application of this technique to other VLBI arrays, including the SKA.

In Chapter 4, the results of multi-epoch observations of the southern starburst galaxy, NGC 253, with the LBA at 2.3 GHz are presented. The chapter begins with a discussion on starburst galaxies, including NGC 253, with particular emphasis of the benefits of high-resolution, wide-field radio interferometry. The observations, calibration and data analysis methods are then presented. The results are used to explore various properties of the starburst region including the ionised medium and a detailed study of the brightest radio supernova in NGC 253.

An improvement of the Monte-Carlo method of Lenc and Tingay (2006) was developed to determine the supernova rate, taking into account an updated peak luminosity distribution of radio SNe at 5 GHz that was derived using data from the literature. The results of this simulation are then discussed, including the effects on the star-formation rate.

Chapter 5 presents the widest, deepest and highest resolution survey of a nearby grand-design, spiral galaxy to date. Here, the compact radio source population of the Whirlpool galaxy M 51 is studied with the EVN at 1.6 GHz, via implementation of the wide-field VLBI technique. An area of $11'.2 \times 6'.9$ is surveyed with a single EVN pointing. Using the simultaneous multi-phase centre function of DiFX, the galaxy was tiled with 192 individual fields of radius of $\sim 20''$. The results of this survey are compared to archived MERLIN and VLA observations, and multi-wavelength data at optical and X-ray wavelengths. The work presented in this chapter aims to provide a complete test space for the framework described in Chapter 2.

Finally, Chapter 6 will present the conclusions of the work discussed in the preceding chapters, including a discussion of future extensions of the research presented in this thesis.

1.4 Statement of Originality

At the time of the realisation of this thesis, VLBI was entering a new era. With the development of the software correlators, the restrictions placed by hardware correlators were finally overcome, thereby, providing the means to explore new and different scientific applications with VLBI, including high time resolution radio astronomy (e.g. the V-FASTR experiment, Wayth et al. 2011) and wide-field surveys of star-forming galaxies and AGN (see the previous sections for more information). With the next generation of radio interferometers focussing on wide-field, deep surveys, the application of DiFX capabilities to a wide range of scientific applications will provide useful preparation.

This thesis was formulated to explore new scientific applications with VLBI, requiring the many capabilities of software correlators. The first part of this thesis tested the suitability of VLBI for targeted SETI. This was the first ever SETI experiment performed with VLBI and successfully demonstrated that the unique properties of VLBI when paired with the DiFX software correlator makes it an efficient discriminator between SETI signals and radio frequency interference. To effectively test the technique, 32768 channels were generated over a bandwidth of

64 MHz per six sub-bands at an unprecedented frequency resolution of 1.953 kHz. The ratio of frequency resolution to bandwidth of this experiment was to date the highest for any VLBI experiment and required development of new techniques to process the data and search for the desired signals.

The next part of the thesis is the third in a series of papers aimed at determining the nature of the compact radio source population, the supernova history and understanding the interstellar medium of the nuclear region of NGC 253 through the use of wide-field VLBI. This research was the first to use multi-epoch VLBI observations, along with multi-wavelength radio data spanning 21 years to develop an accurate model for estimating the radio supernovae rate of the galaxy. The results of this study provided further insight into the interstellar medium and pointed towards a low rate of radio supernova production in NGC 253.

To date little work has been done on surveying face-on star-forming galaxies with VLBI. All studies of these galaxies with VLBI have so far concentrated on the nuclear region or targeted observations of known supernovae, and has paid little or no attention to the surrounding regions. Hence, the final part of this thesis is a major survey of a nearby face-on galaxy, M51 with the EVN. This study is the highest ever resolution, wide-field survey of a nearby grand-design star-forming galaxy, and the first wide-field VLBI study to venture to the edge of the primary beam of an heterogeneous array. This study also aims to test the survey capabilities of wide-field VLBI by performing the first blind survey of a star-forming galaxy with the multi-phase correlation method. Furthermore, the abundance of X-ray, optical and multi-wavelength radio ancillary observations that were used to investigate the individual sources detected with wide-field VLBI, demonstrated the scientific wealth of such a study.

At the conclusion of this PhD thesis, while the use of wide-field VLBI to survey star-forming galaxies is in its infancy, the work generated by this thesis has provided a number of unique opportunities that can be used as the basis for long term studies of these and similar galaxies. Furthermore, this thesis has demonstrated that it is both feasible and attractive to perform targeted SETI with VLBI, which has generated interest at both public and scientific levels.

1.5 Contributions by Others

The work presented in this thesis was carried out between October 2010 and April 2014, at Curtin University. However, the ideas and means to carry out the studies presented in this thesis would not be possible without a collaborative

environment, through interactions with colleagues from Curtin University, the University of Sydney, the University of Manchester, and the Institut de Radioastronomie Millimétrique. Specific contributions by others are as follows:

- Chapter 3 - the LBA observations of Gliese 581 were conducted by Steven Tingay (Curtin University); the idea to use discrete Fourier transform (DFT) to determine the phase variations with time and frequency of potential SETI signals was by John Morgan (Curtin University); and the hypothesis testing to discriminate between false positives from true signals was developed by Cathryn Trott (Curtin University and CAASTRO[13]).

- Chapter 4 - the LBA observations were proposed and scheduled by Emil Lenc (the University of Sydney, and CAASTRO) and Steven Tingay; the ParselTongue script to convert individual channels to sub-bands to allow wide-field VLBI imaging in Difmap and the initial free-free absorption and Monte-Carlo simulation codes were developed by Emil Lenc; and assistance to calibrate the LBA datasets were given by Cormac Reynolds (Curtin University).

- Chapter 5 - development of the parallel ParselTongue code and calibration of the EVN dataset benefited from assistance from Cormac Reynolds; the likelihood ratio method to search for VLBI counterparts using catalogued sources was developed by John Morgan and Cathryn Trott; the primary beam correction model that was incorporated in this study was developed by John Morgan; the calibrated MERLIN data were provided by Megan Argo (the University of Manchester); the calibrated VLA data were provided by Gaelle Dumas (Institut de Radioastronomie Millimétrique); and continuum subtracted Hα Hubble Space Telescope data and X-ray spectra were provided by Roberto Soria (Curtin University).

[13]ARC Centre of Excellence for All-sky Astrophysics

2 A Framework for Wide-Field VLBI

2.1 Introduction

In this chapter, the technique of wide-field VLBI is treated in both a theoretical and practical manner. Starting from the fundamentals of radio interferometry and conventional imaging, the work presented in this chapter aims to: highlight where the standard assumptions are not valid for wide-field VLBI imaging; and to provide suitable methods for overcoming these limitations. However, it should be noted that the purpose of this chapter is not to present a deep treatment of the theory of radio interferometry and synthesis imaging, but to provide a practical framework so the wide-field VLBI techniques employed in the following chapters can be fully understood. Furthermore, where appropriate, imaging and calibration techniques are briefly discussed but will be treated in more detail in the individual chapters. For further information and a deeper discussion of radio interferometry, the reader is referred to the standard texts such as Taylor et al. (1999) and Thompson et al. (2001).

2.2 Fundamentals of Radio Interferometry and Aperture Synthesis

Figure 2.1 depicts a two-element interferometer. The antennas, 1 and 2, are separated by a baseline vector, $\vec{b_\lambda}$, and are pointing towards a radio source located in the far field of the interferometer, defined by the direction vector, $\vec{s_0}$. The wavefront of the radio emission arrives at antenna 1 with a time delay, τ, with respect to antenna 2. In a typical interferometer, the source under observation is tracked via the application of a delay model to correct for τ. This sets the delay

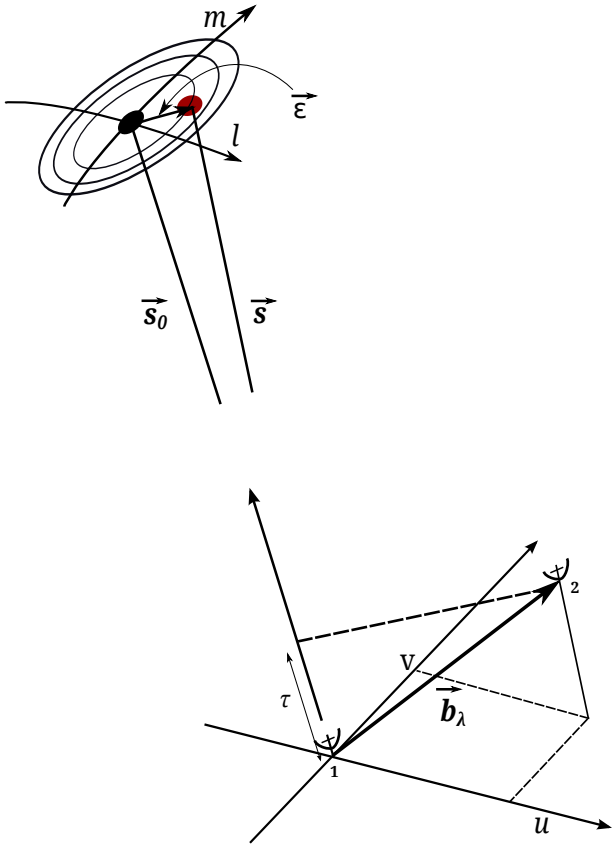

Figure 2.1: A typical two-element interferometer separated by the baseline vector, $\vec{b_\lambda}$. The phase centre represented by the vector $\vec{s_0}$ is the centre of the interferometer's field of view. $\vec{s}$ points in the direction of a source offset from $\vec{s_0}$, by $-\vec{\epsilon} = \vec{s_0} - \vec{s}$. A wavefront from a radio source at the phase centre will arrive at antenna 2 before antenna 1, with a time delay, τ. (Image following Figure 3.2 from Thompson et al. (2001)).

to zero at a location commonly referred to as the phase tracking centre, the phase reference position or simply phase centre.

The signals received by the individual antennas are passed through a number of different electronic circuits designed to amplify the weak signals and select the required frequency band of a finite width centred on ν. The resulting signals from the antennas are then combined in a correlator, which is essentially a voltage multiplier followed by a time integrator (Thompson, 1999). This results in the response of the interferometer, $V_\nu(\tau)$, complex quantities, of discrete samples of frequency and time, known as visibilities, where amplitude and phase are the fundamental observables (Thompson, 1999; Thompson et al., 2001).

If the direction of the phase centre in Figure 2.1 is taken as the vector $\vec{s_0}$,

then the direction vector $\vec{s}$ to an element of the source is offset from $\vec{s_0}$, by $-\vec{\epsilon} = \vec{s_0} - \vec{s}$. The response of the interferometer can be expressed as (Thompson 1999 and Thompson et al. 2001, Chapter 3):

$$V_\nu(\vec{\epsilon}) = |V_\nu|e^{i\phi} \approx \int_\Sigma I_\nu(\vec{\epsilon})e^{-2\pi i\nu\tau}d\Omega, \\ \approx \int_\Sigma I_\nu(\vec{\epsilon})e^{-2\pi i\nu(\vec{b_\lambda}\cdot\vec{\epsilon}/c)}d\Omega, \tag{2.1}$$

where $I_\nu(\vec{\epsilon})$ is the source brightness distribution in solid angle as observed at the location of the antennas, corresponding to a visibility phase, $\phi = 2\pi\nu\tau$ and amplitude, $|V_\nu|$. The integral in Equation 2.1 is one form of the *spatial coherence function* and is taken over the entire surface, Σ, of the celestial sphere. However, in practice the integral is restricted by the field of view of the individual antennas.

As the Earth rotates on its axis, the baseline vector will change orientation and projected length in a plane perpendicular to $\vec{s_0}$. Once the delay model has been applied, a coordinate system can be chosen to describe the projected baselines with respect to $\vec{s_0}$. This is done using a plane perpendicular to the line-of-sight, commonly referred to as the (u, v) plane, where u and v are measured towards the east and north, respectively, and the w axis points along the direction of interest, i.e. $\vec{s_0}$ (Thompson, 1999). The projected baselines in (u, v) coordinates, in practice, are measured in units of wavelengths. The location of the source in the plane of the sky is given by the coordinates (l,m), where, l and m are direction cosines measured with respect to the axes of u and v. Using this coordinate system, the general response of the interferometer to the brightness distribution of the source can be expressed as (Thompson et al., 2001, equation 3.7):

$$V_\nu(u,v) \approx \int\int I_\nu(l,m)e^{-2\pi i[ul+vm+w(\sqrt{1-l^2-m^2}-1)]}\frac{dldm}{\sqrt{1-l^2-m^2}}. \tag{2.2}$$

In many standard VLBI observations, the fields of view are sufficiently small that the third term in the exponential can be ignored i.e. $\sqrt{1-l^2-m^2}-1 \approx 0$. This is an important assumption and will be explored further in Section 2.4.2. Under this assumption, Equation 2.2 simplifies to a two-dimensional form:

$$V_\nu(u,v) \approx \int\int I_\nu(l,m)e^{-2\pi i(ul+vm)}dldm. \tag{2.3}$$

Equation 2.3 can be inverted to recover the brightness distribution of the radio source:

$$I_\nu(l,m) \approx \int\int V_\nu(u,v) e^{2\pi i(ul+vm)} dudv. \tag{2.4}$$

During a typical observation of a few hours, the spatial coherence function, $V_\nu(u,v)$, will be sampled at many points in the (u,v) plane by the different baseline vectors of the array. However, this sampling is not typically complete over the full (u,v) plane, but restricted to discrete locations. The sampling traces out ellipses, whose lengths are dependent on the total observing time, the width are dependent on the number of frequency samples (i.e. number of channels and sub-bands), and the radii on the baseline length. Examples of (u,v) plane sampling are given in Figures 3.2, 4.1 and 5.2.

Thus, it is not possible to invert Equation 2.4 to obtain I_ν. However, by describing the (u,v) plane sampling through the function, $S(u,v)$, such that its value equals zero where there are no measurements, Equation 2.4 can be rewritten as,

$$I^D_\nu(l,m) \approx \int\int S(u,v) V_\nu(u,v) e^{2\pi i(ul+vm)} dudv, \tag{2.5}$$

where $I^D(l,m)$, is referred to as the *dirty image* and is related to the true brightness distribution, $I(l,m)$, via the expression,

$$I^D_\nu \approx I_\nu * B, \tag{2.6}$$

where $*$ denotes convolution, and B is referred to as the *dirty beam* and is related to the sampling function,

$$B(l,m) \approx \int\int S(u,v) e^{2\pi i(ul+vm)} dudv. \tag{2.7}$$

In practice, I_ν can be estimated through a deconvolution process (Cornwell et al., 1999), since the product $B(l,m)$ can be derived from the sampling of the (u,v) plane.

2.3 Wide-Field VLBI

The term "wide-field VLBI" has been used, and will be used often in this document. In Section 1.1.1.1 the idea of imaging over wide fields was introduced, including attempts to overcome various limitations (which will be discussed in greater detail later in this chapter). If the desired field contains multiple compact radio sources, separated by tens of arcseconds or arcminutes, wide-field

VLBI techniques may be applicable. However, before proceeding further, the term "wide-field VLBI" will be treated in a quantitative manner.

The long baselines of VLBI arrays, that result in high angular resolution, differentiate them from short baseline radio interferometers and are typically used to image small fields of a few arcseconds. However, VLBI arrays consist of the same (or similar) parabolic dishes used for many short baseline interferometers, that are able to easily image fields of arcminutes or more[1]. The maximum field of view is imposed by the area of the sky to which the antenna is sensitive at a given wavelength and can be approximated as the FWHM of an unblocked aperture (i.e. the primary beam) Θ (in radians) of each antenna with diameter d, Θ=1.22λ/d. For an interferometer, the angular resolution (or fringe spacing) is θ (in radians) = $\lambda/b_{\rm max}$, where $b_{\rm max}$ is the baseline length.

Since $\Theta/\theta \approx b_{\rm max}/d$, $b_{\rm max}/d$ gives a measure of the number of resolution units across Θ, $(b_{\rm max}/d)^2$ is an estimate of the minimum number of pixels, $n_{\rm pixels}$, required to image to the edge of the primary beam, Θ. Table 2.1 gives the number of resolution units and $n_{\rm pixels}$ for various arrays, which is several orders of magnitude higher for VLBI arrays than for more compact arrays

Thus, in principle, large images of the sky can be generated with VLBI. In the last few years, considerable progress has been made in wide-field VLBI techniques, which will be discussed in detail in this chapter.

2.4 Wide-Field Effects

As discussed in Section 2.3 it is possible to generate large images of the sky with VLBI. However, this is not typically realised due to limits placed upon the field of view by: bandwidth and time-average smearing; non-coplanar baselines; and primary beam effects. It is important to note that these limitations are not exclusive to VLBI and affect most, if not all, types of radio interferometers to some degree. Therefore, in this section the source of the different limitations are discussed for the general case, broadly following the formalism presented by Bridle and Schwab (1999), Perley (1999) and throughout Thompson et al. (2001). Methods to overcome these limitations for wide-field VLBI are also discussed.

[1]In this exercise I am only considering arrays with single pixel feed parabolic antennas.

Table 2.1: Radio Interferometers and Wide-Field Imaging

Array	d (m)	b (km)	$b_{\max}/d$	n_{pixels}
(1)	(2)	(3)	(4)	(5)
ATCA	22	6	272	7.5×10^4
JVLA	25	36	1440	2.07×10^6
eMERLIN	76	220	2895	8.38×10^6
LBA	64†	1702	26593	7.07×10^8
EVN	100	8419	84190	7.09×10^9
VLBA	25	8611	344440	1.19×10^{11}

Notes.
† Occasionally the 70 m Tidbinbilla dish is used in LBA observations; (1) Common radio interferometers; (2) Antenna diameters; For heterogeneous arrays, the diameter of the largest antenna is used; (3) Maximum baseline; (4) Number of resolution units required to image the full primary beam; (5) The minimum number of pixels of the resulting image, defined as $(b/d)^2$. For imaging purposes, this value is required to be at least a factor 3 times greater for proper sampling of the synthesised beam. Adapted from Morgan et al. (2011), Table 1

2.4.1 Image Smearing

2.4.1.1 Bandwidth Smearing

The Fourier transform relation between the visibilities, V_ν, and source intensity distribution, I_ν, in Section 2.2 is assumed to be monochromatic. However, in practice the receiver bandpass and the correlation process, results in multiple channels of a finite width, $\Delta\nu$. Often, these channels are averaged so as to reduce data size and decrease computing time. However, this approach results in an undesirable effect that limits the observable field of view.

For a source located at the phase centre, the visibilities will have phases that are static with respect to frequency and time. However, for a source offset, the visibilities will rotate in both frequency and time resulting from a residual delay and residual delay rate, respectively. Figure 2.2 plots the phase, ϕ as a function of frequency for a point source located $10''$ from the phase centre, while the effect on time averaging is discussed in the next section. The source is observed at 1.65 GHz with a total bandwidth of 64 MHz, and a maximum baseline of 20 Mλ. The blue crosses represent a dataset, with $\Delta\nu = 0.25$ MHz, while the red crosses are for the dataset with frequency averaging ($\Delta\nu = 1$ MHz).

As evident from Figure 2.2, higher frequency averaging of the data leads to

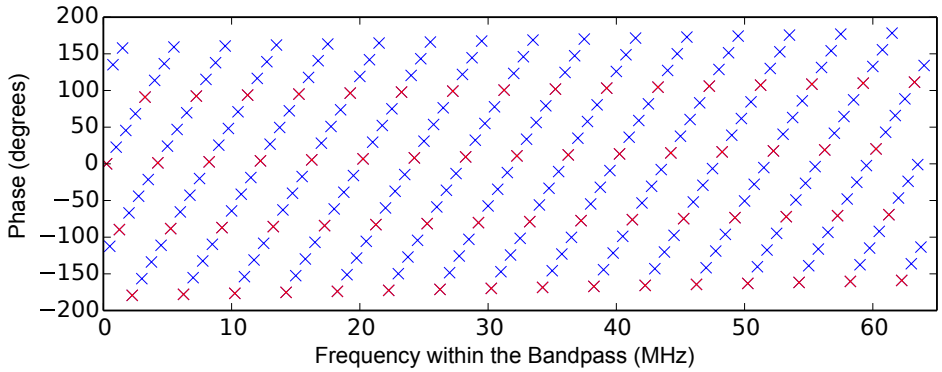

Figure 2.2: The plot displays the variation of the received phase vs bandpass frequency, from a point source located $10''$ from the phase centre. The source is observed with an array of maximum baseline of 20 Mλ, at 1.65 GHz with a bandwidth of 64 MHz. The blue crosses are the dataset with $\Delta\nu = 0.25$ MHz, while the red crosses are for the dataset with higher frequency averaging ($\Delta\nu = 1$ MHz).

an under sampling in frequency space, which can be considered as averaging over the higher frequency variations in the visibilities. This leads to a distortion of the sources in the image plane in the form of radial smearing, that reduces the peak amplitude response, while preserving the integrated flux density. Assuming a Gaussian bandpass function, with circular Gaussian tapering, the reduction of the peak amplitude response due to bandwidth smearing, R_ν, is expressed as (Bridle and Schwab, 1999, Equation 18-29):

$$R_\nu = I_{re}/I_0 \approx \left[1 + \left(\frac{\Delta\nu}{\nu}\frac{\Delta\Theta}{\theta}\right)^2\right]^{-1/2}, \tag{2.8}$$

where I_{re} is the image response due to frequency averaging and I_0 is the image response without frequency averaging, $\Delta\Theta$ is the distance from the phase centre, ν is the observing frequency and θ is the angular resolution as defined in Section 2.3. Figure 2.3 displays the amplitude response for the observation in Figure 2.2 as a function of baseline length for both frequency averaged datasets: $\Delta\nu$=0.25 MHz (blue dashed lines); and $\Delta\nu$=1 MHz (red dashed lines). Higher frequency averaging reduces the sensitivity on the longer baselines for sources that are offset from the phase centre, which is problematic for wide-field VLBI. Methods to overcome this are described in Sect. 2.4.1.3. In general, to reduce the amount of image smearing and amplitude reduction, the fractional bandwidth should be less than the radius of the source in units of the angular resolution i.e. $\Delta\nu/\nu \ll \Delta\Theta/\theta$.

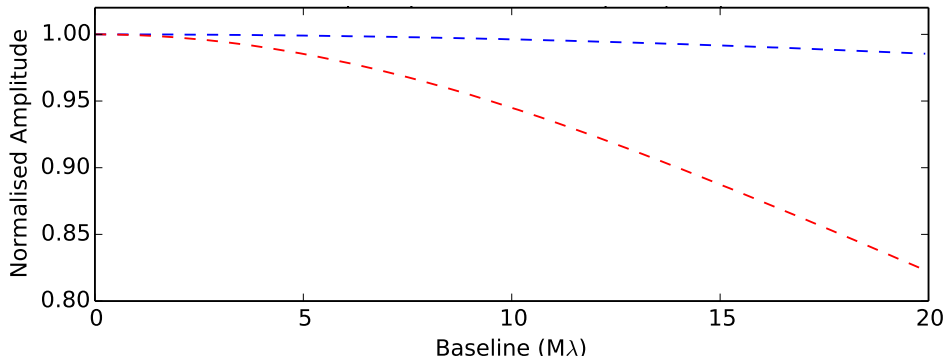

Figure 2.3: The effect of bandwidth averaging on the amplitude response of the array in Figure 2.2, as a function of baseline length, for $\Delta\nu = 0.25$ MHz, (blue dashed line) and $\Delta\nu = 1$ MHz (red dashed line). The reduction is given by Equation 2.8.

2.4.1.2 Time-Average Smearing

Averaging the visibility data in time also leads to a reduction in the peak image amplitude and a smearing in the image plane (Bridle and Schwab, 1999; Thompson et al., 2001). The correlator produces visibilities averaged in time, δt, which are assigned values of u and v corresponding to the mid-points of the averaging intervals (Bridle and Schwab, 1999). However, during this time the baseline vector moves, due to the rotation of the Earth, through an angle equivalent to $\omega_{\rm Earth}\delta t$, where $\omega_{\rm Earth}$ is the angular velocity of the Earth. Large values of δt causes an under sampling of the visibilities, which is displayed in Figure 2.4 for an observation similar to that described in Figure 2.3, for a total observing time of 120 seconds. Figure 2.4 shows the variation of the phase as a function of time for $\delta t = 2$ (blue crosses) and 10 (red crosses) seconds.

However, the consequences in the image plane are somewhat complex (though well defined for an individual visibility, see Figure 2.4) and depend on the location of the source on the celestial sphere (Bridle and Schwab 1999 and Thompson et al. 2001, Sect. 6.4). Nonetheless, like bandwidth smearing the major consequence is a reduction of the peak amplitude response. For a source located near the North or the South Celestial Pole, observed at a distance $\Delta\Theta$ from the phase centre, averaging the visibilities for a time δt reduces the amplitude by a factor $\mathrm{sinc}(\omega_{\rm vis} \cdot \delta t)$, where $\omega_{\rm vis}$ is the frequency of the visibilities due to $\omega_{\rm Earth}$. For $\omega_{\rm vis} \cdot \delta t \ll 1$, the loss in amplitude is $1 - (\pi\omega_{\rm vis} \cdot \delta t)^2/6$ and is approximated by (see Bridle and Schwab 1999),

$$R_t \approx 1 - \frac{\Gamma\pi^2}{12} \cdot \omega_{\rm Earth}^2 \cdot \delta t^2 \cdot (\Delta\Theta/\,\theta)^2, \tag{2.9}$$

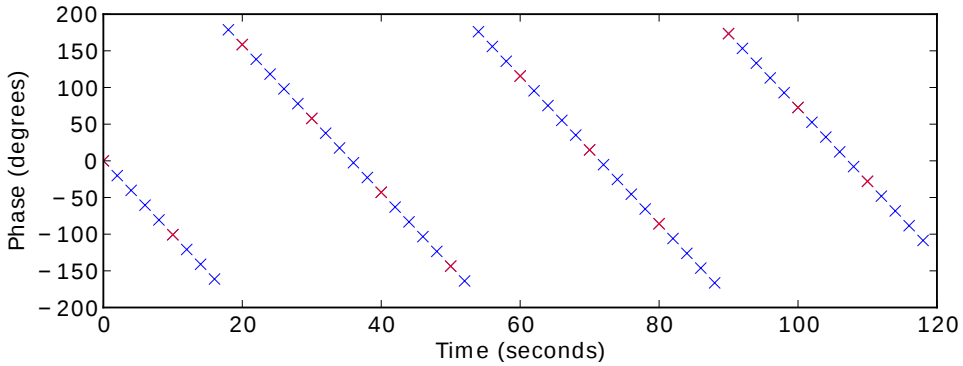

Figure 2.4: The plot displays the variation of the phase as a function of time received from a point source located 10″ from the phase centre. The source is observed with an array of maximum baseline of 20 Mλ, at 1.65 GHz for a total observing time of 120 seconds. The Blue crosses are the dataset with $\delta t = 2$ seconds, while the red crosses are for the dataset with higher time averaging ($\delta t = 10$ seconds).

where Γ depends on the shape of the (u, v) coverage[2] (Bridle and Schwab, 1999). Similar to bandwidth smearing, an increased averaging in time results in a reduction in the amplitude response for a source offset from the pointing centre that scales with increasing baseline. This is displayed in Figure 2.5 where the blue dashed lines are for δt=2 seconds and the red dashed lines are for δt=10 seconds. Like bandwidth/frequency smearing, the amplitude response in the image plane for a source offset from the phase centre is greatly reduced on the long baselines, for increased time averaging. In general, to avoid loss of amplitude due to time averaging, a good rule of thumb is that the rotation of the baseline vector in the direction of interest should be much less than the synthesised beam, $\Delta\Theta\omega_{\rm Earth}\delta t \ll \theta$ (Garrett, 2013).

2.4.1.3 Avoiding Image Smearing

The combined effects of bandwidth and time averaging on the field of view are referred to as image smearing. To avoid the effects of image smearing at any point in the desired field, it is necessary to correlate the data with narrow spectral channels and an integration time that is appropriately short. The limit on the spectral and temporal resolution of the final data product is set by the configuration of the correlator, thus restricting the field of view that can be imaged with minimal loss of amplitude due to image smearing. This is mitigated through

[2]For Square coverage without tapering, Γ=0.2424; Circular coverage without tapering, Γ=0.2485; Circular coverage with Gaussian tapering, Γ=0.2810.

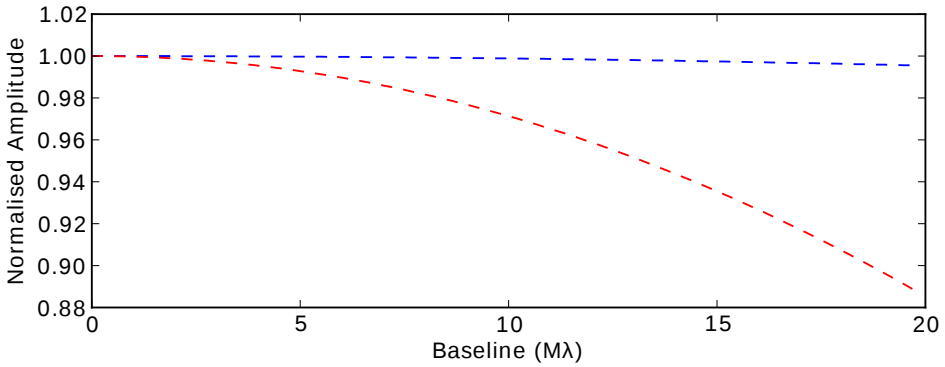

Figure 2.5: The effect of time averaging on the amplitude response of the array as a function of baseline length, for $\delta t = 2$ seconds, (blue dashed lines) and $\delta t = 10$ seconds (red dashed lines). The reduction is given by Equation 2.9.

the use of modern software correlators such as DiFX (Deller et al., 2007, 2011) and SXFC (Kettenis et al., 2009) which have the ability to produce visibilities with high temporal and spectral resolution. One major consequence of this is an increase in the data size, scaling as $\Delta\nu_{\rm bw}/\Delta\nu \times T_{\rm obs}/\delta t$, where $T_{\rm obs}$ is the total observing time and $\Delta\nu_{\rm bw}$ is the total observing bandwidth, shifting the difficulties to those of data storage and processing.

2.4.2 Non-Coplanar Effects

2.4.2.1 The w-term

In Section 2.2, the response of a two-element interferometer, $V(u, v)$, was shown to be related to the brightness of a point source by the Fourier transform relation given by Equation 2.2. Recall that this form can be reduced to a simple two-dimensional Fourier transform (Equation 2.3) for fields of view that are sufficiently small such that the phase arising from the w-term can be ignored[3]. However, as the desired field of view increases (or the offset of the source from the phase centre increases) ignoring the additional phase that arises due to the w-term in Equation 2.2 results in a phase error, $\phi_{\rm e}$, that degrades the quality of the image. This can be estimated as (Cornwell and Perley, 1992; Thompson, 1999),

$$\phi_{\rm e} \approx \pi w(l^2 + m^2). \tag{2.10}$$

[3]This is also valid for arrays aligned in the east-west direction and/or an instantaneous observation where the antennas lie on a plane (Perley, 1999). However this is not applicable for VLBI, and is not discussed here.

For an interferometer the maximum value of w is approximately equal to $b_{\max}/\lambda = 1/\theta$ (Cornwell and Perley, 1992). If the term $\sqrt{l^2+m^2}$ is the radius of the field to be imaged, $\Theta_{\rm f}$, then Equation 2.10 can be rewritten as,

$$\phi_{\rm e} \approx \frac{4\pi\Theta_{\rm f}^2}{\theta}, \tag{2.11}$$

where θ and $\Theta_{\rm f}$ are in radians. Setting an acceptable limit on the phase error (example 0.1 radian, Thompson 1999) yields a maximum field size that can be imaged without introducing unacceptable errors:

$$\Theta_{\rm f} \lesssim \sqrt{\frac{0.1\theta}{4\pi}} \tag{2.12}$$

In this thesis, Equation 2.12 is referred to as the *small field limit*. If the field to be imaged extends beyond the small field limit, the w-term in Equation 2.2 cannot be ignored. This therefore results in non-coplanar visibilities, where the two-dimensional inversion is invalid. Correcting for the effects of the w-term requires the full form of the relationship between the sky brightness and the visibility to be invoked. This is expressed as a three-dimensional Fourier transform, where the sources can be intuitively thought of as lying on the surface of a three-dimensional (l, m, n) space (Cornwell and Perley, 1992; Perley, 1999). This is displayed in Figure 2.6 as a slice through the $(l, m = 0, n)$ space represented by a unit circle, where $n = \sqrt{1-l^2-m^2}$, and the red dots are the radio sources, located on the surface of the circle.

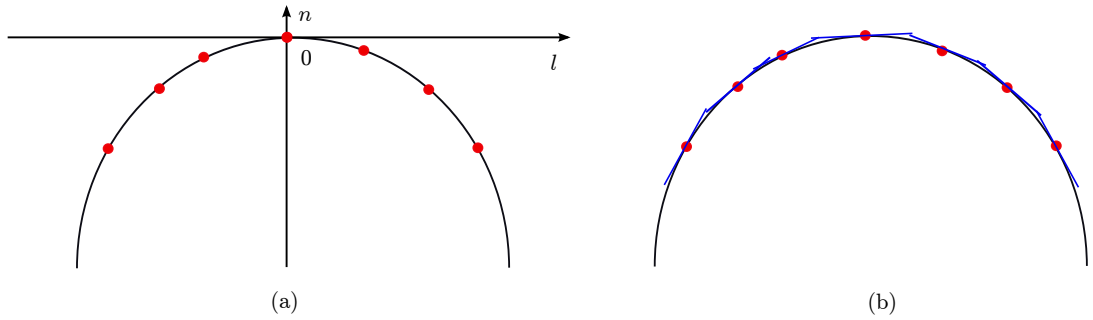

Figure 2.6: The three dimensional image volume and its relation to the sky brightness. (a): The three dimensional transformation of the interferometer response is described as an image volume. The radio sources (red circles) are located on the surface of this volume, which is represented by a unit circle in the $(l, m = 0, n)$ plane. (b): The surface of the sphere is described by small tangents, where the centre of the tangents are treated as separate phase centres where the small field limit in Section 2.4.2.1 is valid.

There exist a number of different techniques to overcome the effects of the

w-term and recover the brightness distribution of the sources. The most obvious method is to simply invert the three-dimensional transform of the visibilities, similar to the two-dimensional case. However, adding the third dimension greatly increases the computing time and since most of the resulting image cube will be empty, it is generally wasteful. Currently, the most common approach to imaging wide fields of view with radio interferometer, is through the w-projection algorithm (Cornwell et al., 2005). The algorithm works by projecting the w-term out of the visibilities, after which the three dimensional function $V(u, v, w)$ is determined purely from the two dimensional function $V(u, v, w = 0)$ (please see Cornwell et al. 2005 for details on this method). However, the w-projection algorithm is only applicable when the entire field of view to be imaged can be transformed in computer memory. This requirement essentially limits the number of image pixels that can be processed in computer memory and may not be efficient for imaging the full primary beam of the VLBI arrays listed in Table 2.1.

2.4.2.2 Multi-Phase Centre Correlation

To image wide fields with VLBI requires very high frequency and time resolution to mitigate the effects of image smearing, which results in very large datasets. For example, to image sources at the edge of the NOAO Bootes field at 1.4 GHz (radius $\approx 18'$) from the Garrett et al. (2005) study without sacrificing the longer baselines of the VLBA, would require 32768 frequency channels over the 64 MHz bandwidth and a time resolution of 5 ms. This would therefore result in a visibility dataset on the order of Terabytes, which would be far too large to be loaded into the memory of currently available workstations. Furthermore, there is a limit on the size of the dataset that can be loaded in AIPS[4] (the currently available software package for VLBI data reduction).

Another solution would be to shift the phase centre of the high frequency and time resolution dataset to a new phase centre, within the desired field. This method has been implemented in software correlators such as DiFX as the technique of multi-phase centre correlation (Deller et al., 2011; Morgan et al., 2011). In this method, the difference between the delay models at the initial phase centre, $\vec{s_0}$ and a new phase centre, $\vec{s_1}$, is computed for each antenna and used to shift the phase centre from $\vec{s_0}$ to $\vec{s_1}$. This shifting can be performed simultaneously on multiple positions, producing multiple datasets with different phase centres

[4]Currently it is $n_{\rm if} \cdot n_{\rm ch} \cdot n_{\rm pol} \leq 65536.$, where $n_{\rm if}$, $n_{\rm ch}$ and $n_{\rm pol}$ are the number of frequency sub-bands, channels and polarisations.

for each shift. Since image smearing increases radially from the phase centre, the new datasets can be averaged in time and frequency before writing to disk. This is described in detail by Morgan et al. (2011).

This method can be thought of as describing the surface of the image volume with a series of small tangential planes (in the visibility/(u, v) plane) at the locations of the desired phase centres, allowing for the simultaneous observation of multiple radio sources, or to perform a blind survey of the full primary beam. This approach is demonstrated in Figure 2.6b and allows the production of many smaller fields that can be averaged down in time and frequency, while preserving the full amplitude response and reducing the size of each dataset. The method of multi-phase centre correlation is similar to *Polyhedron Imaging* (Perley, 1999), where the main difference is that the latter is performed on the post-correlated data, while the former is applied during correlation.

The main difficulty with the method of simultaneously correlating at multiple phase centres stems from the requirement to initially correlate the data with exceedingly high spectral and temporal resolution to limit image smearing at any point within the desired field (Deller et al., 2011). Since this is implemented within the correlator, only the shifted datasets are written to disk (Deller et al., 2011), thus providing smaller, more manageable VLBI datasets to the astronomer which can be treated as a set of standard VLBI datasets (see Sect. 2.5.5).

Another applicable method for wide-field VLBI is Fast Wide-Field Mapping (FWFM, Wucknitz 2010). In FWFM, the full field is separated into four sub-fields, then each sub-field is separated into four smaller fields and so on, until the final field is small enough to avoid the effects of the w-term. The advantage of FWFM like the multi-phase centres, lies in the production of a number of smaller fields to avoid the effects of the w-term, while preserving the full amplitude response and reducing the size of each dataset. However, the main difference between the multi-phase centre correlation method and FWFM is that, the phase shifting is performed on the post-correlated data, while in the former the phase shifting is applied during correlation. The FWFM technique has been successfully tested on the Lenc et al. (2008) field of 28 square degrees with the VLBA at 90 cm by Wucknitz (2010) with the same results as found by Lenc et al. (2008).

2.4.3 Primary Beam Effects

Once the necessary steps have been taken to mitigate image smearing and non-coplanar effects, the main limitation to wide field VLBI results from the primary

beam. In this section, the reception pattern of the primary beam is first discussed, followed by the sensitivity of the array as it relates to the primary beam. Correcting for the primary beam for VLBI will be discussed in Sect. 2.5.3.

2.4.3.1 Characterising the Primary Beam of an Interferometer

For a two element interferometer, the power reception pattern, A_{12}, of the combined beam envelope response is simply the product of the voltage polar diagrams of both antennas, i.e. $A_{12} =\mid F_1 \times F_2 \mid$ (Strom, 2004), where F is the voltage pattern of the individual antenna and is the Fourier transform of the complex voltage distribution of the field incident upon the antenna, f (Strom, 2004). In practice, the form of f (and hence F) is determined by the way in which the aperture of the antenna is illuminated. For a rotationally symmetric, uniformly illuminated antenna with a circular aperture, the radial power pattern, $A(x)$, at an offset x from the pointing centre is given by,

$$A(x) \approx A_{\max} \left[\frac{J_1(2\pi x/\Theta_{\text{bessel}})}{\pi x/\Theta_{\text{bessel}}} \right]^2, \tag{2.13}$$

where J_1 is the Bessel function of the first kind and first order and Θ_{bessel} is the FWHM defined as 0.514 λ/d (Thompson et al. 2001, p.389) and A_{max} is the maximum value of A at the centre of the voltage pattern. However, uniform illumination of the aperture results in strong sidelobes close to the main beam (see Figure 2.7) which may be undesirable. These sidelobes can be reduced by adopting a Gaussian taper to the edges of f, whose Fourier transform, F is also a Gaussian and results in a radial power pattern of the form,

$$A(x)_{\text{taper}} \approx A_{\max} \exp\left(\frac{-x^2}{2\Theta_{\ln}^2} \right), \tag{2.14}$$

where $\Theta_{\ln} = \dfrac{\Theta}{2\sqrt{2\ln(2)}}$ and Θ is the FWHM defined in Section 2.3. Figure 2.7 compares the primary beam response approximated by Equations 2.13 and 2.14 for both pairs and mixed pairs of 100 m and 25 m antennas

While applying a Gaussian taper reduces the relative strength of the sidelobes, it inevitably causes a reduction in aperture efficiency and a broadening of the main beam. For an heterogeneous array, the primary beam of the larger antennas will dominate the response of the array closer to the pointing centre and even beyond the FWHM of the larger antennas. Thus, it is most important to characterise f for the largest antenna in heterogeneous arrays.

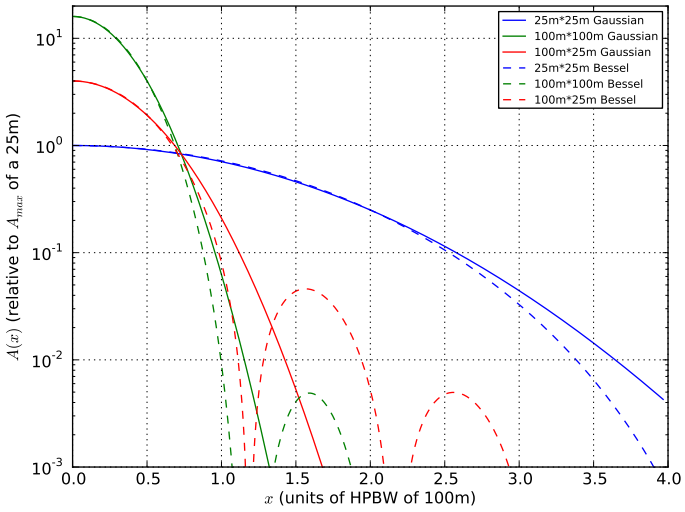

Figure 2.7: The primary beam response via Equations 2.13 & 2.14 for both pairs and mixed pairs of 100 m and 25 m antennas, where the combined response is $\mid F_1 \times F_2 \mid$ (Strom, 2004; Morgan, 2010a).

2.4.3.2 Sensitivity of an Interferometer

The sensitivity of an antenna is described by its System Equivalent Flux Density (SEFD), which takes into account the efficiency, collecting area, and system noise of the antenna. It is defined as the flux density of a point source in the primary beam of an antenna that would cause the noise power in the receiver to be twice that of the system noise in the absence of the source (Thompson et al., 2001). For an array of N elements, the theoretical noise, $\Delta\sigma$, is given by (Wrobel and Walker, 1999),

$$\Delta\sigma = \frac{1}{\eta}\frac{\mathrm{SEFD_{array}}}{\sqrt{2\Delta\nu_{\mathrm{bw}}\mathrm{T_{obs}}}}, \tag{2.15}$$

where η is the system efficiency factor (Wrobel and Walker, 1999), and is typically 0.7 for VLBI[5], $\Delta\nu_{\mathrm{bw}}$ is the observing bandwidth and T_{obs} the observing or total integration time. $\mathrm{SEFD_{array}}$ for the general case is given by Wrobel and Walker (1999),

$$\mathrm{SEFD_{array}} = \left(\sum_{i=1,j=i+1}^{i=N,j=N} (\mathrm{SEFD_i} \times \mathrm{SEFD_j})^{-1}\right)^{-1/2}, \tag{2.16}$$

[5]http://www.evlbi.org/cgi-bin/EVNcalc

However, Equation 2.15 describes the sensitivity at the centre of the primary beam, which is only applicable to small fields close to the pointing centre. The sensitivity of the array for any radial offset from the pointing centre, x, can be derived by scaling the $SEFD_i$ of each antenna by the radial power function, $A(x)_i$. Thus Equation 2.15 becomes (Morgan, 2010a),

$$\Delta\sigma = \frac{1}{\eta\sqrt{2\Delta\nu_{\rm bw}\mathrm{T_{obs}}}}\left(\sum_{i=1,j=i+1}^{i=N,j=N}\frac{A(x)_i \times A(x)_j}{\mathrm{SEFD_i \times SEFD_j}}\right)^{-1/2}. \qquad (2.17)$$

.

Equation 2.17 describes the overall effect of the primary beam reception pattern on the sensitivity of the array; as x increases, $\Delta\sigma$ increases. This effect of the primary beam on the array sensitivity should be corrected for fields were the sensitivity decreases significantly. For wide-field VLBI, this would apply mainly to studies that employ the the multi-phase correlation.

2.5 Wide-Field VLBI Guide

In the previous sections of this chapter, the effects associated with imaging the full primary beam of a VLBI observation and the means to alleviate these effects were discussed. The aim of this section is to describe the steps needed to perform a wide-field VLBI study successfully. While some aspects of wide-field VLBI calibration are not typically considered (e.g. primary beam correction), the majority of the data reduction follows the traditional VLBI methods outlined by the AIPS cookbook[6] and the EVN user guide[7]. Where these are appropriate, the reader will be referred to the necessary sections in both documents.

While there are a number of software packages that can perform many[8] of the VLBI calibration and imaging procedures (e.g. DIFMAP, Shepherd 1997; MIRIAD, Sault et al. 1995; and CASA, McMullin et al. 2007), in this section AIPS[9] is adopted as the default package.

For the remainder of this chapter, it is assumed that the reader has determined the general array parameters such as the number of antennas N, maxi-

[6] `http://www.aips.nrao.edu/CookHTML/CookBook.html`

[7] `http://www.evlbi.org/user_guide/guide/userguide.html`

[8] Correcting for the rate of change of the fringe phase with time and frequency, that results from the very long baselines of VLBI (i.e. fringe-fitting) can only be performed with AIPS

[9] The Astronomical Image Processing System was developed and is maintained by the National Radio Astronomy Observatory, which is operated by Associated Universities, Inc., under cooperative agreement with the National Science Foundation.

mum baseline $b_{\rm max}$, observing frequency ν, number of sub-bands $n_{\rm if}$, the observing bandwidth $\Delta\nu$ and number of polarisations $n_{\rm pol}$.

2.5.1 Pre-Observation

As previously discussed, there are three main effects that need to be considered when performing a wide-field VLBI observation: image smearing; non-coplanar baselines; and primary beam corrections. Studies requiring use of the wide-field VLBI technique can be separated into either the single phase centre case, where the field that will be investigated falls under the small field limit or those where the fields are beyond the small field limit, and requires the use of the multi-phase centres technique.

2.5.1.1 Single Phase Centre

In many cases, image smearing may be the only effect to be considered if the compact objects all lie within a relatively small field as described in Section 2.4.2.1. For example, in Chapter 4, the nuclear starburst of NGC 253 is observed by the LBA with a maximum baseline of 1702 km, at 2.3 GHz. The furthest source detected was located $\sim$4.4″ from the phase centre, nonetheless requires relatively high time and frequency resolution. Using Equation 2.12, the source located at 4.4″ from the phase centre would result in a negligible phase error, ϕ_e of 0.02 radians ($\sim$1°), due non-coplanar effects. Thus, the study in Chapter 4 falls within the small field limit. Similar studies have been performed by Pedlar et al. (1999); Garrett et al. (1999); McDonald et al. (2002); Tingay (2004); Lenc and Tingay (2006, 2009), and represents the early form of wide-field VLBI (see Section 1.1.1.1).

The number of output channels, $n_{\rm ch}$ and integration time, δt required to limit bandwidth and time-average smearing can be determined via Equations 2.8 and 2.9. These should be specified either during the observing proposal and/or through correspondence with the person(s) who will perform the correlation.

2.5.1.2 Multiple-Phase Centres

As mentioned in Sect. 2.4.2.2, if the target objects or the field of interest do not lie within the area where small field limit is valid, simultaneous multi-phase correlation will be required. Initially one would need to determine the values of $n_{\rm ch}$ and δt required to limit the combined bandwidth and time-average smearing, to an acceptable limit, at any location within the desired field. This step is

first performed within the correlator, with the resulting data not written to disk (Deller et al., 2011). Next, there are two procedures that can be adopted which depends on the nature of the study.

First, individual sources detected by shorter baseline arrays (e.g. WSRT, the JVLA, etc) can be used as the positions of new phase centres (see Sect. 2.4.2.2). Examples of this type of study is given by Middelberg et al. (2011); Morgan et al. (2013); Middelberg et al. (2013); and Deller and Middelberg (2014). The amount of averaging in frequency and time for these phase centres will be dependent on the individual source sizes and the uncertainty in the position of the sources, which are generally a couple of arcseconds. For example, (Morgan et al., 2013) imaged 195 known sources within a radius of $30'$ of the centre of M31 with the VLBA at 18 cm. Correlating with sufficient frequency and time resolution to allow imaging of the full field would have resulted in $\sim$ 40 TB of data[10]. However, correlating on the positions of each source, and accounting for possible offsets in positions and source sizes, resulted in $\sim$ 2.5 GB per phase centre after frequency and time averaging, thus reducing the total data size to $\sim$500 GB.

Second, it may be desirable to perform a blind survey of the full field of view through the use of the multi-phase centre technique. This is achieved through the use of a grid of phase centres covering the entire field of view. Since no assumptions on the source positions are made, the distances between the phase centres will determine the amount of averaging in frequency and time. An example of this type of wide-field VLBI is presented in Chapter 5, where the galaxy M51 is surveyed using a grid of 192 phase centres separated by $20''$, resulting in a post-averaged size of 41 GB per phase centre (or a total data size of $\sim$8 TB).

The positions of the phase centres, the relevant number of channels and time integration (both post- and pre-averaged datasets) can be specified either within the observing proposal and/or through correspondence with the person(s) who will perform the correlation.

2.5.2 Calibration/Data Reduction

Once the observation and correlation have been successfully performed, the astronomer will receive the final correlated data. The data reduction of the calibration source for the multi-phase centre and the single-phase centre (i.e. the small field limit) wide-field VLBI datasets will follow the general procedure for calibrating VLBI datasets in AIPS, as outlined in the EVN user guide and Chapter

[10]EVN calculator, `http://www.evlbi.org/cgi-bin/EVNcalc`

9 of the AIPS cookbook.

Once all calibration steps have been satisfactorily completed, for the multi-phase centre study, the final calibration (CL) and bandpass (BP) tables should be copied to all phase centres, and applied via the AIPS task SPLIT. While for the single-phase centre wide-field VLBI (i.e. the small field limit), the calibration tables are applied to the target via SPLIT, separating the target from the multi-source file.

2.5.3 Applying Primary Beam Correction

As discussed in Section 2.4.3, primary beam correction is important for imaging sources whose distance from the pointing centre is large compared to the primary beam, as may be the case for wide-field VLBI. However, not all wide-field VLBI observations would require correction for primary beam effects. For example, the wide-field VLBI project in Chapter 4, the furthest source detected was located $\sim$4.4″ from the phase centre. Using Equation 2.17 the sensitivity of the array at 4.4″ is similar to the sensitivity at the pointing centre to within 1%, thus correction for primary beam effects are not required. However, for the wide-field VLBI study in Chapter 5, since the field to be surveyed is $\sim$6′ from the pointing centre, correction for primary beam effects are required.

Primary beam correction of VLBI observations are not common. An early attempt was conducted by Garrett et al. (2005), where the reduction in the peak flux densities due to the primary beam was estimated for different radial distances from the pointing centre. While, this reduction was compensated for during their calculations, the primary beam correction was not performed on the VLBI datasets. A recent, more successful application of primary beam correction for VLBI was performed on a wide-field VLBA dataset at 21 cm by Middelberg et al. (2011). The process has since been refined by Morgan (2010b), Morgan et al. (2011), Morgan et al. (2013) and Middelberg et al. (2013).

Unlike short baseline arrays such as the JVLA where the primary beam correction is performed in the image plane, the approach taken by Middelberg et al. (2011) determines the primary beam attenuation by calculating the visibility gains relative to the phase centre sensitivity. This requires the assumption that the correction is constant across the entire image (Morgan, 2010a). In Chapter 5, this model is adapted to a wide-field VLBI observation with the EVN at 18 cm and the results are displayed in Figure 2.8.

As the offset from the pointing centre increases, the corrected sensitivity

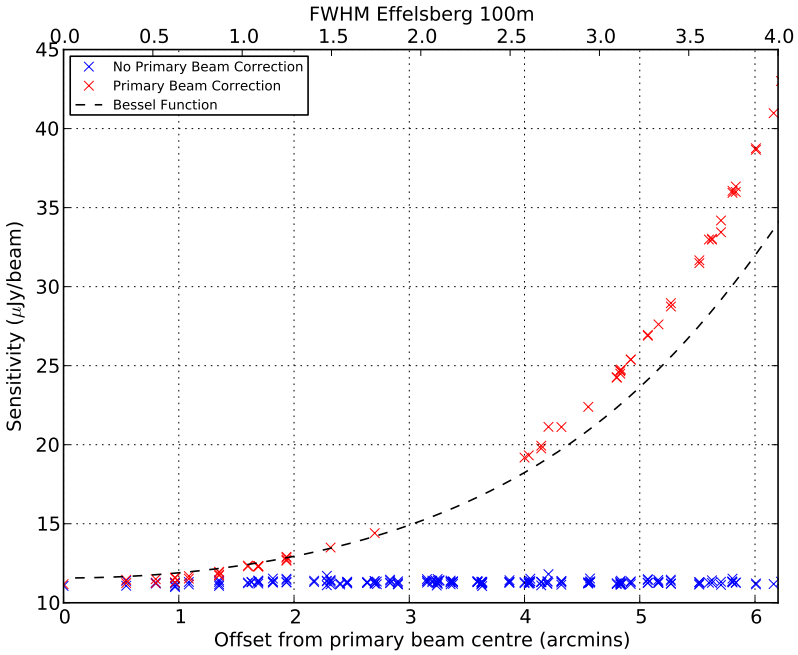

Figure 2.8: Sensitivity plotted against angular distance from the pointing centre. The blue crosses represents the sensitivity of 192 phase centres (from an EVN observation as described in Chapter 5) without correcting for primary beam attenuation. The red crosses are a subset of the 192 phase centres for which were corrected for primary beam attenuation. The model used was adapted from the model described by Middelberg et al. (2011), and applied to the EVN which is described in Sect. 5.3.3. The dashed lines are the theoretical sensitivity of the array using Equation 2.17 for a two-dimensional Bessel function form of Equation 2.13.

deviates from the theoretical values obtained from Equation 2.17 for a two-dimensional Bessel function form of Equation 2.13[11].

Prior to correcting for the primary beam, the data is calibrated using the system temperatures and gains measured throughout the observation and the full observing bandwidth. Which scales and weights the visibilities by the sensitivity of the telescopes. While Equation 2.17 uses only the nominal SEFD and the sensitivity is estimated for the central frequency.

However, the primary beam correction model is far from perfect as it lacks information regarding the individual antennas, since different antennas require different parameters such as: percentage of the parabola illuminated; possible dependence on polarisation due to offset feeds; and deformation of the parabola when observing a source close to the horizon.

[11]A point to note, the correction applied to the visibilities in Chapter 5 and displayed in Figure 2.8 uses the Bessel function as the model for the primary beam.

2.5.4 Imaging Strategy: Single Phase Centre

In the single phase centre case, within the small field limit, only the effects of bandwidth and time-average smearing need be considered. Once the data have been calibrated and applied to the target, the spectral and time averaging requirements are dictated by the desired image size and the maximum baseline of the array. The imaging can be performed using the AIPS task IMAGR, CASA task CLEAN or even DIFMAP, where the latter will require either conversion of channels to sub-bands (see Chapter 4) or division of the dataset into multiple sub-datasets with different image centres via UVFIX.

2.5.5 Imaging Strategy: Multiple-Phase Centres

2.5.5.1 Wide-field imaging

Before proceeding to image multiple phase centres, there are several considerations. First, wide-field VLBI images would mostly consist of pixels without detectable emission from astronomical sources. This is usually true for phase centres with known radio sources previously detected with lower resolution radio interferometers (e.g. Garrett et al. 2005, Lenc and Tingay 2006, Lenc et al. 2008, Lenc and Tingay 2009, Middelberg et al. 2011, Morgan et al. 2013, and Middelberg et al. 2013), which generally results from the lack of high brightness temperature compact components above the detection threshold. Second, the positional accuracy of lower-resolution catalogued radio sources is poor with respect to that achievable with VLBI (see Chapter 5.3.2), in which case the source of interest may lie outside the field of view.

Furthermore, it may be the case that the centroid of the radio emission varies with resolution and/or frequency (Morgan et al., 2013). For example, consider an AGN with a jet that terminates in a hotspot a few arcseconds from the core. At 21 cm with the VLA the AGN may be partially resolved, with the dominating radio source being the hotspot which defines the location of the source. Meanwhile, with VLBI at the same frequency, due to the high resolution the AGN may be resolved into an AGN-core and jet/hotspot morphology, with the core dominating the radio emission. If one is not careful, it is possible to miss the compact radio core altogether. An example of this are given in Chapter 5.

To avoid this undesirable outcome, naturally weighted[12] "dirty images"[13] of the phase centres can be made, covering as wide an area as possible (i.e. as allowed by the number of channels, $n_{\rm ch}$ and integration time), thereby increasing the chance to detect emission. This approach may also benefit from using a reduced array with shorter baselines, which will increase the allowable field of view and/or reduce the computing requirements, albeit being somewhat less sensitive to unresolved sources. This can be done using the AIPS task IMAGR with niter = 0 (i.e. no CLEAN iterations) and setting the parameters NCHAV and CHINC to the required $n_{\rm ch}$, which grids the channels separately onto the same grid, but the imaging is done on the combined grid, reducing image smearing effects. Any pixel with a signal to noise ratio (S/N) above above a pre-specified threshold can be treated as a candidate source. One method for defining the S/N threshold for the multiple-phase centre wide field VLBI approach is discussed in Sect. 5.3.2 (see also Morgan et al. 2013).

Note that since the properties of all phase centres of a particular observation are similar (i.e. frequency, bandwidth, time and frequency resolution, array configuration etc), with the only difference being their position, this process can be performed automatically, for example through the use of pipelines created using the PARSELTONGUE scripting language (Kettenis et al., 2006).

2.5.5.2 Final imaging

Once candidate radio sources have been identified in the wide field maps, the final images can be made. The position of the phase centre can be shifted to that of the source. The dataset can then be averaged in time and frequency to reduce the size of the data on disk. The amount of averaging will be dependent on the requirements of the desired image size, and the maximum baseline of the array. Once this has been decided, imaging the data would then proceed as a typical VLBI imaging exercise.

[12]Natural weighting is preferred as it reduces the rms noise, allowing the chance to detect the fainter sources. However, it compromises on resolution, which in the initial imaging/source detection stage is not entirely undesirable.

[13]Applying the CLEAN method without a priori knowledge of where the source lies in the image plane can produce spurious artefacts that resembles compact sources i.e. non-Gaussian noise.

2.6 Non-Imaging Applications: SETI

This chapter dealt with the theory of radio interferometry and the limitations of attempting to image wide fields using high resolution VLBI. It is clear that the technique of wide-field VLBI is ideally applicable to fields containing multiple bright, compact radio sources distributed over wide fields, such as AGNs (Garrett et al., 2005; Lenc et al., 2008; Middelberg et al., 2011, 2013) and star-forming galaxies (Pedlar et al., 1999; Lenc and Tingay, 2006, 2009; Morgan et al., 2013). Furthermore, the high time and frequency resolution that is required for wide-field VLBI also makes it applicable in the search for extra-terrestrial intelligence (SETI).

With the possible exception of masers, all naturally occurring astrophysical radio signals are spectrally broadened by their underlying emission physics and kinematics (Siemion et al., 2013). It is commonly assumed that any extraterrestrial civilization wishing to make its presence known, would broadcast signals that are clearly different to naturally occurring radio emissions (Siemion et al., 2010). These may be spectrally narrow signals of a few Hz, such as sinusoidal carrier waves associated with frequency or amplitude modulated telecommunications, or temporally narrow radio pulses commonly used in radar (Siemion et al., 2013). Similarly, radio signals that leak from the civilisation's internal communications system would be narrow in frequency but considerably weaker and detectable only at very short distances[14]. As such, SETI experiments are typically conducted at very high spectral resolution.

SETI experiments have not been performed with VLBI to date. The main reasons for this have been the combination of the inability of hardware correlators to produce data with sub-kHz spectral resolution, the lack of appropriate techniques and a shortage of suitable targets. With the advent of software correlators providing the means to conduct surveys with spectral resolutions at the Hz and even sub-Hz level, the first problem is no longer a limiting factor. This, however, shifts the limiting factor to the corresponding increase in data size, requiring a trade-off between the frequency resolution, bandwidth, total observing time and number of baselines. The second problem is addressed in detail in Chapter 3, with the first SETI experiment conducted with VLBI described. Finally, the third obstacle is being overcome by exoplanet surveys, both past and present,

[14]This is not entirely true. The Arecibo Planetary Radar that is used to search for asteroids boasts a 1 MW transmitter at 2.3 GHz, which is sufficiently powerful to be detected at distances >100 light years with current radio interferometers. See Figure 1.6

that are devoted to searching for planets that fall into the category of habitable, and is discussed in Sect. 1.2.2.

3

Searching for Evidence of Extraterrestrial Intelligence with Very Long Baseline Interferometry

Adapted from:
The First Very Long Baseline Interferometric SETI Experiment
H. Rampadarath, J. S. Morgan, S. J. Tingay & C. M. Trott, 2011, The Astronomical Journal, Volume 144, Issue 2, article id. 38

3.1 Introduction

The Search for Extra-Terrestrial Intelligence (SETI) seeks evidence for life in the Universe, through the detection of observable signatures from technologies that are expected to be possessed by advanced civilizations. Such searches are mainly conducted at radio wavelengths (Drake, 2008) and, to a lesser extent, optical wavelengths (Reines and Marcy, 2002).

The goal of SETI experiments conducted at radio wavelengths is to detect signals that are intentionally aimed at broadcasting the civilization's existence to others, and/or signals that unintentionally leak from the civilization's communications system (Siemion et al., 2010; Fridman, 2011). Intentional signals are expected to be narrow in frequency (1 Hz to 1 kHz), while unintentional signals may not be (Tarter, 2001, 2004; Siemion et al., 2010; Fridman, 2011).

An open question is the frequency range over which to search for extra-terrestrial intelligence (Tarter, 2004; Shostak, 2009; Fridman, 2011). The frequency range from 1 to 10 GHz is generally preferred, however after decades this range is still very much unexplored (Tarter, 2004). For leakage signals, the lower

end of this range is preferred (Tarter, 2001, 2004). For deliberate signals from extra-terrestrial intelligence, the most common suggestions are the 1420 MHz hydrogen line and multiples of 1420 MHz, including $\pi \times 1420$ MHz (4462.336275 MHz) (Blair et al., 1992; Harp et al., 2010).

SETI experiments are divided into two categories: (1) sky surveys and (2) targeted searches (Shostak, 2009). The sky surveys make no assumptions about the location of the SETI signals and perform raster scans of the observable sky. Current sky surveys are SETI@home, Astropulse and SERENDIP V conducted with the 300 m Arecibo telescope in Puerto Rico (Werthimer et al., 2001; Siemion et al., 2010). Targeted searches sequentially examine specifically chosen stars that are deemed to have a chance of harbouring a planet that could sustain life (Tarter, 2004; Fridman, 2011). A list of 17,129 stellar systems that are potentially habitable to complex life forms was compiled by Turnbull and Tarter (2003).

Current exoplanet surveys (e.g. *Kepler Space Mission*, Borucki et al. 2010 the High Accuracy Radial velocity Planet Searcher, HARPS[1]) aim to search for Earth-sized planets in and near the habitable zone of Sun-like stars (Borucki et al., 2010). As of February 2012[2], *Kepler* had found over 2,300 planetary candidates, with ∼46 candidates within habitable zones (Batalha et al., 2013). As *Kepler* begins to confirm these planets and proceeds to discover more Earth-like planets in habitable zones, these planets will be investigated for extra-terrestrial intelligence.

This chapter explores the suitability of using Very Long Baseline Interferometry (VLBI) for targeted SETI from potentially habitable planets. SETI is listed under the *The Cradle of Life* Key Science Project for the *Square Kilometre Array* (SKA, Carilli and Rawlings (2004); Tarter (2004); Schilizzi et al. (2010)). This chapter also aims to set a foundation for future VLBI SETI projects, including the use of the long baselines of the SKA.

In this chapter the first SETI experiment conducted with VLBI is presented. Section 3.2 introduces the target for this study, Gliese 581. Section 3.3 discusses the advantages of using VLBI for targeted SETI and describes the technique of using VLBI for SETI. Section 3.4 describes the observations and data analysis, and presents the results of the experiment. Discussions and conclusions are presented in Sects. 3.5 and 3.6, respectively.

[1] `https://www.eso.org/sci/facilities/lasilla/instruments/harps/overview.html`

[2] At the submission of this thesis the number of Kelpler planetary candidates has crosses 3000, with 69 habitable planetary candidates (`http://phl.upr.edu/projects/habitable-exoplanets-catalog`).

3.2 Target

The target for this pilot study is the M-dwarf star Gliese 581 (Gl581), located 20 light-years (ly) distant in the constellation Libra (Udry et al., 2007; Vogt et al., 2010).

In 2007, Udry et al. (2007) announced the discovery of a planet on the edge of Gl581's habitable zone. The planet, Gliese 581d (Gl581d), is the fourth planet in the Gliese 581 system. It has a mass of $5\,M_{\rm Earth}$, an orbital period of 83 days and an orbital semi-major axis of 0.25 AU (∼40 mas). Wordsworth et al. (2010) discussed the effects of surface gravity, surface albedo, cloud coverage and CO_2 density on the surface temperature of Gl581d. Their results showed that Gl581d may have the necessary conditions to sustain liquid water on its surface. Thus, Gl581d may be the first confirmed exoplanet with the possibility to sustain life (Wordsworth et al., 2010).

Vogt et al. (2010) claimed to have discovered a planet well within the habitable zone of Gl581. The suspected planet, Gliese 581g (Gl581g), is located between Gl581d and Gliese 581c (the third planet). Gl581g has a proposed mass $\sim\ 3\,M_{\rm Earth}$, an orbital period of 37 days and an orbital semi-major axis of 0.15 AU (projected angular distance ∼23 mas). The existence of a low mass planet well within the habitable zone of Gl581 has been questioned by Tuomi (2011). The radial velocity measurements used by Vogt et al. (2010) was re-examined by Tuomi (2011), using Bayesian tools as opposed to the periodogram analyses employed to determine the existence of Gl581g. Tuomi (2011) concluded that the radial measurements are consistent with four planets and not six, disputing the claim of Vogt et al. (2010).

No radio emission was detected from the position of Gl581 by the VLA FIRST survey (Becker et al., 1995) above a limiting flux density of 1 mJy at 20 cm.

3.3 Using VLBI for Targeted SETI

3.3.1 VLBI and SETI

Existing VLBI instruments are able to monitor a wide range of frequencies, from 10 MHz (the Low Frequency Array, LOFAR: Stappers et al. (2011)) to 230 GHz (The Event Horizon Telescope: Broderick et al. (2011)), allowing for a possible coverage of the preferred frequency range. In addition, current VLBI systems such

as the LBA and the EVN include some of the most sensitive radio telescopes in the world.

To date there has been little or no use of VLBI in SETI investigations. The SETI project SETI-Italia (Montebugnoli et al., 2001) uses data commensally from the 32 m VLBI Medicina telescope. SETI-Korea (Rhee et al., 2010) has proposed the use of existing and new telescopes from the Korean VLBI Network (KVN) for SETI. In addition, Slysh (1991) proposed to use VLBI or space-VLBI satellites to measure the angular size of suspected SETI radio sources. Pseudo-interferometric observations were conducted by the SETI Institute, using both the Arecibo Telescope and the Lovell Telescope, Jodrell Bank Observatory between 1200 and 1750 MHz (Backus and Project Phoenix Team, 2002). The survey searched for signals from nearby stars with appropriate frequency drift and offset caused by the rotation of the Earth.

3.3.2 Radio Frequency Interference (RFI) Mitigation

Radio frequency interference (RFI) is human-made, unwanted radio emission within the telescope's field of view. Potential sources include mobile phones, radars, television signals, FM-radio, satellites etc. Separating RFI from a real SETI signal is one of the most challenging problems faced by SETI projects. Thousands of hours of computing time are spent identifying and removing RFI from the datasets, before one can search for SETI signals. Since its inception, the SETI@home project has detected over 4.2 billion potential signals. While essentially all these potential signals are RFI, it is possible that therein lies a true extraterrestrial signal (Korpela et al., 2010). VLBI offers several ways of discriminating RFI signals from SETI signals not applicable to single dish or even short baseline radio interferometers.

First, VLBI uses N antennas separated by hundreds to thousands of kilometres giving $N(N-1)/2$ baselines, once the data from independent pairs of telescopes are correlated together. This aspect of VLBI is important, as RFI which is not present at both antennas involved in a baseline does not correlate. An astronomical or SETI compact radio source within the interferometer field of view will be detected on all baselines. This is also true for RFI if it is detectable by both antennas in a baseline. However, even correlated RFI can be easily identified with VLBI, as it produces distinct phase variations in both frequency and time in the correlated output as discussed below.

3.3.3 VLBI Phase Variations

As discussed in Section 2.2, the correlated signals from an interferometer are complex quantities (known as visibilities), with amplitude and phase as the fundamental observables. The amplitudes are proportional to the correlated power of the source, while the phase, ϕ represents the residual time delay that results from the wavefront of the radio emission arriving at one antenna before the other, with a time delay, τ. At the phase centre, the delay (and hence the phase) is set to zero, via application of τ, at the correlator (this is discussed in more details in Section 2.2). This time delay accounts for many different effects, but primarily simple geometry (see Section 2.2 for detailed discussions on this process). A source offset from the phase centre will display a phase, ϕ that is related to its location with respect to the phase centre, and can be expressed as the phase term of Equation 2.3,

$$\phi = \frac{2\pi\nu}{c}(lu + mv), \tag{3.1}$$

where ν is the observing frequency, l and m are the coordinates of the source in the plane of the sky, relative to the phase centre, and u and v are coordinates which describe the instantaneous geometry of the projected baseline, with respect to the phase centre. The reader is referred to Thompson et al. (2001) and Taylor et al. (1999) for details. For a finite observational bandwidth, and for the duration of the observation, the radio source in Equation 3.1 will display a phase change with frequency and time given by,

$$\frac{d\phi}{d\nu} = \frac{2\pi}{c}(lu + mv), \tag{3.2}$$

$$\frac{d\phi}{dt} = \frac{2\pi\nu}{c}\left(l\frac{du}{dt} + m\frac{dv}{dt}\right). \tag{3.3}$$

By measuring the phase change with time and frequency for a given source, its location with respect to the phase centre can be determined using the above equations. Additionally, if the source's position is known, maximum values for both $d\phi/d\nu$ and $d\phi/dt$ can be determined, using maximum values of u or v and du/dt or dv/dt.

3.3.3.1 Determining the Phase Variations with Fourier Transforms

An estimate of $d\phi/dt$ or $d\phi/d\nu$ for a radio source can be determined by the discrete Fourier transform (DFT) of the complex visibilities. For narrow-band

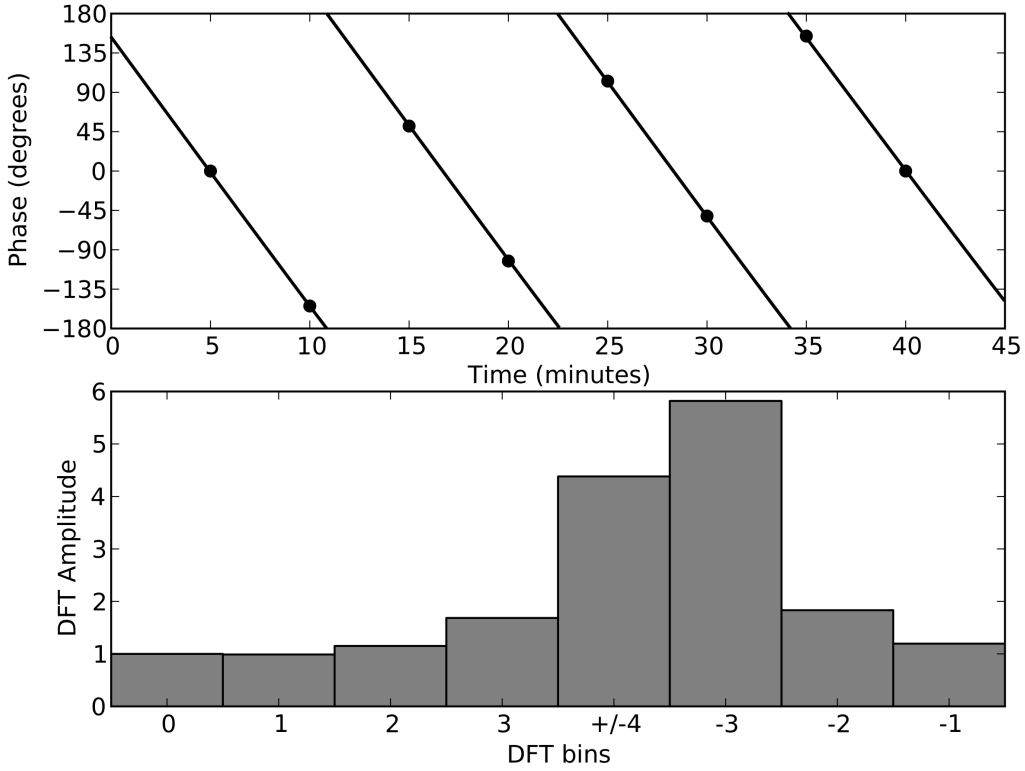

Figure 3.1: The phase variation with time (upper panel), and the corresponding discrete Fourier transform (DFT) for a narrow-band test signal. The DFT bins provide an estimate of the $d\phi/dt$ of the signal. The Nyquist bin at bin ± 4, represents the maximum possible $d\phi/dt$, 180° per data point. Each data point has a sampling time of 5 minutes. The test signal is found to have a $d\phi/dt$ of -135° per point, equivalent to 3 turns over the time range. However, due to ambiguities $d\phi/dt$ of this signal can be generalised to $-135 \pm 360n^\circ$ per data point, where n is a wide range of positive and negative integers. The same principle applies in determining $d\phi/d\nu$ for broad-band signals, where the DFT is applied to the complex visibilities as a function of frequency.

(persistent or intermittent in time) and broad-band signals, DFTs can be applied to the complex visibilities as a function of time to determine $d\phi/dt$ and frequency to determine $d\phi/d\nu$, respectively.

This method is illustrated in Figure 3.1. The upper panel shows the phase of a narrow-band test signal as a function of time, with a sample time of 5 minutes per point over a 40 minute observation. The lower panel displays the corresponding discrete power spectrum obtained by applying DFTs to the complex visibilities.

A signal with little or no phase change in time or frequency (implying a source close to the phase centre) will appear in bin zero. However, a signal with high

phase change with time (as the test signal in Figure 3.1) is indicative of a source far from the phase centre, probably RFI, and will appear in a different bin. The height of the DFT amplitude of bin zero compared with the others gives an indication of the signal to noise of any signal which comes from the phase centre.

There are, however, ambiguities in signals with $d\phi/dt$ greater than the Nyquist frequency. The component of the test signal located in the -3 bin can be generalised as $d\phi/dt = -135 \pm 360n^\circ$ per data point, where n is a range of positive and negative integers. The $d\phi/dt$ of the Nyquist bin, due to ambiguities is $\pm 360n^\circ$ per data point[3].

3.4 Searching for SETI Signals from Gliese 581

3.4.1 Observations

Gl581 was observed on 2007 June 19, for 8 hours in the 20 cm wavelength band by three stations of the Long Baseline Array (LBA): the 64 m Parkes (Pa) antenna of the Australia Telescope National Facility (ATNF); the ATNF Australia Telescope Compact Array (ATCA) in phased array mode; and the ATNF Mopra (Mp) 22 m antenna. The observation was conducted in three frequency pairs of 64 MHz bandwidth centred on: 1262,1312; 1362,1412; 1462,1512 MHz, in dual-polarisation mode. The uv coverage is shown in Figure 3.2. This configuration gives a maximum resolution of 127 mas. The observations of Gl581 were phase referenced to the ICRF2 source 1510−089 (J1512-0905, RA = $15^{\rm h}12^{\rm m}50.532925^{\rm s}$; Dec = $-09^\circ05'59.82961''$, J2000), a calibrator located 2.14 degrees from Gl581 (Fey et al., 2004). B1510-089, shows an unresolved core with extended structure to the North-East of the core at 2.3 GHz (Fey and Charlot, 1997), and 327 MHz (Rampadarath et al., 2009) on the longest baselines of the Very Long Baseline Array (VLBA). The longest baseline of our observation (ATCA-Pa) is a factor of 9 less than the longest VLBA baseline, hence, B1510-089 is expected to be unresolved in our observations.

A phase-referencing cycle of 5 minutes (2 minutes on calibrator, 3 minutes on Gl581 at RA = $15^{\rm h}19^{\rm m}26.33^{\rm s}$; Dec = $-07^\circ43'20.94''$, J2000) was employed. A single observation block consisted of 8×5 minute phase-referencing cycles. The entire observation comprised 12×40 minute observational blocks switching between the three frequency pairs (Table 1).

[3]The reader is refereed to Bracewell (2000) for further details on discrete Fourier transforms

The data were correlated using the DiFX software correlator (Deller et al., 2007, 2011), with a frequency resolution of 1.953 kHz per spectral channel, and converted to the standard FITS format. The lowest and highest 5 MHz (2500 channels) were discarded from each band due to band edge drop-off in sensitivity. The data files were then sub-divided into five datasets of 4000 channels each and one dataset of 1268 channels at each centre frequency.

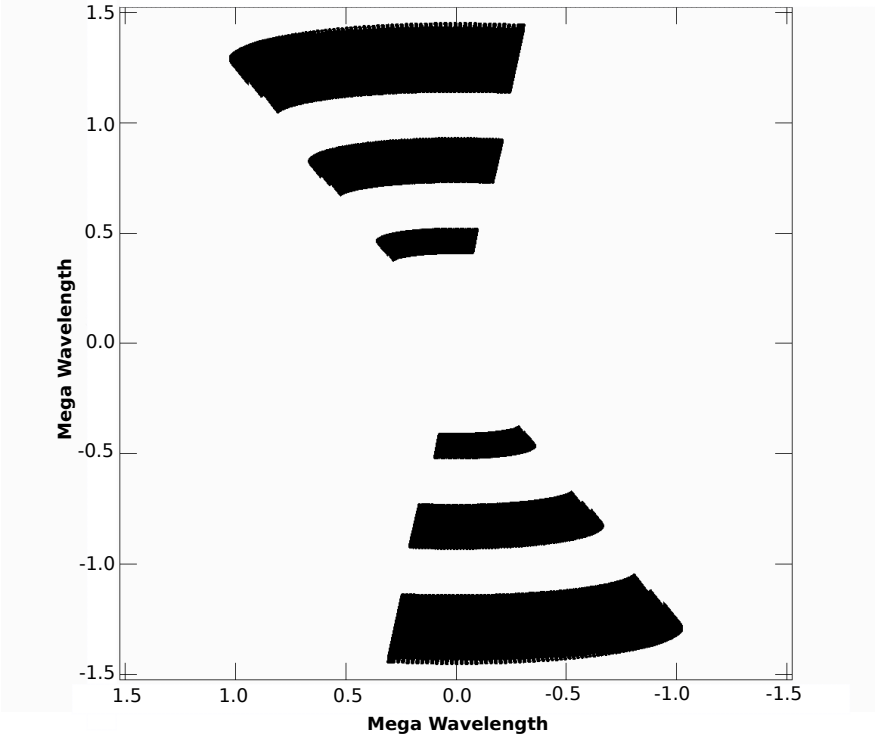

Figure 3.2: uv coverage of the LBA observation of the Gl581 system, in units of mega wavelengths. The x-axis plots the u coordinates, while the v coordinates is on the y-axis.

3.4.2 Gl581 Coordinates

The calculation of the phase variations with time and frequency, as described in Sect. 3.3.3 requires the target to be located at the phase centre. In a typical VLBI experiment, this would be easily verified as the source in question would be radio bright. However, since Gl581 is not known to be a radio emitter, its position at the time of observation needs to be calculated and due to its proximity to Earth, effects such as proper motion and parallax must be accounted for in order to determine the position of Gl581 to a high degree of accuracy.

Table 3.1: OBSERVATION TIMES AND THE CORRESPONDING FREQUENCY PAIRS.

UT	Frequency Pairs (MHz)
07:40:00-08:30:00	1262,1312
08:30:00-09:10:00	1362,1412
09:10:00-09:50:00	1462,1512
09:50:00-10:30:00	1262,1312
10:30:00-11:10:00	1362,1412
11:10:00-11:50:00	1462,1512
11:50:00-12:30:00	1262,1312
12:30:00-13:10:00	1362,1412
13:10:00-13:50:00	1462,1512
13:50:00-14:30:00	1262,1312
14:30:00-15:10:00	1362,1412
15:10:00-15:30:00	1462,1512

Notes. The observation was sub-divided into 12 separate sessions, that alternated between 3 frequency pairs.

The position of Gl581 at the time of the LBA observation was computed using a reference position of Gl581 (RA and Dec) and the barycentric coordinates of the Earth (in AU) at the time of the observation (obtained from NASA's Jet Propulsion Laboratory HORIZONS on-line solar system data and ephemeris computation service[4]).

The reference position for Gl581 was taken from the *Hipparcos* catalog (Perryman et al., 1997). Gl581 was observed multiple times between 1989.85 and 1993.21 by the *Hipparcos* satellite (Perryman et al., 1997). Using the astrometric information gathered during these ∼3 years, a mean position at the reference epoch, 1991.25, of RA(J1991.25)=$15^h19^m26.825^s$; Dec(J1991.25)=$-07°43'20.210''$, was calculated, including; positional errors: $e_{\rm RA}$ = 1.99 mas and $e_{\rm Dec}$=1.34 mas, and a parallax of 159.52 ± 2.27 mas. A proper motion of RA = −1227.67 ± 3.54 mas/yr; Dec = −97.78 ± 2.43 mas/yr, was also taken from the *Hipparcos* catalog. The position calculated for Gl581 at the VLBI observation date, is RA(J2000)=$15^h19^m26.206^s$; Dec(J2000)=$-07°43'17.555''$. This calculation has a positional uncertainty of ±53 mas, largely due to the cumulative effect of the uncertainty in the proper motion measured by the *Hipparcos* 1991 observation.

Since the calculated position is offset from the correlated position of Gl581 (ΔRA = $0.519''$ and ΔDec = $2.655''$), the Gl581 data needs to be shifted. Cor-

[4] `http://ssd.jpl.nasa.gov/horizons.cgi`

recting for this positional difference is described in the next section. Note, due to the high time and frequency resolution of this observation, no amplitude losses are expected due to bandwidth and time smearing on the longest baselines at this distance from the pointing centre.

3.4.3 Data Reduction and Calibration

The data reduction and calibration were performed using AIPS. Shifting the Gl581 data to the new position calculated in Sect. 3.4.2, would be very difficult since the Gl581 data were sub-divided into multiple datasets, each with different sub-bands containing more than 1000 channels. Since a positional offset produces a corresponding phase change in time and frequency of a radio source (see Sect. 3.3.3), it was instead easier to shift the calibrator position prior to calibration in the *opposite sense* to produce almost precisely the same effect. The shift was done via the AIPS task UVFIX.

Once flagging and phase-only calibration (fringe-fitting and self-calibration) were carried out on the phase centre shifted calibrator, the phase solutions were transferred and applied to the Gl581 datasets. This should result in the GL581 system being located at the phase centre of the GL581 dataset. After calibration, further analysis was carried out using the PARSELTONGUE scripting language (Kettenis et al., 2006) and the numerical python package, NUMPY[5]. The flagging, phase calibrations and transfer of solutions were implemented separately for the frequency pairs listed in Table 3.1.

3.4.4 Expected Upper limits to $d\phi/d\nu$ and $d\phi/dt$ for the Gl581 system

The uncertainty in the position of Gl581 (53 mas) and the semi-major axes of the planets (Gl581d = 40 mas and Gl581g = 23 mas) are added in quadrature to produce a positional uncertainty of 66 mas and 57 mas of Gl581d and Gl581g, respectively. The positional uncertainty places upper limits on the delay ($d\phi/d\nu$) and rate ($d\phi/dt$) expected for a SETI signal from Gl581. From Equations 3.2 & 3.3 the upper limits are: $(d\phi/d\nu)_{\rm max} = (1.2 \times 10^{-10})^\circ$ per spectral channel[6] and $(d\phi/dt)_{\rm max} = (2 \times 10^{-4})^\circ$ per second or $(6 \times 10^{-2})^\circ$ per data point, after averaging each scan. Since these estimates are close to zero, signals from either planets will

[5] `http://numpy.scipy.org/`

[6] 1 spectral channel = 1.95 kHz

be expected to appear at the zeroth DFT bin in Figure 3.1 i.e. consistent with a signal at the phase centre.

Additional uncertainty in the delay and rate are expected from calibration errors, particularly the stability with time of the phase calibrator. The phase of the calibrator was found to be relatively stable over the full bandwidth. Applying the DFT method to the calibrator across the 6 IFs, each of 64 MHz bandwidth and 64 channels per IF, the signal was found at the zeroth bin, consistent with a signal at the phase centre. For the phase rate, the sampling was not as high as the delay (i.e 8 points, separated by 5 mins each over 40 mins). While the stability of the calibrator may not be ideal, applying the DFT method, nonetheless results in the signal appearing in the zeroth and 1st bin (i.e. 0-45 degrees in Fig 3.1). This is consistent with the simulations of a source at the phase centre, that is affected by noise. The errors of the phase calibrator was therefore, ignored since the DFT method would be sensitive to any real signal appearing at or near the phase centre.

3.4.5 Analysis

3.4.5.1 Search for Candidate SETI Signals

After correlation and calibration our dataset consisted of 8 hours of data for the three baselines, divided into 12×40 minute observational blocks. Each 40 minute observation block was divided into three minute scans of Gl581, consisting of two second time-averaged complex visibilities and 32768 spectral channels. Before any further analysis was performed, each scan was vector-averaged along the time axis (for three minutes) leaving the observational blocks as arrays of data, with 32768 channels and 8 time integrations.

Since the star Gl581 is not a radio source (see Sect. 3.2), the dataset was not expected to contain any continuum emission. The dataset therefore consisted almost entirely of Gaussian noise at the thermal noise level with a few narrow spectral lines, possibly transient RFI. Any SETI signals present are expected to be weak compared to RFI. For data containing only weak signals (signal to noise ratio, $S/N \ll 1$), the mean of the amplitudes of the complex visibilities can be used as a proxy for the thermal noise (Thompson et al., 2001, Sect. 9.3). However, the mean is biased by RFI. To avoid this bias, the median of the amplitudes of the complex visibilities was used in place of the mean as a proxy for the thermal noise.

3.4.5.2 Broad-band signals

Each vector-averaged scan was searched along the channel axes for visibilities with amplitudes of signal-to-noise ratio (S/N) > 5. Detected signals were then checked to see if they occur on all baselines. Signals found on all baselines were plotted as a function of channel and visually searched for instances of five or more adjacent channels displaying coherent amplitudes and phases, typical of a real signal. Signals found satisfying these criteria were selected as broad-band signals. There were 22 groups of signals satisfying these requirements, selected as broad-band SETI candidates.

3.4.5.3 Narrow-band signals

The observational blocks, consisting of 32768 channels and 8 time integrations, were vector-averaged along the time axis, leaving 1-dimensional datasets of 32768 channels. The data were then searched on a per channel basis for visibilities with S/N > 5. Detected visibilities were then checked to see if they occur on all baselines. There were 200 signals satisfying these requirements, selected as narrow-band SETI candidates.

It is also possible to search for a shift of the narrow-band signals in frequency due to the Doppler effect. However, for a signal emanating from either Gl581g or Gl581d, would experience a maximum frequency drift of ∼4 kHz in 8 hrs. Since this corresponds to only two frequency channels (channel width = 1.95 kHz) it won't be taken into account during the search, however it might be used to confirm possible detections.

3.4.5.4 Frequency Distribution of the Candidate Signals

Figure 3.3 shows the frequency distribution of the SETI candidate signals (1525-1534 MHz), with the 200 narrow-band (grey) and the 22 broad-band (black) candidate signals. Australian Space to Earth geostationary satellites, Optus' Mobilesat and the INMARSAT[7] based systems, marketed in Australia by Telstra are known to operate at frequencies in the range 1525-1559 MHz (Symons, 1998). The close match between the transmission frequencies of the satellites and our candidate signals suggests that many or all of our detected signals may be RFI coming from these satellites.

[7]The International Mobile Satellite Organisation (INMARSAT) is an international treaty organisation with sixty seven member countries including Australia. INMARSAT operates a GSO satellite system for global, mobile communications on land, sea and in the air

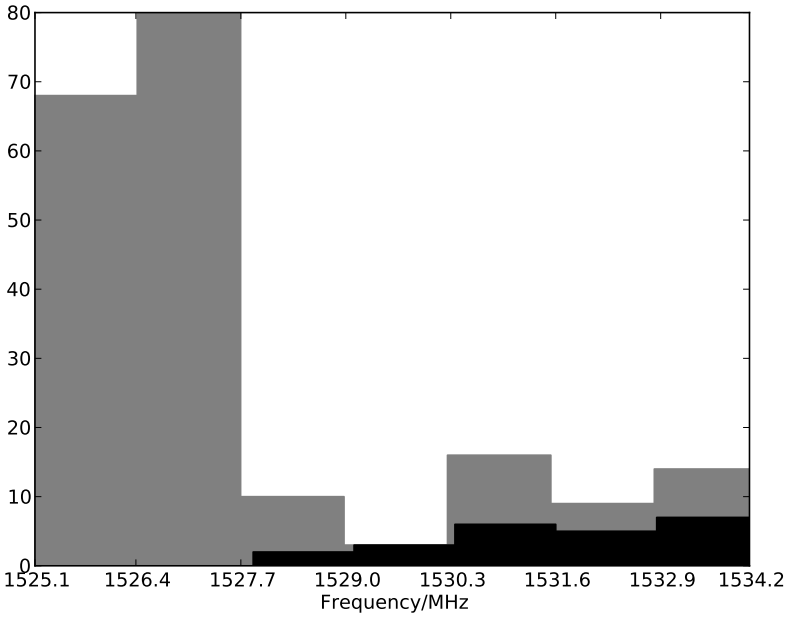

Figure 3.3: Distribution of the SETI candidate signals, 200 narrow-band emission (grey) and 22 broad-band events (black). The SETI candidate signals fall within the operating frequency range (1525-1559 MHz) of the geostationary Australian Space-Earth transmission satellites, Inmarsat-Optus.

3.4.5.5 Phase Variation of broad-band Candidate SETI Signals

Recall from Sect. 3.3.3, $d\phi/d\nu$ is dependant on the location of the signal with respect to the phase centre. To obtain $d\phi/d\nu$ for the 22 broad-band SETI candidates, DFTs were applied to the complex visibilities as a function of frequency, as described in Sect. 3.3.3.1. The maximum expected $d\phi/d\nu$ for a radio signal from the planets is $(1.2 \times 10^{-10})^\circ$ per spectral channel (Sect. 3.4.4). This phase variation is effectively zero at the level of frequency sampling in the observations.

Figure 3.4 shows the $d\phi/d\nu$ for the 22 broad-band SETI candidates. The horizontal dashed lines indicate the $d\phi/d\nu$ range expected for a radio signal from the Gl581 system. Any signals with a $d\phi/d\nu$ range that crosses the horizontal dashed lines on all three baselines are considered as possibly originating from the Gl581 system, and merit further investigation. None of the 22 broad-band signals has satisfied this criterion, and are thus rejected as originating from the Gl581 planets.

A large percentage of the signals are clustered around $d\phi/d\nu = 45^\circ$ per spectral channel on the shortest baseline (ATCA-Mp) in Figure 3.4. Using equation 3.2, and assuming a North-South baseline of projected length, v = 0.5 Mλ

(see Figure 3.2), this phase variation implies a minimum distance of $\sim 10^{\circ}$ from the phase centre (c.f. declination of Gl581 $\simeq$ -7° , geostationary satellite declination $\simeq +5^{\circ}$). This effect is less clear on the longer baselines since the rapidly rotating phase of the complex visibilities along both the frequency and time axes leads to averaging losses (smearing).

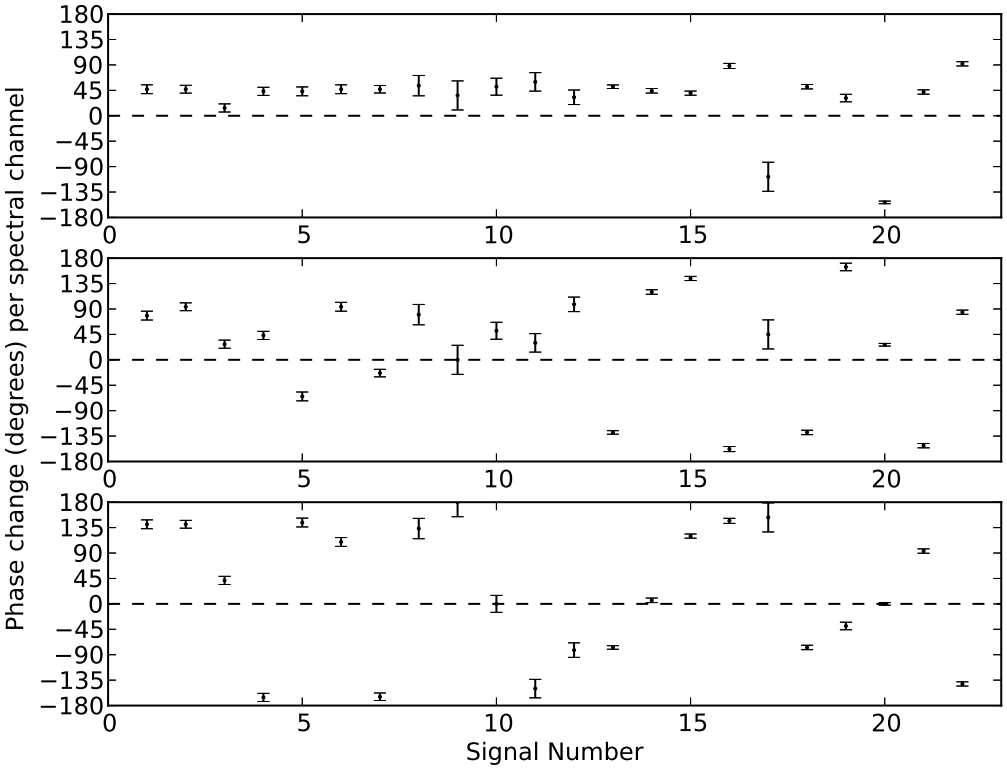

Figure 3.4: The $d\phi/d\nu$ range for the 22 SETI broad-band candidate signals, for the three baselines is plotted on the y-axis (*upper panel:* ATCA-Mp; *centre panel*: ATCA-Pa; *lower panel:* Mp-Pa). The error bars give the range of possible $d\phi/d\nu$ (or bin widths) for each signal. The x-axis gives the event number (1-22). The dashed line marks the maximum $d\phi/d\nu$ expected for a radio signal from Gl581, effectively zero at this resolution.

3.4.5.6 Phase Variation of Narrow-Band Candidate SETI Signals

The discrete power spectra of the 200 narrow-band SETI candidate signals were obtained by application of DFTs to the complex visibilities as a function of time. As discussed in Sect. 3.4.4, the maximum $d\phi/dt$ expected from a radio signal originating from either of the planets is 2×10^{-4} degrees per second. Such a slow varying signal is expected to behave as a signal from the phase centre, where

most of its power appears in bin zero of the DFT power spectrum on the three baselines.

To determine whether any of the signals are from the Gl581 system, classical detection theory was employed to test the hypothesis that the signal is located at the phase centre. Hypothesis testing compares the likelihood that any given signal is consistent with a source located at the phase centre, to the likelihood that it is consistent with a source located away from the phase centre, or from RFI. This is the classical *Neyman-Pearson* (NP) approach to hypothesis testing, or signal detection (Kay, 1998, chap. 3). The classical detection method has the advantages of providing robust estimation of errors and an efficient method of discriminating false positives from true signals.

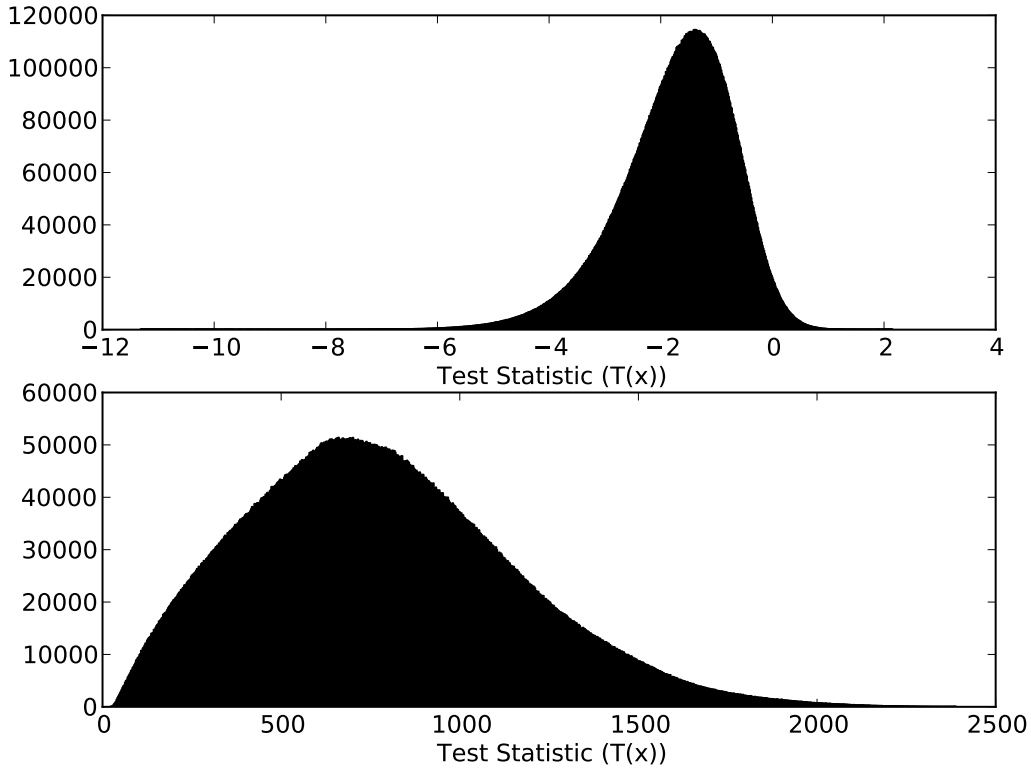

Figure 3.5: Log-scale distribution of test statistics, $\ln[T(x)]$ obtained from Monte-Carlo simulations for both 1. Signal-absent (upper plot), and 2. Signal-present (lower plot). Note the very different ranges plotted on the x-axis.

Table 3.2: SIGNALS IN DIRECTION OF GL581 WITH $\ln[T(x)] > 2$

Frequency			Baseline Specific log of the Test Statistic		
(MHz)	UT	$\ln[T(x)]$	ATCA-Mp	ATCA-Pa	Pa-Mp
(1)	(2)	(3)	(4)	(5)	(6)
1531.69080115	13:10:00-13:50:00	2.39	1.92	-0.30	0.77
1533.62972030	09:10:00-09:50:00	3.11	6.12	-1.36	-1.65
1533.80206867	13:10:00-13:50:00	3.50	2.19	0.66	0.66
1527.85017443	09:10:00-09:50:00	4.21	4.89	1.40	-2.07
1527.50351919	11:10:00-11:50:00	6.51	16.91	-4.95	-5.45
1527.56227431	11:10:00-11:50:00	7.25	11.04	-0.27	-3.52
1525.18856723	09:10:00-09:50:00	14.84	30.53	-15.32	-0.37
1527.50156068	09:10:00-09:50:00	26.19	17.86	2.87	5.47
1532.03158088	09:10:00-09:50:00	86.19	88.27	0.03	-2.10
1527.56423282	09:10:00-09:50:00	242.77	1782.83	-1305.76	-234.30

Notes.
(1) The central observing frequency; (2) The observing (UT) time period; (3) The sum of the log of the test statistics of the individual baselines, which is taken as the final test statistic; (4)-(6) The log of the test statistics of the individual baselines.

3.4.5.7 Hypothesis Testing and Monte-Carlo Simulations

For Gaussian-distributed noise in the complex visibilities, the amplitudes of the DFT bins are Rician-distributed. The two hypotheses are as follows: (1) *The alternative hypothesis*, H_1; signal-present - a source located at the phase centre has most of the power concentrated in bin zero, yielding a Rice distribution of amplitudes with parameters (amplitude and variance) determined by the data S/N and noise level; (2) *The null hypothesis*, H_0; signal-absent - a source located away from the phase centre, yielding power in a bin other than bin zero, with the same Rician parameters. The ratio of the likelihoods for bin zero to the next highest bin is the test statistic.

The test statistic is compared to a threshold to determine our level of confidence that the signal is real. To determine the threshold, we simulate 10^6 signal-present (i.e. at the phase centre) and 10^6 signal-absent sources, with the non-phase centre signals distributed randomly in the field. Since the aim of this test is to determine the power distribution of the DFT bins of the detected signals, and not the significance of the detection, the S/Ns used for both the signal present and absent cases reflect that found in our dataset. In addition, given that we expect the primary signals in the data to be RFI, rather than true signals, we also simulate zero-mean Gaussian noise with random RFI spikes located

at a single time point in the visibilities for both the signal present and absent cases. Figure 3.5 plots the log-scale distribution of the test statistics for both the signal-present cases (upper plot) and the signal-absent cases (lower plot). The thresholds were chosen to minimise the chance of false-positives, i.e *Type I error* (Kay, 1998, chap. 3). From Figure 3.5 the thresholds are the maximum log of the test statistic for the signal-absent case ($\ln[T(x)] = 2$), and the minimum log of the test statistic for the signal-present case ($\ln[T(x)] = 35$).

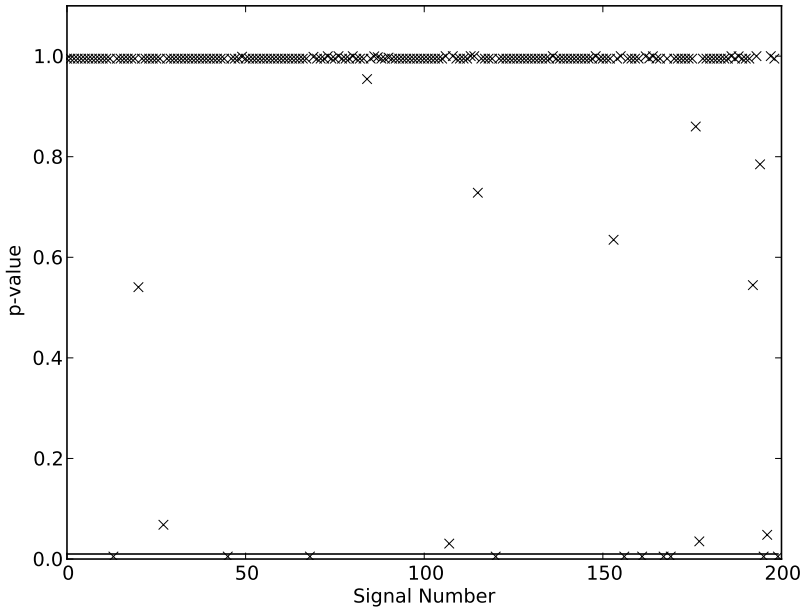

Figure 3.6: Distribution of p-values for the 200 narrow-band signals. The p-values represent the error in rejecting the null hypothesis, H_0 (signal-absent). The line plots the p = 0.01 significance value. Signals at or below this line can be considered inconsistent with the signal-absent hypothesis, and require further analysis. The signals at p=1 all have test statistics lower than the minimum test statistic of the simulated signal-absent distribution (Figure 3.5), and are assigned a p-value of 1.

The method was then applied to the 200 narrow-band signals, where the overall test statistic, $T(x)$, was taken as the product of the test statistics of the individual baselines. Ten narrow-band signals were found to have $\ln[T(x)] > 2$, of which only two are beyond $\ln[T(x)] = 35$ (Table 3.2). The data are expected to be consistent with no signal present at the phase centre (i.e. consistent with the null hypothesis). The significance level of rejecting the null hypothesis (the p-value) for the 200 signals were found by integrating the probability distribution of the signal-absent test statistic, obtained from the simulations. A small p-value

($p \leq 0.01$) corresponds to a signal that may not be consistent with the null hypothesis, and warrants further investigation. Figure 3.6 shows the p-values of the 200 signals. Most of the 200 signals were found to have a p-value greater than 0.01, with ten signals having a p-value of < 0.01.

Eight signals lie between both distributions ($2 < \ln[T(x)] < 35$). These signals are found to be inconsistent with both hypotheses, and reflect the limitations of our simple analysis; namely the the simulation of both the signal present and absent cases do not reflect the real signals perfectly, and the need for the overall test statistic to have a value in excess of the threshold, rather than those for the individual baselines.

Table 3.2 lists $\ln[T(x)]$ along with the test statistic for the individual baselines for all 10 events with $\ln[T(x)] > 2$. For all but one of the 10 events, $\ln[T(x)] < 2$ if the shortest baseline (ATCA-Mp) is excluded. For all 10 events the test statistic is far greater for the shorter baseline than for the other baselines. While this may point towards the shorter baseline detecting more flux, it is unlikely to be from a real source, since the test statistic of the 20 signals detected by the most sensitive baseline (ATCA-Pa) shows little or no significance. This is not consistent with a source at the phase centre. It is, however, more consistent with RFI distant from the phase centre. We can therefore easily exclude these signals as being from the GL581 system.

3.5 Discussion

We present the first VLBI SETI experiment. This pilot study demonstrates that the fundamental properties of VLBI makes it an ideal technique for targeted SETI. With multiple baselines, mas resolution, and mJy sensitivities, RFI can be easily identified and rejected using automated techniques, while being sensitive to very weak signals.

Our search method targeted signals that are five times the baseline sensitivity, which were then cross-referenced over three baselines, to identify corresponding signals. Hence, the amplitude sensitivity of our array was limited to our least sensitive baseline over an 8×3 minute observing interval, for narrow-band signals (ATCA-Mp; $1\sigma = 0.31$ mJy) and a single 3 minute scan for broad-band signals (a factor of $\sqrt{8}$ less sensitive)[8].

[8]The sensitivity limits were derived using the System Equivalent Flux Densities (SEFD) for the individual antennas at 1400 MHz; ATCA=68 Jy, Pa=40 Jy, Mp=340 Jy.

Our experiment finds no evidence for radio signals > 1.55 mJy ($= 5\sigma$) within the frequency range of 1230 - 1544 MHz from the region of Gl581. We can therefore place an upper limit of 7 MW Hz^{-1} on the power output of any isotropic emitter located in this planetary system, within this frequency range. It should be noted that the power of the Arecibo planetary radar transmitter is $\sim$ 1 MW (Black, 2002; Tarter, 2004). Assuming an aperture efficiency of 50% at $\lambda =$ 21 cm, the directive power output corresponding to an isotropic power output of $\sim$6 TW. Over a bandwidth of 5.4 Hz (Black et al., 2001), this emission would have the flux density of a $\sim$200 Jy radio source (or 650 mJy if integrated over our channel width of 1.953 kHz) at a distance of 20 ly.

3.5.1 Using current VLBI instruments for SETI

Since this was a proof-of-concept observation, two differences between this experiment and a typical VLBI observation should be noted. Firstly the baseline lengths in this experiment were short by VLBI standards. Baselines one or even two orders of magnitude longer would significantly reduce the amount of correlated RFI. Secondly, most VLBI observations are carried out using more than three antennas. Increasing the number of baselines to four or more constrains both the phase and amplitude closure relations[9], drastically increasing the quality of calibration. This would also provide the opportunity for image plane searching. However, it would likely be computationally expensive as a technique for searching over very wide frequency ranges. Relaxing the single baseline five times median limit could enhance the sensitivity beyond that of the weakest baseline.

We should also note that the width of the DFT bin is not a fundamental limit on the determination of the phase variation. A least-squares fit would allow the delay and delay rate to be determined more accurately. Essentially, the error on these parameters is limited by the signal to noise. Certainly the LBA has been used for astrometry at the sub-milliarcsecond level (Deller et al., 2009b,a). Observations of spacecraft have proven VLBI astrometry techniques for very weak narrow-band sources (Avruch et al., 2006) and suggest that VLBI might even allow the detection of the orbital motion of SETI signals. Furthermore, it is possible to confirm of the location of the candidate SETI signals through the measurement of the Doppler shift. However, this may require higher frequency

[9]The sum of the phases on any triangle of three baselines, and the combined amplitude ratio of four baselines contains information only on the true visibility of the source itself, all other errors cancel out (Thompson et al., 2001, chap. 9).

resolution than that used in this study.

While the techniques discussed in this chapter are ideal for targeted SETI, we also note the possibility of carrying out SETI commensally with normal VLBI operations. SETI target stars (Turnbull and Tarter, 2003) would be expected to be present in the field of view of the antennas for VLBI observations reasonably regularly. Using the techniques discussed in Deller et al. (2011) and Morgan et al. (2011) it would be possible to produce visibility datasets for any target star in the primary beam. Additionally, direct analysis of the voltages (the baseband data) although computationally expensive, could also be implemented at the correlator in an efficient manner to search for signals from extraterrestrial intelligence. A possible model for this is the V-FASTR transient search currently running at the VLBA operations centre (Wayth et al., 2011; Thompson et al., 2011).

In addition, VLBI is undergoing a transition from traditional recording systems towards real-time correlation via network connections (so called e-VLBI). This has led to VLBI being used for rapid follow-up of transient sources. These developments, the wide range of frequencies covered by VLBI instruments, and the huge added value that VLBI techniques bring to a targeted SETI search make VLBI the natural choice for follow-up observations to confirm a potential SETI signal. However, more accurate positions are needed for target stars for future experiments with higher angular resolution. Such positions will be provided in the near future by the high-quality optical astrometry of *Gaia* (Bastian and Schilbach, 1996).

3.5.2 SETI and the Square Kilometre Array (SKA)

A sensitive and advanced radio telescope, the Square Kilometre Array (SKA) is currently being planned for the coming decades[10].

At 1400 MHz, the addition of long baselines to the SKA will provide an astrometric precision of $\sim$3 μ-arcseconds (Fomalont and Reid, 2004). In addition, the SKA is expected to achieve sub-μJy sensitivities (Carilli and Rawlings, 2004; Dewdney et al., 2013) At $\sim$20 ly the SKA would probe an isotropic luminosity of a few kWHz^{-1}, far below the power output of radars and telecommunication satellites (see Figure 1.6). The fields of view will be $\sim$27 square degree for the low frequency component of the SKA, SKA-low and $\sim$1 square degrees for the higher frequency component SKA-mid (Dewdney et al., 2013). These capabilities will make the SKA the fastest, most sensitive and widest field of view

[10] `http://www.skatelescope.org/about/project/`

survey instrument in astronomy. However, for the SKA to be used for SETI, suitable targets are required. Such targets are currently being provided by current space missions (e.g. the Kepler mission, Borucki et al. 2010; Batalha et al. 2013.), and ground-based surveys (e.g. High Accuracy Radial velocity Planet Searcher, HARPS[11]). Furthermore, future space missions such as the Transiting Exoplanet Survey Satellite (TESS)[12] and PLAnetary Transits and Oscillations of stars (PLATO)[13] are expected to increase the number of confirmed habitable exoplanets.

3.6 Summary

The discoveries of potential habitable planets are no doubt fuelling a renewed excitement in SETI. With current VLBI systems we are able to search these candidates for signals from extra-terrestrial civilizations over a wide range of frequencies, and with high sensitivity. This proof-of-concept VLBI SETI experiment presents, by use of the fundamentals of VLBI, appropriate techniques for future VLBI SETI projects, including the SKA. The main results of this study is summarised below:

1. By utilising the fundamental properties of VLBI, this study demonstrated that VLBI is well suited for targeted SETI surveys. With N antennas separated by hundreds to thousands of kilometres resulting in $N(N-1)/2$ independent baselines, VLBI provides an efficient discriminator between targeted SETI and RFI signals. Furthermore, the high astrometric capabilities of VLBI allow localisation (with respect to the phase centre) of a signal through the measurements of its phase variations with time and frequency. Thus, a planet with a radio emitting civilisation will display characteristic phase variations that are related to their location relative to the host star, assuming that the star is at the phase centre;

2. The technique was tested on a three antenna LBA observation (maximum resolution = 127 mas) of the planetary system, Gliese 58 with two habitable planetary candidates. The observations were conducted between 1230 MHz and 1544 MHz separated into six sub-bands of 64 MHz bandwidth, with a frequency resolution on 1.953 kHz;

[11] https://www.eso.org/sci/facilities/lasilla/instruments/harps/overview.html
[12] http://tess.gsfc.nasa.gov/
[13] http://sci.esa.int/plato/42276-summary/

3. Candidate signals were selected based upon the following criteria: (i) amplitude greater than five times the baseline sensitivity; (ii) detected on all baselines. Signals satisfying both criteria were searched in time for single channel (narrow band events and in frequency for multiple channel (broadband) events. The phase variations with time and frequency were computed for signals found satisfying both criteria, through the use of discrete Fourier transform. A total of 222 potential SETI signals (200 narrow band and 22 broad band) were detected and by using automated data analysis techniques were ruled out as originating from the Gliese 581 system;

4. The study finds no significant signals that are consistent with being emitted from the Gliese 581 system above a flux limit of 1.55 mJy (5σ) within the frequency range of 1230 - 1544 MHz. This therefore places an upper limit of 7 MW Hz^{-1} on the power output of any isotropic emitter located in this planetary system, within this frequency range;

5. This study shows that VLBI is ideal for targeted SETI including follow-up observations. The techniques presented are equally applicable to next-generation interferometers, such as the long baselines of the Square Kilometre Array.

4

A Multi-Epoch Wide-Field VLBI Survey of the Nuclear Starburst Region of NGC 253

Adapted from:

Multi-epoch Very Long Baseline Interferometric Observations of the Nuclear Starburst Region of NGC 253: Improved Modeling of the Supernova and Star formation Rates

H. Rampadarath, J. S. Morgan, E. Lenc, & S. J. Tingay, 2014, The Astronomical Journal, Volume 147, Issue 1, article id. 5

4.1 Introduction

Starburst galaxies are defined as galaxies that are currently undergoing a period of intense star-formation, mainly within (but not exclusive to) the nuclear region, at a rate that cannot be maintained over their lifetime (Weedman, 1987; Lehnert and Heckman, 1996). The radio emission from such galaxies is not dominated by an active supermassive black hole, but by thermal and non-thermal emission that traces the star-forming activity (e.g. McDonald et al. 2002). The thermal emission is the result of free-free (or thermal bremsstrahlung) radiation from gas ionised by hot, young stars, while the non-thermal emission is from synchrotron radiation due to the acceleration of electrons to relativistic speeds by the core-collapse of massive stars to form Type II or Type Ibc supernovae (Pedlar et al., 1999; Weiler et al., 2002; McDonald et al., 2002). Interaction of the supernovae with the local circumstellar medium generates a hot, shocked region that produces a prompt emission typically observed as a radio supernova (RSN) (Weiler et al., 2002; Chevalier et al., 2006). As the RSNe expand into the surrounding interstellar medium, they evolve into supernova remnants (SNRs), forming shells

that emit non-thermal synchrotron radiation that can be visible over many years (Woltjer, 1972; Ulvestad and Antonucci, 1997; Ferreira and de Jager, 2008).

Studies of SNRs within nearby starbust galaxies can provide important information on the astrophysical processes occurring within these galaxies. Obscuration by dust and gas limit observations at shorter wavelengths, while radio wavelengths are largely unaffected. In addition, high-resolution, wide-field radio interferometry offers an opportunity to detect and resolve individual SNRs (e.g. McDonald et al. 2002; Tingay 2004; Lenc and Tingay 2006, 2009; Fenech et al. 2010). Such observations over multiple epochs allow monitoring of the evolution of existing SNRs and the detection of new RSNe and/or SNRs, enabling the supernova and star formation history of the galaxy to be reconstructed. Such studies have been successfully applied to nearby starburst galaxies such as: M82 (Pedlar et al., 1999; McDonald et al., 2002; Beswick et al., 2006; Fenech et al., 2010; Gendre et al., 2013); Arp 220 (Rovilos et al., 2005; Lonsdale et al., 2006; Parra et al., 2007; Batejat et al., 2011); Arp 299 (Ulvestad, 2009; Romero-Cañizales et al., 2011; Bondi et al., 2012); NGC 4945 (Lenc and Tingay, 2009); and NGC 253 (Ulvestad and Antonucci, 1997; Tingay, 2004; Lenc and Tingay, 2006). These studies have provided a wealth of information concerning RSNe and the evolution of SNRs, the star-formation and supernova rates of the host galaxies, and the interstellar medium of the starburst region. For example, almost three decades of observations have identified $\sim$100 compact sources in M82 (Fenech et al., 2010), where most have been resolved into parsec-scale shell-like structures (Muxlow et al., 1994; Beswick et al., 2006; Fenech et al., 2010). In addition, these multi-epoch observations have been instrumental in measuring the expansion speeds of the resolved SNRs (2,000 - 11,000 kms^{-1}), and with giving a direct estimate of the supernova rate (0.09 yr^{-1}) in M82. The discovery of new sources such as SN2008iz (Brunthaler et al., 2009b) and the radio transient 43.78+59.3 (Muxlow et al., 2010) would not have been possible without regular radio monitoring of M82. In addition, by combining multi-wavelength, high resolution radio observations of 46 compact sources in M82, McDonald et al. (2002) were able to identify low-frequency spectral turnovers, due to free-free absorption by the surrounding ionised medium.

As one of the nearest star-forming galaxies, NGC 253 has been extensively studied from gamma-rays to radio wavelengths. Recently, as part of the Advanced Camera for Surveys (ACS) Nearby Galaxy Survey Treasury (ANGST), Dalcanton et al. (2009) estimated the distance to NGC 253 as 3.47 $\pm$ 0.24 Mpc, 3.46 $\pm$ 0.07 Mpc and 3.40 $\pm$ 0.09 Mpc. The weighted average of the Dalcanton

et al. (2009) distance estimates, 3.44 ± 0.13 Mpc, is used as the assumed distance to NGC 253 in this chapter.

The first high-resolution, wide-field radio interferometric observations of NGC 253 were made by Turner and Ho (1985, hereafter TH85) with the Very Large Array (VLA) at 15 GHz (2 cm). With a resolution of $0''.21 \times 0''.10$, TH85 discovered nine compact sources (designated TH1 to TH9) within the central nuclear region. Following the results of TH85, Ulvestad and Antonucci conducted almost a decade of multi-frequency radio (1.8, 5, 8.3, 15 and 23 GHz) observations of the nuclear star-forming region of NGC 253 with the VLA, that culminated in a series of papers (Antonucci and Ulvestad, 1988; Ulvestad and Antonucci, 1991, 1994, 1997); they identified 64 individual compact sources, including the original nine from TH85. Spectral index measurements were obtained for the 17 brightest sources between frequency pairs of 5/15 and 8.3/23 GHz. Almost half of the 17 sources were identified with thermal HII regions while the remaining sources were taken to be associated with SNRs. Over the course of their survey, no new RSNe or SNRs appeared and the radio flux densities of the detected SNRs were found to be stable (Ulvestad and Antonucci, 1997, hereafter UA97). This led to an estimate for the upper limit on the supernova rate of 0.3 yr^{-1} by UA97.

In an attempt to resolve the low frequency radio emission in the inner 300 pc, Tingay (2004) conducted the first wide-field VLBI observations of NGC 253. The observations were carried out with the Australian Long Baseline Array (LBA) at 1.4 GHz and matched the angular resolution of the UA97 23 GHz VLA observations. While the observations detected only two sources (TH7 and TH9), Tingay (2004) showed that the radio emission at low frequencies is absorbed by ionised gas with a free-free optical depth range at 1 GHz of $\tau_0 \backsimeq 2.5$ to > 8. This result was consistent with observations between 0.33 - 1.5 GHz with the VLA (Carilli, 1996) and radio-recombination line (RRL) modelling of the nuclear region of NGC 253 (Mohan et al., 2002).

Motivated by these indicators of free-free absorption in NGC 253, Lenc and Tingay (2006, hereafter LT06) began a program to observe the nuclear region of this galaxy with the LBA. Their observations, conducted in 2004 at 2.3 GHz, were higher in sensitivity and resolution than Tingay (2004) and covered the region observed by UA97. They identified six compact sources, which were also seen in the higher frequency observations with the VLA (UA97). One of the sources, 5.48-43.3 was also resolved into a shell-like structure approximately 90 mas (1.7 pc) in diameter. Combining the LT06 data with the multi-wavelength radio data from UA97, the spectra of 20 compact sources in the nuclear region of NGC 253

were found to be consistent with the free-free absorption interpretation of Tingay (2004). The results indicated that while the free-free optical depth is highest towards the supposed nucleus, it varies significantly ($\tau_0 \simeq 1$ to > 20) throughout the nuclear region, implying variations in the gas density. Of the 20 sources, eight were found to have flat spectral indices, indicative of thermal H II regions, while the remaining sources were taken to be associated with SNRs due to their steep spectral indices at high frequencies. With no new sources detected in NGC 253 over almost two decades, LT06 developed a Monte-Carlo method based on the work of Ulvestad and Antonucci (1991), to estimate the upper limit on the supernova rate. Their model took into consideration improved distance measurements, a median free-free opacity, and the sensitivity limits of six observations over a 17 yr period. A value of 2.4 yr^{-1} was derived for the upper limit on the supernova rate. This high value suggests that there may be a large number of undetected RSNe, with observations over that period only detecting the rare, bright events. Detecting weaker or short-lived SNRs would provide tighter constraints on the supernova rate. However, this can only be done through frequent, high sensitivity, high resolution observations of NGC 253.

The results from multi-epoch, wide-field LBA observations at 2.3 GHz of the nuclear region of NGC 253 are presented in this chapter. Section 4.2 describes the observations, data analysis methods and the sources detected, including cross identifications with previous observations and investigations of possible flux density variations. Free-free absorption modelling of the spectra is described in Section 4.5.1. The morphology of the resolved SNR, 5.48-43.3, is examined in detail in Section 4.5.2. An improvement to the Monte-Carlo method of LT06 is presented with new estimates of the upper limits on supernova and star-formation rates within the inner 300 pc region of NGC 253 in Sections 4.5.3 & 4.5.4. The results are summarised in Section 4.6.

4.2 Observations

NGC 253 was observed at 2.3 GHz with the LBA at three epochs as described in Table 4.1. The observations were carried out with: the 64 m Parkes (Pa) antenna of the Australia Telescope National Facility (ATNF); the ATNF Australia Telescope Compact Array (ATCA)[1], used as a phased array; the ATNF Mopra (Mp) 22 m antenna; the University of Tasmania's 26 m antenna near Hobart (Ho);

[1] 5 × 22 m antennas were used for the 2006 & 2008 epochs, while 4 × 22 m antennas were used for the 2007 epoch.

Table 4.1: 2.3 GHz LBA multi-epoch observations

Epoch	2006	2007	2008
Observing Date	May 12/13	June 22/23	June 5/6
Array*	LBA	LBA	LBA+TID
Observing Time (hrs)	12	12	10
Frequency Range (MHz)	2269-2333	2268-2332	2226-2290
Bandwidth (MHz)	64	64	64
Sub-bands × Channels	4×16	4×16	4×16
Polarization:			
PA ATCA MP	RCP&LCP	RCP&LCP	RCP&LCP
CD HO TID	RCP	RCP	RCP
CLEAN beam (mas×mas):			
Wide-field array	147×51 @ −71°	134×48 @ −72°	86×33 @ −88°
Full array	15 ×13 @ 0.1°	15×15 @ −29°	16×13 @ 37°
$\sigma^\dagger$ (mJy beam^{-1})	0.39	0.44	0.18

Notes.

* LBA refers of the antennas: PA ATCA MP CD HO

† Wide-field image CLEAN RMS.

and the University of Tasmania's 30 m antenna near Ceduna (Cd). In addition, the 70 m NASA Deep Space Network antenna at Tidbinbilla (Tid) was used for the 2008 epoch. The data for each observation were recorded from 4 × 16 MHz sub-bands in the frequency ranges given in Table 4.1. All bands had dual circular polarization at Parkes, ATCA, and Mopra, with right circular polarization only at the remaining antennas. Table 4.1 lists the parameters associated with the LBA observations. During each observation, 3 minute scans of NGC 253 (centred on: RA = $00^{\rm h}47^{\rm m}$ $33.178^{\rm s}$; Dec = $-25°17'$ $17''.060$ [J2000.0]) were scheduled, alternating with 3 minute scans of a nearby phase reference calibration source, PKS J0038-2459 (RA = 00^h 38^m 14.735^s; Dec = $-24°$ $59'$ $02''.235$ [J2000.0]), located 2.13 degrees from the target. The recorded data for all epochs were correlated using the DiFX software correlator (Deller et al., 2007) with an integration time of 2 seconds and 64 frequency channels across each 16 MHz sub-band (channel widths of 0.25 MHz). The (u, v) coverage for the 2007 and 2008 epochs are shown in Figure 4.1.

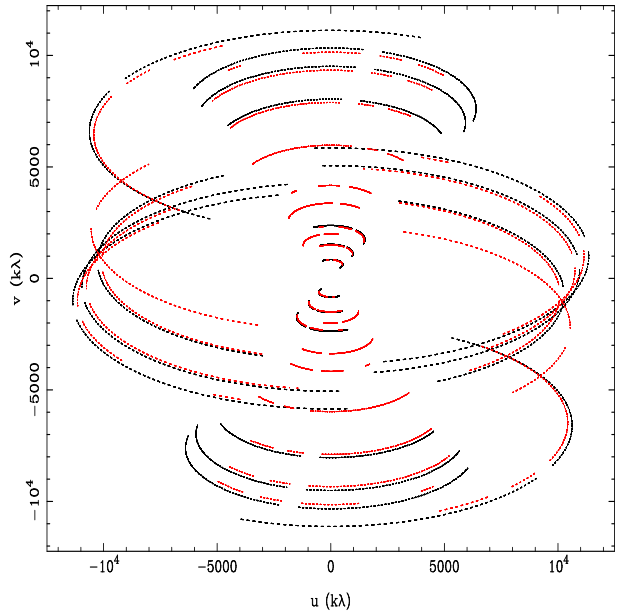

Figure 4.1: (u, v) coverage of the 2007 (black) and 2008 (red) LBA epochs at 2.3 GHz (band centre frequency for each baseline only). The (u, v) coverage for the 2006 epoch (not plotted) was similar to the 2007 (u, v) coverage.

4.3 Calibration and Data Reduction

The initial data reduction and calibration were performed using the data reduction package AIPS. Prior to calibration, flagging of data during times at which each of the antennas were known to be slewing and time ranges that contained known bad data, were carried out via application of flag files and information provided by the observing logs. Data from the first 30 seconds of each scan from baselines involving ATCA or Parkes were flagged, in order to eliminate known corruption of the data at the start of each scan at these two telescopes.

During correlation, nominal (constant) SEFD values (in Jansky) for each antenna were applied to the correlation coefficients. The nominal calibration was refined by application of antenna system temperatures (in Kelvin) measured during the observation, along with the gain (in Jansky per Kelvin) for each antenna. Further refinements to the amplitude calibration were derived from simultaneously recorded ATCA observations of PKS J0038-2459, which is a bright, compact radio source, unresolved at this frequency on the LBA baselines. Since the LBA does not resolve out any extended structure, the ATCA and LBA baselines will measure the same flux density. Thus, the flux density measured at the ATCA can be used to check and refine the amplitude calibration for the LBA data. Suitable simultaneous recorded ATCA data were obtained for all but the

2008 observation.

The NRAO's Very Long Baseline Array (VLBA) calibrator survey routinely observes PKS J0038−2459 at 2.3 GHz, but did not in 2008. Figure 4.2 plots the 2.3 GHz light curve of PKS J0038−2459 for eight epochs between 1997 to 2010, obtained from the LBA and the VLBA. The error bars for the LBA are ±10% and were taken to represent the absolute flux density errors, associated with the calibration of the measured flux densities (Reynolds, 1994). However, the flux densities obtained from the VLBA/USNO calibrator, provided no error measurements. Thus, to keep the measurements/estimation consistent a ±10% conservative amplitude error was assumed. A weighted least-squares fit was used to interpolate to the flux density of PKS J0038−2459 at the time of the 2008 LBA observation. The fit gave a flux density of 337 mJy, with a 1σ error of 19 mJy at the time of the 2008 observation. This flux density was used to refine the amplitude calibration for the 2008 LBA data, by defining a model with this flux density in DIFMAP (Shepherd, 1997). The DIFMAP task GSCALE was used to determine corrections to the uncalibrated amplitudes of PKS J0038−2459 from the model.

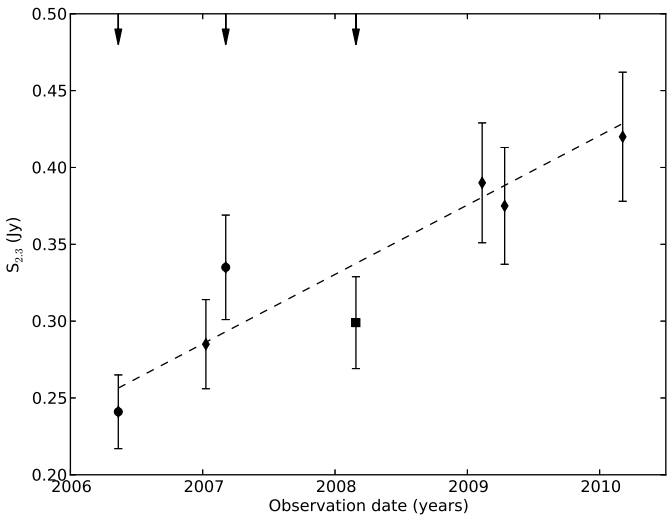

Figure 4.2: Light curve of the PKS J0038-2459 from 2006 to 2010 at 2.3 GHz. The data are from the Bordeaux VLBI Image Database and the USNO Radio Reference Frame Image Database (points) and the LBA fluxes derived from our 2006 and 2007 observations (circles). A least-squares fit to the data was used to interpolate the flux density of the calibrator during the 2008 epoch. The resulting fit produced a standard deviation, σ = 19 mJy. The square point plots the final imaged flux density following amplitude refinement for the 2008 epoch. The arrows indicate the dates of the LBA observations.

Following amplitude calibration refinement, global fringe-fitting solutions were determined for PKS J0038−2459 (AIPS task FRING) with a three minute solution interval, finding independent solutions for each of the 16 MHz bands. The delay and phase solutions were examined and, following editing of bad solutions, applied to PKS J0038−2459. The PKS J0038−2459 data were exported to DIFMAP, where the data were vector-averaged over 30 s, flagged of bad data and imaged using standard imaging techniques (deconvolution and self-calibration of both phase and amplitude). The resulting images of PKS J0038-2459 for the 2006, 2007 and 2008 epochs show a highly compact source, with no significant structure on these baselines at this frequency to a dynamic range[2] of 400. The final calibration solutions (phase and amplitude) of PKS J0038−2459 were exported via the DIFMAP task, CORDUMP[3] (Lenc and Tingay, 2009) to an AIPS-compatible solutions table. The solutions table was then transferred to AIPS and applied to all sources in the dataset. The PKS J0038-2459 data were also used to derive a bandpass calibration via the AIPS task BPASS which was applied to the NGC 253 data. The edge channels of each band were flagged from the data set (2 channels from both the lower and upper edge of each 16 channel band). The final calibration solutions were applied to both PKS J0038−2459 and NGC 253 and the visibility data exported as FITS files.

DIFMAP was used as the preferred imaging tool over AIPS for this study as it presented more flexible flagging and imaging tools which provided a faster turn around time, that was convenient for the project.

The combined loss of amplitude due to image smearing at the field's edge (radius of $\sim 10''$ from the phase centre) using Equations 2.8 and 2.9 is $\sim 3\%$ on the longest baseline (Hobart - Ceduna). Thus, to allow imaging of the inner 300 pc at a resolution of ~ 15 milli-arcseconds (mas), the NGC 253 dataset was not averaged in time or frequency. To facilitate imaging in DIFMAP, the frequency channels were converted into sub-bands. This conversion allowed DIFMAP to treat the frequency channels independently in the (u, v) plane rather than averaging them together, thus avoiding any further bandwidth smearing effects during the imaging process.

NGC 253 imaging was initially performed with a reduced resolution by excluding data from the Hobart and Ceduna antennas (the longest baselines). The imaging parameters were chosen to closely match the imaging parameters of LT06, with cellsize of 11 mas and application of natural weighting to minimise noise at

[2]Defined as the ratio of peak of image to peak of brightest artefact.

[3]`http://www.atnf.csiro.au/people/Emil.Lenc/tools/Tools/Cordump.html`

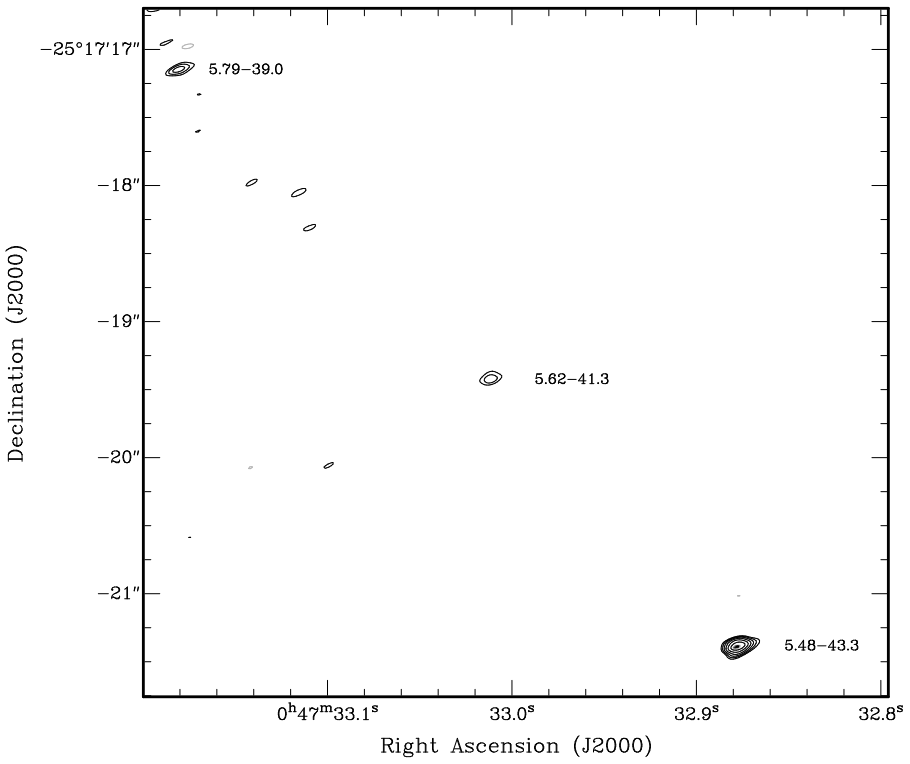

(a)

Figure 4.3: Wide-field VLBI image of NGC 253 with the LBA at 2.3 GHz of the 2006 epoch and the RMS noise level is 0.39 mJy beam^{-1}. The peak is 10.4 mJy beam^{-1}. The contours are $(-3\sqrt{2}\sigma, 3(\sqrt{2})^n\sigma)$, where σ is the RMS noise of each image and n = 1,2,3,...,7

the expense of resolution. Figure 4.3 displays the resulting contour images of NGC 253 for the three epochs. The 1σ noise measurement for the three images are listed in Table 4.1. The 1σ noise levels at the 2006 and 2007 epochs are 2-3 times higher than at the 2008 epoch, which can be attributed to the absence of the 70 m Tidbinbilla antenna in 2006/07. However, the 1σ noise of the 2008 image is 28% lower than that of the LT06 (2004 epoch) image due to increased bandwidth.

Figure 4.4 shows the images of the SNR 5.48-43.3 for the three epochs. The images were made with the full array (i.e. including data from both Hobart and Ceduna), with natural weighting and a cell size of 4 mas.

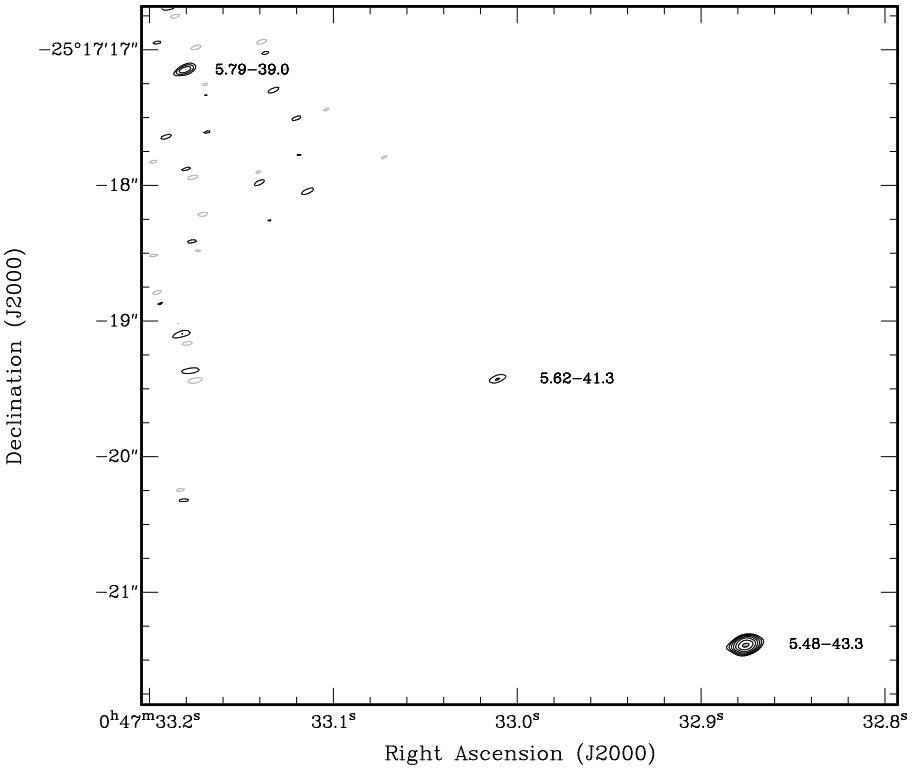

(b)

Figure 4.3: Wide-field VLBI image of NGC 253 with the LBA at 2.3 GHz of the 2007 epoch. The RMS noise level is 0.44 mJy beam^{-1}and the peak is 11.8 mJy beam^{-1}. The contours are $(-3\sqrt{2}\sigma, 3(\sqrt{2})^n\sigma)$, where σ is the RMS noise of each image and n = 1,2,3,...,7

4.4 Identification of Sources and Flux Density Measurements

A number of detected sources are clearly visible in Figure 4.3. We used the source extraction software, BLOBCAT (Hales et al., 2012) to identify and measure the flux densities of compact sources in the three images. Seven sources were detected above 5σ by BLOBCAT in the 2008 epoch, while only the three brightest sources (5.48-43.3, 5.62-41.3 and 5.79-39.0) were found via BLOBCAT for the less sensitive 2006 and 2007 epochs (see Table 4.2).

Included in Table 4.2 are the flux densities for the compact sources detected in the 2004 epoch by LT06. Only three of these sources were detected in all four 2.3 GHz LBA epochs (i.e. 2004, 2006, 2007 and 2008), while three were detected in only the 2004 and 2008 epochs, with one possible additional source detected solely in the 2008 image. The flux density of the sources detected by

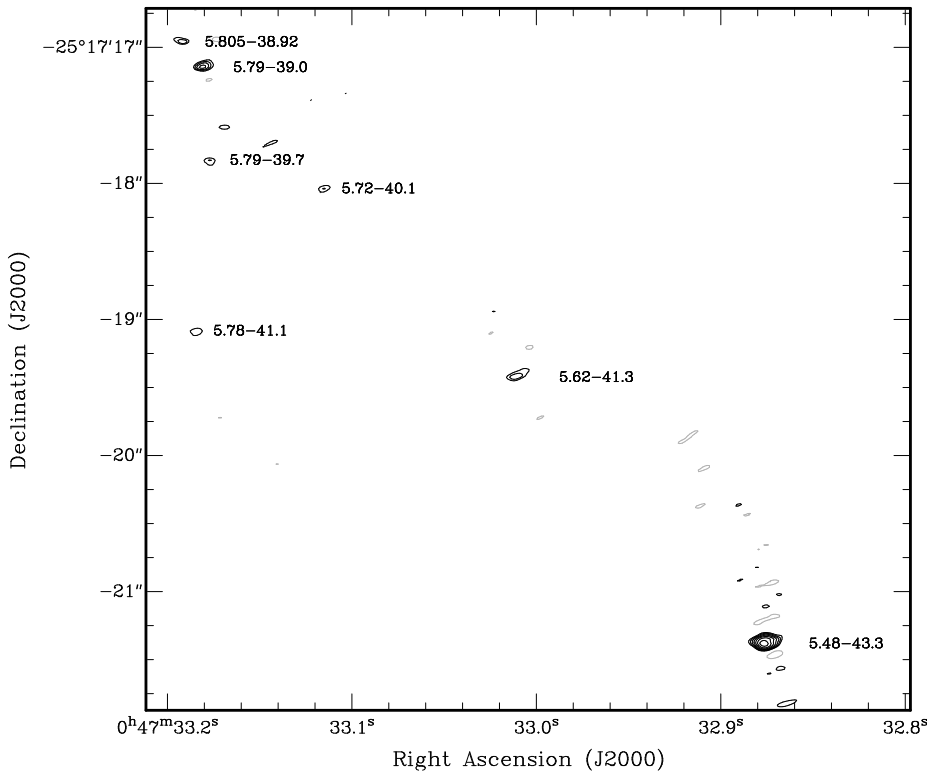

(c)

Figure 4.3: Wide-field VLBI image of NGC 253 with the LBA, including Tidbinbilla, at 2.3 GHz of the 2008 epoch. The RMS noise level is 0.18 mJy beam^{-1}and the peak is 7.9 mJy beam^{-1}. The contours are $(-3\sqrt{2}\sigma, 3(\sqrt{2})^n\sigma)$, where σ is the RMS noise of each image and n = 1,2,3,...,7

LT06 were also estimated via BLOBCAT and found to agree with LT06's values within measurement errors. For comparison, the published source flux densities of LT06 are included in Table 4.2. While stacking of the 2004 and 2008 images improved image noise by a factor of $\sqrt{2}$, the resulting image did not reveal any additional sources.

Errors in the flux-density estimates have two different origins. Firstly, there is the overall uncertainty in the absolute flux density scale for the LBA, estimated as $\pm\,10\%$ (Reynolds, 1994). Secondly, there are the errors in determining the flux density by BLOBCAT, which ranges from 5 - 10%. Both terms are added in quadrature for the 2006 and 2007 observations. For the 2008 observation, we determine a third contribution to the error, which is described in Section 4.4.1.

Table 4.2 lists cross identifications with sources detected at 15 GHz and 23 GHz by UA97 and at 2.3 GHz with the LBA by LT06. The mean difference between our 2008 and LT06's 2004 J2000.0 source positions was found to be 8 mas, with a standard deviation of 5 mas, which is $\sim$ 10% of the beam-width.

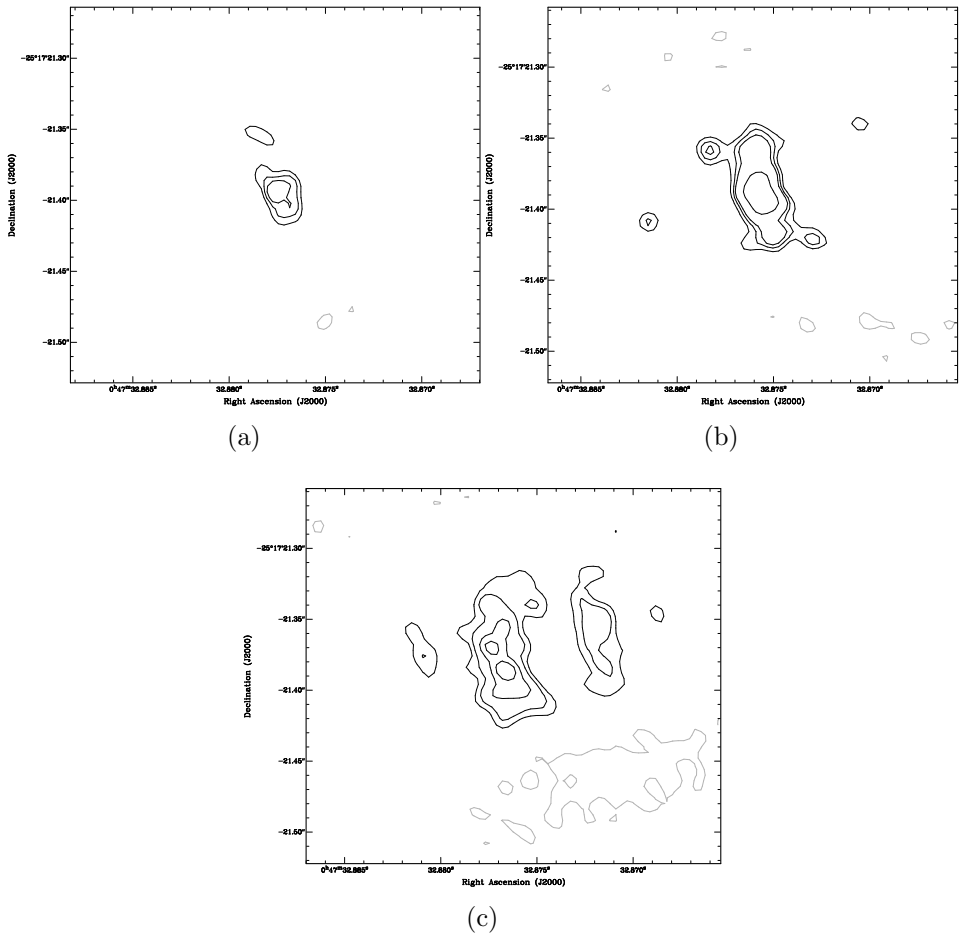

Figure 4.4: 2.3 GHz Australian LBA images of 5.48-43.3. (a): *2006 epoch.* The RMS noise of the image is 0.22 mJy beam^{-1}and the peak flux density is 1.6 mJy beam^{-1}. The beam size is 15×14 mas at a position angle (PA) of 0.1° .(b): *2007 epoch.* The RMS noise of the image is 0.26 mJy beam^{-1}and the peak flux density is 3.8 mJy beam^{-1}. The beam size is 15×14 mas at a PA of −85° . (c): *2008 epoch.* The RMS noise of the image is 0.13 mJy beam^{-1}and the peak flux density is 2.61 mJy beam^{-1}. The beam size is 16×13 mas at a PA of 37° . The contours of the three epochs are (-3σ, nσ) where, n = 3, 4, 5, 10, 15 and σ is the respective image RMS noise.

The mean position difference between our 2008 J2000.0 source position and the B1950.0 source positions of the 23 GHz sources from UA97 is 87 mas, with a standard deviation of 51 mas, which matches LT06 results. This is approximately one LBA beam-width and $\sim$ 67% of the VLA 23 GHz beam-width. Therefore it is possible that the sources detected by the LBA are related to the lower resolution UA97 sources. Thus, the three LBA observations presented here, as well as LT06 did not detect any new radio sources in NGC253.

Table 4.2: Compact Sources Detected with the LBA at 2.3 ghz

Position (J2000.0)												
RA	Dec	Identification			Peak Flux Density (mJy beam^{-1})				Integrated Flux Density (mJy)			
(00^h47^m)	($-25°\,17'$)	UA97	TH85	LT06	S_P^{2004}	S_P^{2006}	S_P^{2007}	S_P^{2008}	S_I^{2004}	S_I^{2006}	S_I^{2007}	S_I^{2008}
(1)	(2)	(3)	(4)	(5)	(6)	(7)	(8)	(9)	(10)	(11)	(12)	(13)
32.876	21.383	5.48−43.3	TH9	Y	8.6 ± 0.9	13.5± 1.6	16.0 ± 1.9	7.8 ± 01.2	32.0 ± 3.2	22.8 ± 2.4	30.2 ± 3.4	25.1 ± 9.9
33.012	19.425	5.62−41.3	TH7	Y	1.7 ± 0.2	2.7 ± 0.6	2.4± 0.5	1.3 ± 0.3	8.8 ± 0.9	6.3± 0.8	5.7 ± 0.8	6.8 ± 2.7
33.115	18.039	5.72−40.1	TH6	Y	1.5 ± 0.2	<2.0	<2.2	1.0 ±0.2	3.8 ± 0.4	<2.0	<2.2	3.0 ± 1.2
33.185	19.084	5.78−41.1	....	N	<1.2	<2.0	<2.2	0.9 ±0.2	<1.2	<2.0	<2.2	4.6 ± 1.8
33.177	17.830	5.79−39.7	TH3	Y	1.8 ± 0.2	<2.0	<2.2	1.0 ±0.2	6.2 ± 0.6	<2.0	<2.2	3.2 ± 1.3
33.181	17.148	5.79−39.0	TH2	Y	2.4 ± 0.2	4.1 ± 0.6	4.9 ± 0.7	2.6 ±0.4	5.7 ± 0.6	7.8 ± 1.0	7.3 ± 0.9	5.9 ± 2.3
33.193	16.949	5.805−38.92	...	Y	2.1 ± 0.2	<2.0	<2.2	1.5 ± 0.3	6.8 ± 0.7	<2.0	<2.2	2.4 ± 1.0

Notes.

(1) & (2) The VLBI 2.3 GHz source positions for the 2008 epoch. Units of right ascension are seconds and units of declination are arcseconds; (3) Source identifications with 1.3 and 2 cm sources from UA97; (4) Source identifications with 2 cm sources from TH85; (5) Sources detected (Y) or not-detected (N) by LT06's 2.3 GHz LBA observation; (6-9) 2.3 GHz LBA peak flux density for epochs 2004 - 2008; (10-13) 2.3 GHz LBA integrated flux density for epochs 2004 - 2008. Flux density values for the 2004 epoch were obtained from LT06.

4.4.1 Variations in the Flux Density

Lower integrated flux densities are recorded for all sources except for 5.79−39.0 in the 2008 epoch compared to the 2004 epoch (see Table 4.2 and Figure 4.5). Since it was necessary to interpolate the flux density of a variable calibrator to obtain a value for the 2008 epoch (see Section 4.3) it would not be surprising if there were an error on the flux density scale. Considering that SNR 5.48-43.3 is $\sim 6''$ from the pointing centre, it is possible that the flux errors may be influenced by non-coplanar effects. Shifting the field centre to SNR 5.48-43.3 with the AIPS task UVFIX and imaging produced similar results as Table 4.2. This is expected since, using Equation 2.12 non-coplanar effects should dominate at radii >10 arcseconds. Given the covariance of the flux densities between 2006 and 2008 (and possibly for the other epochs too) this would appear to be the case. Adjusting empirically for the difference in flux density between 2006 and 2008 by taking the mean of each, we find that we must increase the absolute flux density calibration of the 2008 epoch by 20%[4]. After this adjustment, no source appears significantly variable with the exception of 5.805-38.92, whose decrease in flux density would still be a 9σ error (assuming of course that the distribution of the errors is Gaussian).

To investigate whether the flux density decrease is genuine we used the AIPS task UVMOD to simulate datasets with the same (u, v) coverage and noise level as the 2004 and 2008 LBA datasets. In UVMOD the parameter FACTOR was set to zero to allow the injection of the fake sources at the same positions as the real ones. The fake sources were injected with the properties (i.e. size, position angle, integrated flux density and position) of the sources detected by LT06. The resulting datasets were exported and imaged in DIFMAP following the procedure described in Section 4.3. The integrated flux densities of the injected sources were measured with BLOBCAT and plotted in Figure 4.6 (left plot) against the model flux densities. If the flux density decrease in the observed dataset were due to only source variability, the measured (or recovered) flux densities would be equal to the injected flux densities, represented by the dashed lines. The deviation of the UVMOD flux densities from the dashed lines follows a similar trend to the observed flux densities (right plot of Figure 4.6).

The effect of CLEAN bias is known to produce a systematic underestimate of flux densities (Becker et al., 1995) by redistributing flux density from sources to

[4]Note, this 20% correction has not been applied to the 2008 flux densities in table 4.2 or figure 4.5.

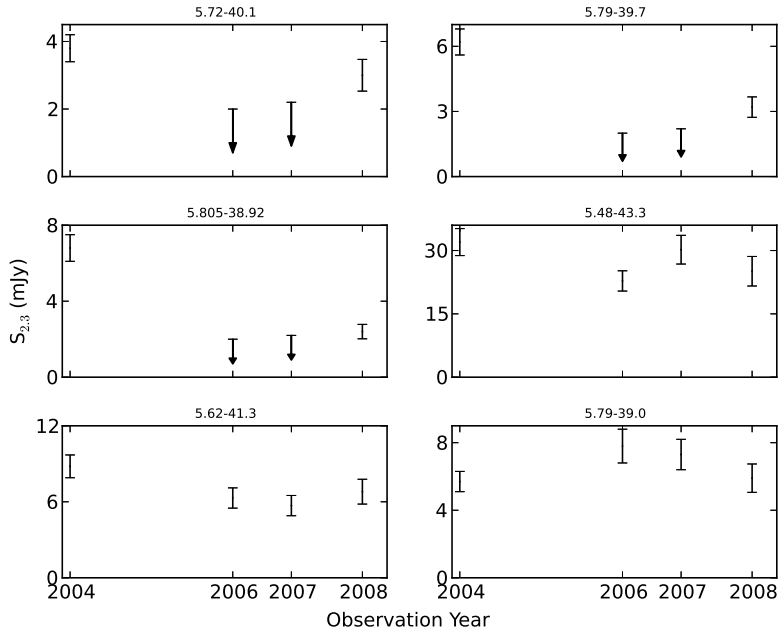

Figure 4.5: Light curves of the compact sources detected in all 2.3 GHz observations (2004, 2006, 2007 and 2008). The integrated flux densities (from Table 4.2) are plotted on the y-axis, while the observation date is listed on the x-axis. 5σ upper limits are represented by arrows for epochs without detections. The error-bars are the 10% absolute flux density and BLOBCAT measurement errors added in quadrature (see Section 4.4).

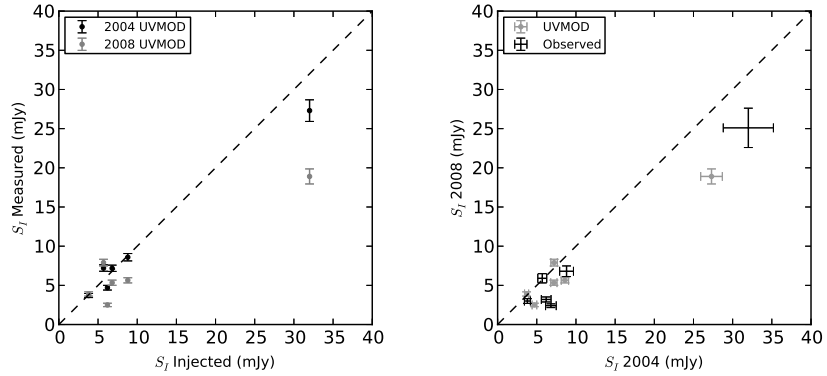

Figure 4.6: *Left:* The integrated flux densities of the fake sources (x-axis) injected into the modelled datasets via UVMOD are plotted against the recovered integrated flux densities for the 2004 (black points) and 2008 (grey points) modelled datasets. *Right:* The recovered integrated flux densities of the fake sources for the 2004 and 2008 modelled datasets (grey points) are compared. For comparison the observed integrated flux densities listed in Table 4.2 for the 2004 and 2008 epochs are plotted (black points). The dashed lines represents where y=x.

noise peaks in the image during deconvolution. The magnitude of the flux density redistributed is generally independent of flux density, and thus the fractional error

is largest for weak sources. This effect may have a stronger effect in the 2008 image (as compared to the 2004 image) due to the presence of high side-lobes. The high side-lobes may have resulted from the combination of poor (u, v) coverage and an increased sensitivity due to a higher bandwidth.

The RMS[5] difference between the 2008 recovered flux densities and the model flux densities is 37%, which is added in quadrature with the absolute flux density scaling and measurement errors for the 2008 epoch (see Section 4.4) and listed in Table 4.2. The resulting flux density decrease of 5.805−38.92 is then reduced to a significance of 4.5σ. While this variability may be due to unaccounted for calibration errors, we cannot rule out contributions from intrinsic variability.

4.5 Discussion

4.5.1 Radio Spectra and Free-Free Absorption Modelling of Compact Sources in NGC253

A downturn in the spectra of the compact sources in NGC 253 at low frequencies was observed previously by Tingay (2004) and LT06. Different mechanisms were explored by LT06 to explain the observed effect including; a simple power law, a power law spectrum with free-free absorption by a screen of ionised gas, and a self-absorbed bremsstrahlung spectrum. LT06 demonstrated that the spectra of the sources were consistent with a free-free absorbed power-law spectrum, given by the following equation:

$$S(\nu) = S_0(\nu/\mathrm{GHz})^{\alpha} e^{-\tau_\nu}, \tag{4.1}$$

where

$$\tau_\nu = \tau_0(\nu/\mathrm{GHz})^{-2.1} \tag{4.2}$$

and α is the optically thin intrinsic spectral index, τ_0 is the free-free optical depth at 1 GHz, and S_0 is the intrinsic flux density of the source at 1 GHz. Similar spectra have been obtained for compact sources in other nearby starburst galaxies, such as M82 (McDonald et al., 2002), Arp 220 (Parra et al., 2007), and NGC 4945 (Lenc and Tingay, 2009). We therefore adopt this model and the method described by LT06.

[5]We define the root mean square (RMS) difference between the modelled (S_m) and the recovered (S_r) flux densities, as $\sqrt{1/n\Sigma[(S_m - S_r)^2/S_m^2]}$

Table 4.3: Summary of Flux Density Measurements for Radio Sources in ngc 253

	LBA					VLA				
VLA ID	$S_{1.4}$	$S_{2.3}^{2004}$	$S_{2.3}^{2006}$	$S_{2.3}^{2007}$	$S_{2.3}^{2008}$	S_5	$S_{8.3}$	S_{15}	S_{23}	S_{23}^{BCT}
(1)	(2)	(3)	(4)	(5)	(6)	(7)	(8)	(9)	(10)	(11)
4.81-43.6	<1.8	<1.2	<2.0	<2.2	<0.9	1.4 ± 0.2	....	0.4 ± 0.3	....	1.4 ± 0.3
5.48-43.3	16 ± 0.2	32.0 ± 3.2	22.8 ± 2.4	30.2 ± 3.4	25.1 ± 9.9	27.1 ± 2.7	20.5 ± 1.0	12.5 ± 1.3	9.8 ± 1.0	13.1 ± 0.9
5.49-42.2	<1.8	<1.2	<2.0	<2.2	<0.9	....	1.1 ± 0.2	....	0.8	....
5.54-42.2	<1.8	<1.2	<2.0	<2.2	<0.9	2.8 ± 0.4	2.7 ± 0.24	3.4 ± 0.4	4.5 ± 0.5	9.2 ± 1.7
5.59-41.6	<1.8	<1.2	<2.0	<2.2	<0.9	....	3.0 ± 0.3	....	5.7	....
5.62-41.3	6 .0 ± 0.6	8.8 ± 0.9	6.3 ± 0.8	5.7 ± 0.8	6.8 ± 2.7	9.8 ± 1.0	7.3 ± 0.4	7.5 ± 0.8	5.8 ± 0.6	10.7 ± 1.4
5.65-40.7	<1.8	<1.2	<2.0	<2.2	<0.9	....	1.5 ± 0.2	....	1.2 ± 0.3	....
5.72-40.1	<1.8	3.8 ± 0.4	<2.0	<2.2	3.0 ± 1.2	7.7 ± 0.8	6.5 ± 0.4	7.8 ± 0.8	7.9 ± 0.8	21.9 ± 2.3
5.73-39.5	<1.8	<1.2	<2.0	<2.2	<0.9	....	2.4 ± 0.2	....	2.8 ± 0.4	....
5.75-41.8	<1.8	<1.2	<2.0	<2.2	<0.9	7.0 ± 0.7	4.8 ± 0.3	3.1 ± 0.4	2.6 ± 0.4	....
5.78-39.4	<1.8	<1.2	<2.0	<2.2	<0.9	....	16.9 ± 0.9	....	9.7 ± 1.0	29.9± 1.2
5.79-39.0	<1.8	5.7 ± 0.6	7.8 ± 1.0	7.3 ± 0.9	5.9 ± 2.3	38.6 ± 3.9	48.0 ± 2.4	40.3 ± 4.0	35.8 ± 3.6	38.4 ± 0.9
5.79-39.7	<1.8	6.2 ± 0.6	<2.0	<2.2	3.2 ± 1.3	....	....	∼4.1 ± 0.5	∼1.6 ± 0.3	....
5.78-41.1	<1.8	<1.2	<2.0	<2.2	4.6 ± 1.8	4.7 ± 0.5	3.2 ± 0.3	1.9 ± 0.3	1.0 ± 0.3	....
5.805-38.92	<1.8	6.8 ± 0.7	<2.0	<2.2	2.4 ± 1.0	....	....	∼3.0 ± 0.4	∼1.9 ± 0.3	8.9± 1.1
5.87-40.1	<1.8	<1.2	<2.0	<2.2	<0.9	3.8 ± 0.4	2.1 ± 0.2	1.4 ± 0.3	0.7 ± 0.3	....
5.90-37.4	<1.8	<1.2	<2.0	<2.2	<0.9	4.0 ± 0.5	4.0 ± 0.3	5.9 ± 0.7	6.7 ± 0.7	9.1 ± 1.2
5.95-37.7	<1.8	<1.2	<2.0	<2.2	<0.9	1.2 ± 0.2	....	0.6 ± 0.3	....	....
6.00-37.0	<1.8	<1.2	<2.0	<2.2	<0.9	5.9 ± 0.6	3.5 ± 0.2	2.4 ± 0.4	1.7 ± 0.3	....
6.40-37.1	<1.8	<1.2	<2.0	<2.2	<0.9	2.9 ± 0.4	....	1.3 ± 0.3	....	0.8±0.2

Notes.

(1) Source identification given by UA97; (2) 1.4 GHz flux density with the LBA by Tingay (2004); (3 - 6) flux density at 2.3 GHz from 2004 (LT06) and this work (2006-2008), where the superscript indicates the observation year. Upper limits on the flux (5σ) are provided for sources that have not been detected; (7 - 10) The flux densities at 5, 8.3, 15 and 23 GHz with the VLA by UA97; (11) 23 GHz VLA flux densities by Brunthaler et al. (2009a)

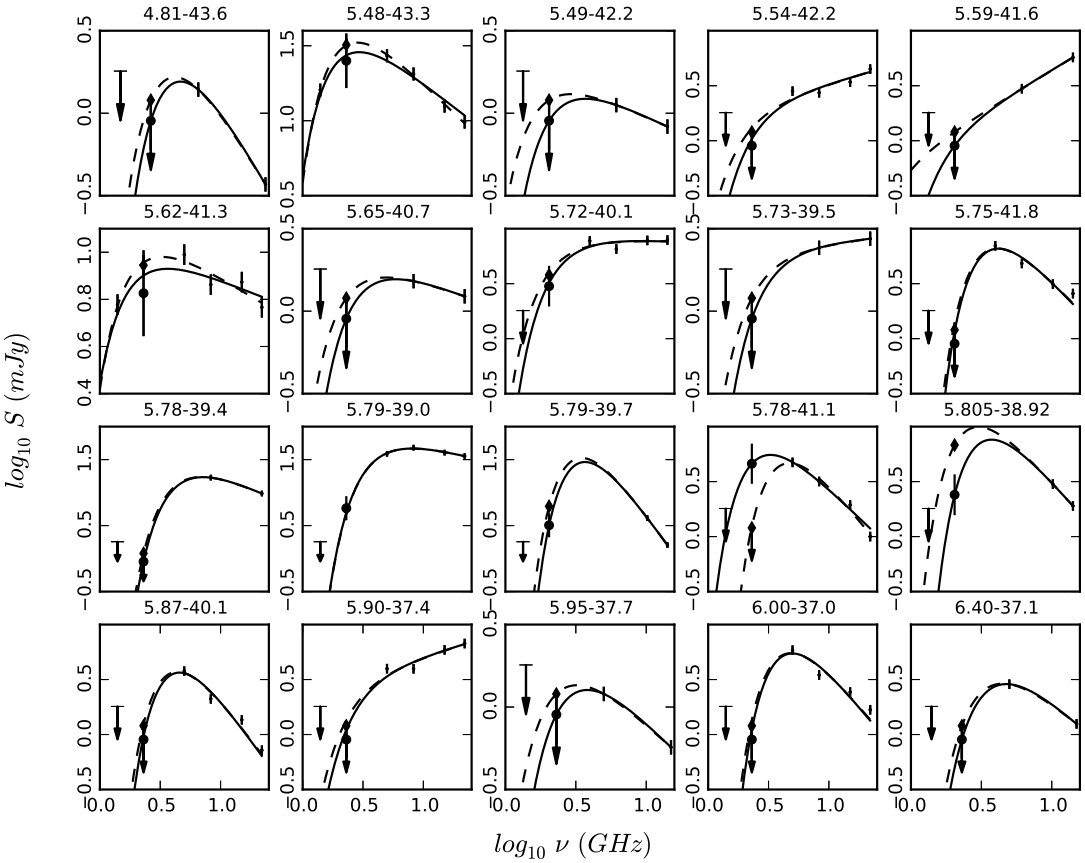

Figure 4.7: Measured flux densities (symbols with error bars) and free-free absorption models (lines) for 20 UA97 sources. The solid lines plots the free-free model derived using the 2008 2.3 GHz flux density values (star points). For comparison the free-free model derived with LT06's 2004 2.3 GHz flux density values (dashed lines) are included. The 3 and 5 σ upper limits are shown for sources not detected at 1.4 GHz (1.8 mJy) and 2.3 GHz (1.2 mJy [2004] and 0.9 mJy [2008]).

To model the free-free absorption towards the compact sources within NGC 253 we compile multi-wavelength radio flux density measurements for these sources from the literature (listed in Table 4.3), including: 1.4 GHz LBA data (Tingay, 2004); 2.3 GHz LBA data (LT06 and this chapter); 23 GHz, 15 GHz, 8.3 GHz and 5 GHz VLA data (UA97).

Brunthaler et al. (2009a) detected 10 UA97 sources at 23 GHz with the VLA (A configuration) in 2004. They reported higher flux densities for all sources compared to UA97, at the same frequency. Only the source 5.79−39.0 (the assumed core TH2) was similar in both epochs within a 10% error. The authors attributed the higher flux densities in their data to a larger beam ($\sim$ 40%). To keep the spectral modelling consistent with LT06, and maintain a comparable beam size

with the LBA 2.3 GHz images, the flux densities from Brunthaler et al. (2009a) were not used.

Table 4.4: Parameters of the free-free absorption models for all compact sources.

Source	S_0^{2004}	α^{2004}	τ_ν^{2004}	S_0^{2008}	α^{2008}	τ_ν^{2008}	Type
(1)	(2)	(3)	(4)	(5)	(6)	(7)	(8)
4.81-43.6	19.92±12.81	−1.46±0.62	9.16±5.16	24.1±16.4	−1.53±0.73	11.59±6.84	S
5.48-43.3	105.6±0.3	−0.77±0.01	3.30±0.02	76.4±0.13	−0.63±0.01	2.89±0.01	S
5.49-42.2	2.31±0.53	−0.33±0.15	2.19±1.65	2.47±0.84	−0.35±0.24	4.12±3.11	T
5.54-42.2	1.54±0.18	0.33±0.06	2.54±1.66	1.68±0.30	0.3±0.09	4.21±2.60	T
5.59-41.6	0.72±0.04	0.67±0.03	0.29±1.12	0.77±0.11	0.65±0.07	2.23±2.30	T
5.62-41.3	16.11±0.04	−0.31±0.01	1.82±0.02	12.25±0.07	−0.21±0.01	1.49±0.02	T
5.65-40.7	2.71±0.73	−0.25±0.17	3.46±2.28	2.89±1.02	−0.27±0.24	5.40±3.66	T
5.72-40.1	8.25±0.37	−0.02±0.02	4.12±0.53	9.03±0.94	−0.05±0.04	5.70±1.23	T
5.73-39.5	2.07±0.47	0.09±0.12	3.59±2.33	2.21±0.65	0.07±0.17	5.52±3.58	T
5.75-41.8	76.97±5.12	−1.16±0.04	17.46±0.64	86.16±5.80	−1.20±0.04	18.98±0.66	S
5.78-39.4	121.18±2.49	−0.81±0.01	22.67±0.51	129.41±3.35	−0.83±0.01	24.61±0.67	S
5.79-39.0	150.79±0.59	−0.46±0.01	17.58±0.08	149.60±2.32	−0.46±0.01	17.45±0.26	S
5.79-39.7	4899.0±2737.6	−2.58±0.93	25.15±10.52	5244.7±2959.9	−2.6±1.14	30.09±13.9	S
5.78-41.1	75.97±5.53	−1.38±0.04	17.09±0.60	33.03±4.71	−1.07±0.08	6.20±0.88	S
5.805-38.92	87.74±25.72	−1.23±0.15	8.26±1.68	97.7±49.61	−1.27±0.55	15.24±7.14	S
5.87-40.1	70.27±36.82	−1.50±0.51	16.00±6.63	84.0±16.12	−1.57±0.11	18.17±1.33	S
5.90-37.4	2.30±0.35	0.35±0.07	4.72±2.30	2.48±0.48	0.32±0.09	6.20±3.05	T
5.95-37.7	5.08±1.94	−0.80±0.30	4.45±2.67	6.15±2.89	−0.87±0.42	6.89±4.37	S
6.00-37.0	82.41±8.22	−1.32±0.05	17.28±0.80	94.1±9.4	−1.37±0.05	18.98±0.82	S
6.40-37.1	25.72±12.40	−1.10±0.47	12.35±5.91	31.17±15.94	−1.17±0.55	14.78±7.40	S

Notes.
(1) Source ID, see column (1) Table 4.3; (2 - 4) Derived parameters for the 2004 epoch of Equation 4.1;
(5 - 7) Derived parameters for the 2008 epoch of Equation 4.1; (8) LT06 classification of radio sources in NGC 253: S=Supernova Remnant; T=Thermally dominated HII region. The superscript indicates the LBA 2.3 GHz epoch.

Figure 4.7 presents multi-epoch monitoring of the free-free spectra of 20 compact sources in NGC 253. The free-free spectra obtained by LT06 are plotted as dashed lines, while the solid lines are the spectra derived using the 2008 2.3 GHz LBA data. For sources not detected in the 2008 observation, an upper limit of 0.9 mJy beam^{-1} (5σ) was adopted. Table 4.4 lists the fitted free parameters α, τ_0, and S_0 for each compact source. Included for reference are the values of the parameters for the 2004 data. Differences in the free-free spectra and derived parameters between 2004 and 2008, while potentially large, are still within our errors, suggesting no evidence for changes in the free-free absorbing medium between epochs. These results further confirm the free-free absorption interpretation of Tingay (2004) and LT06.

From the radio spectra, LT06 deduced that eight[6] of the 20 sources were thermally dominated H II regions (indicated with a flat intrinsic spectrum, $\alpha > -0.4$) and the remaining 12 as consistent with steep intrinsic power-law spectra typical of RSNe or SNRs. We find no difference in the source classification in our study.

The flux density for the sources with spectra consistent with RSNe or SNRs, ranges from 2 - 30 mJy at 5 GHz. The relationship between the rise time and peak luminosity for core-collapse supernovae by Chevalier et al. (2006) predicts a rise time $\leq$110 days. A typical RSNe follows a power law decay that begins after this fast rise, and would be detectable over many years. However, no such decay has been observed for these compact sources over two decades, suggesting that they are probably very old SNRs.

4.5.2 The Supernova Remnant 5.48-43.3

4.5.2.1 Morphology and Small-scale Features

The brightest source in NGC 253 at 2.3 GHz, 5.48-43.3, is the only fully resolved SNR in the starburst galaxy with the full LBA array (i.e. including the long baselines of Cd and Ho). In Figure 4.8 we present the two high sensitivity VLBI images of 5.48-43.3 (the 2004 and 2008 epochs), restored with a beam size of 13×15 mas and beam position angle of 58° . The contours were chosen to represent identical surface brightness levels in both images.

As first noted by LT06, 5.48−43.3 appears to be a shell-type SNR, with a diameter of ∼70 - 90 mas (1.4 - 1.8 pc). At both epochs, the structure of 5.48−43.3 is dominated by the eastern lobe, which has a higher flux density than the western lobe by a factor of 3. This may be the result of interactions with a denser interstellar medium in the direction of the eastern lobe.

Comparing the epochs, we notice that there are several differences in the lobes. Such apparent changes in the small scale structures are possibly due to ambiguities caused by the combination of structural evolution and image fidelity limitations, resulting from incomplete sampling of the (u, v) plane. The effects of (u, v) plane sampling on the appearance and evolution of complex small-scale structures, within spherically symmetric shell-like sources, are well documented by Heywood et al. (2009); they demonstrated that sparse (u, v) plane sampling, and the non-uniqueness of deconvolution, can add complex azimuthal structure

[6]A typographical error was made in table 3 of LT06. The spectral index of 5.805-38.92 should be -1.20 and not 1.20

to a radio brightness distribution that is in reality morphologically simple.

One striking feature of the Heywood et al. (2009) results is the departure from a spherically symmetric shell to a two-lobed structure (similar to SN 1987A, Ng et al. 2011 and 5.48−43.3) when the (u, v) plane coverage lacks intermediate baselines, similar to the (u, v) coverage of both the 2004 (see Figure 2 of LT06) and the 2008 (Figure 4.1) observations. Thus, it is possible that 5.48-43.3 possesses a spherically symmetric (or slightly elliptical) morphology that is not recovered due to low sensitivity associated with sparse sampling of the (u, v) plane. This effect is noticeable in the epochs without the intermediate baselines to Tidbinbilla (2006 and 2007), with the non-detection of the weaker, western lobe.

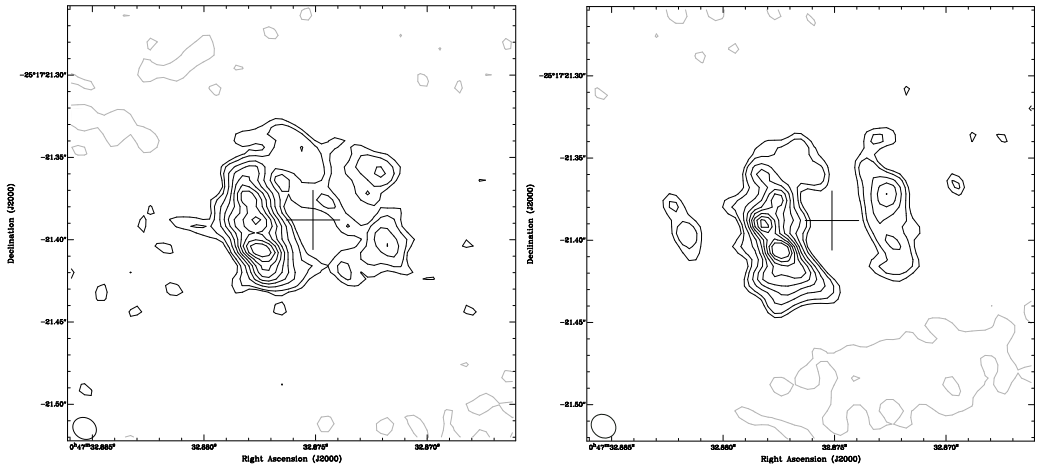

Figure 4.8: LBA images of 5.48-43.3 at 2.3 GHz taken on from 2004 April 16/17 (left) from LT06 and 2008 June 5/6 (right). The contours in both images corresponds to −15%, 15, 20%, 30%, 40%, 50%, 60%, 70%, 80%, and 90% of the 2004 peak (2.4 mJy beam^{-1}). Both images are restored with the same beam, 13×15 mas with a position angle of 58° . The cross indicates the assumed source centre used to obtain the radial flux profile in Figure 4.9.

4.5.2.2 Expansion of 5.48-43.3

With multiple high resolution observations at the same frequency, it may be possible to determine the expansion speed of 5.48-43.3. In order to carry out such measurements, we use the AIPS task IRING to measure radial profiles (averaged in azimuth) of the source at each epoch. This method has been successfully implemented to determine the expansion speed of resolved SNRs in M82 (Beswick et al., 2006; Fenech et al., 2010). Owing to differences in the small-scale structure between the two epochs (as discussed in the previous section), determination of the geometrical centre of 5.48-43.3 is difficult. To account for any positional offset

between the epochs, the position of the peak surface brightness in the 2008 image was aligned to the position of the 2004 peak surface brightness, using the AIPS task OGEOM. A common geometrical centre for both images was estimated by visual inspection, and indicated by the crosses in Figure 4.8. Using this position as the reference point, the radial profiles were obtained by measuring the integrated flux density within a series of 4 mas thick annuli, and are plotted in Figure 4.9. No discernible expansion between the two epochs can be seen in Figure 4.9. At the smaller radii, higher integrated flux densities were recovered for the 2004 image. This is possibly due to differences in the short spacings of the (u, v) coverages and/or deeper cleaning in the 2008 image.

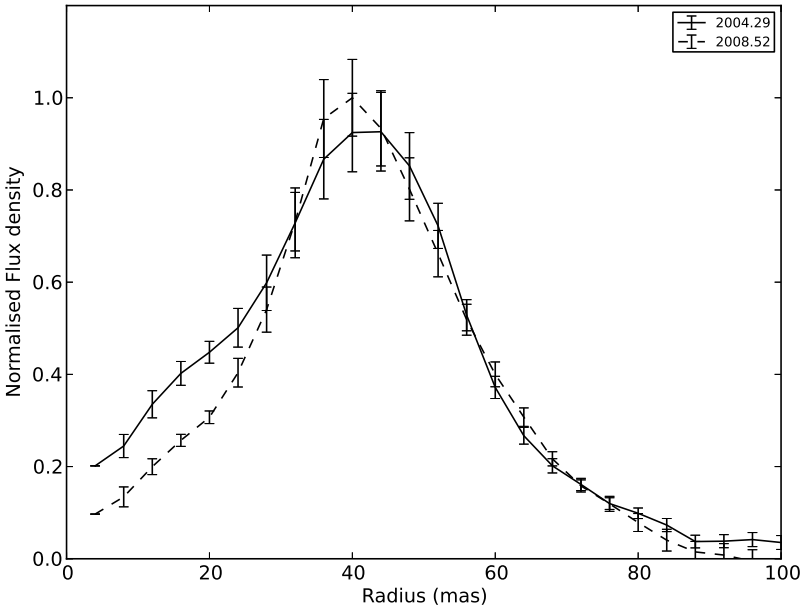

Figure 4.9: Comparing the radial flux density profile of the SNR 5.48-43.3 for the 2004 (solid line) and 2008 (dashed line) observations.

If we consider an upper limit of the expansion speed on $\nu = 10^4$ km s^{-1} (Beswick et al., 2006; Fenech et al., 2010) for SNRs in NGC 253, an expansion of ~ 2.2 mas, $\sim 15\%$ of the 2.3 GHz LBA beam, is expected for 5.48−43.3 over 4.3 years between the 2004 and 2008 LBA observations. To measure the expansion of 5.48−43.3, multiple observations separated by >10 years with the current LBA baselines, or observations with longer baselines (>3000 km) separated by >5 years would be needed.

4.5.3 The Supernova Rate in NGC 253

4.5.3.1 Lower limit estimation

A lower limit on the supernova rate can be estimated based on the number of detected SNRs, their size, and an assumed expansion rate (LT06). Based upon the method by Ulvestad and Antonucci (1994) and an assumed radial expansion rate of 10^4 km s^{-1}, LT06 estimated the lower limit of the supernova rate to be $0.14(v/10^4 \text{ km s}^{-1})$, where v is the expansion velocity. Our results from Section 4.5.2 are consistent with this as the minimum supernova rate.

4.5.3.2 Previous estimates of the supernova rate upper limit

No new sources have been detected in NGC 253 after two decades of multi-wavelength, high resolution radio observations. The consequences of the non-detections for estimates of the supernova rate were first investigated by Ulvestad and Antonucci (1991, hereafter UA91). They assumed a hypothetical population of RSNe whose flux densities at 5 GHz peak 100 days after the optical maxima and decay as the -0.7 power of time (Weiler et al., 1986, 1989). The RSNe population was assumed to have peak luminosities uniformly distributed between 5 and 20 times that of Cas A, and an NGC 253 distance of 2.5 Mpc (TH85) was also assumed. UA91 found that $\sim$2/3 of the RSNe that occurred during the 18 month period between two 5 GHz epochs should be detectable above the second epoch's sensitivity limit. By assuming the events are Poisson distributed in time, UA91 determined with 95% confidence an upper limit to the supernova rate of 3.0 yr^{-1} in NGC253. This model was used to estimate the supernova rate upper limit for two subsequent 5 GHz epochs, $\sim$1.4 yr^{-1} for a third epoch 2.5 years later (Ulvestad and Antonucci, 1994) and $\sim$0.3 yr^{-1} for a fourth epoch, 4.0 years later (UA97).

With new distance measurements for NGC 253 (3.94$\pm$0.5 Mpc, Karachentsev et al. 2003) and two additional high resolution observations, LT06 developed a new model based on the principles of UA91 and using new data: an 8.3 GHz[7] VLA observation by Mohan et al. (2005); and a 2.3 GHz LBA observation by LT06. The RSNe at 2.3 GHz were assumed to peak 200 days after the optical maxima at the same flux density as at 5 GHz (see Weiler et al. 1986). LT06 also considered the effects of free-free absorption by adjusting the flux densities of the RSNe with

[7]LT06 erroneously lists a 5.0 GHz observation in place of the 8.3 GHz observation by Mohan et al. (2005).

Equation (4.1), assuming a median value of $\tau_0 = 6$. The number of RSNe that occur between epochs was determined via a Poisson-distributed random number, given a specified supernova rate. The radio luminosities of the RSNe were allowed to evolve using the parametric equation of (Weiler et al., 1986) into supernova remnants (SNRs) and then, given the time and sensitivity of the observation, a test was made to determine if each SNR could be detected. A Monte Carlo simulation was used to drive the model ($\sim$ 10000 iterations), where the proportion of SNRs detected, $\beta_{\rm SN}$, at the end of each epoch was obtained. The simulation was seeded with an initial supernova rate of 0.1 yr^{-1} producing a confidence level for the $\beta_{\rm SN}$ at each epoch. Using linear interpolation, the supernova rate required to drive the simulation to a 95% confidence limit was determined and the simulation was repeated until the confidence limit was achieved. The resulting supernova rate was then used to seed the next epoch and the process was continued until all epochs were processed.

Using this model, LT06 found that the increased distance, combined with the effects of free-free absorption, decreased $\beta_{\rm SN}$ which resulted in an upper limit of the supernova rate at the end of the final epoch of 2.4 yr^{-1}. A summary of the model parameters used by Ulvestad and Antonucci (1991, 1994, 1997) and LT06 to derive upper limits on the supernova rate are listed in Table 4.5.

4.5.3.3 Determining a new supernova rate upper limit

With additional high resolution radio observations of NGC 253 since LT06, improved distance measurements to NGC 253, and availability of a more realistic RSNe luminosity function (Lien et al., 2011), it is worth revisiting the estimates of the upper limit on the supernova rate. The additional NGC 253 observations are the three new 2.3 GHz LBA observations in this chapter, plus 23 GHz VLA observations by Brunthaler et al. (2009a) and 15 GHz VLA observation by Mohan et al. (2005). Figure 4.10 gives a time-line of all observations of NGC 253 used to determine the supernova rate. To further constrain the upper limit on the supernova rate with these observations, we have developed a new model based on the principles of Ulvestad and Antonucci (1991) and LT06, as well as incorporating suggested improvements by LT06.

Improved core-collapse supernovae peak luminosity distribution

At 5 GHz and 2.3 GHz our hypothetical RSN is the same as that used by UA91 and LT06 (see previous section and Table 4.5). At 8.3 GHz, 15 GHz and 23 GHz

Table 4.5: Summary of input parameters to different supernova rate models of ngc 253

Input Parameters	UA	LT06	This Chapter
No. of Epochs	4	6	11
ΔF	$\mathcal{U}$(5,20)	$\mathcal{U}$(5,20)	Log-Gaussian
Frequency, ν (GHz)	5	2.3 & 5	2.3, 5, 8.3, 15 & 23
T_r (days)	100	200 & 100	200, 100, 100, 70 & 50
β	-0.7	-0.7	-0.7
Spectral Index, α ..	...	0	time-dependent†
τ_0	...	6*	6
Distance (Mpc)	2.55	3.94	3.44

Notes.
UA - Ulvestad and Antonucci (1991, 1994, 1997);
ΔF - Type II Supernovae peak luminosity distribution in units of Cas A luminosity at 5 GHz = 7.34 $\times$ 10^{24} ergs s^{-1} Hz^{-1};
$\mathcal{U}$(5,20) - uniform distribution between 5 to 20 mJy;
T_r - Time after optical peak to reach radio peak luminosity at ν GHz;
β - RSNe luminosity decay with time (Weiler et al., 1986, 1989);
† $\alpha^5_{2.3}$ from Weiler et al. (1986), α^{23}_5 from Weiler et al. (2007);
τ_0 - free-free optical depth at 1 GHz;
* Median value based upon the results of LT06

we assume that the RSN luminosity peaks 100, 70 and 50 days after the optical maximum at the same luminosity as at 5 GHz. This assumption closely agrees with the light curves of SN 1993J (Weiler et al., 2007).

In the models of UA91 and LT06, the distribution of the 5 GHz peak luminosities of RSNe was assumed to be uniformly distributed between 5 and 20 times the luminosity of Cas A. This assumption follows Weiler et al. (1989), who came to this conclusion after comparing the peak flux densities at 5 GHz of 16 Type II supernovae (three detections and 13 upper limits). Since the study by Weiler et al. (1989) there have been many more new detections of Type II as well as Type Ibc supernovae in the radio. Thus it is worth re-investigating the 5 GHz peak luminosity distribution of these objects.

Table 4.6 lists 51 core-collapse (29 Type II & 22 Type Ibc) supernovae whose 5 GHz peak flux density have either been detected or estimated via spectral index[8] or extrapolation using the models by Chevalier (1982) or (Weiler et al., 2002). This table is represented graphically in Figure 4.11, where the Type Ibc

[8]For peak flux densities detected at 8.4 GHz, a spectral index of 0 is assumed, following SN1993J (Weiler et al., 2007)

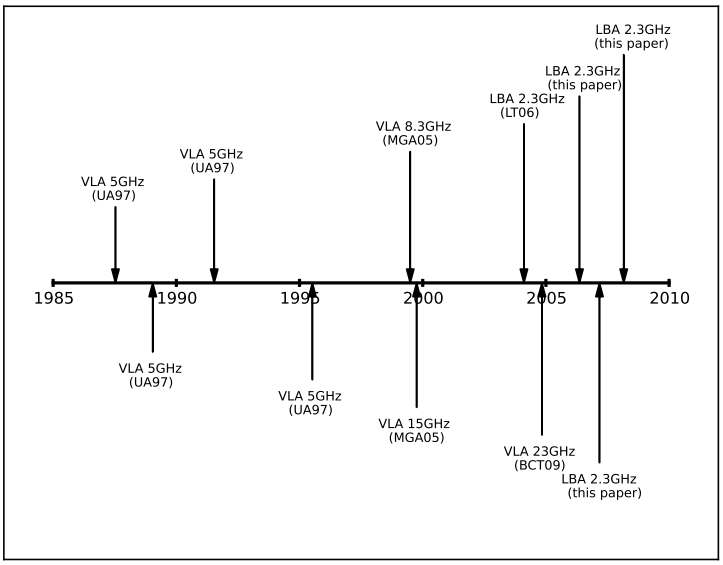

Figure 4.10: Time-line of observations used to estimate the upper limits on the supernova rate in NGC 253 by Ulvestad and Antonucci (1991, 1994, 1997), LT06 and this chapter. The new observations introduced in the model by this chapter are the VLA 8.3 GHz & 15 GHz (MGA05), VLA 23 GHz (BCT09) and three LBA 2.3 GHz (this chapter) observations.
NOTE: MGA05 - Mohan et al. (2005); BCT09 - Brunthaler et al. (2009a).

(grey symbols) and Type II (black symbols) luminosity ratio to Cas A's at 5 GHz is plotted on the y-axis and their distances on the x-axis. Included in the plots are the 5 GHz peak luminosity upper limits for 34 core-collapse supernovae not detected in the radio (Table 4.7), that follow the average 3σ detection limit of the VLA (the dashed lines, from Berger et al. 2003). Using the detected core-collapse supernovae listed in Table 4.6, we derived a more accurate luminosity distribution at 5 GHz shown in Figure 4.12. The data are divided into bins of size $\Delta\log_{10}(L_{5;CasA}{}^{9}) = 1$. The dashed line presents the best fit Gaussian with mean luminosity ratio of 245.5, standard deviation of 1.27 and $\chi^2 = 0.018$. This distribution is similar to that presented by Lien et al. (2011).

However, this analysis ignores the upper limits (Table 4.7) entirely, and so we should consider whether these offer any significant additional information. While their true luminosities are unknown, we need to determine if, given the upper limits, these supernovae are distributed differently from those in Figure 4.12. To examine this we calculate the probability (or p-value), using the cumulative

[9] $L_{5;CasA}$ is the RSNe 5 GHz peak luminosity ratio to Cas A's

distribution function derived from the Gaussian distribution in Figure 4.12, that a supernova will have a luminosity less than the upper limits listed in Table 4.7. The p-values (Table 4.7), although on average are lower than 0.5, are probably consistent with the chosen luminosity function given that the upper limits may not have been observed at a time corresponding to when the peak flux density actually occurs. However, detailed work on testing whether the upper limits in Table 4.7 are consistent with the chosen model are beyond the scope of this chapter.

Table 4.6: OBSERVED 5 GHz PEAK FLUX DENSITY OF CORE-COLLAPSE SUPERNOVA

Name	Galaxy	Type	Distance	Detected?	S_5	L_6	$L_{5;CasA}$	Ref.
(1)	(2)	(3)	(4)	(5)	(6)	(7)	(8)	(9)
SN1983N	M83	Ibc	4.5	D	40.10	9.72	132.45	1
SN1984L	NGC 4991	Ibc	21.7	D	4.59	25.86	352.54	2
SN1990B	NGC 4568	Ibc	18.2	D	1.26	4.99	68.08	3
SN1994I	M51	Ibc	8.0	D	16.20	12.50	170.38	4
SN1998bw	ESO184-G082	Ibc	37.3	D	37.40	622.59	8487.24	5
SN2000C	NGC 2415	Ibc	59.0	E	0.19	7.79	106.18	6
SN2001B	IC391	Ibc	24.0	D	2.56	17.64	240.51	6
SN2001ci	NGC 3079	Ibc	17.0	D	1.06	3.67	50.06	6
SN2002ap	NGC 628	Ibc	7.3	D	0.45	0.29	3.94	7
SN2002cj	ESO582-G5	Ibc	106.0	D	0.22	29.58	403.19	6
SN2002dg	Anon.	Ibc	215.0	E	0.09	50.88	693.65	6
SN2003L	NGC 3506	Ibc	92.0	D	2.56	258.75	3527.31	8
SN2003bg	MCG-05-10-15	Ibc	19.6	D	52.81	242.74	3309.07	9
SN2004cc	NGC 4568	Ibc	18.0	E	3.26	12.64	172.28	10
SN2004dk	NGC 6118	Ibc	23.0	D	1.80	11.39	155.31	10
SN2004gq	NGC 1832	Ibc	26.0	D	5.75	46.51	634.00	10
SN2007bg	Anon.	Ibc	152.0	D	1.10	304.91	4156.62	11
SN2007gr	NGC 1058	Ibc	7.7	D	1.00	0.71	9.67	12
SN2008D	NGC 2770	Ibc	27.0	E	3.00	26.17	356.72	13
SN2009bb	NGC 3278	Ibc	40.0	D	12.00	229.73	3131.69	14
SN2010as	NGC 6000	Ibc	27.3	D	1.40	12.48	170.19	15
PTF11qcj	SDSS*	Ib	124.0	D	5.43	998.98	13618.22	16
SN1970g	NGC 5457	II	7.2	D	2.50	1.55	21.14	17
SN1974E	NGC 4038	II?	20.9	D	1.24	6.48	88.35	18
SN1978K	NGC 1313	II	4.1	D	518.00	104.19	1420.28	18
SN1979C	NGC 4321	IIL	22.0	D	12.40	71.81	978.91	18
SN1980K	NGC 6946	IIL	7.0	D	2.45	1.44	19.58	18
SN1981k	NGC 4258	II	6.6	D	5.15	2.68	36.59	18
SN1982aa	NGC 6052	II	66.0	D	19.10	995.48	13570.58	18,19
SN1985L	NGC 5033	II	12.9	D	1.56	3.11	42.34	20
SN1986E	NGC 4302	II	16.8	D	0.33	1.11	15.19	21
SN1986J	NGC 891	IIn	12.0	D	135.00	232.60	3170.83	18
SN1988Z	MCG+03-28-022	IIp	94.5	D	1.85	197.67	2694.71	22
SN1993J	M81	IIb	3.6	D	96.90	15.28	208.26	23
SN1995N	MCG-02-38-17	IIn	24.0	E	9.00	62.03	845.56	24
SN1997eg	NGC 5012	II	40.0	E	10.00	191.44	2609.74	25
SN1998S	NGC 3877	II	17.0	E	1.04	3.60	49.02	26
SN1999em	NGC 1637	II	7.8	E	0.30	0.22	2.98	26

Continued on next page

Table 4.6 – continued from previous page

Name	Galaxy	Type	Distance	Detected?	S_5	L_5	$L_{5;CasA}$	Ref.
(1)	(2)	(3)	(4)	(5)	(6)	(7)	(8)	(9)
SN2000ft	NGC 7469	II?	70.0	D	1.76	103.30	1408.25	27
SN2001ig	NGC 7424	IIb	11.5	D	21.90	34.65	472.41	28
SN2001gd	NGC 5033	IIb	20.0	D	7.96	38.10	519.34	29
SN2004dj	NGC 2403	IIp	3.6	E	1.90	0.29	4.02	30
SN2004et	NGC 6946	II	5.5	E	2.50	0.90	12.34	31
SN2006jd	UGC 4179	IIb	76.8	D	2.22	156.39	2131.91	32
SN2008ax	NGC 4490	IIp	8.1	D	4.00	3.13	42.70	33
SN2008iz	M82	II	3.2	E	180.00	22.05	300.64	34
SN2011cb	PGC 69707	IIb	29.2	D	0.73	7.46	101.73	35
SN2011dh	M51	IIp	8.0	D	7.80	6.02	82.04	36
SN2011ei	NGC 6925	IIb	28.5	D	0.56	5.48	74.72	37
A25	Arp220	IIp	44.8	E	0.30	7.20	98.21	38
A27	Arp220	IIp?	44.8	E	0.75	18.01	245.52	38

Notes
(1) SN standard name; (2) Host galaxy; (3) SN type; (4) Estimated distance in Mpc, from references and NASA/IPAC Extragalactic Database (NED), where appropriate; (5) D - peak flux detected at 5 GHz; E - peak flux at 5 GHz estimated; (6) Peak Flux Density at 5 GHz, units mJy; (7) Peak luminosity at 5 GHz; units = 10^{26} ergs s^{-1} Hz^{-1}; (8) Luminosity ratio to Cassiopeia A (Cas A) 5 GHz peak luminosity: 7.34 $\times$ 10^{24} ergs s^{-1} Hz^{-1}; * SDSS J131341.57+471757.2.
Ref: 1. Sramek et al. (1984); 2. Weiler et al. (1986); 3. van Dyk et al. (1993); 4. Weiler et al. (2011); 5. Kulkarni et al. (1998); 6. Berger et al. (2003); 7. Berger et al. (2002); 8. Soderberg et al. (2005); 9. Soderberg et al. (2006a); 10. Wellons et al. (2012); 11. Salas et al. (2013); 12. Soderberg et al. (2010); 13. Soderberg et al. (2008); 14. Bietenholz et al. (2010); 15. Ryder et al. (2010a); 16. Corsi et al. (2014); 17. Weiler et al. (1989); 18. Weiler et al. (2002); 19. Metcalfe et al. (2005); 20. van Dyk et al. (1998); 21. Montes et al. (1997); 22. Williams et al. (2002); 23. Weiler et al. (2007); 24. Chandra et al. (2009); 25. Lacey et al. (1998); 26. Pooley et al. (2002); 27. Pérez-Torres et al. (2009); 28. Ryder et al. (2004); 29. Stockdale et al. (2007); 30. Beswick et al. (2005); 31. Argo et al. (2005); 32. Chandra et al. (2012); 33. Roming et al. (2009); 34. Gendre et al. (2013); 35. Krauss et al. (2012); 36. Ryder et al. (2011a); 37. Milisavljevic et al. (2013); 38. Bondi et al. (2012).

Improved spectral indices

Weiler et al. (1986, 2007) showed that the spectral index between 6 cm and 20 cm evolves with time, for a number of RSNe. This has also been shown to be true for SN 1993J for wavelength pairs of 1.2/2 cm, 2/3.6 cm and 3.6/6 cm (Weiler et al., 2007). Thus, it is expected that 2.3/5 GHz, 5/8.3 GHz, 5/15 GHz and 5/23 GHz spectral indices will display similar variations with time. To account for this, we have included light curves that best describe the spectral indices between 6 & 20 cm from SN 1980k (Weiler et al., 1986) and between 6 & 3.6 cm, 6 & 2 cm, 6 & 1.2 cm from SN 1993J (Weiler et al., 2007).

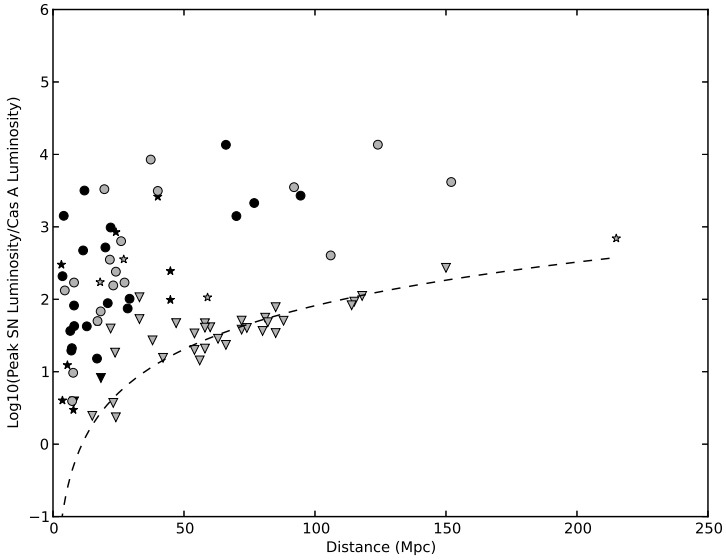

Figure 4.11: The 5 GHz peak luminosity ratio to Cas A as a function of distance for Type II SNe (black points) and Type Ibc SNe (grey points). The circles and stars are supernovae with detected and estimated peak luminosities (29 Type II and 22 Type Ibc, see Table 4.6). The upside down triangles are supernovae whose peak luminosities have not been detected (2 Type II and 32 Type Ibc, see Table 4.7). The dashed lines is the average 3σ detection limit of the VLA from Berger et al. 2003.

The new supernova rate upper limit

Table 4.8 lists the results of applying the improved model parameters described above and listed in column 4 of Table 4.5, to the Monte-Carlo simulation of LT06 (see Section 3.3.2). We find that the proportion of SNRs detected, $\beta_{\rm SN}$ at the end of each epoch are relatively consistent, with minor variations between 0.66 and 0.84. The major changes occur during epochs where the sensitivity varies by almost an order of magnitude. The consistently high $\beta_{\rm SN}$ resulted in an upper limit on the supernova rate of $\nu_{\rm SN} = 0.2$ yr^{-1} at the end of the final epoch. The results of the simulation indicate that the radio observations are detecting 60% - 80% of all SNRs in NGC 253, thus pointing to the possible existence of a small population of undetected SNRs. Moreover, the fact that no RSNe or SNRs has been observed in NGC 253 during 21 years of radio observation suggests a low rate of RSNe production in NGC 253.

The final result for $\nu_{\rm SN}$ agrees with estimates determined from near infrared (NIR) observations of the [FeII] line (0.2 yr^{-1}) by Rosenberg et al. (2013). Observations of the [FeII] line have been shown to be a strong tracer of shocks

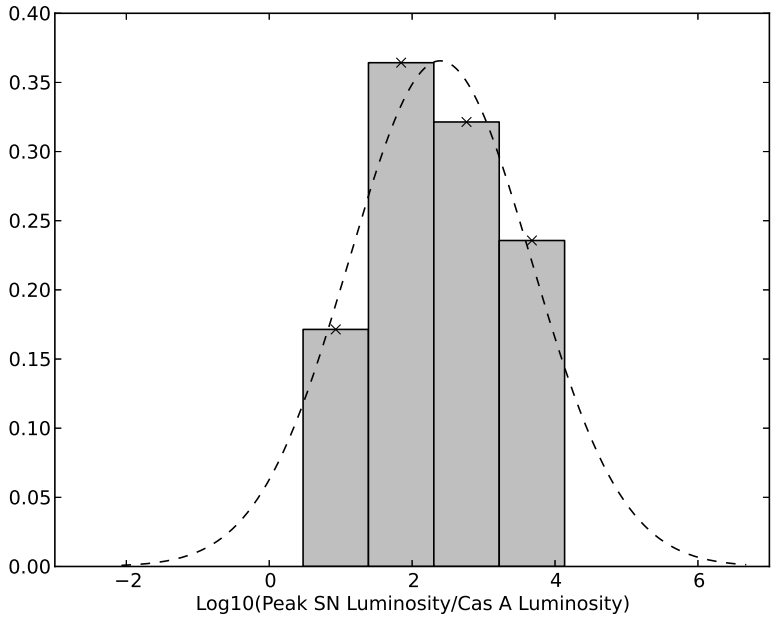

Figure 4.12: Normalised radio luminosity distribution at 5 GHz of 51 core-collapse supernovae as a function of $\log_{10}(L_{5;CasA})$. The x-axis mirrors the y-axis of Figure 4.11 and is given in Table 4.6. The data are binned to $\Delta\log_{10}(L_{5;CasA}) = 1$. The dashed curve shows a non-linear least-squares fitted Gaussian to the underlying data (black x's). The resulting fit: mean $\log_{10}(L_{5;CasA})$= 2.39, standard deviation, $\sigma_{SD} = 1.27$ and $\chi^2 = 0.018$.

associated with SNRs (Rosenberg et al., 2012, 2013). Dust grains in the interstellar medium containing Fe atoms are destroyed via the shocks. The process releases the Fe atoms, which are then ionised by the interstellar radiation field. In the post shock region, Fe^+ is excited by electron collisions, causing it to emit at NIR wavelengths. However, there are possible contributions to the [FeII] line from shocks due to other processes such as mergers (Rosenberg et al., 2012). Thus, it is possible that the NIR [FeII] observations are overestimating the supernova rate upper limit.

The major uncertainty in our model arises from the RSNe peak luminosity distribution. First, the detection of RSNe has primarily been through follow-up observations of optical supernovae, resulting in a small and incomplete sample, whose luminosity depends on the sensitivity of the survey. Second, there is the possibility that many RSNe are not visible in the optical due to extinction and we may be looking at a slightly different sub-population

Further uncertainty comes from the assumed rise time of the RSNe at the different frequencies. In this model, for simplicity, constant rise times (the time

Table 4.7: PEAK FLUX DENSITY UPPER LIMITS OF UNDETECTED CORE-COLLAPSE SUPERNOVA AT 5 GHz

Name	Galaxy	Type	Distance	S_5	L_5	$L_{5;CasA}$	p-value	Ref.
(1)	(2)	(3)	(4)	(5)	(6)	(7)	(8)	(9)
SN1980I	NGC 4374	Ibc	22.0	<0.50	<2.90	<39.47	0.27	1,2
SN1980N	NGC 1316	Ibc	33.0	<0.60	<7.82	<106.58	0.39	1
SN1981B	NGC 4536	Ibc	33.0	<0.30	<3.91	<53.29	0.30	1
SN1999ex	IC 5179	Ibc	54.0	<0.07	<2.48	<33.77	0.25	3
SN2000cr	NGC 5395	Ibc	54.0	<0.04	<1.47	<19.98	0.20	3
SN2000ew	NGC 3810	Ibc	15.0	<0.07	<0.18	<2.46	0.06	3
SN2000fn	NGC 2526	Ibc	72.0	<0.05	<2.79	<38.05	0.26	3
SN2001M	NGC 3240	Ibc	56.0	<0.03	<1.05	<14.32	0.17	3
SN2001ai	NGC 5278	Ibc	118.0	<0.05	<8.16	<111.29	0.39	3
SN2001bb	IC 4319	Ibc	72.0	<0.06	<3.72	<50.73	0.29	3
SN2001ef	IC 381	Ibc	38.0	<0.12	<1.99	<27.09	0.23	3
SN2001ej	UGC 3829	Ibc	63.0	<0.04	<2.09	<28.48	0.23	3
SN2001is	NGC 1961	Ibc	60.0	<0.07	<3.02	<41.10	0.27	3
SN2002J	NGC 3464	Ibc	58.0	<0.09	<3.42	<46.64	0.28	3
SN2002bl	UGC 5499	Ibc	74.0	<0.05	<2.95	<40.19	0.27	3
SN2002bm	MCG013219	Ibc	85.0	<0.07	<5.71	<77.78	0.35	3
SN2002cg	UGC 10415	Ibc	150.0	<0.07	<19.92	<271.58	0.51	3
SN2002cp	NGC 3074	Ibc	80.0	<0.04	<2.68	<36.54	0.26	3
SN2002dn	IC 5145	Ibc	115.0	<0.04	<6.80	<92.76	0.37	3
SN2002ge	NGC 7400	Ibc	47.0	<0.13	<3.44	<46.84	0.29	3
SN2002gy	UGC 2701	Ibc	114.0	<0.04	<6.06	<82.67	0.35	3
SN2002hf	MCG05320	Ibc	88.0	<0.04	<3.71	<50.52	0.29	3
SN2002hn	NGC 2532	Ibc	82.0	<0.04	<3.54	<48.26	0.29	3
SN2002ho	NGC 4210	Ibc	42.0	<0.05	<1.14	<15.54	0.17	3
SN2002hy	NGC 3464	Ibc	58.0	<0.07	<2.98	<40.60	0.27	3
SN2002hz	UGC 12044	Ibc	85.0	<0.03	<2.51	<34.18	0.25	3
SN2002ji	NGC 3655	Ibc	23.0	<0.04	<0.27	<3.71	0.08	3
SN2002jj	IC 340	Ibc	66.0	<0.03	<1.72	<23.45	0.21	2
SN2002jp	NGC 3313	Ibc	58.0	<0.04	<1.53	<20.85	0.20	3
SN2002jz	UGC 2984	Ibc	24.0	<0.03	<0.17	<2.35	0.06	3
SN2003jd	MCG0159021	Ibc	81.0	<0.05	<4.08	<55.65	0.31	4
SN2011hp	NGC 4219	Ibc	23.7	<0.20	<1.34	<18.32	0.19	5
SN2005cs	M51	II	8.0	<0.37	<0.29	<3.89	0.08	6
SN2009mk	PGC 474	IIb	18.3	<0.15	<0.60	<8.19	0.12	7

Notes.
Where appropriate symbols and headings have same meaning as Table 4.6; Column (8) The probability the supernova's peak radio luminosity is actually less than the observed upper limits given the cumulative distribution function derived from Figure 12; Only core-collapse supernovae that were observed in the radio within 200 days of the optical maximum are selected. **Ref:** 1. Weiler et al. (1989); 2. Weiler et al. (1986); 3 Berger et al. (2003); 4. Soderberg et al. (2006b); 5. Ryder et al. (2011b); 6. Stockdale et al. (2005); 7. Ryder et al. (2010b)

to reach maximum radio luminosities) were assumed for the hypothetical RSNe at the different frequencies. However, this has been observed to be variable for different RSNe (e.g. Weiler et al. 1986, 2002). Additionally, the relation between the rise time and peak luminosity has also been observed to be variable (Chevalier

et al., 2006) and does not necessarily follow a one-to-one relationship as assumed in the model presented.

Further refinement to the supernova rate of NGC 253 could be obtained from either a large unbiased sample of the peak flux densities of RSNe, or direct observations of the RSNe population in NGC 253. Both possibilities can be provided by the *Square Kilometre Array*[10], (SKA) and new generation telescopes, such as the Karl G. Jansky VLA[11] (JVLA). The sensitivity of both instruments may provide the opportunity to detect a population of weak SNRs that are faint due to either free-free absorption or intrinsic properties. The SKA is expected to have a Type II supernova detection rate of $\sim$620 yr^{-1} deg^{-2} out to a redshift $z \sim 5$ (Lien et al., 2011). The JVLA and precursors to the SKA may provide a detection rate of $\sim$160 yr^{-1} deg^{-2} out to redshift $z \sim 3$ (Lien et al., 2011).

Table 4.8: Supernova Rate Upper Limits from Monte Carlo Simulations

Epoch	Time (yr)	ν (GHz)	Sensitivity (mJy)	β_{SN} -	ν_{SN} (yr^{-1})
(1)	(2)	(3)	(4)	(5)	(6)
1	...	5.0	...	...	
2	1.5	5.0	3.0	0.746	<2.71
3	2.5	5.0	3.0	0.713	<1.04
4	4.0	5.0	3.0	0.683	<0.53
5	4.0	8.3	0.3	0.803	<0.34
6	0.25	15	0.6	0.838	<0.33
7	4.5	2.3	1.2	0.697	<0.25
8	0.5	23	2.0	0.661	<0.24
9	1.7	2.3	2.0	0.676	<0.22
10	0.8	2.3	2.2	0.689	<0.21
11	1.0	2.3	0.9	0.791	<0.20

Notes.
(1) Number of NGC 253 observing epochs starting from the first VLA 5 GHz in Figure 4.10; (2) Time between epochs; (3) Observed frequency; (4) The 5σ sensitivity of the observations; (4) Detection threshold for each epoch, 5σ; (5) Proportion of RSNe detected at the end of each epoch; (6) Supernovae rate based upon all observations prior to and including that epoch.

4.5.4 Star Formation Rate

With new upper limits on the supernova rate, we can provide a new estimate for the star formation rate (SFR) in NGC 253. Following Condon (1992), the SFR

[10] `http://www.skatelescope.org/`
[11] `https://science.nrao.edu/facilities/vla`

can be determined directly from the supernova rate (and vice versa). By assuming that all stars with mass $> 8M_{\odot}$ eventually form supernovae, the relation between SFR and the supernova rate is given by:

$$\left[\frac{SFR(M \geq 5\ M_{\odot})}{M_{\odot}\ \mathrm{yr}^{-1}}\right] = 24.4 \left[\frac{\nu_{\mathrm{SN}}}{\mathrm{yr}^{-1}}\right] \tag{4.3}$$

Using the new supernova rate upper limits of $\nu_{\mathrm{SN}} < 0.2\ \mathrm{yr}^{-1}$ (Section 4.5.3), we find $SFR(M \geq 5\ M_{\odot}) < 4.9\ M_{\odot}\ \mathrm{yr}^{-1}$. We can compare this upper limit to estimates from independent methods. If one assumes that the main contribution to the observed radio luminosity in a starburst are from RSNe, SNRs and thermal HII regions, then the SFR of that region is directly proportional to its radio luminosity at the observed radio wavelength and can be calculated using the relation given by Condon (1992) and Haarsma et al. (2000). Ott et al. (2005) observed a total flux density of 0.59 Jy for NGC 253 at 24 GHz. Using the relation by Haarsma et al. (2000) and the data from Ott et al. (2005) we obtain $SFR(M \geq 5\ M_{\odot}) = 9.3\ M_{\odot}\ \mathrm{yr}^{-1}$. Additional observations of NGC 253 at 23 GHz (total flux density of 0.56 Jy) by Takano et al. (2005) give a similar $SFR(M \geq 5\ M_{\odot}) = 8.7\ M_{\odot}\ \mathrm{yr}^{-1}$ for the ∼300 pc nuclear region, using the same method.

The $SFR(M \geq 5\ M_{\odot})$ can also be determined from far infrared (FIR) emission using equation 26 from Condon (1992). From FIR luminosity measurements with *IRAS*[12] (Radovich et al., 2001) and scaling for the new distance 3.44 Mpc, the SFR is 1.3 - 2.0 $M_{\odot}\ \mathrm{yr}^{-1}$ for the inner ∼300 pc nuclear region and 2.6 - 3.2 $M_{\odot}\ \mathrm{yr}^{-1}$ for the entire galaxy. FIR luminosity measurements of the inner ∼350 pc nuclear region by *Spitzer*[13] (Paglione and Abrahams, 2012) lead to an estimate of 2.7 $M_{\odot}\ \mathrm{yr}^{-1}$. It is encouraging that the $SFR(M \geq 5\ M_{\odot})$ calculated using different estimators are in broad agreement with each other. However, the differences point to the existence of systematic or intrinsic differences between the different estimators.

The supernova rate derived from the FIR luminosity (via Equation 20 from Condon 1992) is 0.05 - 0.13 yr^{-1} and is similar to the lower limit of the supernova rate deduced from expansion rates (LT06).

[12] `http://irsa.ipac.caltech.edu/IRASdocs/exp.sup/ch1/index.html`
[13] `http://www.spitzer.caltech.edu/`

4.6 Summary

We have presented the results of multi-epoch observations of the southern starburst galaxy, NGC 253 with the LBA at 2.3 GHz. The results presented here are complementary to previous 2.3 GHz LBA observations by Lenc and Tingay (2006). We find the following results:

1. Seven compact sources were detected in the highest sensitivity observation (the 2008 epoch). All sources were identified with higher-frequency VLA observations (UA97), while six were identified with a 2.3 GHz LBA detections by LT06. The three brightest sources were also detected in the lower sensitivity observations (2006 and 2007).

2. The shell-like SNR, 5.48-43.3, was successfully imaged with the highest resolution in all three epochs. The structure in the 2008 image shows a double-lobed morphology which is dominated by the eastern lobe. The weaker, western lobe was not detected in the 2006 and 2007 observations, which is attributed to lower sensitivity and fidelity, due the lack of the 70 m Tidbinbilla antenna.

3. Observed differences in the small-scale structure of 5.48−43.3 between the 2004 (LT06) and the 2008 (this chapter) observations can be explained by deconvolution errors associated with sparse (u, v) plane sampling. No discernible expansion has been observed for 5.48−43.3 between the 2004 and 2008 epochs.

4. The spectra of the 20 compact sources in NGC 253 from LT06 are compared with the spectra obtained with the new 2.3 GHz LBA flux density measurements (2008 epoch). As with LT06, we find that the spectra fit a free-free absorption model, with little difference in the spectra between the epochs.

5. Our results show no change in the classification of the compact sources by LT06. 12 of the 20 sources have steep spectra associated with SNRs, while the remaining eight have flat intrinsic power-law spectra ($\alpha > 0.4$), indicative of H II regions.

6. We derive an improved RSNe peak luminosity distribution at 5 GHz using data from the literature for 51 core-collapse supernovae (29 Type II & 22 Type Ibc).

7. We estimate a value for the upper limit of the supernova rate of 0.2 yr^{-1} for the inner 300 pc of NGC 253, using an improved model that is based upon the principles of UA91 and LT06. This result was found to be consistent with estimates from near infrared (NIR) observations.

8. The results of our model indicate that the radio observations are detecting 60% - 80% of all SNRs in NGC 253, thus pointing to the possible existence of a small population of undetected SNRs. Moreover, no RSNe or SNRs has been observed in NGC 253 during 21 years of radio observation suggests a low rate of RSNe production in NGC 253.

9. A new upper limit to the star formation rate of $SFR(M \geq 5\ M_{\odot}) < 4.9\ M_{\odot}\ \mathrm{yr}^{-1}$ is estimated directly from the supernova rate limits for the inner 300 pc region of the galaxy, which is consistent with independent estimates.

5

Probing the Compact Radio Source Population of the Whirlpool Galaxy with Wide-Field VLBI

5.1 Introduction

The formation of stars is a fundamental astrophysical process that takes place in almost all galaxies along the Hubble sequence (Kennicutt, 1998) and as such plays a major role in galaxy evolution. Star formation can occur in isolated areas or over the entire galaxy, resulting in a range of 6-7 orders of magnitude in galaxy star formation rates (Kennicutt, 1998). Galaxies that are continuously forming stars over the entire galaxy (hereafter star-forming galaxies) typically host rich populations of young stars and star clusters, HII regions, giant molecular clouds, and supernova remnants (SNRs). Furthermore, it is not uncommon for star-forming galaxies to host low luminosity Seyfert AGN at their cores: (e.g. Ford et al. 1985; Pellegrini et al. 2000; Lenc and Tingay 2009; Perez-Torres et al. 2010; Rampadarath et al. 2010; Paggi et al. 2013; Panessa and Giroletti 2013), suggesting possible connections between star formation and low luminosity AGN activity in these galaxies (e.g. Netzer 2009).

Nearby star-forming galaxies are ideal laboratories for understanding the nature of supernovae (SNe), SNRs, and the nuclear environment on parsec and sub-parsec scales through the use of wide-field, high resolution radio observations. Through the use of multi-epoch, wide-field, high resolution radio monitoring, it is possible to construct the star formation and SNe history of these galaxies. This was attempted by Rampadarath et al. (2014) for NGC 253, through the use of data spanning 21 years (see Chapter 4). Similar studies have been conducted for nearby edge-on, star-forming galaxies: M82 (Pedlar et al., 1999; McDonald et al., 2002; Beswick et al., 2006; Fenech et al., 2010); Arp 220 (Rovilos et al., 2005;

Lonsdale et al., 2006; Parra et al., 2007; Batejat et al., 2012); Arp 299 (Ulvestad, 2009; Romero-Cañizales et al., 2011; Bondi et al., 2012); NGC 4945 (Lenc and Tingay, 2009); NGC 253 (Ulvestad and Antonucci, 1997; Tingay, 2004; Lenc and Tingay, 2006); and M31 (Morgan et al., 2013), and nearby face-on, spiral galaxies: M83 (Turner and Ho, 1994; Cowan et al., 1994; Maddox et al., 2006); M51 (Crane and van der Hulst, 1992; Turner and Ho, 1994; Maddox et al., 2007); NGC 300 (Pannuti et al., 2000); NGC 7793 (Pannuti et al., 2002); and NGC 6946 (Lacey et al., 1997). Furthermore, there have been numerous surveys of face-on, spiral galaxies with VLBI, focussing on the nuclear regions (e.g. Bietenholz et al. 2004; Giroletti and Panessa 2009; Bontempi et al. 2012; Panessa and Giroletti 2013; Doi et al. 2013).

Here, the results of the deepest, widest, highest resolution radio survey of a nearby, grand design spiral galaxy are presented. The target for this survey is the Whirlpool galaxy, M51 (NGC 5194), that is currently undergoing an interaction with a smaller companion, NGC 5195. Like most spiral galaxies, M51 is actively forming stars, predominantly (but not exclusively) within its spiral arms (Calzetti et al., 2005; Kaleida and Scowen, 2010), with a slightly enhanced formation of young, massive star clusters towards NGC 5195 (Kaleida and Scowen, 2010).

Recent distance estimates place M51 at 8.4 ± 0.7 Mpc (Vinkó et al., 2012). With a nearly face-on orientation, M51 is ideal for population and morphology studies at all wavelengths. Furthermore, in the last 70 years, M51 has hosted four optically observed supernovae (SNe): the Type Ia SN 1945A (Kowal and Sargent, 1971); the Type Ib/c SN 1994I (Puckett et al., 1994); the Type Ib/c SN 2005cs (Muendlein et al., 2005); and the Type IIb SN 2011dh (Griga et al., 2011). In addition, high resolution radio observations of the nuclear region with the VLA reveals the presence of a bidirectional jet, which is associated with a low-luminosity Seyfert 2 AGN located within the nucleus of M51, that interacts with the surrounding interstellar medium (Crane and van der Hulst, 1992; Bradley et al., 2004; Maddox et al., 2007).

The first high resolution radio survey of M51 was performed by Maddox et al. (2007) at 20 and 6 cm, with the VLA. With a resolution of $1.5'' \times 1.2''$ at both wavelengths, Maddox et al. (2007) detected 107 compact radio sources, distributed throughout the disk of M51 but predominantly concentrated within the inner 2 kpc nuclear region. Maddox et al. (2007) compared the results of the radio observations with multi-wavelength observations and found: 44 radio sources with large HII counterparts; 24 with stellar cluster counterparts; 13 with X-ray counterparts, most probably X-ray binaries or micro-blazars; and six radio

sources associated with Hα emission, possibly young SNRs with resolved shells. Maddox et al. (2007) estimated the age for these SNRs to be $\sim$ 2000-3300 yr.

Through application of the improved technique of wide-field VLBI, as discussed in Chapter 2, with the European VLBI Network (EVN), the full disk of M51 ($11'.2 \times 6'.9$) is surveyed for faint, compact radio sources at 18 cm. Section 5.2 describes the observations, wide-field correlation, calibration, and data reduction methods that were employed within this study. In Section 5.3, the wide-field VLBI imaging, source detection methods, and primary beam correction are discussed, including images of the sources detected. The multi-wavelength and multi-resolution ancillary data (radio and optical) used in this study are presented, including data reduction steps, in Section 5.4. Discussion of the sources detected is presented in Section 5.5, including comparisons with the ancillary data and previous results obtained from the literature. Finally, in Section 5.6, the results are summarised.

5.2 Observations, Correlation and Data Reduction

5.2.1 Observations

M51 was observed on November 7$^{\rm th}$ 2011 for 8 hrs (UT: 01:30 - 09:30) at 18 cm with a single-pointing of the EVN. The experiment was performed using the Effelsberg (Ef), Jodrell Bank 76 m Lovell dish (Jb1), a single Westerbork dish (Wb), Medicina (Mc), Onsala 25 m (On), Svetloe (Sv), Zelenchukskaya (Zc), Badary (Bd), Urumqi (Ur), and Shanghai (Sh) antennas. During the observation, 5 minute scans of M51 (centred on: RA = $13^{\rm h}29^{\rm m}$ $52.698^{\rm s}$; Dec = $+47°11'$ $42''.930$ [J2000.0]) were scheduled, alternating with 1 minute scans of a phase reference calibration source, J1332+4722 (RA = $13^{\rm h}$ $32^{\rm m}$ $45.246424^{\rm s}$; Dec = $+47°$ $22'$ $22''.667700$ [J2000.0]) located $31'.14$ from M51.

The recorded VLBI data were composed of 8×16 MHz sub-bands, dual polarisation and 2-bit data sampled at the Nyquist rate, resulting in a total data rate of 1024 Mbps, producing a 1σ point source sensitivity (at the pointing centre) of 6μJy[1]. Figure 5.1 shows an optical image overlaid with the sensitivity contours of the EVN observation, taking into account the different primary beam of each antenna (see Sect. 2.4.3.2). The angular size of M51 ($11'.2 \times 6'.9$) allows most

[1]The EVN sensitivity calculator: `http://www.evlbi.org/cgi-bin/EVNcalc`

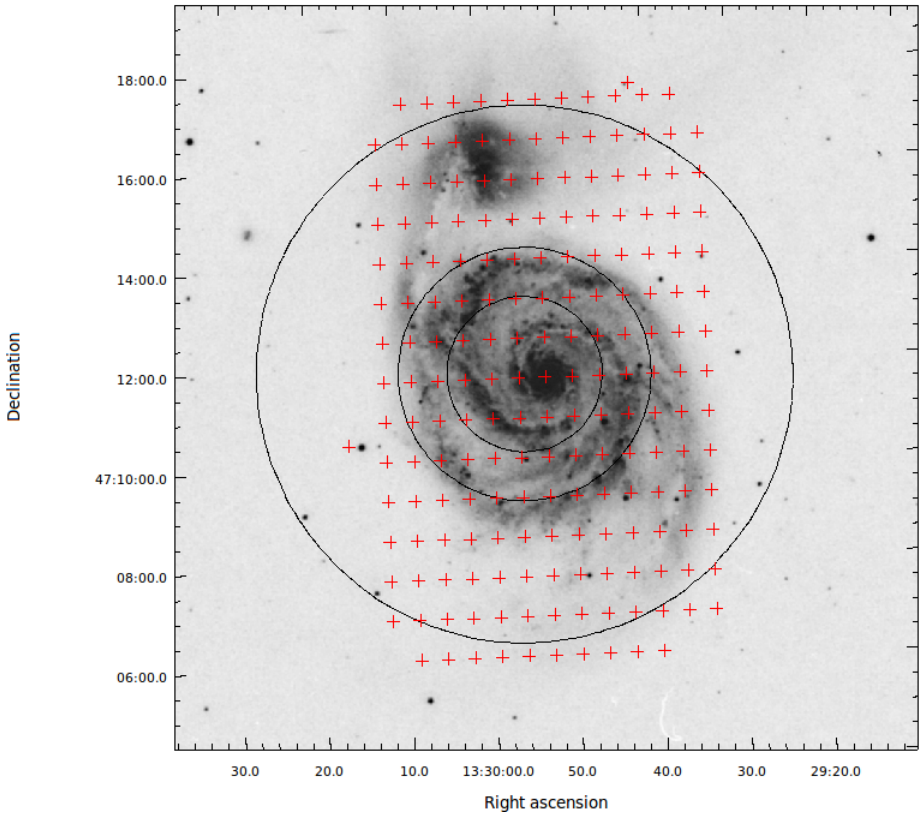

Figure 5.1: Optical image of M51 from the Space Telescope Science Institute digitised plate archives (image credit: DS9 image server), overlaid with the sensitivity contours of the EVN. The contours are 6.7 μJy, 7.5 μJy and 13 μJy, and are the theoretical sensitivity taking into account the SEFD, effective area and data rate of the individual antennas, and the total observing time, bandwidth and the primary beams of the individual antennas. The red crosses are the positions of 192 simultaneous multi-phase centres obtained through DiFX used to survey M51 with the EVN.

of the galaxy to lie within the primary beam of the 100 m Effelsberg antenna at this wavelength ($\sim 7'.5$). Figure 5.2 shows the (u, v) coverage of the EVN observation. The maximum projected baseline is approximately 45 Mλ (Lovell-Shanghai), while the shortest projected baseline (Jb1-Ef) is 1.5 Mλ, hence structures with an angular size larger than 150 mas (5.7 pc at the distance of M51) are resolved (i.e. structures with intensity variations on larger angular scales are not detected).

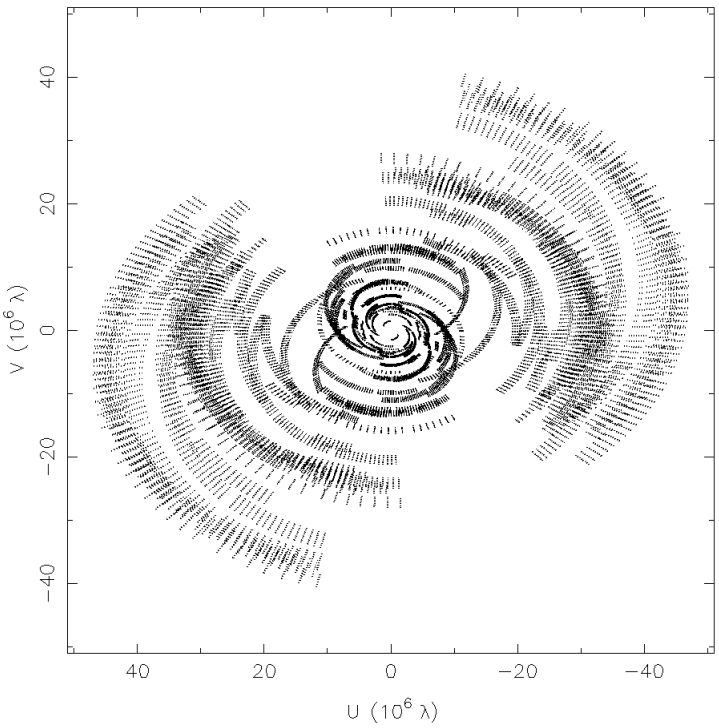

Figure 5.2: The (u, v) coverage of the 10-station EVN observation at 18 cm (centre frequency per sub-band, for each baseline only).

5.2.2 Correlation

To successfully survey the entire disk of M51 for compact radio sources with the full capabilities of the EVN requires application of the technique of multi-phase centre correlation described in Sect. 2.4.2.2. This was achieved through the use of the DiFX software correlator (Deller et al., 2007, 2011), at the Max-Planck Institue for Radio Astronomy, Bonn, Germany. Prior to correlation, the data were shipped via courier from each station to Bonn, where the correlation was performed with a high performance computer cluster comprising 60 computer nodes (8 cores each).

The correlation was initially performed with sufficient frequency and time resolution (488 Hz and 1 ms) to restrict amplitude losses below 5% at a radius of $6'$ on the longest baseline due to image smearing (see Sect. 2.4.1). Then using the simultaneous multi-phase correlation method, the field was separated into 192 individual phase centres, allowing the effects of non-coplanar to be mitigated as described in Section 2.4.2. The locations of the phase centres are shown in Figure 5.1.

To minimise cumulative amplitude errors to less than 5% due to non-coplanar

baselines, bandwidth, and time-average smearing on the longest baseline per phase centre, each sub-band (of 16 MHz bandwidth) was correlated with 128 channels (125 kHz) and time resolution of 1 second, resulting in a data size of 41 GB per phase centre. The correlated data were transferred to the iVEC Petabyte Data Store[2] located in Perth, Western Australia, using the network data transfer protocol gridFTP[3].

5.2.3 Data Reduction

5.2.3.1 Data Preparation

During correlation, the clock at the Badary antenna experienced a glitch that caused it to skip ahead by 1s. This resulted in a separation of the final correlated data per phase centre, at the time of the clock skip, into two individual FITS files. Concatenation of the two correlated files per phase centre to form the individual visibility FITS via the AIPS task FITLD takes ∼2 hours on a standard iCore 7 desktop computer. Extending this process to 192 phase centres would require more than 300 hrs of computing time, which is almost tripled when considering read and write time of the FITS data to disk.

In order to concatenate the 192 phase centres in a time that is suitable for this project, the Curtin ATNF VLBI Experiment (CAVE), which is a high performance computing cluster located at the Australia Telescope Compact Array (ATCA), Narrabri, NSW was used. CAVE comprises 14 computer nodes, where the nodes are quad-core 2.7 GHz AMD Sunfire x86 machines, with 16 GB memory and 400 GB disk capacity each. The main disk space (8 TB × 3) is located on a single centralised node (hereafter, CAVE-STORE). The cluster is owned by Curtin University and operated by the Australia Telescope National Facility (ATNF). To use the multiple nodes of CAVE effectively for the concatenation, we made use of the ParselTongue scripting language (Kettenis et al., 2006). ParselTongue allows the execution of multiple AIPS tasks simultaneously on a number of remote computers via the PARALLELTASK module.

Figure 5.3 provides a schematic diagram of the concatenation process. The correlated datasets are copied from the iVEC Petabyte Data Store to the 8 TB data storage on CAVE-STORE. Before starting the concatenation process, the ParselTongue server is started on the individual nodes[4]. Executing the Parsel-

[2] `http://www.ivec.org/`

[3] `http://www.globus.org/toolkit/docs/latest-stable/gridftp/`

[4] See the ParselTongue online documentation `http://www.jive.nl/jivewiki/doku.php`

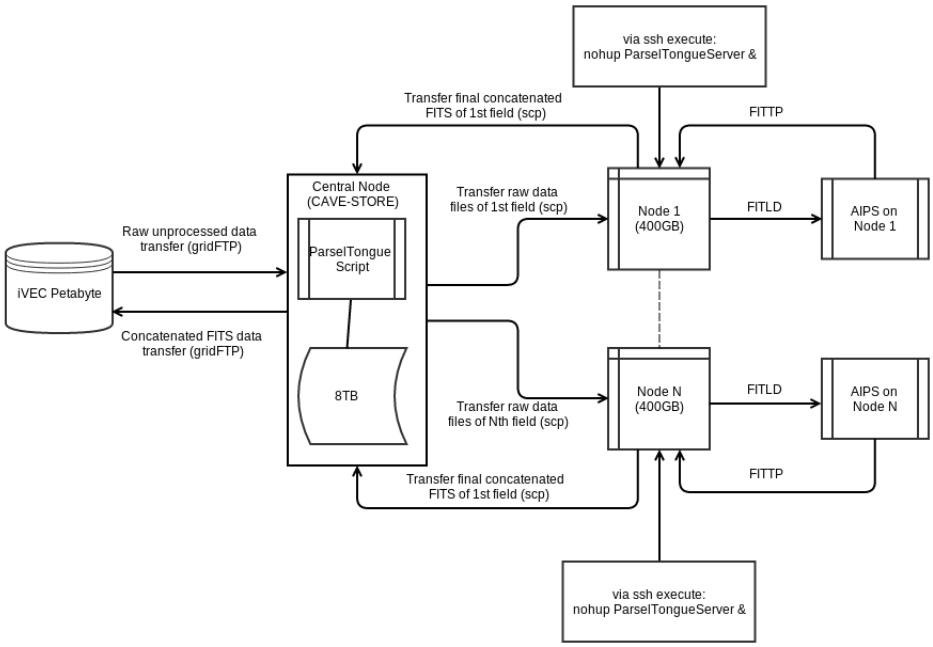

Figure 5.3: Schematic diagram of the overall procedure used to concatenate the correlated data that were spilt due a clock glitch at the Badary antenna. The entire process was executed on a 14 node high performance computer cluster, CAVE using a combination of the remote and parallelisation capabilities of ParselTongue. The diagram follows the data from its raw state located at the iVEC Petabyte Data Store, to the final concatenated version, which is stored at both iVEC and CAVE-STORE. Please see the text for details.

Tongue script on CAVE-STORE begins by copying the datasets to the individual nodes, such that the datasets for the N^{th} phase centre is sent to the N^{th} node. After the data are copied, FITLD loads and concatenates both datasets to AIPS and the result written to disk (via FITTP), copied to CAVE-STORE, and eventually copied to iVEC. Note, the data processing on the individual nodes is executed in parallel.

Due to the limited storage space and network connection between iVEC and CAVE-STORE, the datasets were separated into ∼1 TB groups (∼ 25-30 phase centres) for processing. The time taken to process ∼1 TB of data on two nodes on CAVE was 13.5 hrs[5], resulting in a total time of ∼87 hrs to concatenate the 192 phase centres.

[5]The processing time per 1 TB group can be speeded up by using multiple nodes i.e. three nodes would reduce the time to 9 hrs, four nodes to 6.8 hrs etc. However, CAVE is a shared cluster and only two nodes were fully available for this project at any time.

5.2.3.2 Calibration

The data reduction and calibration were performed using the data reduction package AIPS. Prior to calibration, flagging of data during times at which each of the antennas were known to be slewing and time ranges that contained known bad data, was carried out via application of flag files and information provided in the observing logs. Corrections to the amplitudes in cross-correlation spectra from the auto-correlations were obtained via ACCOR. The amplitude calibration was refined by application of antenna system temperatures (in Kelvin) measured during the observations, along with the gain (in Janskys per Kelvin) for each antenna. Following the amplitude calibration refinement, a single value of the delay (i.e. phase against frequency) was determined for each antenna, polarization and 16 MHz sub-band using two minutes of data on the bright radio source, 3C 345 (AIPS task FRING). Global fringe-fitting solutions were determined for J1332+4722 (AIPS task FRING) with a one minute solution interval, finding independent solutions for each of the 16 MHz sub-bands. The delay and phase solutions were examined and, following editing of bad solutions, applied to J1332+4722. The J1332+4722 data were then exported to DIFMAP, where the data were vector-averaged over 30 s, flagged of bad data, and imaged using standard imaging techniques (deconvolution and self-calibration of both phase and amplitude). The resulting image of J1332+4722 is shown in Figure 5.4. The image shows no evidence for extended structure on these baselines at this frequency to a dynamic range of 2500, for regions in the image away from the inner side-lobes around the source. The final calibration solutions (phase and amplitude) from J1332+4722 were exported via the DIFMAP task, CORDUMP[6] (Lenc and Tingay, 2009) to an AIPS-compatible solution table. The solution table was then transferred to AIPS and applied to all sources in the dataset. The final calibrated J1332+4722 data were also used to derive a bandpass calibration via the AIPS task BPASS. The edge channels of each band were flagged (5 channels from both the lower and upper edge of each 128 channel band). The final calibration solutions were then applied for a first imaging pass for each phase centre[7].

[6] `http://www.atnf.csiro.au/people/Emil.Lenc/tools/Tools/Cordump.html`

[7] Here AIPS was used as the preferred imaging tool as opposed to DIFMAP in Chapter 4. Unlike DIFMAP, it is possible to use ParselTongue to produce AIPS pipelines to calibrate, flag and image the high number of fields that resulted from this project.

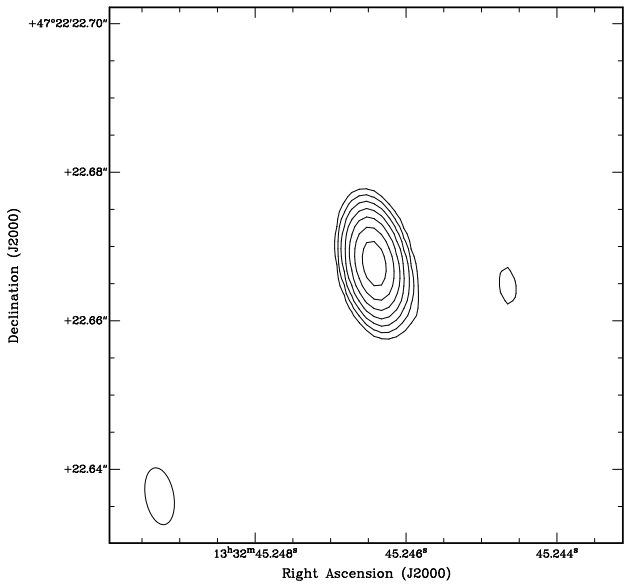

Figure 5.4: Contour map of the calibrator J1332+4722, with a dynamic range of $\sim$ 2500 between the peak flux density and the RMS for regions in the image away from the inner side-lobes around the source.. The contours begin at $\pm 1\%$ the peak flux (226.02 mJy/beam), and increase in increments of $2^n\%$ of the peak flux, where n are integers.

5.3 Imaging, Source Detection and Results

5.3.1 Wide-field VLBI Imaging

Prior to imaging, data affected by RFI were manually flagged via the AIPS tasks SPFLAG and EDITR. Data from the Mc antenna were found to be corrupted by RFI. Initial attempts at selective RFI removal were found to be time consuming and the entire antenna was flagged, improving the final sensitivity. Furthermore, data with u coordinate < 50 Mλ which are susceptible to RFI due to the low fringe rate were also flagged. The flag tables along with the final calibration and bandpass tables were copied and applied to all phase centres via SPLIT.

Initial imaging was restricted to a maximum baseline of 7.5 Mλ (resolution to 27.6 mas). This allowed a reduction in the number of channels (32) per sub-band and increased time averaging (5 seconds), while keeping the total amplitude loss due to time and bandwidth smearing $< 5\%$. Moreover, the decreased resolution lowered the number of pixels required to image a radius of $21''$ per phase centre and, therefore, the data size per phase centre, thus reducing the computation required to image the phase centres.

Dirty maps of the phase centres were produced via the AIPS task IMAGR, using parameters: cellsize = 2.7 mas; image size = 16384 $\times$ 16384 pixels; and

natural weighting. Finally, 512 pixels were removed from the image edges, to reduce aliasing effects. This resulted in image sizes of 15360 pixels × 15360 pixels, covering $41'' \times 41''$ per phase centre. The AIPS task IMEAN was then used to obtain the RMS noise levels across the entire image, allowing comparisons with the peak flux densities.

Prior to imaging, the effects of the primary beam were corrected for a subset (62) of the 192 phase centres as described in Sects. 2.5.3 and 5.3.3. No significant differences in the peak signal to RMS noise ratio (S/N) were found after primary beam correction compared to the S/N of the same phase centres without primary beam correction (see Figure 5.5 and Sect. 5.3.3 for a detailed discussion on the primary beam model). Since most of these images will be composed of empty pixels, applying the primary beam correction to all phase centres would be an inefficient use of computing resources. Therefore, the primary beam was not corrected for the remaining 130 phase centres and would be applied only to the images with candidate sources.

The distribution of the peak S/N for the 192 phase centres is displayed in Figure 5.6. Six phase centres were found to have a peak S/N $> 7\sigma$, with the remaining phase centres distributed between 5σ and 6.3σ. While the six peak S/N are indeed real detections (and are discussed in Section 5.5), it is possible that there are real detections with S/N $< 7\sigma$.

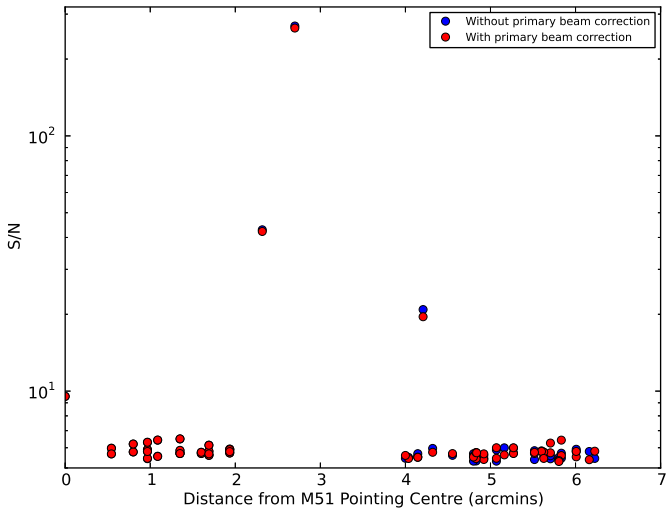

Figure 5.5: The peak signal to noise ratio (S/N) of 62 phase centres with (red circles) and without (blue circles) primary beam correction, as a function of distance from the pointing centre.

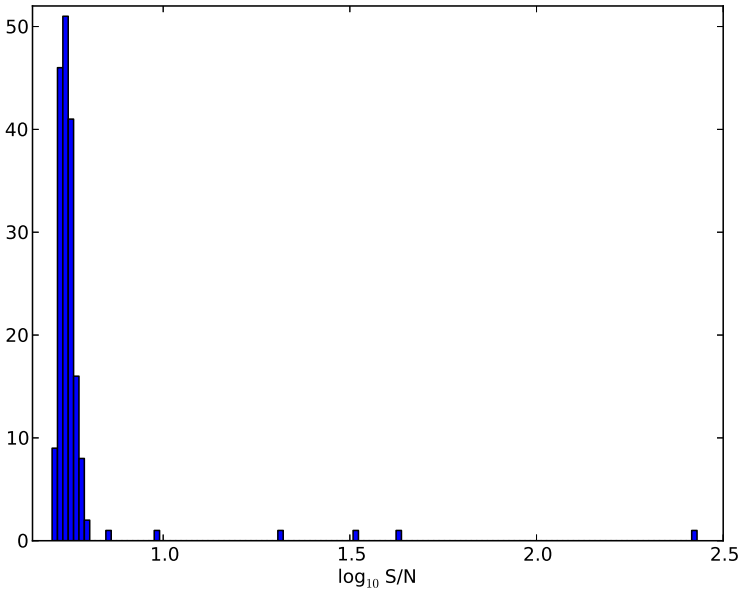

Figure 5.6: The distribution of the peak signal to noise ratio (S/N) for the 192 phase centres, where the x-axis is plotted in logscale.

5.3.2 Source Identification

5.3.2.1 Defining the detection threshold

While there are clear detections with S/N $> 7\sigma$, what is the actual threshold for determining a real detection in the wide-field VLBI images? Consider a VLBI image of pixel size $n_{\text{pixels}} \times n_{\text{pixels}}$. Since multiple phase centres are simply a way to image a large field through N_{field} small fields, the total number of pixels is $N_{\text{field}} \times n_{\text{pixels}} \times n_{\text{pixels}}$ (Morgan et al., 2013)

Figure 5.7 plots the pixel distribution of a single 15360 pixel $\times$ 15360 pixel wide-field VLBI image, representing a blank region of the sky. The field covered by this image was found to be devoid of known radio sources from the FIRST (Becker et al., 1995) and Maddox et al. (2007) radio catalogues[8], and lacked pixels with flux density above the Gaussian noise threshold. The distribution was found to follow a Gaussian distribution (the red line), indicating that the pixels of the wide-field VLBI images are Gaussian distributed[9]. Thus, the probability that a pixel exists with S/N less than some threshold, S_m, is given by the cumulative

[8]See Section 5.3.2 for a description of these radio source catalogues

[9]Note that this is only valid if the data are free from real sources and RFI (achievable through careful flagging). This is shown empirically in Morgan et al. (2013) and Figure 5.7

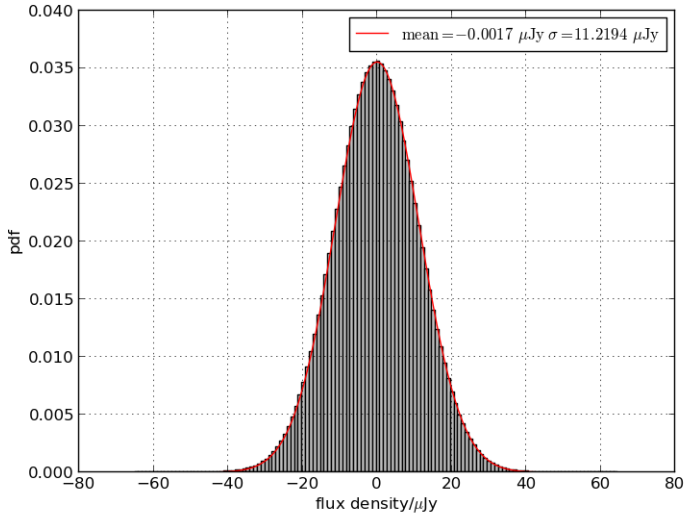

Figure 5.7: Histogram showing the pixel distribution of a single 15360 pixels × 15360 pixels wide-field VLBI image. The red line represents a non-linear least squares Gaussian fit to the distribution, with the mean and standard deviation given inset.

distribution function of the positive half of the Gaussian distribution,

$$P(\mathrm{S/N} \leq S_m) = \mathrm{erf}\left(\frac{S_m - \mu}{\sigma_{SD}\sqrt{2}}\right), \tag{5.1}$$

where erf(x) is the error function associated with the Gaussian distribution and σ_{SD} and μ are the standard deviation and mean of the Gaussian distribution, respectively. If we assume a Gaussian distribution with mean $\mu = 0$, and standard deviation $\sigma_{SD} = 1$, the argument of Equation 5.1 becomes $S_m/\sqrt{2}$. It is, however, more applicable to determine the probability that S/N is above S_m, is simply,

$$P(\mathrm{S/N} \geq S_m) = 1 - \mathrm{erf}\left(\frac{S_m}{\sqrt{2}}\right) \tag{5.2}$$

Equation 5.2 is the probability that an image pixel of S/N is above a given threshold, S_m, for Gaussian noise. Thus, the presence of real sources would be evident by the existence of pixels with S/N $> S_m$. The reciprocal of Equation 5.2 is thus the equivalent frequency of occurrence, N_{freq}, which is a measure of the total number of image pixels such that a single pixel will have S/N equivalent to S_m.

By assuming the pixel brightness distribution in the wide-field images is Gaussian distributed, from Equation 5.2, one 5.8σ pixel would be expected on average

in every 15360 pixel × 15360 pixel image and one 6.7σ pixel in 192 images, assuming no astronomical sources. Thus, any peak flux density with S/N $\geq 6.7\sigma$ is taken as a candidate detection.

5.3.2.2 Using Prior Catalogues to Search for Faint Sources

The detection threshold calculated in Sect. 5.3.2.1, assumes that each pixel in the images are independent. This may not entirely be the case, as pixels within an area defined by the synthesised beam may be correlated. In this analysis, the correlation between neighbouring pixels is neglected since the pixel size is large relative to the resolution, and as such the detection threshold calculated in Sect. 5.3.2.1 is a more conservative estimate.

There is a possibility that real sources exist in the wide-field images below this limit. To determine this probability and to search for sources below the 6.7σ limit, the likelihood ratio (LR) method described by Morgan et al. (2013) is applied. This method calculates the likelihood that each pixel in a VLBI image is associated with a catalogued source, (the alternative hypothesis, H_1), or a noise spike, (the null hypothesis, H_0). This calculation is made assuming the noise in each image is Gaussian distributed and the RMS of the noise does not vary across an individual image (Morgan et al., 2013), and is expressed as the following ratio,

$$\mathrm{LR} = \frac{p(H_1)}{p(H_0)}, \tag{5.3}$$

where p(H_0) is the likelihood the pixel is a noise spike and is taken as the Cumulative Distribution Function of the positive half of the Gaussian distribution, while p(H_1) is the likelihood the pixel is associated with a catalogued source and is dependent on the position of the pixel in relation to a catalogued source position/morphology as defined by Morgan et al. (2013). LR images can be generated corresponding to the VLBI images, containing the LR values for each pixel (see Section 2.5 of Morgan et al. 2013 for a detailed description of this method).

This LR method is used to search for VLBI counterparts to sources detected in M51 by the FIRST survey (Becker et al., 1995) and Maddox et al. (2007). In their analysis, Morgan et al. (2013) found that the results of the LR test did not give a significant advantage over simply detecting bright pixels due to the poor constraints on the position given by the lower resolution catalogues. Given the better positional accuracy provided by the VLA FIRST (Becker et al., 1995) and

the Maddox et al. (2007) surveys, it may be possible to search for sources below the 6.7σ limit.

Before applying the LR method, the AIPS task UVFIX was used to produce visibilities centred on the catalogued positions allowing the data to be averaged in frequency and time, with little loss of amplitude response due to image smearing. Dirty images were generated for each of the catalogued source positions with the full array[10], using parameters: cellsize = 0.5 mas; image size listed in Table 5.1; and natural weighting. In addition, the outer 512 pixels removed prior to applying the LR method. The required VLBI parameters to search for sources from both catalogues are listed in Table 5.1.

Table 5.1: LR Search Parameters

Catalogue	Source Count	B_{maj} ($''$)	Image size (pixels)
(1)	(2)	(3)	(4)
FIRST	15	5	7936
Maddox (20 cm)	96	1.51	1984

Notes.
(1) Catalogue of radio sources in M51; (2) Number of sources detected in M51 by both catalogues; (3) Major axis of the survey beam; (4) Number of pixels per dimension required to image the field of size B_{maj}

LR images were generated for each catalogued source and the position of the maximum LR value was visually compared to the corresponding VLBI peak pixel S/N. Pixels with $\log_{10}(\mathrm{LR}) > 10$ and $\mathrm{S/N} > 6.7\sigma$ were taken as confirmed detections. Tables 5.2 and 5.3 list the LR values for the confirmed detections along with the corresponding VLBI image parameters for confirmed detections, and the non-detection with the highest LR value for both surveys. As with the results of Morgan et al. (2013), the LR test was found to be more dependent on the VLBI pixel S/N (i.e. $p(H_0)$), than the positional constraints given by the lower resolution catalogues.

An example of this is displayed in Figure 5.8b, where a 22σ VLBI pixel was discovered $\sim 6''$ from two FIRST sources, but has $\log_{10}(\mathrm{LR})$ values >100 when

[10]This test was also conducted for the reduced array of maximum baseline of 7.5 Mλ. However there was no difference in the final result compared to the full array.

compared with both FIRST sources. However, pixels that were found to have better positional constraints (i.e. higher values of p(H_1)) nevertheless resulted in lower LR values. As such no significant advantage is given by the LR method over simply detecting the brightest pixels and thus, it is difficult to determine whether pixels with S/N$< 6.7\sigma$ are indeed real detections, and are henceforth considered as resulting from noise.

Of the three Maddox et al. (2007) sources detected by the EVN, two were found with very good agreement between the VLBI and lower resolution source positions (see Figure 5.8c). It may be possible to use estimates of the positional error of the Maddox et al. (2007) survey to improve the LR method and increase the chance of detecting sources below 6.7σ. However, this is beyond the scope of this study.

Table 5.2: Results of Likelihood Ratio Analysis of the Vla First Catalogue

$VLBI_{peak}$ (μJy beam^{-1}) (1)	σ (μJy beam^{-1}) (2)	S/N ($VLBI_{peak}/\sigma$) (3)	$-\log_{10}(p(H_o))$ (4)	$-\log_{10}(p(H_1))$ (5)	$\log_{10}(LR)$ (6)
326.42[a]	11.75	27.77	169.4	0.49	168.9
233.00[b]	10.03	23.24	118.9	0.89	118.0
231.16[b]	10.09	22.90	115.7	1.09	114.6
84.13[c]	8.96	9.39	20.5	1.09	19.4
53.35[†]	9.00	5.93	8.8	0.60	8.2

Notes.
Source identification (see Table 5.5): [a] 3005+1035; [b] A single VLBI source (3016+1024) located between two FIRST sources. See Figure 5.8b; [c] 2952+1142.
[†] The non-detection with the highest LR; (1) Flux density of the brightest pixel from images made with the full EVN array; (2) The 1σ of the individual images obtained through fitting a Gaussian distribution to the histogram of pixel fluxes; (3) Signal to noise ratio; (4) The probability the brightest pixel in the image is a noise spike, i.e. a source of S/N ratio would occur by chance once in every $1/10^{-log_{10}(p(H_o))}$ pixels; (5) Likelihood the pixel is related to a catalogued source based upon position; (6) The likelihood ratio parameter of the brightest pixel in the image. See text for details.

The brightest observed noise pixel in 15 $\times$ 7936 $\times$ 7936 pixels covering the FIRST catalogued position is 5.93σ. Likewise, it is 5.59σ in 96 $\times$ 1984 $\times$ 1984 pixels for the Maddox et al. (2007) catalogue. Furthermore, the weakest detection in Table 5.3 would occur as a Gaussian noise spike once in $\sim 10^{17}$ pixels. The very clear separation between the weakest detection and brightest noise spike was

Table 5.3: Results of Likelihood Ratio Analysis of Maddox Catalogue

$\mathrm{VLBI_{peak}}$ (μJy beam^{-1}) (1)	σ (μJy beam^{-1}) (2)	S/N ($\mathrm{VLBI_{peak}}/\sigma$) (3)	$-\log_{10}(\mathrm{p(H}_o\mathrm{))}$ (4)	$-\log_{10}(\mathrm{p(H_1)})$ (5)	$\log_{10}(\mathrm{LR})$ (6)
327.26[a]	17.33	18.31	74.5	0.49	74.0
317.42[b]	30.23	10.82	26.9	0.40	26.5
86.07[c]	10.12	8.51	17.0	0.30	16.7
47.48[†]	8.52	5.57	7.9	0.60	7.3

Notes. Symbols and headings have same meaning as Table 5.2
Source identification (see Table 5.5): [a] 3005+1035; [b] 3011+1041; [c] 2952+1142.

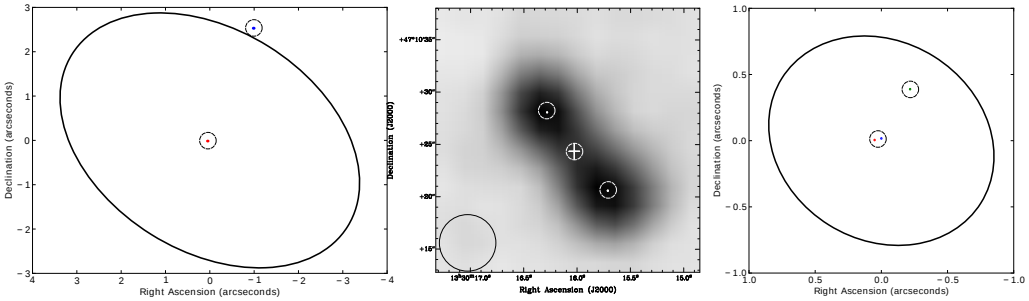

Figure 5.8: (a) The location of the peak VLBI pixel with respect to the catalogued position of the nearest corresponding FIRST source. The circles are: red (3005+1035); and blue (2952+1142). (b) The location of the single VLBI source (3016+1024; white cross) located between two FIRST sources (greyscale). The ellipse gives the FIRST beam size (see Table 5.1). (c) The location of the peak VLBI pixel with respect to the catalogued position of the nearest corresponding 20 cm Maddox et al. (2007) source. The circles are: red (3005+1035); green (3011+1041); blue (2952+1142). The ellipse in both (a) and (c) are the beam sizes of the respective surveys, centred on the catalogued position. The size of the circles indicate the astrometric error on the catalogued positions via the relationship, $\mathrm{B_{maj/min}} \cdot \sigma / 2S_P$, where $\mathrm{B_{maj/min}}$ is the major or minor beamsize, σ is the RMS noise in the catalogue images and S_P is the peak flux density of the catalogued source (Morgan et al., 2013). Dashed circles have been placed around the sources to aid the reader.

validated upon visual inspection of both the VLBI and LR maps. Furthermore, while there may be emission from sources less than 6.7σ in the wide field VLBI images, the test conducted here does not provide any evidence to indicate that this is the case. Hence, 6.7σ is adopted as the detection threshold in the wide-field images.

5.3.3 Primary Beam Correction

Primary beam corrections were applied to the phase centres containing pixels above 6.7σ, following the method outlined in Section 2.5.3. In our model the EVN antennas are assumed to have a symmetric beam (assuming perfect illumination), given by the beam size at the central observing frequency, with both the right and left circular polarizations having the same pointing centres (i.e. no beam squint). The dependence of the primary beam is estimated for each antenna and frequency sub-band using the parameters listed in Table 5.4. The primary beam response is assumed to follow the two-dimensional Bessel function of Equation 2.13, and is calculated for the duration of the observation, using the measured system temperatures for each antenna and then applied to the visibilities. The variation of the primary beam sensitivity with distance from the pointing centre is shown in Figure 2.8, and the S/N of the detected sources, both before and after primary beam correction are shown in Figure 5.5. Applying the primary beam correction, in principle should decrease the noise contributions from the individual antennas, thereby increasing the S/N. However, this is not seen in Figure 5.5. In fact there seems to be a slight decrease in S/N further from the phase centre, indicating the existence of inaccuracies in the primary beam model.

Primary beam corrections in VLBI observations are uncommon and to date have been applied to a subset of EVN antennas (Morgan et al., 2011) and the VLBA (Middelberg et al., 2011; Morgan et al., 2013; Middelberg et al., 2013). While the method used in this chapter to correct for primary beam errors broadly follows the methods of previous studies, amplitude errors will unavoidably remain. For the EVN, unlike the VLBA array, the difference in antenna sizes (from 100 m to 25 m) results in very different primary beam responses. Moreover, during the course of the observations the different physical characteristics of the individual elements produce varied effects on the overall primary beam response of the array[11]. Furthermore, the exact characteristics of each antenna in the EVN (except for Ef to a certain degree) are unknown and a number of assumptions were required to be made (e.g uniform illumination of the full dish, symmetric beam, no beam squint, no parallactic rotation and a perfect parabola defined by a Bessel function), which would no doubt affect the final correction. However, while there are uncertainties the final flux density values are considerably closer to the true values than not applying the primary beam correction.

Finally, for radio sources within the HPBW of the Ef primary beam (radius =

[11]Note:- this is also true for the VLBA

$\sim 3.8'$), we estimate the residual error is on the order of 10%. While for sources beyond the Ef primary beam, an error of 20% is estimated for the residual errors. This term is added in quadrature with the other sources of error and listed in Table 5.5.

Table 5.4: Primary Beam Model Parameters

	Model Parameters			
	SEFD	Diameter	ν_{beam}	Beamwidth
Antenna	(Jy)	(m)	(MHz)	($'$)
(1)	(2)	(3)	(4)	(5)
Ef*	19	100	1660	7.88
Jb1	44	76	1438	9.43
Mc	600	32	1438	22.4
Bd	240	32	1438	22.4
Sv	360	32	1438	22.4
Zc	240	32	1438	22.4
On	320	25	1438	28.6
Sh	670	25	1438	28.6
Wb	420	25	1438	28.6
Ur	270	25	1438	28.6

Notes.

* Obtained from the Ef calibration pages at:
`www.mpifr-bonn.mpg.de/effelsberg/astronomers`
(1) Antenna designation; (2) the theoretical SEFD of the antenna; (3) Antenna diameter, assuming full illumination; (4) Reference frequency of the antenna. The exact value is unimportant and serves only as reference and was arbitrarily chosen for all but Ef; (5) Beamwidth at $\nu_{\rm beam}$, assuming perfect illumination. Assumed to be the same for all polarisations

5.3.4 Flux Density and Size Measurements

In total six sources were found with flux densities above 6.7σ and are listed in Table 5.5. Following the correction for the amplitude response of the primary beam, the positions of the six sources were shifted to the image centre via UVFIX, averaged in frequency, and finally imaged.

CLEANed images were obtained using data from the full array via the AIPS task IMAGR. The images were made with cellsize = 0.5 mas, imsize = 4096 pixels $\times$ 4096 pixels, and 100 clean iterations. Briggs robust parameter 4 was used to

Table 5.5: Compact Sources Detected with the EVN at 18 cm

	Position (J2000.0)					IMFIT Size			
	RA	Dec	Θ		S_{IMFIT}	Major	Minor	Identification	
Source	13^h	47°	$(')$	S/N	(μJy)	(mas)	(mas)	Maddox	FIRST
(1)	(2)	(3)	(4)	(5)	(6)	(7)	(8)	(9)	(10)
2952+1142$^\diamond$	$29^m52.7102^s$	$11'\,42.7465''$	0	9.7	140.1±16.0	8.8±1.1	1.9 ±0.9	53	Y
3005+1035	$30^m5.1381^s$	$10'\,35.7896''$	2.39	43	457.2±79.6	12.8±1.9	9.3±1.9	104	Y
3005+1010‡	$30^m5.1057^s$	$10'\,10.924''$	2.60	269	4306.7±431	6±0.1	-	-	N
3011+1041	$30^m11.0087^s$	$10'\,41.1393''$	3.27	32.7	559.7±63.9	6.1±3.0	-	107	N
2932+1123	$29^m32.1262^s$	$11'\,23.1175''$	3.52	7.1	188.1±51.5	8.4±2.2	3.1±1.5	-	N
3016+1024	$30^m16.0265^s$	$10'\,24.3525''$	4.17	20.8	455.2±64.5	5.1±0.6	-	-	Y

Notes.

$^\diamond$at M51 Centre; ‡SN2011dh; Sources with multiple components (2952+1142 and 3005+1035), only the brightest component is given. (1) Source name; (2) & (3) Source position; (4) Angular distance to the centre of M51. At 8.4 Mpc, $1' \approx 2.44$ kpc; (5) Signal to noise ratio of the source in the wide-field source detection maps; (6) Flux density measured from IMFIT using a single 2-D Gaussian component; (7) & (8) Source sizes measured via IMFIT; (9) Cross identification with the (Maddox et al., 2007) survey; (10) Detected by FIRST (Y), or not (N).

weight the images as it was found to produce an acceptable compromise between sensitivity and resolution. The final images are displayed in Figure 5.9, with their location in the M51 field displayed in Figure 5.10.

Measurements of flux density and size were obtained by fitting a single 2D Gaussian component via IMFIT, with independent measures of flux density from BLOBCAT (Hales et al., 2012) and source sizes from fitting a circular Gaussian to the visibilities via MODELFIT in DIFMAP (Shepherd, 1997). The measurements are listed in Table 5.5, including cross identifications with the FIRST (Becker et al., 1995) and Maddox et al. (2007) surveys. The different measurements of flux density and source size were found to be consistent, so only the IMFIT values of flux density and source size are included in Table 5.5.

Furthermore, to search for possible emission associated with extended structures, lower resolution maps were made with a (u, v) range taper of 10 Mλ for all sources and are included in Figure 5.9 (the red contours). Each source will be discussed in detail in Section 5.5.

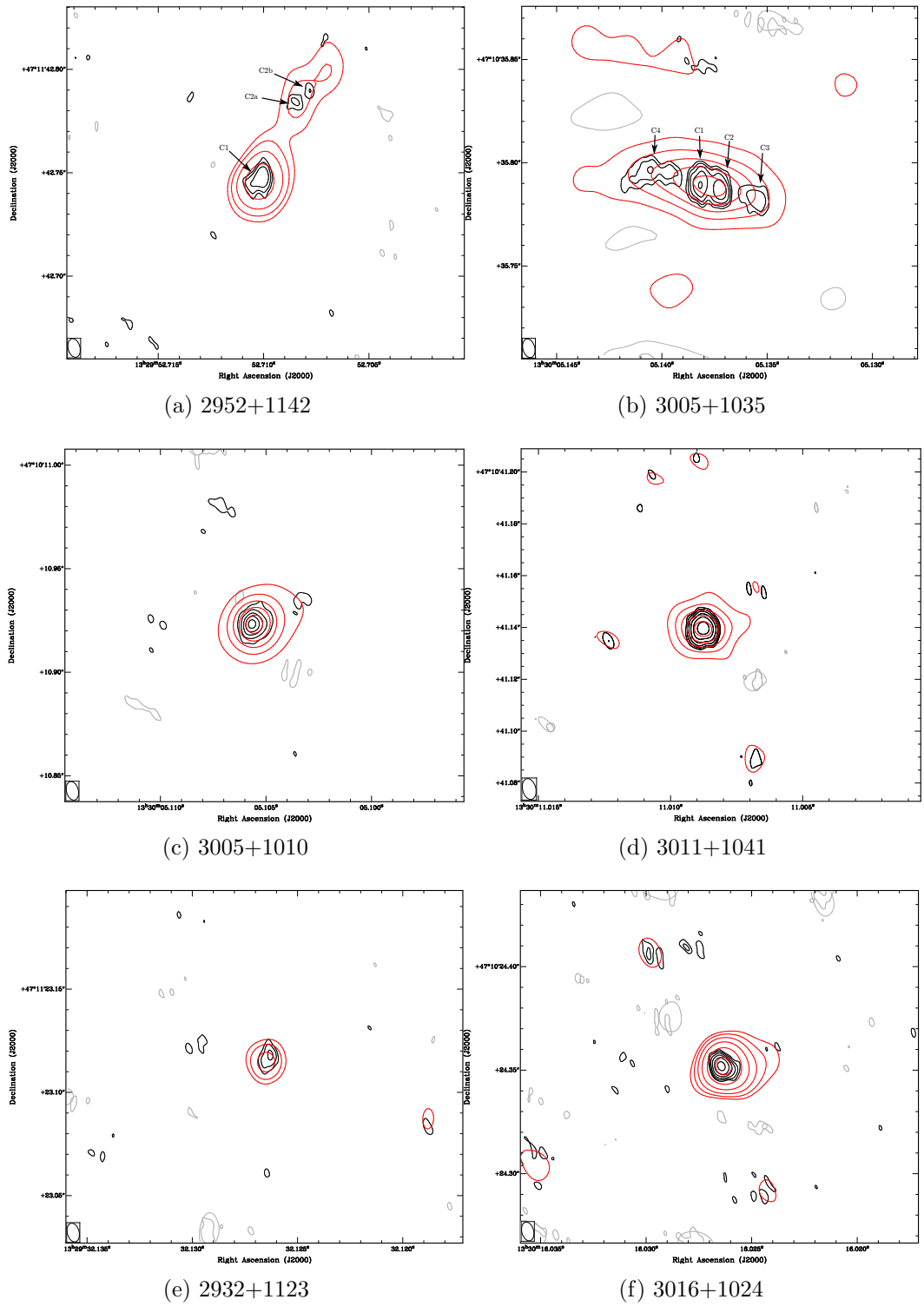

(a) 2952+1142 (b) 3005+1035

(c) 3005+1010 (d) 3011+1041

(e) 2932+1123 (f) 3016+1024

Figure 5.9: Sources detected with the full array of the EVN at 18 cm. The black contours are full resolution images with robust weighting 4, with a beam size = 9.86 mas × 5.92 mas and position angle = 14.3° . The lowest contours (for all but 3005+1010) are at $\pm 3\sigma$, and increase in multiples of $\sqrt{2}$, where σ is the RMS of the images found via IMEAN: 9.1 μJy beam^{-1} (2952+1142); 17.4 μJy beam^{-1}(3005+1035); 18.3 μJy beam^{-1} (3011+1041); 18.0 μJy beam^{-1} (2932+1123); 18.6 μJy beam^{-1} (3016+1024). The contours of 3005+1010 begins at $\pm 10\%$ the peak flux (3.26 mJy/beam), and increases in increments of 20% the peak flux. The sources were also imaged with a (u, v) range taper of 10 Mλ (red contours), with a resulting a beam size = 25.3 mas × 21.2 mas and position angle = -4.9° . The first contours are $\pm 3\sigma$, and increases in multiples of $\sqrt{2}$ for; 2952+1142 (σ=10.5 μJy beam^{-1}), 2932+1123 (σ=21.8 μJy beam^{-1}) and 3016+1024 (σ=24.4 μJy beam^{-1}). While the remaining sources the contours begin at $\pm 10\%$ the peak flux (3005+1035, 506.6 μJy beam^{-1}; 3005+1010, 4.27 mJy beam^{-1}; and 3011+1041, 552.6 μJy beam^{-1}), and increases in increments of 20% the peak flux.

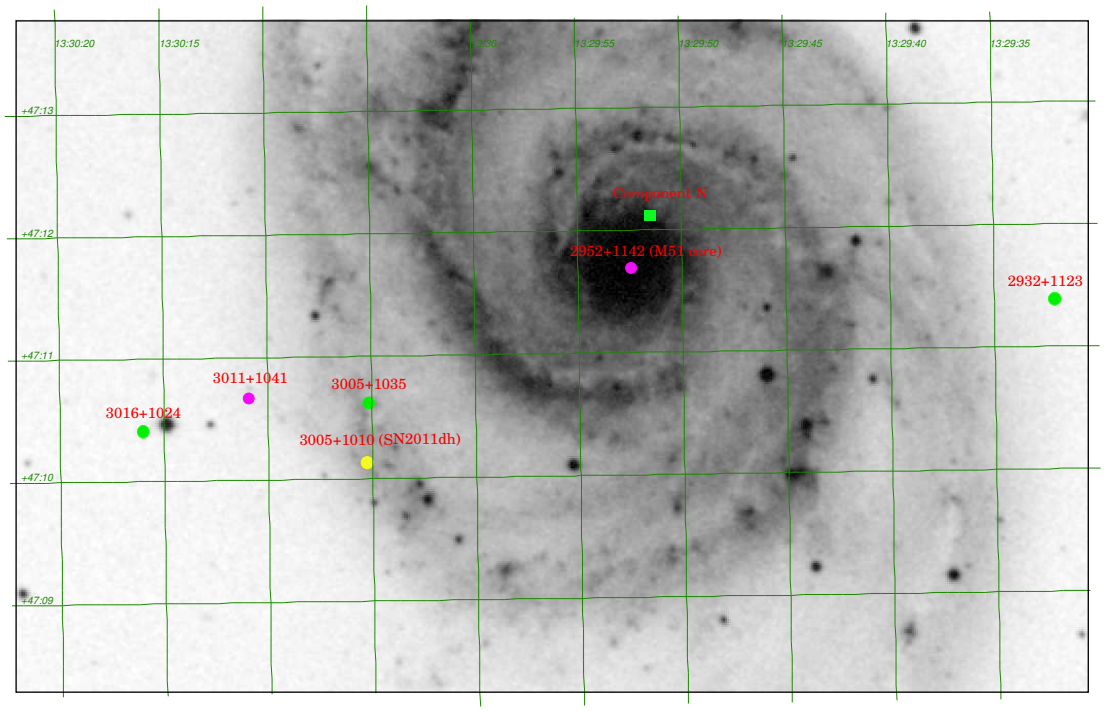

Figure 5.10: Location of the six sources detected with the EVN (filled circles) shown in Figure 5.9 and listed in Table 5.5. The pink sources are flat spectrum sources ($-0.5 \leq \alpha \leq 0.5$) and the green are steep spectrum sources $\alpha \geq 0.5$. The yellow source is the supernova SN 2011dh, that exploded 159 days prior to our EVN observation (see Section 5.5.3). The square represents a steep spectrum source detected with MERLIN at 18 cm (designated Component N) but not the EVN at 18 cm (see Section 5.5.2).

5.4 Multi-wavelength Ancillary Data

To understand the nature of the compact sources detected in the wide-field VLBI images, multi-wavelength data were obtained from either public archives via the internet, or from collaborators. Here, the data from different facilities that were used to complement the VLBI results are described, including any data processing and analysis that was required.

5.4.1 Radio Continuum

Pre-calibrated visibility data (phase, amplitude and bandpass) from both the VLA (G. Dumas, private communication) and MERLIN (M. Argo, private communication) arrays were obtained for this study and are listed in Table 5.6. The visibility data were imported and the entire M51 system ($11'.2 \times 6'.9$) was imaged in AIPS using IMAGR, with Briggs robust parameter 4. Initial imaging of the full

MERLIN array revealed a bright $\sim$5 μJy beam^{-1} radio source coincident with the VLBI source 3005+1035 and a weak detection above 300 μJy beam^{-1} (i.e. 5σ) at the centre of M51. By discarding the longest baselines ($>$ 0.8Mλ) and continuum subtracting 3005+1035, deeper images were made revealing a number of radio sources, including diffuse, extended emission around the core, previously detected only with the VLA. MERLIN sources coincident with the VLBI detected sources (Table 5.5) were found via BLOBCAT, using background RMS maps obtained from the source finding algorithm AEGEAN (Hancock et al., 2012), which were confirmed via visual inspection. These results will be discussed in the individual source discussions in Section 5.5.

Table 5.6: Archival Radio Continuum Observations

Array	Observation date (dd/mm/yy)	Frequency (GHz)	CLEAN beam B_{maj} ($''$)	RMS sensitivity (μJy)	Reference
MERLIN	02/07/2005	1.66	0.34	50	1
VLA-A	05/04/2002	1.43	1.5	23	2,3
VLA-A	03/10/2004	1.43	1.08	12	3
VLA-C	31/08/1999	4.86	2.19	66	4
VLA-C	18/08/2001	4.86	3.64	24	3
VLA-B	11/12/2003	4.86	1.47	12	2,3
VLA-D	28/10/2001	8.43	6.47	17	3
VLA-C	05/04/2004	8.43	2.1	11	3

Notes.
(1) M.Argo (private communication); (2) Maddox et al. (2007); (3) G.Dumas (private communication, Dumas et al. 2011); (4) VLA Archive

5.4.2 Optical

Optical images of the M51 system were acquired from the Hubble Space Telescope (HST) online archive. A six-pointing mosaic of the galaxy pair was obtained with the Advanced Camera for Surveys (ACS) on board the HST in four filters: B (F435W); V (F555W); I (F814W); and Hα + R (F658N) (Ubeda, 2014). The images were released to the public to commemorate the HST's 15$^{\text{th}}$ anniversary[12]. All necessary data reduction and calibration were performed by the Hubble Heritage Team prior to the data release (Mutchler et al., 2005). The final surface

[12]HST observing program, 10452; P.I Steven V. W. Beckwith

brightness of the images are given in units of electrons per second, es^{-1}, converted to flux density by the expression,

$$S_{\lambda_{\rm eff}} = C_{\rm es^{-1}} \cdot 3631 \cdot 10^{-[(AB_{\rm mag}-A)/2.5]}, \tag{5.4}$$

where, $F_{\lambda_{\rm eff}}$ is the flux density (in Janskys) at the effective optical wavelength, $AB_{\rm mag}$ defines the absolute physical flux density for a point source of 1 es^{-1} for a particular ACS filter (Sirianni et al., 2005), and A is the Galactic foreground colour magnitude extinction towards M51. The values of $AB_{\rm mag}$ and A for the different HST filters are listed in Table 5.7. The parameter $C_{\rm es^{-1}}$ is the total count of es^{-1} for the source in question, obtained via an aperture using the software package CIAO[13] (Fruscione et al., 2006) as part of the astronomical imaging and data visualization application SAOIMAGE[14] DS9. Here, the Johnson-Cousins *UBVRI* magnitudes are estimated from $F_{\lambda_{eff}}$ via the Spitzer magnitude/flux density online converter[15].

Table 5.7: Parameters of the HST ACS Filters

Filter	Colour	$\lambda_{\rm eff}$ (Å)	$AB^{*}_{\rm mag}$ (mag)	$A^{\dagger}$ (mag)
F435W	B	4450	25.67	0.125
F555W	V	5510	25.72	0.091
F814W	I	8060	25.94	0.053
F658N	Hα	6563	22.77	0.08

Notes.
*Sirianni et al. 2005; †Obtained from the NASA/IPAC Extragalactic Database

5.5 Discussion

5.5.1 Fraction of Sources Detected

Of the 107 radio sources detected in M51 by the Maddox et al. (2007) VLA survey, we report three confirmed detections. Similarly, of the 15 sources in the

[13]Chandra Interactive Analysis of Observations v4.5; `http://cxc.harvard.edu/ciao/index.html`

[14]`http://hea-www.harvard.edu/RD/ds9/site/Home.html`

[15]`ssc.spitzer.caltech.edu/warmmission/propkit/pet/magtojy/`

same region detected by the VLA FIRST survey (Becker et al., 1995), three were detected[16]. For a more realistic estimate of the proportion of detected sources we restrict ourselves to the catalogued sources that are bright enough to be detected above the 6.7σ threshold of the EVN observation. The catalogued flux densities were adjusted to 18 cm by using the spectral indices provided by the catalogues, and the sensitivity at the EVN phase centres were corrected for primary beam effects. This leaves 70 sources from the Maddox et al. (2007) VLA survey and 15 from the FIRST survey. Assuming no catalogued sources are resolved, the fraction of VLBI sources detected compared to the Maddox et al. (2007) and VLA FIRST surveys are 3/70 and 3/15, respectively.

Considering sources from the Maddox et al. (2007) survey not associated with HII regions, the detection rate is 3/32, while the VLBI detection rate for sources with peak flux density > 1 mJy in the (Maddox et al., 2007) survey is 2/5. The fraction of sources detected from the FIRST survey (3/15) and Maddox et al. (2007) sources with flux density > 1 mJy (2/5), closely agrees with the detection rates of previous wide-field VLBI surveys (e.g. Middelberg et al. 2011; Morgan et al. 2013; Middelberg et al. 2013). However, the fraction of Maddox et al. (2007) sources not associated with HII regions detected with VLBI (3/32) is significantly lower than the previous wide-field VLBI studies.

At 1.6 GHz, our observations would be less affected by free-free absorption compared to Maddox et al. (2007) 1.4 GHz observations (e.g Tingay 2004). It is likely that the majority of the radio sources in M51 detected by Maddox et al. (2007) are fully resolved at our VLBI resolution, suggesting perhaps either lack of compact radio emission from sources associated with stellar clusters or the expansion of supernova remnants (SNRs) beyond the maximum size detectable with our observations.

Maddox et al. (2007) estimated that the typical sizes for SNRs in M51 range between $0.3''$ and $0.5''$, (i.e. 12.2 - 20.4 pc). Considering the maximum source size resolvable with our observations is $0.14''$ ($\sim$6 pc; see Section 5.2.1), the non-detections are not surprising. Assuming an expansion velocity of 21,000 km s^{-1} for core-collapse supernovae in M51 (Weiler et al., 2011; Bietenholz et al., 2012) gives an age of 570 - 950 yr for the largest and 280 years for the smallest shell sources.

[16]Two sources were detected by both surveys - the core of M51 and source 3005+1035

5.5.2 The M51 Nuclear Region

5.5.2.1 A Faint Seyfert Radio Nucleus

The VLBI observation resolves the radio source at the nucleus of M51 into multiple components (2952+1142, Figure 5.9a). The main feature is a compact source (labelled C1) marginally resolved in the high resolution images (black contours), and unresolved in the 10 Mλ image. Located to the north of C1 are two weaker sources (labelled C2a and C2b), which are blended into a single, elongated structure that appears to be connected to C1 in the 10 Mλ image. Components C2a and C2b are unresolved sources with total flux densities of 51.5 $\pm$ 9.1 μJy and 54.6 $\pm$ 10.2 μJy, respectively. The separation of C2a and C2b from C1 are $\sim$ 41.5 mas ($\sim$ 1.69 pc) and $\sim$ 49.4 mas ($\sim$ 2.01 pc), respectively.

VLBI observations of a distance limited sample (<22 Mpc) of Seyfert galaxies, at 18 and 6 cm, have revealed similar structures to M51 within their nuclei (Giroletti and Panessa, 2009; Bontempi et al., 2012; Panessa and Giroletti, 2013). Here, the detected VLBI flux density is dominated by a high brightness temperature ($\log_{10}\mathrm{T}_B > 7.5$) parsec-scale source with a flat/intermediate spectrum ($0.3 \leq \alpha \leq 0.6$), accompanied by fainter, steep spectrum extended components. The flat/intermediate spectrum, high T_B sources are taken as evidence for non-thermal processes driven by jet-producing central engines typical of radio-quiet and radio loud quasars and AGNs (Bower and Backer, 1998; Doi et al., 2013).

Using the relation for brightness temperature, $\mathrm{T}_B = \frac{S(\nu)}{2k\theta_{\mathrm{maj}}\theta_{\mathrm{min}}} \left(\frac{c}{\nu}\right)^2$ (Bontempi et al., 2012), where: $S(\nu)$ is the flux density at frequency ν; k - the Boltzmann constant; θ_{maj} & θ_{min} are the major and minor deconvolved sizes in radians; and c is the speed of light, a value of $\log_{10}\mathrm{T}_B \sim 6.6$ is obtained for C1. Both the T_B and luminosity (10^{18} W Hz^{-1}) of C1 are within the typical range of values for low luminosity AGNs within Seyfert galaxies (Panessa and Giroletti, 2013). Therefore, components C2a and C2b are, most probably, hotspots associated with a jet or thermal outflow.

5.5.2.2 Previous VLBI observations

Bontempi et al. (2012) observed M51 with the EVN at both 18 and 6 cm and were unable to detect any emission above 3σ (75 and 160 μJy beam^{-1} at 18 and 6 cm, respectively). However, they searched within a 1$''$ radius centred on the VLA FIRST position RA = $13^{\mathrm{h}}\,29^{\mathrm{m}}\,52.804^{\mathrm{s}}$, Dec = $+47^{\circ}\,11'\,40.065''$, which would mean that the VLBI position in Table 5.5 was beyond their search field.

The raw, uncalibrated datasets for both observations (Experiment ID: EG037D and EG037C. PI: Giroletti) were obtained from the EVN data archive. Using the calibration tables generated by the EVN pipeline, both datasets were imaged as described in Section 5.3.1.

The core-jet structure was detected only in the 18 cm data at the expected position with a similar size, flux density and morphology as seen in the wide-field observation presented in Section 5.3.4. The non-detection at 5 GHz is attributed to the poor sensitivity of the observation (σ=50 μJy beam^{-1}), caused by the loss of Ef for 90% of the time due to high winds. Assuming a flat to intermediate spectrum ($-0.5 \leq \alpha \leq 0.5$), the expected flux density of 2952+1142 at 6 cm would be less than $3\sigma = 150$ μJy beam^{-1}.

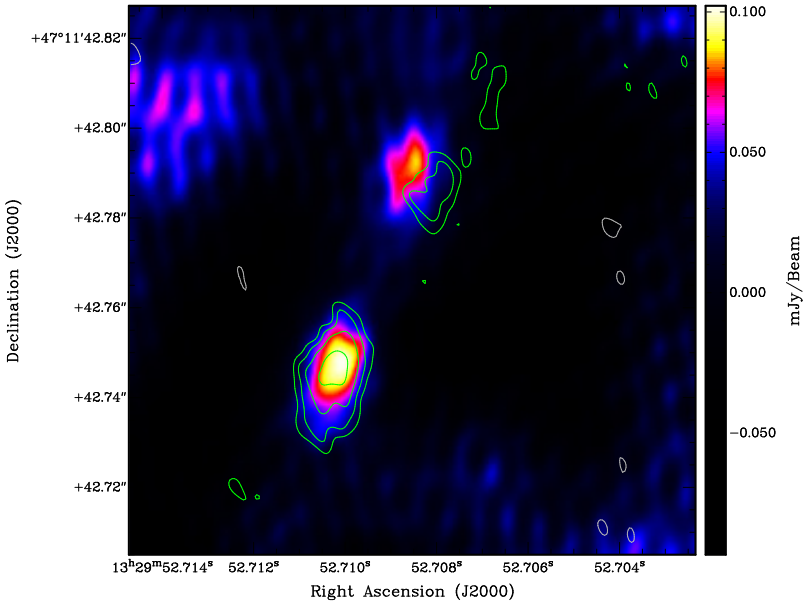

Figure 5.11: VLBI images of the Seyfert nucleus of M51 for the 2008 epoch (colour) with the Bontempi et al. (2012) dataset and the 2011 epoch (contours). Both epochs were imaged with a beam size of 18.5 mas × 11.0 mas with a P.A. = -3.71° . The RMS noise, σ in both images are 19.2 μJy beam^{-1} and 8.9 μJy beam^{-1} for the 2008 and 2011 images respectively. While the peak fluxes are 102.3 ± 21.0 μJy beam^{-1} (2008) and 84.7 ± 14.7 μJy beam^{-1} (2011). The first contours of the 2011 image are at $\pm 3\sigma$, and increase in multiples of $\sqrt{2}$. The offset in position of the low surface brightness structures between epochs is 7.53 mas. A third EVN observation has been requested to investigate the nature of this offset.

The images from both epochs (2008 and 2011) at 18 cm are compared in Figure 5.11, where the contours of the 2011 epoch are overlaid on the 2008 epoch

(colour image). A restoring beam of size 18.5 mas × 11.0 mas with a P.A. = -3.71° was used for the 2011 epoch so as to match the 2008 epoch. While the compact radio core is found at the same position in both epochs, the lower brightness compact source associated with a jet/thermal outflow shows an apparent lateral shift in position of 7.53 mas between epochs.

With a time difference of 3.69 years, and assuming that the difference in position results from motion within M51, gives a speed of 0.27c. Furthermore, the peak brightness of the jet/hotspot has decreased between epochs (80.2 μJy beam^{-1}, 2008; 44.2 μJy beam^{-1}, 2011), which may be associated with the apparent motion. Molecular aperture synthesis HCN observations of M51 by Kohno et al. (1996) reveals a twisted velocity field resulting from the existence of a dense rotating molecular disk that is aligned to the nuclear jet of M51, and the circular rotation of the galactic disk plane. However, the maximum velocity of this field (450-500 km s^{-1}) is too low to result in the apparent motion of the pc-scale jet. Furthermore, the direction of the apparent motion suggests that the jet may be precessing. While jet precession is not uncommon in radio bright AGNs (e.g Conway and Murphy 1993; Appl et al. 1996; Lu and Zhou 2005), it is yet to be observed for low luminosity Seyfert galaxies. In addition, outward proper motions have been observed (at the 3σ level) in the jets of the Seyfert galaxy NGC 5506 on pc scales (Middelberg et al., 2004). It is possible that the apparent motion could be the result of a combined effect of forward bulk motions of the jet interacting with the rotation observed by Kohno et al. (1996).

It is, however, possible that the position shift can be the result of systematic factors (e.g. poor calibration), since the hotspots displaying the apparent motions are $\sim$4σ detections. This is unlikely since the positions of the phase calibrator and C1 between both epochs were found to agree to within less than 1 mas. Whether this apparent motion is indeed intrinsic to M51 is difficult to ascertain with only two epochs. Therefore, a request has been made to observe the nuclear region of M51 with a third higher sensitivity observation with the EVN at 18 cm to determine whether this is indeed intrinsic to the parsec-scale jet of M51, the results of which will be discussed in a later paper.

5.5.2.3 A Multi-wavelength Perspective

Figure 5.12 shows the complex nuclear region of M51 with increasing resolution. The VLA-A image at 20 cm (resolution $\sim$1.08″) and the higher resolution MERLIN 18 cm images (resolution $\sim$0.34″) reveal an area of ring-like emission to

the north of the core (hereafter, the northern bubble) and a dense area of emission to the south, referred to as an extranuclear cloud (XNC), that may have resulted from interactions of a nuclear jet with the surrounding ISM (Crane and van der Hulst, 1992; Terashima and Wilson, 2001; Maddox et al., 2007). Maddox et al. (2007) measured peak flux densities for the nucleus at both 20 cm (2.08 mJy beam^{-1}) and 6 cm (1.14 mJy beam^{-1}), giving a moderately flat spectrum (α = -0.49). The MERLIN image shows the more compact regions where the ejecta are strongly interacting with the surrounding medium. Also shown in the image is a slightly extended source located $\sim$30$''$ ($\sim$1.22 kpc) from the nuclear radio source, which is discussed later in Section 5.5.2.5.

The radio emission from the nuclear region, including the XNC and the northern bubble, closely follows the X-ray observations from *Chandra* (Terashima and Wilson, 2001; Maddox et al., 2007). The X-ray spectrum of the nuclear source was found to be dominated by emission from cold plasma near the nucleus, indicating obscuration of the AGN by a column density of hydrogen atoms, $N_H > 10^{24}$ cm^{-1}. The AGN is only observed in hard X-rays (>10 kev) (Terashima and Wilson, 2001), with an X-ray luminosity of 1.1×10^{41} erg s^{-1}. The X-ray spectra of both the XNC and northern bubble are described by thermal plasma models, with the temperatures suggesting heating due to shocks (Terashima and Wilson, 2001).

High resolution 6 cm (Crane and van der Hulst, 1992) and 3 cm (Bradley et al., 2004) VLA observations of the nucleus reveals a narrow jet-like feature emanating from the nucleus and terminating in the XNC. [O III] line measurements of narrow line regions within the nuclear region, and along the direction of the narrow jet-like feature, find evidence for shock heating of the gas (Bradley et al., 2004) at the location of the XNC, indicating continuous fuelling of the XNC by the radio jet. However, no evidence has been found for shock ionisation in narrow line regions within the direction of the northern bubble (Bradley et al., 2004), suggesting the northern bubble may therefore be from a previous ejection cycle of the Seyfert nucleus of M51 (Crane and van der Hulst, 1992; Maddox et al., 2007). Interestingly, jet hotspots were detected with VLBI only in the direction of the northern bubble (components C2a and C2b). However, the VLBI image of the AGN core is slightly elongated in the direction of the southern jet, and may be the launching point for the jet.

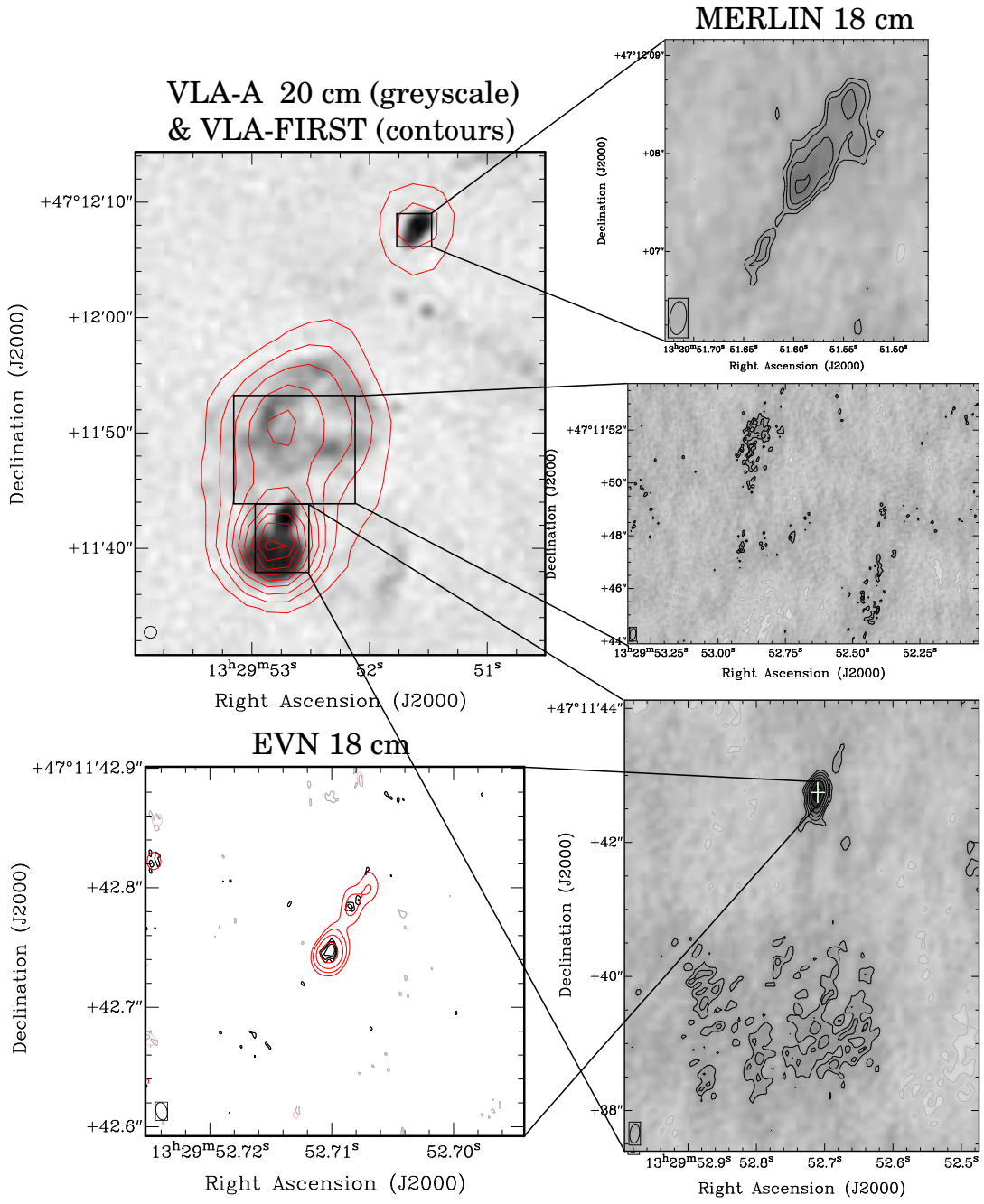

Figure 5.12: Increasing resolution of the nuclear region, XNC, northern bubble and a bright source located $\sim 30''$ ($\sim$1.22 kpc) from the core. *VLA*: VLA FIRST (20 cm) contours overlaid on a VLA-A grey-scale image. The bottom contours are at 15% the peak flux (11.49mJy beam^{-1}, and increase in increments of 10% the peak flux ; *MERLIN*: The first contours are at $\pm 3\sigma$, and increases in multiples of $\sqrt{2}$, where $\sigma = 50\mu$Jy beam^{-1}; *EVN*: see Figure 5.9a. The white cross indicates the location of the EVN source within the lower resolution images.

5.5.2.4 Estimating the Star Formation rate

The star formation rate (SFR) of a galaxy is directly proportional to its radio luminosity, L_ν at wavelength ν, assuming that all the radio emission is associated with star formation (Condon, 1992; Haarsma et al., 2000). An estimate of the flux density associated with star formation within the inner nucleus of M51 can be obtained by subtracting the compact VLBI components from the MERLIN data. A total flux density of 2.68 ± 0.14 mJy was recovered from the MERLIN 18 cm observation, and 0.25 ± 0.02 mJy from the EVN observation. Subtraction yields a flux density for the extended radio emission at 18 cm of 2.43 ± 0.14 mJy. However, there may be contributions to the extended emission from the jet components that were resolved by the EVN observations. Since this cannot be distinguished by the MERLIN observations, the flux density of the extended emission places an upper limit on the radio emission associated with star formation and hence the SFR

Using the standard relations given in Condon (1992), Haarsma et al. (2000), and Condon et al. (2002), along with the implied standard IMFs (Salpeter, 1955; Miller and Scalo, 1979), we derive an upper limit for the star formation rate of $SFR(M \geq 5\,M_\odot) < 0.044\,M_\odot \mathrm{yr}^{-1}$ (or $SFR(M \geq 0.1\,M_\odot) < 0.24\,M_\odot \mathrm{yr}^{-1}$) for the inner nuclear region of M51, which is ∼10% the total star formation rate of the entire galaxy (3.4 $M_\odot \mathrm{yr}^{-1}$) derived via infrared and ultraviolet observations (Calzetti et al., 2005).

5.5.2.5 Component N: a possible fossil radio lobe

The VLA and MERLIN images reveal an object located to the north of the core of M51 that was not detected in the EVN observations. The object, hereafter component N, was found to have a steep spectrum (α_{6cm}^{20cm} = -0.7) by Maddox et al. (2007, Source # 37), dominated by synchrotron radio emission, thus suggesting it is possibly a jet hotspot associated with the Seyfert nucleus of M51, a SNR or a background AGN.

The MERLIN 18 cm image in Figure 5.12 reveals a complicated structure, elongated in the direction of M51's Seyfert nucleus, atypical of SNRs. Moreover, the lack of detection of high brightness temperature emission with the EVN suggests it may be a background AGN whose core has either been scatter broadened or a background galaxy without a compact radio core. This is supported by the lack of X-ray emission associated with this object, since the interstellar medium of M51 may be absorbing the X-ray photons. A faint optical source (B mag =

23.1; I mag = 21.6) was found in the HST images to be coincident with the position of the peak radio surface brightness of component N, which may either be a star cluster or associated with the radio source. However, if component N is indeed a background AGN, it would require the unlikely scenario of being seen through the disk of M51 at a distance of 1.44 kpc from the Seyfert nucleus, with a structure aligned towards the core and having an optical source within M51 coincident with its peak surface brightness.

The method of estimating quasar alignment by Edmunds and George (1985) was used to determine the probability of a chance alignment of a background AGN within 30″ from the Seyfert nucleus of M51. Edmunds and George (1985) investigated the expected number of random alignments, Λ, in a field of area A, with a surface density of sources, κ for random clustered and unclustered fields and found it to be approximately,

$$\Lambda = \frac{2\pi}{3} p_{\max} d_{\max}^3 A \kappa^3, \tag{5.5}$$

where $d_{\max}$ is the distance between the two furthest sources, $p_{\max}$ is the distance between the outer two sources, such that the product $d_{\max} \cdot 2p_{\max}$ forms a rectangle enclosing all points of interest. The number density of quasars from the FIRST survey is ∼90 quasars per square degree (White et al., 1997) and the total area surveyed in this study is $11.2' \times 6.9'$. Thus, using Equation 5.5, $\Lambda \ll 1$ for the inner region of M51 i.e. $d_{\max} = 30''$ and $p_{\max} = 6''$. There is, therefore, a very low probability of a chance alignment within the central region of M51, suggesting that component N and the nucleus of M51 are most probably physically related. Thus, component N is most likely a jet hotspot associated with the Seyfert nucleus of M51.

However, with no evidence of a continuous jet in the northern region of M51, and the lack of X-rays, component N may be a fossil radio lobe associated with past AGN activity from the core of M51. Fossil radio lobes have been detected in a few radio galaxies such as 3C 388 (Jones and Preston, 2001; Gentile et al., 2007) and IC 2476 (Cordey, 1987), with a few "dying galaxies" with evidence for fossil radio lobes (e.g. Parma et al. 2007; Murgia et al. 2012). Radio lobes or hotspots are powered by energy from an AGN via jets of plasma. When the AGN undergoes a fading or dying stage, the jets and eventually the hotspots will expand adiabatically into the surrounding medium, and disappear due to the loss of the continuous production of plasma (Murgia et al., 2012). It is possible that this eventually leads to the loss of the high brightness temperature component,

leaving behind a diffuse shell.

5.5.3 Radio Supernovae

At the time of our observations, M51 had been the host to four optically observed supernovae (SNe): the Type Ia SN 1945A (Kowal and Sargent, 1971); the Type Ib/c SN 1994I (Puckett et al., 1994); the Type Ib/c SN 2005cs (Muendlein et al., 2005); and the Type IIb SN 2011dh (Griga et al., 2011). Of the four SNe, radio emission has been detected in only SN 1994I (Weiler et al., 2011) and SN 2011dh (Krauss et al., 2012; Bietenholz et al., 2012; Horesh et al., 2013), which will now be discussed.

5.5.3.1 SN 1994I

Almost a decade after the explosion, Maddox et al. (2007) detected radio emission from SN 1994I. However, no radio emission above the detection threshold of 50.0 μJy beam^{-1} was found in the VLBI images at the position of SN 1994I. Given that our observation was almost a decade from the Maddox et al. (2007) observation, it is possible that SN 1994I has faded below our sensitivity and/or expanded beyond the EVN's maximum resolvable size. Adjusting the 1.4 GHz flux density from Maddox et al. (2007) with a spectral index of -1.04 (Maddox et al., 2007), the peak flux density of SN 1994I at 1.65 GHz at the time of the Maddox et al. (2007) observation would have been 134.9μJy beam^{-1}. The SNe light curve model of Weiler et al. (2002) indicates that the flux density, S decreases with time following a power-law, $S \propto t_{age}^{\beta}$, where t_{age} is SN age and β=-1.42 for SN 1994I (Weiler et al., 2011). At the time of our observation (age of 6428 days) a 1.65 GHz peak flux density of 59.5 μJy beam^{-1} is estimated, which is just above our detection threshold. Furthermore, the expansion of SN 1994I has been well studied and follows the form 1.29(t_{age}/1 day) μas (Weiler et al., 2011), which estimates a size of 8.3 mas at the time of our observation. The estimates of size and flux density are just within the limits of our EVN observation, however as these estimates are model dependent it is not surprising that SN 1994I was not detected.

5.5.3.2 SN 2011dh

Our VLBI observations were conducted 159 days after the explosion date (2011 May 31, hereafter t_0) of SN 2011dh. The observations detect a compact un-

resolved source with a flux density of 4.306 ± 0.024 mJy at the position of SN 2011dh (source 3005+1010).

The position of our peak flux is offset from the VLBI positions reported by Martí-Vidal et al. (2011) at 22 GHz 14 days after t_0 and Bietenholz et al. (2012) at 8.4 GHz 179 days after t_0, by 1.9 mas and 2.3 mas, respectively. The positional measurements were obtained using the same phase reference source, with the same reference position. The offset in position with the higher frequency VLBI is less than half the synthesised beam of our 18 cm EVN observation.

With EVN observations at 8.4 GHz 179 days after t_0, Bietenholz et al. (2012) estimated the radius of the shock front of SN 2011dh to be 0.25±0.08 mas. The radius of the shock front was also estimated up to 92 days after t_0 via the radio spectral energy distribution, fitted to a synchrotron self-absorption (SSA) model (Krauss et al., 2012; Bietenholz et al., 2012). Combining the results of both observations, the radius of SN 2011dh, $r_{\rm 2011dh}$, is found to follow a power-law, given by $r_{\rm 2011dh} = 5.85 \times 10^{15} (t_{age}/30{\rm days})^{0.92}$ cm. At $t_{age} = 159$ days, $r_{\rm 2011dh} = 2.71{\times}10^{15}$ cm ≈ 0.11 mas, which is $< 1\%$ of the synthesised beam of our EVN observation.

SN 2011dh has been observed intensively with the JVLA across several frequency bands between 1.4 to 43 GHz (Krauss et al., 2012; Horesh et al., 2013) between $t_{age} = 4$ to $t_{age} = 93$ days after t_0. With a detection of SN 2011dh at 159 days after t_0, it may be possible to provide constraints to the light curve model of Horesh et al. (2013). Figure 5.13 includes the 4.9/5 GHz data from Krauss et al. (2012) and Horesh et al. (2013), with the 1.65 GHz flux density values determined via the spectral index between the 1.4 and 1.8 GHz flux densities at each epoch from Krauss et al. (2012). The lines are model fits to the light curves, which are described below.

The radio emission from a supernova (SN) arises through the interaction of the SN ejecta with the circumstellar medium (CSM) (Weiler et al., 1986, 2002). The resulting radio light curve is then a result of the competing effects from the declining non-thermal radio emission and the more rapid declining thermal (free-free) and non-thermal synchrotron self-absorption (SSA) as the ejecta propagates through the CSM. This relationship is generalised in a parametric model by Weiler et al. (2002), which allows for power-law variations in key quantities and can be written in the simplified form,

$$S = K1 \left(\frac{\nu}{5\,{\rm GHz}}\right)^{\alpha} \left(\frac{t_{age} - t_0}{1\,{\rm day}}\right)^{\beta} \left(\frac{1 - e^{\tau_{\rm opt}}}{\tau_{\rm opt}}\right) {\rm mJy}, \tag{5.6}$$

where α describes the frequency dependency (or spectral index), $K1$ is a scaling factor and is related to the flux density at 5 GHz 1 day after the explosion, and β describes the power-law dependency of the flux density with the SN age, $t_{\rm age}$ (Weiler et al., 2002). The absorption term, $\tau_{\rm opt}$, describes an internal absorption by material mixed with the emitting component, which assumes a planar geometry (Weiler et al., 2002; Horesh et al., 2013). Both the early light curve ($t < 15$ days) and the radio spectra ($t < 93$ days) were found to be consistent with absorption due to SSA (Krauss et al., 2012; Horesh et al., 2013). The absorption mechanism in Equation 5.6 is therefore taken to be of the non-thermal SSA form and is defined by the optical depth, $\tau_{\rm opt}$, given as,

$$\tau_{\rm opt} = K5 \left(\frac{\nu}{5\,{\rm GHz}}\right)^{\alpha-2.5} \left(\frac{t_{\rm age} - t_0}{1\,{\rm day}}\right)^{\delta}, \tag{5.7}$$

where $K5$ is the optical depth 1 day after the explosion and δ describes the power-law dependency of $\tau_{\rm opt}$ with the SN age, $t_{\rm age} - t_0$ (Weiler et al., 2002).

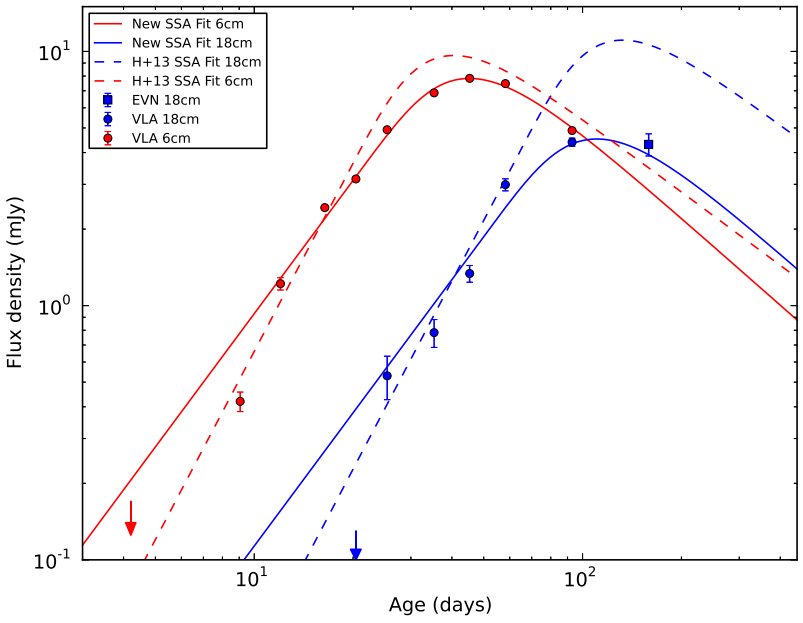

Figure 5.13: Light curve of SN 2011dh at 5 GHz (red points) and 1.65 GHz (blue points). The 5 GHz flux density was obtained from the JVLA (Krauss et al., 2012; Horesh et al., 2013), while the 1.65 GHz comprised data from the JVLA (blue circles) and the EVN observation (blue square) from this study. The lines are non-linear least-square fits to Equation 5.6, from this study (solid lines) and from Horesh et al. (2013, dashed lines). The arrows are upper limits on the flux density from Horesh et al. (2013) obtained with the JVLA at these times.

The dashed lines in Fig 5.13 are the model using Equation 5.6 derived by Horesh et al. (2013), using 22.5 GHz JVLA data for $t < 15$ days. While the model from Horesh et al. (2013) is a better fit to the observed data for the early rise of the light cure, it clearly over-estimates the flux density for the later times. Using the 4.9/5 GHz data, a new SSA model fit to the light curve was obtained for Equation 5.6, which provides a better overall fit to the observed data. The resulting parameters were then used to determine the model light curve at 1.65 GHz. The resulting fit parameters are α = -1.30, β = -1.14, δ=-2.88, $K1$ = 928.5 mJy, and $K5$= 5.5$\times$ 10^4 and are displayed in Figure 5.13 (the solid lines).

The difference between the model fits can be explained through their estimates of $\tau_{\rm opt}$, which are displayed in Figure 5.14. At the early stages of the SN expansion, the CSM is optically thick ($\tau_{\rm opt} \gg 1$) and gradually becomes optically thin ($\tau_{\rm opt} \leq 1$) as the SN expands into the surrounding ISM (Weiler et al., 2002), coinciding with the emission of the peak radio brightness. Furthermore, the time at which the medium becomes optically thin is dependent on the frequency of emission. Thus, in deriving the model fit using the 22.5 GHz data, Horesh et al. (2013) underestimated the optical depth (Figure 5.14, blue dashed lines) and, therefore, the attenuation of the flux density at the lower frequencies.

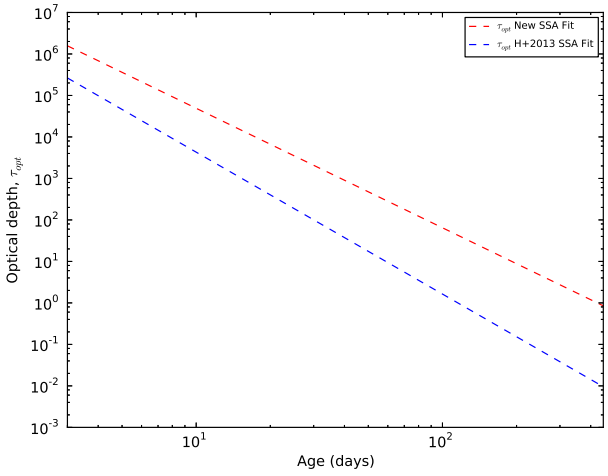

Figure 5.14: SSA optical depth, τ_{opt}, obtained via Equation 5.7 using the parameters by Horesh et al. (2013), (blue dashed lines) and this study (red dashed lines) at 1.65 GHz.

5.5.4 Background Radio Sources

5.5.4.1 3011+1041

Radio/X-ray Correlation. The radio source 3011+1041 was detected with the VLA at both 20 cm (500±22 μJy beam^{-1}) and 6 cm (482±50 μJy beam^{-1}) by Maddox et al. (2007), giving a flat radio spectrum (α = -0.03). Comparing the radio position with archived *Chandra* X-ray data, they found a 10^{37} ergs s^{-1} counterpart, making it the brightest X-ray/radio overlap in their survey. However, no Hα emission was found at the source position from the HST ACS archive, leading Maddox et al. (2007) to suggest that 3011+1041 may be a microquasar in a radio-loud state during the time of the VLA observations. If indeed this source is a microquasar, its luminosity at 5 GHz would be a factor of two more luminous than the most luminous one discovered to date (GRO J1655-40: Hjellming and Rupen 1995, Tingay et al. 1995).

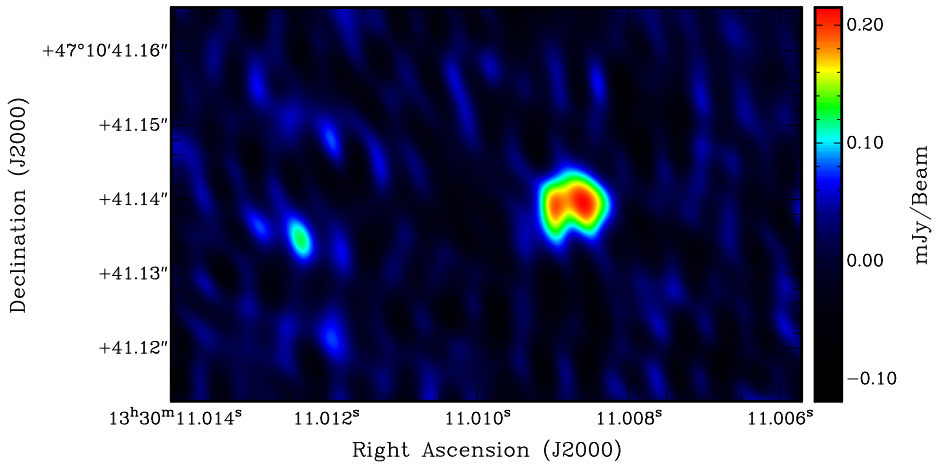

Figure 5.15: A higher resolution EVN image of 3011+1041 made with Briggs robustness = 0, cellsize of 0.1 mas. Beam size = 6.23 mas × 3.19 mas, position angle = 13.7° and image RMS = 21.9 μJy beam^{-1}.

The VLBI image (Figure 5.9d) reveals a compact, relatively unresolved source with a total EVN flux density (see Table 5.5) matching the VLA flux density within measurement errors. Since there is little or no extended emission resolved by our VLBI observations, the radio emission seen with the VLA and EVN is emanating from the same compact region, a few mas in size. Re-imaging the VLBI data with a higher resolution by setting the Briggs robust parameter to 0 and adopting a cellsize of 0.1 mas, reveals a double morphology, resembling a core-jet structure typically seen in radio galaxies or AGN. The resulting image

is shown in Figure 5.15, with the peak surface brightness of the components of 270 μJy beam^{-1} and 233 μJy beam^{-1}, separated by 4.3 mas. To the east of the double, at a distance of 38.6 mas from the brightest component of 3011+1041, is a weak unresolved source with peak surface brightness of 123 μJy beam^{-1} that may be a jet hotspot related to 3011+1041.

The radio and X-ray luminosity of microquasars, such as GRO J1655-40, are variable over time as the systems change from jet-dominated to a disk-dominated states (see Fender et al. 2004 for a discussion of the states and their transitions). Furthermore, the radio and X-ray flux densities have been shown to follow a tight correlation of the form $S_{\rm X} \propto S_{\rm R}^{0.62}$, which is thought to be due to a non-linear coupling between the jet and the inner accretion flow for stellar mass black holes (Fender et al., 2004; Corbel et al., 2013). Figure 5.16 plots the radio light-curve for 3011+1041 taken from archival data as described in Section 5.4.1, and the X-ray light curve from data obtained from the *XMM-Newton* and *Chandra* archive (R. Soria, private communication). It is clear that the emission in both radio and X-rays display variability (within a factor of 5), with a possible correlation near the rise of the X-ray flux. However, the lack of simultaneous radio and X-ray measurements makes it difficult to test the radio/X-ray correlation. It is also possible that the non-detection with MERLIN at 1.6 GHz (black arrow) hints toward a possible quenching of the radio due to jet suppression, typically seen during the X-ray outburst of microquasars (Fender et al., 2004).

The X-ray Spectrum. Figure 5.17 shows the combined X-ray spectrum of the six *Chandra* observations used in Figure 5.16 via CIAO and the X-ray spectral fitting package XSPEC[17] (Arnaud, 1996) (R. Soria, private communication). The spectrum is fitted with a simple power-law (red lines) with a low line-of-sight column density, $N_H = 2 \times 10^{20}$ cm^{-1}, photon index[18] $\gamma = 1.8^{+0.4}_{-0.2}$, and an average flux $S_{\rm X}$ (2-10 keV)=9.7$\times$10^{-15} ergs s^{-1} cm^{-2}. The spectrum is dominated by a soft X-ray component and lacks a hard X-ray component which suggests either a suppression of jet production (Fender, 2001) in microquasars/X-ray binaries or a spectrum consistent with a low-luminosity AGN (Nandra and Pounds, 1994; Terashima and Wilson, 2003; Civano et al., 2011).

Since there is evidence for a jet-like structure in the EVN image (Figure 5.15), there may be insufficient gas surrounding the core to allow interaction of the jet to produce shocks that are visible in the X-rays. Moreover, jet-suppression in

[17] heasarc.gsfc.nasa.gov/docs/xanadu/xspec/index.html

[18] γ is related to the spectral index, α commonly used in radio astronomy by $\gamma = 1+\alpha$, where, $S \propto \nu^{-\alpha}$

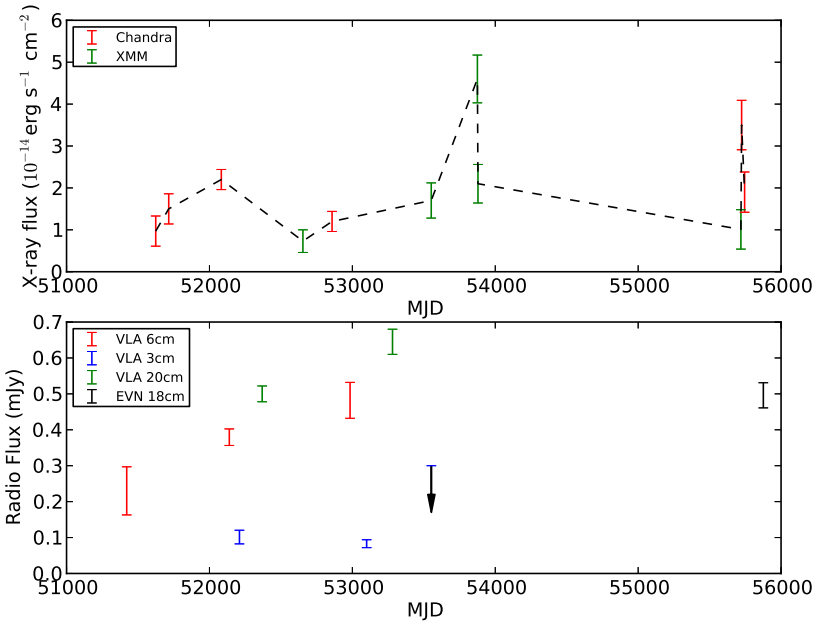

Figure 5.16: Radio and X-ray flux densities plotted against observed time (in Modified Julian Date, MJD). The measurements for the VLA and MERLIN radio flux densities were obtained from the literature (Maddox et al., 2007) and imaging of archive VLA, MERLIN data described in Section 5.4.1. The X-ray measurements were taken from the *XMM-Newton* X-ray satellite archive and *Chandra* X-ray archive (Observation ID: 12562 [PI: Pooley]; 12668 [PI: Sodeberg]; 3932 [PI: Terashima]; 13812-13816, 15496 & 15553 [PI: Kuntz])(R. Soria, private communication).

microquasars/X-ray binaries is associated with a reduction in the radio emission (Fender, 2001), which is not observed for this source.

Optical/X-Ray. The ratio between X-ray and optical luminosity is considered to be a reliable indicator of X-ray source classification (Comastri, 2004). The relationship is defined as (see Maccacaro et al. 1988; Barger et al. 2002; McHardy et al. 2003):

$$\log_{10}(S_{\rm X}/S_{\rm opt}) = \log_{10} S_{\rm X} + 5.5 + R_{\rm mag}/2.5, \tag{5.8}$$

where $S_{\rm opt}$ is the optical flux (in cgs) and $R_{\rm mag}$ is the Johnson-Cousins R-band magnitude. The distribution of $\log_{10}(S_{\rm X}/S_{\rm opt})$ for spectroscopically identified X-ray AGN from ROSAT (Hasinger et al., 1998), ASCA (Akiyama et al., 2003), Chandra (Giacconi et al., 2001) and XMM-Newton (Mainieri et al., 2002; Fiore et al., 2003) surveys fall within -1$<$ $\log_{10}(S_{\rm X}/S_{\rm opt}) < 1$, while for stellar mass sources, such as x-ray-binaries and microquasars, $\log_{10}(S_{\rm X}/S_{\rm opt}) > 10$.

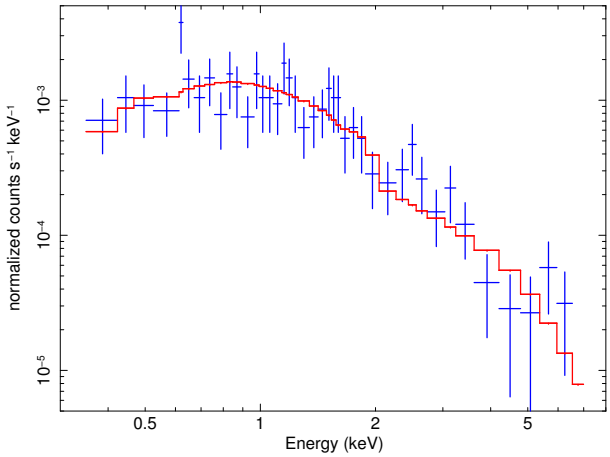

Figure 5.17: X-ray spectrum, in normalized photon counts of 3011+10.41 (blue crosses), from combining the six *Chandra* images used in Figure 5.16. The red line plots the best fit power-law to the spectrum (see text for details). Image courtesy: R. Soria, Private communication.

Since the HST lacks an R-band filter, to estimate the $R_{\rm mag}$ of 3011+1041, the fluxes of the HST B, V and I bands were first estimated as described in Section 5.4. The R-band flux (10.26 μJy) was calculated via a non-linear least squares fit to the flux densities of the B, V and I bands, from which a value of 21.1 for $\rm R_{mag}$ was determined. Substituting the values into Equation 5.8 results in $\log_{10}(S_{\rm X}/S_{\rm opt})$ = -0.03, indicating that 3011+1041 is likely a background AGN.

Radio Loudness and AGN Classification. Since 3011+1041 is classified as a background AGN based upon the optical and X-ray flux ratios, we can classify the AGN type from its radio loudness parameter, R_L defined as (Terashima and Wilson, 2003; Ho, 2008),

$$R_L = \frac{\nu S_\nu(5\ \text{GHz})}{S_X(2-10\ \text{kev})}. \tag{5.9}$$

Substituting S_ν(5 GHz) = 482 μJy and S_X(2-10 kev) = 9.7 $\times$ 10^{-15} ergs $\rm s^{-1}$ $\rm cm^{-2}$, gives $\log_{10}(R_L) \sim$ -2.5. 3011+1041 therefore, falls within the region of radio-loud radio galaxies, Seyferts and low-luminosity AGNs (see Figure 4 of Terashima and Wilson 2003 and Figure 10 of Ho 2008).

5.5.4.2 3005+1035

The radio source 3005+1035 is resolved into four components with the EVN at 18 cm (Figure 5.9b), where the components are labelled C1 to C4 in order of decreasing peak surface brightness.

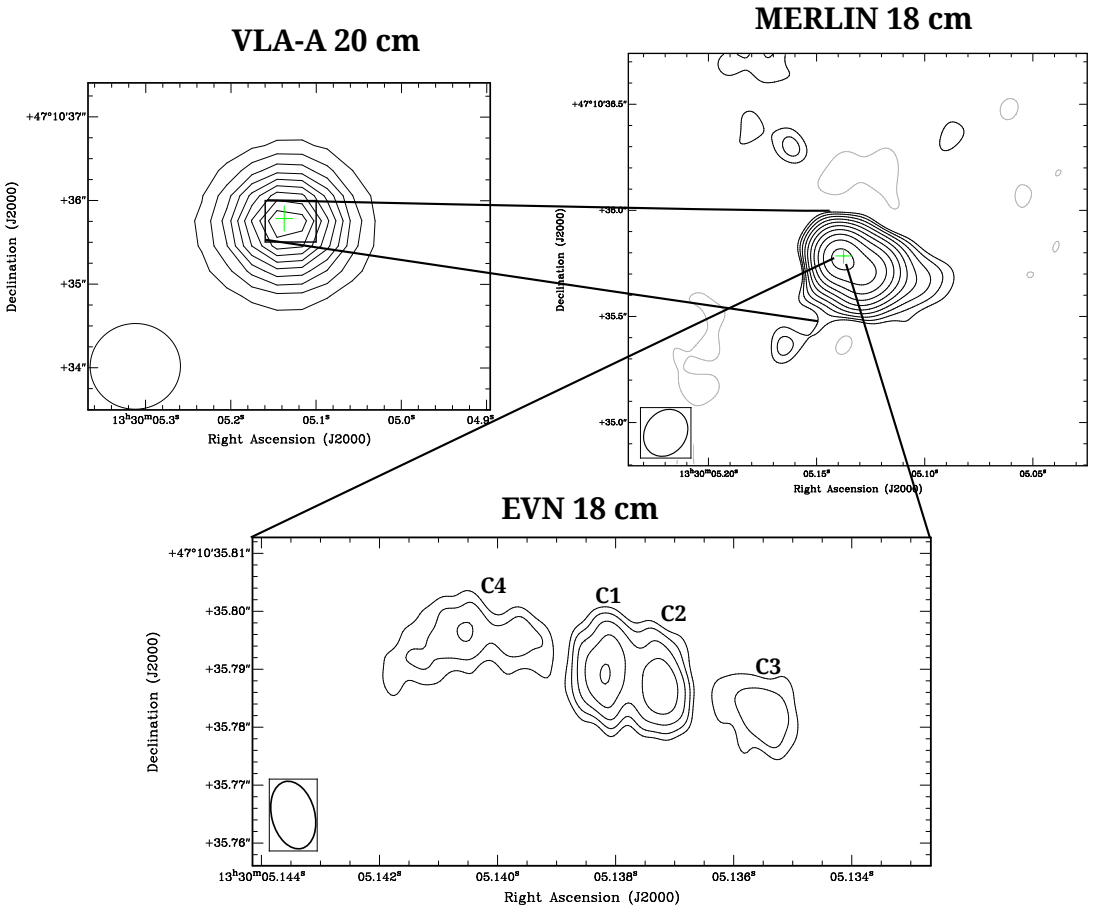

Figure 5.18: Radio images of the radio source 3005+1035. *VLA-A*: Contours begin at ±10% the peak flux density (11.8 mJy beam^{-1}), and increases in increments of 10% of the peak flux density. *MERLIN*: Image was made with the full MERLIN array (i.e. including the long baselines to Cambridge), which resulted in a beam size of $0.196'' \times 0.164''$. The contours begin at $\pm 3\sigma_{\rm image}$ and increase with multiples of $\sqrt{2}$, where $\sigma_{\rm image} = 60.3$ μJy beam^{-1}. *EVN*: The image is a zoomed in version of the one shown in Figure 5.9b, where C1 - C4 are the different components, labelled in order of decreasing peak surface brightness. The green crosses mark the position of C1, which is the peak flux density in the VLBI image.

Table 5.8 lists the different properties of the four components, including the position of the peak surface brightness, peak and total flux densities, size of the component's major axis and brightness temperature. For reference, C1 is taken as the core of 3005+1035. The VLBI morphology of 3005+1035 shows evidence

for a two-sided jet emanating from an active nucleus. However, without higher frequency VLBI observations it is difficult to determine which is the core that hosts the active nucleus. The similarity of both C1 and C2, in terms of size, flux density and brightness temperature suggests that they are, most probably, radio lobes/hotspots resulting from jets emanating from an unresolved, fainter active nucleus.

Table 5.8: VLBI DETECTED COMPONENTS OF 3005+1035

	Position of S_P						
VLBI	RA	Dec	Θ_{C1}	S_P	S_I	B_{maj}	$\log_{10}$ T_B
Source	(13^h30^m)	($47^\circ\,10'$)	(mas)	(μJy beam^{-1})	(μJy)	(mas)	(K)
(1)	(2)	(3)	(4)	(5)	(6)	(7)	(8)
C1	5.1381415	35.789622	0	211.7±25.6	457.2±65.2	12.8	6.26
C2	5.1372858	35.787308	9.72	199.8±24.6	414.0±59.1	10.98	6.34
C3	5.1355557	35.782491	27.5	99.1±17.3	313.0±65.3	14.65	5.98
C4	5.1404641	35.794635	24.2	91.8±16.6	650.2±128.6	32.03	5.61

Notes.
(1) VLBI component defined in Figure 5.18; (2) & (3) VLBI source position; (4) Angular separation of the S_P of each component from the S_P of C1; (5) Peak flux density; (6) Integrated flux density; (7) Size of the major axis from IMFIT; (8) Brightness temperature at ν MHz derived from the Rayleigh-Jeans formalism: $(c^2 S_I)/(2\pi B_{\rm maj} k \nu^2)$, where c is the speed of light and k the Boltzmann constant.

In lower resolution radio maps of M51 with the VLA and MERLIN, 3005+1035 is the brightest radio source in the M51 system. Figure 5.18 shows the VLA-A 20 cm and MERLIN 18 cm maps in relation to the EVN 18 cm map (represented by the green crosses). In the FIRST survey the source is unresolved at 20 cm with a total flux density of 12.64 ± 0.14 mJy, while at higher resolution VLA-A, a total flux density of 13.38 ± 1.50 mJy is recovered from the unresolved 20 cm VLA-A image in Figure 5.18. This is similar to the peak flux density obtained by Maddox et al. (2007): 9.6 mJy beam^{-1} at 20 cm and 4.3 mJy beam^{-1} at 6 cm, giving an intermediate spectral index of −0.66. The MERLIN 18 cm image displayed in Figure 5.18 shows an elongated structure, closely resembling the one-sided core-jet morphology of AGNs and quasars on kpc-scales (Bridle and Perley, 1984). The total flux density as measured (via BLOBCAT) from the MERLIN image is 9.95 ± 1.00 mJy, recovering ∼ 80% of the flux density of the VLA-A at 18 cm (after correcting the 20 cm flux density with a spectral index of -0.66). Subtracting the total VLBI flux density listed in Table 5.8 from the MERLIN 18 cm flux density gives 8.12 ± 1.01 mJy, which may result from thermal and

non thermal emission from star formation and non-thermal emission from kpc-scale jets.

No counterparts were found in the HST and Chandra images corresponding to the position of 3005+1035. This is not unexpected considering that it is viewed through one of the spiral arms of M51, in a region with a high density of star clusters.

5.5.4.3 3016+1024

VLA-A 20 cm observations of the radio source 3016+1024 shows a morphology (see Figure 5.19) similar to nearby powerful FR II radio galaxies such as Cygnus A (Carilli and Barthel, 1996) and Pictor A (Perley et al., 1997), displaying the morphological components common to these type of galaxies. These sources are composed of a compact, high surface brightness temperature, typically flat spectrum source at the centre, from which elongated radio jets end in high surface brightness hotspots (Carilli and Barthel, 1996).

The source was detected as a partially resolved double radio source in the FIRST survey with total flux densities of 12.56±0.63 mJy and 11.67±0.58 mJy for the southern and northern lobes, respectively. The higher resolution VLA-A 20 cm image resolves the double sources into two radio lobes and a central radio source, with evidence for elongated radio jets ending in hotspots at the extremities of the radio lobes. The VLA-A image recovered 82% and 71% of the FIRST flux of the southern and northern lobes, respectively. The central source was found to have a total flux density of 2.15±0.04 mJy at 1.4 GHz and 0.98±0.01 mJy at 5 GHz (VLA-B 5 GHz data listed in Table 5.6), giving a spectral index of -0.62.

The central radio source is unresolved with the higher resolution MERLIN 18 cm observations, with total flux density of 0.97±0.14 mJy. However, there is evidence for low surface brightness emission ($\sim$150 μJy beam^{-1}) along the direction of the southern lobe/jet (see Figure 5.19), and at the location of the peak VLA-20 cm surface brightness component of the northern lobe (not shown in Figure 5.19). The VLBI observation only detects the central radio source, showing a slightly elongated structure extending from the compact source in the direction of the southern jet, suggesting that the southern jet/lobe may be relativistically beamed towards our line of sight. From the total flux density and major axis size of the central source we obtain a brightness temperature of $\log_{10}$ T_B = 7.1, typical of AGN (e.g. Bower and Backer 1998; Ulvestad et al. 2005).

In the standard FR I/FR II classification model (Fanaroff and Riley, 1974)

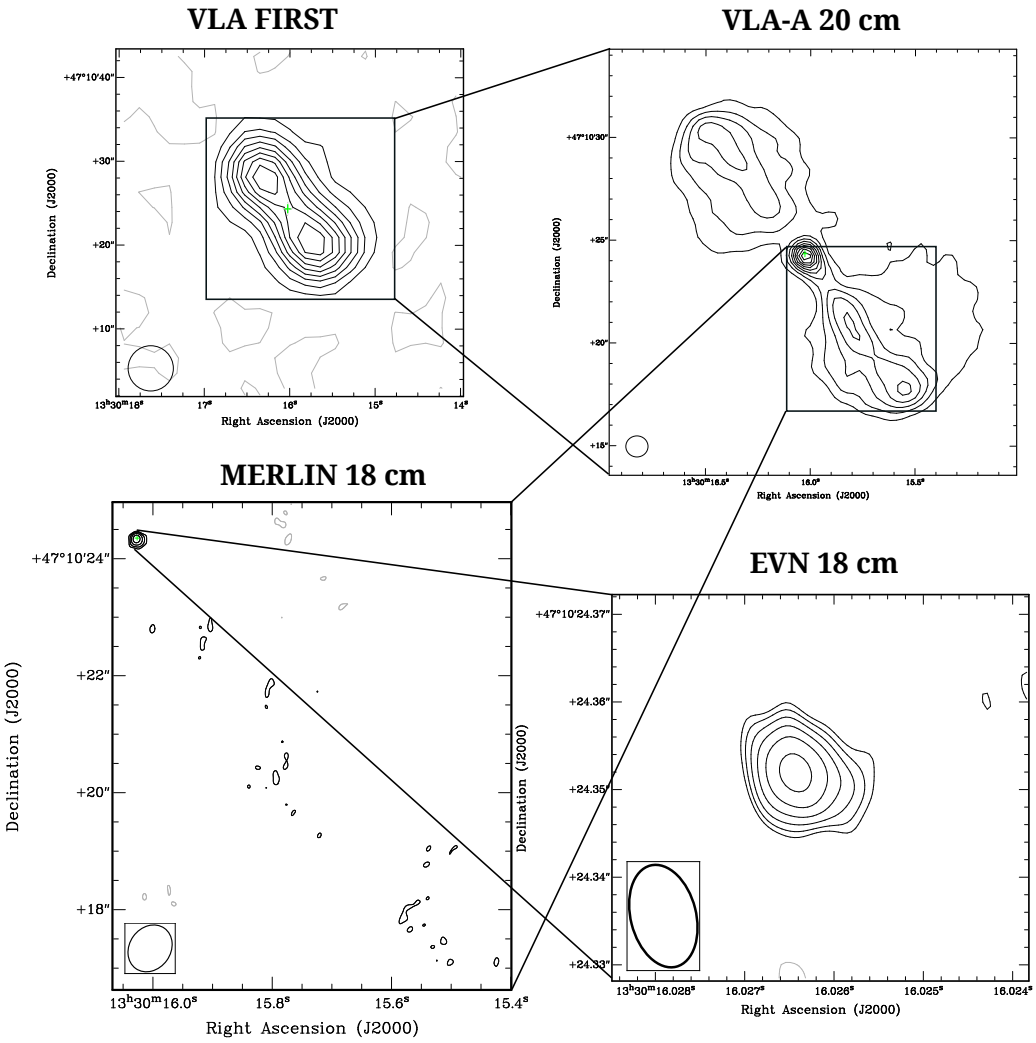

Figure 5.19: Radio images of the source 3016+1024. *VLA*: the contours of both the FIRST and VLA-A images begin at ±10% the peak flux density (6.02 mJy beam^{-1}& 0.982 mJy beam^{-1}, respectively), and increases in increments of 10% of the peak flux density. *MERLIN*: the first contours are at $\pm 3\sigma$, and increases in multiples of $\sqrt{2}$, where $\sigma = 50\mu$Jy beam^{-1}; *EVN*: a zoomed in version of the one shown in Figure 5.9f. The green crosses indicates the location of the EVN source within the lower resolution images.

both types of radio sources can be divided by radio luminosity, where the dividing luminosity is 10^{25} W Hz^{-1} at 1.4 GHz (below lies the FR I and above the FR II galaxies). Based upon the morphology shown in Figure 5.19, it is possible to classify 3016+1024 as an FR II galaxy. Assuming a minimum luminosity of 10^{25} W Hz^{-1}, and with a total flux density at 1.4 GHz of 2.15 mJy, 3016+1024 would be at a minimum distance of $\sim$ 6246 Mpc ($z \geq 0.95$). Note, placing Cygnus A

at 6246 Mpc would result in a total flux density ∼5 mJy at 1.4 GHz[19].

From the Sloan Digital Sky Survey (SDSS) Data Release 9 (Ahn et al., 2012), an optical source was found to be coincident with the position of the central radio source of 3016+1024. The R-band optical data were obtained through the SDSS Science Archive Server in the "corrected frame" format, which have been calibrated in nanomaggies[20] per pixel, and have had a sky-subtraction applied. Using the software package CIAO (see Section 5.4.2) a total flux density of 13.11 nanomaggies or 47.6 μJy is obtained, which is equivalent to an R_{mag} of 19.5.

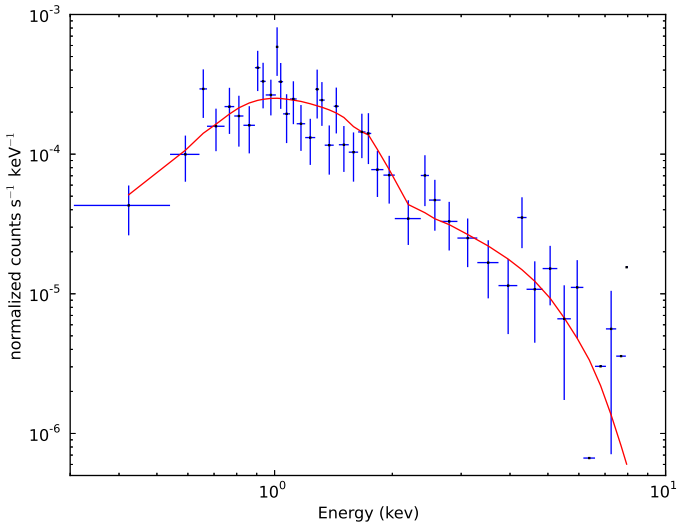

Figure 5.20: X-ray spectrum, in normalized photon counts of 3016+1024 (blue crosses), from combining ten *Chandra* images obtained from the archive database. The red line plots the best fit power-law to the spectrum (see text for details). Image courtesy: R. Soria, Private communication.

The VLA 1.4 GHz radio contours were overlaid on a *Chandra* X-ray map of the M51 system (R.Soria private communication), showing an X-ray source coincident with the position of the central radio source of 3016+1024. A combined X-ray spectrum was derived using 10 epochs obtained from the *Chandra* X-ray archive (listed in Figure 5.17) and the X-ray spectral fitting package fitting package XSPEC (Arnaud, 1996). Figure 5.20 presents the X-ray spectrum fitted with a simple power-law (red lines) with a low line-of-sight column density towards M51, N_H

[19] Assuming the Flux density of Cygnus A is $S_{1.4\mathrm{GHz}} = 1598$ Jy at a distance of 247.2 Mpc (Bîrzan et al., 2004).

[20] A star of brightness 1 nanomaggie has a magnitude of 22.5 in any band, or a flux density of 3.631 μJy. (www.sdss3.org/dr9/help/glossary.php)

$= 1.8 \times 10^{20}$ cm^{-1}, photon index, $\gamma = 1.97^{+0.x}_{-0.x}$ and an average flux, $S_{\rm X}$ (0.3-10 keV)=4.6 $\times$ 10^{-15} ergs s^{-1} cm^{-2}. The spectrum is dominated by a soft X-ray component consistent with an AGN (Nandra and Pounds, 1994; Terashima and Wilson, 2003; Civano et al., 2011). Using Equation 5.9, 3016+1024 is found to have a radio loudness parameter, R_L = -1.97, placing it in the regime of radio loud radio galaxies (see Figure 4 of Terashima and Wilson 2003 and Figure 10 of Ho 2008).

5.5.4.4 2932+1123

While 2932+1123 is not the weakest VLBI source in our sample, it has the lowest S/N ratio (see Table 5.5) which results from a high RMS noise due the source's position at the edge of the primary beam of Ef[21]. Its positional offset in RA is $3.49'$ and $19.6''$ in Dec from the M51 centre placing it at the edge of the M51 disk and beyond the survey area of Maddox et al. (2007). At the VLBI position of 2932+1123, a radio source is detected in the VLA-A 20 cm image with a peak flux density of 237$\pm$49 μJy beam^{-1}, however no corresponding source was found in the VLA-B 6 cm image above 60 μJy beam^{-1} (five times the image RMS given in Table 5.6), suggesting the source is a steep spectrum source ($\alpha < -1.10$, $S \propto \nu^{\alpha}$). No counterparts were found in any of the X-ray or optical archives used in this study, which may be due to its location beyond the disk of M51, at the edge of many telescopes' pointing centre, where the sensitivity is poor. However, given its location it is possible to classify this object as a background source, possibly an AGN.

5.6 Summary

The results of the deepest, widest VLBI survey of a nearby grand design spiral galaxy are presented. The target for our study was the Whirlpool galaxy (M51, NGC 5194), that is undergoing a merger with its smaller companion, NGC 5195. To attempt to understand the nature of this system, we made use of a wealth of multi-wavelength ancillary data from radio, optical and X-ray observatories. Furthermore, this study was the first to successfully image the primary beam of a heterogeneous VLBI array. The data were obtained through the various online

[21]Recall that the sensitivity reduces with increasing distance from the pointing centre due to primary beam effects. See Sects. 2.4.3 and 2.5.3.

archive databases or via private communications from collaborators. Below the main findings of this study are summarised:

1. A total of six sources were found within a region of $11'.2 \times 6'.9$, where two are identified as belonging to M51 and the remaining four as background AGNs;

2. All six sources were found to have counterparts in one or more lower resolution radio surveys of the M51 system;

3. Our VLBI observations detect a pc-scale, core-jet structure associated with the Seyfert nucleus of M51;

4. Comparison with an archived EVN observation, of the M51 nuclear region, taken 3.69 years previously, reveals a possible positional shift of the parsec-scale jet corresponding to 0.27c;

5. A star formation rate of $SFR(M \geq 5\,M_{\odot}) < 0.044\,M_{\odot}\,\mathrm{yr}^{-1}$ (or $SFR(M \geq 0.1\,M_{\odot}) < 0.24\,M_{\odot}\,\mathrm{yr}^{-1}$) was estimated for the inner nuclear region of M51;

6. Using archival MERLIN 18 cm data, a bright elongated, steep spectrum source is detected 1.22 kpc from the core of M51. Based on the results from VLA 20, 6 and 3 cm data, including the non-detection in the X-ray, we suggest that this source may be a fossil radio lobe associated with the Seyfert nucleus of M51;

7. Using a combination of multi-wavelength radio observations, X-ray and optical data, the nature of the background AGNs were studied in detail;

8. The Type IIb supernovae, SN 2011dh was imaged at 18 cm, 159 days after the date of explosion. Combining the results from this study with those from the literature, an improved model of the radio light curves at 6 cm and 18 cm was derived. Differences between previous models are attributed to an underestimation of the optical depth of the CSM;

9. A VLBI detection rate of 3/15 VLA FIRST sources was found to be consistent with previous wide-field VLBI studies, however, the VLBI detection rate of 3/32 sources from the Maddox et al. (2007) survey is significantly lower than the other wide-field VLBI studies. We attribute the lower detection rate as being due to either these sources are either star clusters that

lack high brightness temperature components or an expansion of supernova remnants beyond our maximum detectable size;

10. Assuming a typical expansion rate of 21,000 km s^{-1} for core-collapse supernovae in M51 gives an age of 570 - 950 yr for the largest and 280 years for the smallest shell sources in M51.

6 Conclusions

6.1 Thesis Summary

This thesis reports on three different applications of the technique of wide-field VLBI: (i) a proof of concept study, that investigated the use of high frequency resolution VLBI to be used for targeted SETI; (ii) an investigation into the interstellar medium and supernova history of the nearby starburst galaxy NGC 253 using multi-epoch wide-field VLBI observations; and (iii) using a heterogeneous VLBI array to perform the widest, deepest, and highest resolution study of the compact radio source population of a nearby face on star-forming galaxy, M51. The results of these studies are briefly summarised as follows.

6.1.1 The First VLBI SETI Experiment

By utilising the fundamental properties of VLBI, this study demonstrated that VLBI is well suited for targeted SETI surveys. With N antennas separated by hundreds to thousands of kilometres resulting in $N(N-1)/2$ independent baselines, VLBI provides an efficient discriminator between targeted SETI and RFI signals. Furthermore, the high astrometric capabilities of VLBI allow localisation (with respect to the phase centre) of a signal through the measurements of its phase variations with time and frequency. Thus, a planet with a radio-emitting civilisation will display characteristic phase variations that are related to the location of the planet relative to the host star, assuming that the star is at the phase centre.

The technique was tested on a three antenna LBA observation (maximum resolution = 127 mas) of the Gliese 581 system, located 20 light years away and host to two habitable planetary candidates. The maximum distance of the

planets from Gliese 581 star is ∼66 mas, thus any signal emanating from any of the planets will display phase variations with time and frequency that are effectively zero at the resolution, limited bandwidth and integration time of this experiment. The observations were conducted between 1230 MHz and 1544 MHz, separated into six sub-bands of 64 MHz bandwidth. To produce the high spectral resolution required of SETI experiments, the DiFX software correlator was used to generate 32768 channels over each 64 MHz sub-band. The ratio of frequency resolution to bandwidth of this experiment was to date the highest for any VLBI experiment and required development of new techniques to process the data and search for the desired signals.

Candidate signals were selected based upon the following criteria: (i) amplitude greater than five times the baseline sensitivity; (ii) detected on all baselines. Both narrow-band and broad-band events satisfying both criteria were searched for. The phase variations with time and frequency were computed for signals found satisfying both criteria, through the use of discrete Fourier transform. A total of 222 potential SETI signals (200 narrow band and 22 broad band) were detected and by using automated data analysis techniques were ruled out as originating from the Gliese 581 system.

No evidence for radio signals > 1.55 mJy (5σ) within the frequency range of 1230 - 1544 MHz were found from the region of Gl581, thus, placing an upper limit of 7 MW Hz^{-1} on the power output of any isotropic emitter located in this planetary system, within this frequency range. This study shows that VLBI is ideal for targeted SETI including follow-up observations. The techniques presented are equally applicable to next-generation interferometers, such as the long baselines of the Square Kilometre Array.

6.1.2 Star-Forming Galaxies

6.1.2.1 NGC 253

A multi-epoch wide-field VLBI survey of the southern starburst galaxy, NGC 253, is presented. The observations were conducted with the LBA at 2.3 GHz during the years 2006, 2007 and 2008. This research is the third in a series of papers aimed at determining the nature of the compact radio source population, the supernova history and understanding the interstellar medium of the nuclear region of this galaxy through the use of wide-field VLBI. Since the nuclear region of NGC 253 is within the small field limit of the LBA at 2.3 GHz only bandwidth

and time averaging smearing were considered. The images revealed seven sources that were detected by previous radio interferometric observations of this galaxy, with no significant changes (flux density and size) detected.

The brightest supernova remnant in NGC 253, SNR 5.48−43.3, was imaged with the highest sensitivity and resolution to date (the 2008 epoch), revealing a double-lobed morphology which is dominated by the eastern lobe. However, the weaker, western lobe was not detected in the 2006 and 2007 observations, which is attributed to lower sensitivity and fidelity, due the lack of the 70 m Tidbinbilla antenna. Comparisons with previous observations of similar resolution and frequency give an upper limit of 10^4 km s^{-1} for the expansion speed of this remnant.

The results of this survey were combined with multi-wavelength radio interferometric observations from the literature to derive the spectra of 20 known sources in NGC 253, which were found to fit a free-free absorption model. Based upon spectral index, 12 steep-spectra sources were found to be associated with SNR, while the remainder (flat to inverted spectrum) are possibly HII regions. The results were found to be consistent with previous studies.

A supernova rate of $<$0.2 yr^{-1} was estimated for the inner nuclear region (300 pc), using a model that improves on previous methods by incorporating: an improved radio supernova peak luminosity distribution at 5 GHz, that was derived through the use of literature data; a time-dependent spectral index model based upon RSNe observations; and multi-wavelength radio data spanning 21 years. The results of the model indicates that all radio observations are detecting 60% - 80% of all SNRs in NGC 253. Moreover, with no new SNe or SNR detected in 21 years, the possible existence of a small population of undetected supernova remnants, arising due to a low rate of radio supernovae production in NGC 253, is suggested.

A star formation rate of $SFR(M \geq 5\ M_{\odot}) < 4.9\ M_{\odot}$ yr^{-1} was estimated using the standard relation between supernova and star-formation rates. Our improved estimates of supernova and star-formation rates are consistent with studies at other wavelengths.

6.1.2.2 M51

This study is the highest resolution, wide-field survey of a nearby face-on star-forming galaxy, and the first wide-field VLBI study to venture to the edge of the primary beam of an heterogeneous array. Here, the entire disk of the Whirlpool

Galaxy, M51 (77 arcminutes squared) is surveyed through the implementation of the technique of simultaneous multi-phase correlation, to circumvent the difficulties arising due to non-coplanar effects and image smearing, on a single 8 hr pointing with the EVN at 18 cm. The phase centres (192 in total) were also corrected for image smearing and primary beam effects, prior to imaging. Wide-field images of the 192 phase centres resulted in the detection of six sources in total: the Seyfert nucleus; the supernova SN 2011dh; and four background AGNs.

The results of this survey were compared to catalogued radio sources from the VLA and the fraction of sources were related to previous wide-field VLBI studies. The low detection rate is attributed to many of the VLA sources lacking compact high brightness emission such as, stellar clusters and HII regions, and/or the expansion of SNR beyond our maximum detectable size. Assuming a typical expansion rate of 21,000 km s^{-1} for core-collapse SNe in M51 gives an age of 570 - 950 yr for the largest and 280 years for the smallest shell sources in M51.

The VLBI observation resolves the low-luminosity Seyfert nucleus of M51 into a parsec-scale core-jet structure typical of AGN (brightness temperature of $10^{6.6}$ K and luminosity of 10^{18} W Hz^{-1}). In addition, through a combination of lower-resolution radio interferometer data (MERLIN and VLA), a possible fossil radio lobe located 1.44 kpc from the Seyfert nucleus is revealed. An upper limit of the star formation rate of $SFR(M \geq 5M_{\odot}) < 0.044\ M_{\odot}\,\mathrm{yr}^{-1}$ was estimated for the inner nuclear region of M51 through the standard relations of radio emission and star formation rate. The supernova SN2011dh was imaged 159 day after its explosion and was used to provide a more robust estimate on the light curve at 18 and 6 cm. Multi-resolution radio images of two of the background AGN reveals complex morphologies that are indicative of powerful radio galaxies. The properties of the background AGNs were investigated in detail through the use of X-ray, optical and radio ancillary data.

6.2 Scope for Future Work

6.2.1 SETI, VLBI and the SKA

The proof-of-concept study presented in Chapter 3, opens the possibility of conducting future SETI surveys with current and future VLBI arrays. As discussed in Section 3.5, future VLBI SETI surveys can make use of longer baselines and more than three antennas allowing for the application of more accurate calibration techniques. Furthermore, the multi-phase correlation technique can be used to target multiple SETI candidates within a single pointing.

Targets for future VLBI SETI surveys are being provided by current space missions (e.g. the Kepler mission), and ground-based surveys (e.g. High Accuracy Radial velocity Planet Searcher, HARPS[1]). In addition, future space missions such as the Transiting Exoplanet Survey Satellite (TESS)[2] and PLAnetary Transits and Oscillations of stars (PLATO)[3] are expected to increase the number of confirmed habitable exoplanets. To have a realistic chance of a detection, requires the majority of these targets to be continuously surveyed. One method for achieving this with VLBI (and the future SKA telescope), is through the execution of SETI experiments commensally with normal operations and processed through automated techniques, similar to the V-FASTR project (Wayth et al., 2011; Thompson et al., 2011).

However, with a commensal-type survey the target cannot be specified and the the survey is dependent on a chance alignment of a SETI target within the VLBI primary beam. Nonetheless, with the major VLBI facilities providing almost daily observations, this chance can be quite high. Furthermore, to use the baseline-based technique would require phase-calibration of the data, which may not be ideal for an automation process. However, for the commensal method to be successful, further pathfinder experiments with the various VLBI instruments should be conducted.

Finally, the most important application of this technique is with the future SKA telescope. However, this can only be a reality through successful deployment of SETI commensally with current VLBI instruments.

[1] `https://www.eso.org/sci/facilities/lasilla/instruments/harps/overview.html`
[2] `http://tess.gsfc.nasa.gov/`
[3] `http://sci.esa.int/plato/42276-summary/`

6.2.2 Star-Forming Galaxies

6.2.2.1 NGC 253 and the supernova rate model

Through the use of multi-epoch high resolution radio observations, a statistical model was developed in this thesis to estimate the supernova rate of the starburst galaxy, NGC 253. However, it is possible to apply this model to other starburst/star forming galaxies. To date there are a few star forming (and starburst) galaxies that have been subjected to frequent high resolution radio observations (see Chapters 4 and 5 for a comprehensive list). Furthermore, current and future instruments such as wide-field VLBI, Australian Square Kilometre Pathfinder (ASKAP)[4], the JVLA, e-MERLIN[5] and the future SKA can provide high sensitivity, multi-wavelength observations of the compact radio sources within these and many more galaxies, thus providing the means to improve the supernova rate model into a more robust generalised model that can be used to further our understanding of the supernova rate history of star forming galaxies.

Applying the multi-phase correlation method to survey the entire disk of NGC 253 ($27'.5 \times 6'.8$) would allow the detection of multiple background AGNs, the results of which can be used to probe the ISM of NGC 253 through scatter broadening measurements. Furthermore, combining the results with the free-free absorption measurements would provide a very powerful tool in understanding the three-dimensional structure of the nearby star forming galaxy. In addition, it would be possible to measure the expansion rate of SNR $5.48-43.3$ through multiple VLBI observations.

6.2.2.2 M51

The study presented in Chapter 5 provides a number of interesting possibilities for further studies of M51. As discussed in Section 5.5.2.2, the parsec scale jet appears to move with a velocity of ~ 0.27c between 2008 and 2011. Furthermore, the flux density appears to have decreased within the 3 years between both observations. It is possible that this shift is due to a precessing jet, arising from complex velocity fields within the nucleus of M51. It is however possible that the position shift can be the result of systematic factors (e.g. poor calibration), since the hotspots displaying the apparent motions are $\sim 4\sigma$ detections. Whether this apparent motion is indeed intrinsic to M51 is difficult to ascertain with only two epochs

[4] `http://www.atnf.csiro.au/projects/askap/index.html`
[5] `http://www.e-merlin.ac.uk/`

of observation. A request has been made to observe the nuclear region of M51 with a third higher sensitivity observation with the EVN at 18 cm to determine whether this is indeed intrinsic to the parsec-scale jet of M51.

The results of the analysis of Component N suggests that this may be a fossil radio lobe, associated with the Seyfert nucleus. One definite probe of this would be to look for synchrotron ageing. A multi-wavelength VLA and VLBI survey would be able to search for the spectral break that is indicative of synchrotron ageing. If so this would be the first confirmed detection of this process in a nearby star-forming/Seyfert galaxy.

Evidence for the quenching of low frequency radio emission due to free-free absorption have been found within edge-on starburst galaxies such as NGC 253, M82 and Arp 220. However, to date this (or a similar) effect has not been observed in face-on galaxies. The possibility of free-free (or synchrotron-self) absorption can be investigated through the use of further multi-wavelength interferometric observations to obtain the spectra of individual sources in M51.

It is interesting to note that of the three Maddox et al. (2007) sources detected by the EVN, two were found with very good agreement between the VLBI and lower resolution source positions (Figure 5.8c). Further work on using the estimates of the positional error of the Maddox et al. (2007) survey to improve the LR method and increase the chance of detecting sources below 6.7σ in the M51 fields are being planned.

6.2.3 Wide-field VLBI surveys of star-forming galaxies

Chapter 5 presents a blind survey of radio sources in M51. The results demonstrated that wide-field VLBI surveys of nearby star-forming galaxies are able to provide a wealth of information concerning the individual galaxies and the compact radio sources within these galaxies. This was done through the use of 192 phase centres to image the entire galaxy to search for compact radio sources. However, of the 192 phase centres, only six provided positive detections indicating that most of the computing time was spent on imaging empty fields. To improve the computing time and efficiency of the survey, the number of phase centres could have been reduced through consideration of only sources detected with the VLA. However, with a detection rate of 3/70 sources this would also provide a similar situation.

Future wide-field VLBI surveys would therefore benefit from the e-MERLIN

array[6], which provides intermediate resolution between compact arrays such as the VLA and VLBI arrays. Furthermore, with a sensitivity[7] at 18 and 6 cm $<6\mu$Jy beam^{-1} would allow the detection of faint sources that would be detected with high sensitivity wide-field VLBI surveys. In the M51 survey, 3/6 sources were detected by the MERLIN array (precursor to e-MERLIN), and of the remaining three sources, two were not detected due to low sensitivity (and possibly imperfect calibration), and the third source was the supernova SN 2011dh that exploded six years after the MERLIN observation. Thus, the use of e-MERLIN to detect radio sources that can be used as phase centres, would greatly increase the efficiency of future wide-field VLBI surveys.

[6]This is valid for northern sources that are visible only with the e-MERLIN array
[7]`http://www.e-merlin.ac.uk/tech/`

Bibliography

Ahn, C. P., Alexandroff, R., Allende Prieto, C., and et al. (2012). The Ninth Data Release of the Sloan Digital Sky Survey: First Spectroscopic Data from the SDSS-III Baryon Oscillation Spectroscopic Survey. *ApJS*, 203:21.

Akiyama, M., Ueda, Y., Ohta, K., Takahashi, T., and Yamada, T. (2003). Optical Identification of the ASCA Medium Sensitivity Survey in the Northern Sky: Nature of Hard X-Ray-Selected Luminous Active Galactic Nuclei. *ApJS*, 148:275.

Alexandroff, R., Overzier, R. A., Paragi, Z., and et al. (2012). A search for active galactic nuclei in the most extreme UV-selected starbursts using the European VLBI Network. *MNRAS*, 423:1325.

Antonucci, R. R. J. and Ulvestad, J. S. (1988). A large family of compact radio sources in the starburst nucleus of NGC 253. *ApJL*, 330:L97.

Appl, S., Sol, H., and Vicente, L. (1996). Misalignment and curvature effects in extragalactic radio sources. *A&A*, 310:419.

Argo, M. K., Beswick, R. J., Muxlow, T. W. B., Pedlar, A., Fenech, D., and Thrall, H. (2005). MERLIN monitoring of recent core-collapse supernovae. *Mem. Soc. Astron. Italiana*, 76:565.

Arnaud, K. A. (1996). XSPEC: The First Ten Years. In Jacoby, G. H. and Barnes, J., editors, *Astronomical Data Analysis Software and Systems V*, volume 101 of *Astronomical Society of the Pacific Conference Series*, page 17.

Avruch, I., Pogrebenko, S. V., and Gurvits, L. I. (2006). VLBI observations of spacecraft. In *Proceedings of the 8th European VLBI Network Symposium*.

Backus, P. R. and Project Phoenix Team (2002). Project Phoenix: SETI Observations from 1200 to 1750 MHz with the Upgraded Arecibo Telescope. In Stanimirovic, S., Altschuler, D., Goldsmith, P., and Salter, C., editors, *Single-Dish Radio Astronomy: Techniques and Applications*, volume 278 of *Astronomical Society of the Pacific Conference Series*, pages 525–527.

Barger, A. J., Cowie, L. L., Brandt, W. N., Capak, P., Garmire, G. P., Hornschemeier, A. E., Steffen, A. T., and Wehner, E. H. (2002). X-Ray, Optical, and Infrared Imaging and Spectral Properties of the 1 Ms Chandra Deep Field North Sources. *AJ*, 124:1839.

Bastian, U. and Schilbach, E. (1996). GAIA, the successor of HIPPARCOS in the 21st century. In Schielicke, R. E., editor, *Reviews in Modern Astronomy*, volume 9 of *Reviews in Modern Astronomy*, page 87.

Batalha, N. M., Rowe, J. F., Bryson, S. T., and et al. (2013). Planetary Candidates Observed by Kepler. III. Analysis of the First 16 Months of Data. *ApJS*, 204:24.

Batejat, F., Conway, J. E., Hurley, R., Parra, R., Diamond, P. J., Lonsdale, C. J., and Lonsdale, C. J. (2011). Resolution of the Compact Radio Continuum Sources in Arp220. *ApJ*, 740:95.

Batejat, F., Conway, J. E., Rushton, A., Parra, R., Diamond, P. J., Lonsdale, C. J., and Lonsdale, C. J. (2012). Rapid variability of the compact radio sources in Arp220. Evidence for a population of microblazars? *A&A*, 542:L24.

Becker, R. H., White, R. L., and Helfand, D. J. (1995). The FIRST Survey: Faint Images of the Radio Sky at Twenty Centimeters. *ApJ*, 450:559.

Berger, E., Kulkarni, S. R., and Chevalier, R. A. (2002). The Radio Evolution of the Ordinary Type Ic Supernova SN 2002ap. *ApJL*, 577:L5.

Berger, E., Kulkarni, S. R., Frail, D. A., and Soderberg, A. M. (2003). A Radio Survey of Type Ib and Ic Supernovae: Searching for Engine-driven Supernovae. *ApJ*, 599:408.

Beswick, R. J., Muxlow, T. W. B., Argo, M. K., Pedlar, A., Marcaide, J. M., and Wills, K. A. (2005). Monitoring of the Prompt Radio Emission from the Unusual Supernova SN 2004dj in NGC 2403. *ApJL*, 623:L21.

Beswick, R. J., Riley, J. D., Marti-Vidal, I., and et al. (2006). 15 years of very long baseline interferometry observations of two compact radio sources in Messier 82. *MNRAS*, 369:1221.

Bietenholz, M. F., Bartel, N., and Rupen, M. P. (2004). The Location of the Core in M81. *ApJ*, 615:173.

Bietenholz, M. F., Brunthaler, A., Soderberg, A. M., Krauss, M., Zauderer, B., Bartel, N., Chomiuk, L., and Rupen, M. P. (2012). VLBI Observations of the Nearby Type IIb Supernova 2011dh. *ApJ*, 751:125.

Bietenholz, M. F., Soderberg, A. M., Bartel, N., Ellingsen, S. P., Horiuchi, S., Phillips, C. J., Tzioumis, A. K., Wieringa, M. H., and Chugai, N. N. (2010). VLBI Observations of the Type I b/c Supernova 2009bb. *ApJ*, 725:4.

Bîrzan, L., Rafferty, D. A., McNamara, B. R., Wise, M. W., and Nulsen, P. E. J. (2004). A Systematic Study of Radio-induced X-Ray Cavities in Clusters, Groups, and Galaxies. *ApJ*, 607:800.

Black, G. J. (2002). Planetary Radar Astronomy. In Stanimirovic, S., Altschuler, D., Goldsmith, P., and Salter, C., editors, *Single-Dish Radio Astronomy: Techniques and Applications*, volume 278 of *Astronomical Society of the Pacific Conference Series*, page 271.

Black, G. J., Campbell, D. B., and Ostro, S. J. (2001). Icy Galilean Satellites: 70 cm Radar Results from Arecibo. *Icarus*, 151:160.

Blair, D. G., Norris, R. P., Troup, E. R., Twardy, R., Wellington, K. J., Williams, A. J., Wright, A. E., and Zadnik, M. G. (1992). A narrow-band search for extraterrestrial intelligence (SETI) using the interstellar contact channel hypothesis. *MNRAS*, 257:105.

Bolatto, A. D., Warren, S. R., Leroy, A. K., Walter, F., Veilleux, S., Ostriker, E. C., Ott, J., Zwaan, M., Fisher, D. B., Weiss, A., Rosolowsky, E., and Hodge, J. (2013). Suppression of star formation in the galaxy NGC 253 by a starburst-driven molecular wind. *Nature*, 499:450.

Bolton, J. G., Gardner, F. F., and Mackey, M. B. (1963). A Radio Source with a Very Unusual Spectrum. *Nature*, 199:682.

Bondi, M., Pérez-Torres, M. A., Herrero-Illana, R., and Alberdi, A. (2012). The nuclear starburst in Arp 299-A: from the 5.0 GHz VLBI radio light-curves to its core-collapse supernova rate. *A&A*, 539:A134.

Bontempi, P., Giroletti, M., Panessa, F., Orienti, M., and Doi, A. (2012). Physical properties of the nuclear region in Seyfert galaxies derived from observations with the European VLBI Network. *MNRAS*, 426:588.

Boomsma, R., Oosterloo, T. A., Fraternali, F., van der Hulst, J. M., and Sancisi, R. (2005). Extra-planar H I in the starburst galaxy NGC 253. *A&A*, 431:65.

Borucki, W. J., Koch, D., Basri, G., Batalha, N., Brown, T., Caldwell, D., Caldwell, J., Christensen-Dalsgaard, J., Cochran, W. D., DeVore, E., Dunham, E. W., Dupree, A. K., Gautier, T. N., Geary, J. C., Gilliland, R., Gould, A., Howell, S. B., Jenkins, J. M., Kondo, Y., Latham, D. W., Marcy, G. W., Meibom, S., Kjeldsen, H., Lissauer, J. J., Monet, D. G., Morrison, D., Sasselov, D., Tarter, J., Boss, A., Brownlee, D., Owen, T., Buzasi, D., Charbonneau, D., Doyle, L., Fortney, J., Ford, E. B., Holman, M. J., Seager, S., Steffen, J. H., Welsh, W. F., Rowe, J., Anderson, H., Buchhave, L., Ciardi, D., Walkowicz, L., Sherry, W., Horch, E., Isaacson, H., Everett, M. E., Fischer, D., Torres, G., Johnson, J. A., Endl, M., MacQueen, P., Bryson, S. T., Dotson, J., Haas, M., Kolodziejczak, J., Van Cleve, J., Chandrasekaran, H., Twicken, J. D., Quintana, E. V., Clarke, B. D., Allen, C., Li, J., Wu, H., Tenenbaum, P., Verner, E., Bruhweiler, F., Barnes, J., and Prsa, A. (2010). Kepler Planet-Detection Mission: Introduction and First Results. *Science*, 327:977.

Bower, G. C. and Backer, D. C. (1998). 7 Millimeter VLBA Observations of Sagittarius A*. *ApJL*, 496:L97.

Bracewell, R. N. (2000). *The Fourier transform and its applications*.

Bradley, L. D., Kaiser, M. E., and Baan, W. A. (2004). Physical Conditions in the Narrow-Line Region of M51. *ApJ*, 603:463.

Bridle, A. H. and Perley, R. A. (1984). Extragalactic Radio Jets. *ARA&A*, 22:319.

Bridle, A. H. and Schwab, F. R. (1999). Bandwidth and Time-Average Smearing. In Taylor, G. B., Carilli, C. L., and Perley, R. A., editors, *Synthesis Imaging in Radio Astronomy II*, volume 180 of *Astronomical Society of the Pacific Conference Series*, page 371.

Broderick, A. E., Fish, V. L., Doeleman, S. S., and Loeb, A. (2011). Constraining the Structure of Sagittarius A*'s Accretion Flow with Millimeter Very Long Baseline Interferometry Closure Phases. *ApJ*, 738:38.

Brunthaler, A., Castangia, P., Tarchi, A., Henkel, C., Reid, M. J., Falcke, H., and Menten, K. M. (2009a). Evidence of a pure starburst nature of the nuclear region of NGC 253. *A&A*, 497:103.

Brunthaler, A., Menten, K. M., Reid, M. J., Henkel, C., Bower, G. C., and Falcke, H. (2009b). Discovery of a bright radio transient in M 82: a new radio supernova? *A&A*, 499:L17.

Calzetti, D., Kennicutt, Jr., R. C., Bianchi, L., and et al. (2005). Star Formation in NGC 5194 (M51a): The Panchromatic View from GALEX to Spitzer. *ApJ*, 633:871.

Campbell, R. M. (2004). Recent Results from the EVN Mark IV Data Processor at JIVE. In Vandenberg, N. R. and Baver, K. D., editors, *International VLBI Service for Geodesy and Astrometry 2004 General Meeting Proceedings*, page 123.

Carilli, C. L. (1996). Free-free absorption towards the nucleus of NGC 253: further evidence for high pressures in the starburst nucleus. *A&A*, 305:402.

Carilli, C. L. and Barthel, P. D. (1996). Cygnus A. *A&A Rev.*, 7:1.

Carilli, C. L. and Rawlings, S. (2004). Motivation, key science projects, standards and assumptions. *New Astronomy Reviews*, 48:979.

Cassan, A., Kubas, D., Beaulieu, J.-P., Dominik, M., Horne, K., Greenhill, J., Wambsganss, J., Menzies, J., Williams, A., Jørgensen, U. G., Udalski, A., Bennett, D. P., Albrow, M. D., Batista, V., Brillant, S., Caldwell, J. A. R., Cole, A., Coutures, C., Cook, K. H., Dieters, S., Prester, D. D., Donatowicz, J., Fouqué, P., Hill, K., Kains, N., Kane, S., Marquette, J.-B., Martin, R., Pollard, K. R., Sahu, K. C., Vinter, C., Warren, D., Watson, B., Zub, M., Sumi, T., Szymański, M. K., Kubiak, M., Poleski, R., Soszynski, I., Ulaczyk,

K., Pietrzyński, G., and Wyrzykowski, Ł. (2012). One or more bound planets per Milky Way star from microlensing observations. *Nature*, 481:167.

Chandra, P., Chevalier, R. A., Chugai, N., Fransson, C., Irwin, C. M., Soderberg, A. M., Chakraborti, S., and Immler, S. (2012). Radio and X-Ray Observations of SN 2006jd: Another Strongly Interacting Type IIn Supernova. *ApJ*, 755:110.

Chandra, P., Stockdale, C. J., Chevalier, R. A., Van Dyk, S. D., Ray, A., Kelley, M. T., Weiler, K. W., Panagia, N., and Sramek, R. A. (2009). Eleven Years of Radio Monitoring of the type IIn Supernova SN 1995N. *ApJ*, 690:1839.

Chevalier, R. A. (1982). Self-similar solutions for the interaction of stellar ejecta with an external medium. *ApJ*, 258:790.

Chevalier, R. A., Fransson, C., and Nymark, T. K. (2006). Radio and X-Ray Emission as Probes of Type IIP Supernovae and Red Supergiant Mass Loss. *ApJ*, 641:1029.

Civano, F., Brusa, M., Comastri, A., and et al. (2011). The Population of High-redshift Active Galactic Nuclei in the Chandra-COSMOS Survey. *ApJ*, 741:91.

Clark, B. G. (2003). A Review of the History of VLBI. In Zensus, J. A., Cohen, M. H., and Ros, E., editors, *Radio Astronomy at the Fringe*, volume 300 of *Astronomical Society of the Pacific Conference Series*.

Clarke, C. J., Bonnell, I. A., and Hillenbrand, L. A. (2000). The Formation of Stellar Clusters. *Protostars and Planets IV*, page 151.

Cocconi, G. and Morrison, P. (1959). Searching for Interstellar Communications. *Nature*, 184:844.

Comastri, A. (2004). Compton-Thick AGN: The Dark Side of the X-Ray Background. In Barger, A. J., editor, *Supermassive Black Holes in the Distant Universe*, volume 308 of *Astrophysics and Space Science Library*, page 245.

Condon, J. J. (1992). Radio emission from normal galaxies. *ARA&A*, 30:575.

Condon, J. J., Cotton, W. D., and Broderick, J. J. (2002). Radio Sources and Star Formation in the Local Universe. *AJ*, 124:675.

Conway, J. E. and Murphy, D. W. (1993). Helical jets and the misalignment distribution for core-dominated radio sources. *ApJ*, 411:89.

Conway, R. G., Kellermann, K. I., and Long, R. J. (1963). The radio frequency spectra of discrete radio sources. *MNRAS*, 125:261.

Corbel, S., Coriat, M., Brocksopp, C., Tzioumis, A. K., Fender, R. P., Tomsick, J. A., Buxton, M. M., and Bailyn, C. D. (2013). The 'universal' radio/X-ray flux correlation: the case study of the black hole GX 339-4. *MNRAS*, 428:2500.

Cordey, R. A. (1987). IC 2476 - A possible relic radio galaxy. *MNRAS*, 227:695.

Cornwell, T., Braun, R., and Briggs, D. S. (1999). Deconvolution. In Taylor, G. B., Carilli, C. L., and Perley, R. A., editors, *Synthesis Imaging in Radio Astronomy II*, volume 180 of *Astronomical Society of the Pacific Conference Series*, page 151.

Cornwell, T. J., Golap, K., and Bhatnagar, S. (2005). W Projection: A New Algorithm for Wide Field Imaging with Radio Synthesis Arrays. In P. Shopbell, M. Britton, & R. Ebert, editor, *Astronomical Data Analysis Software and Systems XIV*, volume 347 of *Astronomical Society of the Pacific Conference Series*, page 86.

Cornwell, T. J. and Perley, R. A. (1992). Radio-interferometric imaging of very large fields - The problem of non-coplanar arrays. *A&A*, 261:353.

Corsi, A., Ofek, E. O., Gal-Yam, A., and et al. (2014). A Multi-wavelength Investigation of the Radio-loud Supernova PTF11qcj and its Circumstellar Environment. *ApJ*, 782:42.

Cowan, J. J., Roberts, D. A., and Branch, D. (1994). Radio observations of M83 and its supernova remnants. *ApJ*, 434:128.

Crane, P. C. and van der Hulst, J. M. (1992). The radio jet in M51. *AJ*, 103:1146.

Crocker, A. F., Bureau, M., Young, L. M., and Combes, F. (2011). Molecular gas and star formation in early-type galaxies. *MNRAS*, 410:1197.

Dalcanton, J. J., Williams, B. F., Seth, A. C., and et al. (2009). The ACS Nearby Galaxy Survey Treasury. *ApJS*, 183:67.

Davidge, T. J. (2011). Shaken, not Stirred: the Ancestry of the Starburst Galaxy NGC 253. In Carignan, C., Combes, F., and Freeman, K. C., editors, *IAU Symposium*, volume 277 of *IAU Symposium*, pages 13–16.

Dellar, A. and Brisken, W. F. (2009). Software correlators in radio astronomy. *SPIE Newsroom*.

Deller, A. T., Brisken, W. F., Phillips, C. J., Morgan, J., Alef, W., Cappallo, R., Middelberg, E., Romney, J., Rottmann, H., Tingay, S. J., and Wayth, R. (2011). DiFX-2: A More Flexible, Efficient, Robust, and Powerful Software Correlator. *PASP*, 123:275.

Deller, A. T. and Middelberg, E. (2014). mJIVE-20: A Survey for Compact mJy Radio Objects with the Very Long Baseline Array. *AJ*, 147:14.

Deller, A. T., Tingay, S. J., Bailes, M., and Reynolds, J. E. (2009a). Precision Southern Hemisphere VLBI Pulsar Astrometry. II. Measurement of Seven Parallaxes. *ApJ*, 701:1243.

Deller, A. T., Tingay, S. J., Bailes, M., and West, C. (2007). DiFX: A Software Correlator for Very Long Baseline Interferometry Using Multiprocessor Computing Environments. *PASP*, 119:318.

Deller, A. T., Tingay, S. J., and Brisken, W. (2009b). Precision Southern Hemisphere Pulsar VLBI Astrometry: Techniques and Results for PSR J1559-4438. *ApJ*, 690:198.

Dent, W. A. (1965). Variation in the Radio Emission of 3C273 and Other Quasi-Stellar Sources. *AJ*, 70:672.

Dewdney, P., Hall, P., Schilizzi, R., and Lazio, T. (2009). The square kilometre array. *Proceedings of the IEEE*, 97(8):1482.

Dewdney, P. E., Turner, W., Millenaar, R., Lazio, J., and Cornwell, T. J. (2013). *SKA1 System Baseline Design*. SKA Office, Manchester. `http://www.skatelescope.org/wp-content/uploads/2012/07/SKA-TEL-SKO-DD-001-1_BaselineDesign1.pdf`.

Doi, A., Asada, K., Fujisawa, K., Nagai, H., Hagiwara, Y., Wajima, K., and Inoue, M. (2013). Very Long Baseline Array Imaging of Parsec-scale Radio Emissions in Nearby Radio-quiet Narrow-line Seyfert 1 Galaxies. *ApJ*, 765:69.

Drake, F. (2008). SETI – The Early Days and Now. In A. H. Bridle, J. J. Condon, & G. C. Hunt, editor, *Frontiers of Astrophysics: A Celebration of NRAO's 50th Anniversary*, volume 395 of *Astronomical Society of the Pacific Conference Series*, page 213.

Drake, F. D. (1961). Project ozma. *Physics Today*, 14(4):40.

Dumas, G., Schinnerer, E., Tabatabaei, F. S., Beck, R., Velusamy, T., and Murphy, E. (2011). The Local Radio-IR Relation in M51. *AJ*, 141:41.

Edmunds, M. G. and George, G. H. (1985). On the statistics of quasar alignments. *MNRAS*, 213:905.

Efstathiou, G. (2000). A model of supernova feedback in galaxy formation. *Monthly Notices of the Royal Astronomical Society*, 317(3):697.

Ehrenfreund, P., Irvine, W., Becker, L., and et al. (2002). Astrophysical and astrochemical insights into the origin of life. *Reports on Progress in Physics*, 65:1427.

Fanaroff, B. L. and Riley, J. M. (1974). The morphology of extragalactic radio sources of high and low luminosity. *MNRAS*, 167:31P.

Fender, R. P. (2001). Powerful jets from black hole X-ray binaries in low/hard X-ray states. *MNRAS*, 322:31.

Fender, R. P., Belloni, T. M., and Gallo, E. (2004). Towards a unified model for black hole X-ray binary jets. *MNRAS*, 355:1105.

Fenech, D., Beswick, R., Muxlow, T. W. B., Pedlar, A., and Argo, M. K. (2010). Wide-field Global VLBI and MERLIN combined monitoring of supernova remnants in M82. *MNRAS*, 408:607.

Ferreira, S. E. S. and de Jager, O. C. (2008). Supernova remnant evolution in uniform and non-uniform media. *A&A*, 478:17.

Fey, A. L. and Charlot, P. (1997). VLBA Observations of Radio Reference Frame Sources. II. Astrometric Suitability Based on Observed Structure. *ApJS*, 111:95.

Fey, A. L., Ma, C., Arias, E. F., Charlot, P., Feissel-Vernier, M., Gontier, A.-M., Jacobs, C. S., Li, J., and MacMillan, D. S. (2004). The Second Extension of the International Celestial Reference Frame: ICRF-EXT.1. *AJ*, 127:3587–3608.

Fiore, F., Brusa, M., Cocchia, F., Baldi, A., and et al. (2003). The HELLAS2XMM survey. IV. Optical identifications and the evolution of the accretion luminosity in the Universe. *A&A*, 409:79.

Fomalont, E. and Reid, M. (2004). Microarcsecond astrometry using the SKA. *New Astronomy Reviews*, 48:1473.

Ford, H. C., Crane, P. C., Jacoby, G. H., Lawrie, D. G., and van der Hulst, J. M. (1985). Bubbles and jets in the center of M51. *ApJ*, 293:132.

Fridman, P. A. (2011). SETI: The transmission rate of radio communication and the signal's detection. *Acta Astronautica*, 69:777.

Fruscione, A., McDowell, J. C., Allen, G. E., and et al. (2006). CIAO: Chandra's data analysis system. In *Society of Photo-Optical Instrumentation Engineers (SPIE) Conference Series*, volume 6270 of *Society of Photo-Optical Instrumentation Engineers (SPIE) Conference Series*.

Gaidos, E. (2013). Candidate Planets in the Habitable Zones of Kepler Stars. *ApJ*, 770:90.

Garrett, M. (2013). Radio Astronomy MSc. course Lecture 7: Calibration and Advanced radio interferometry. Retrieved from: www.astron.nl/ mag/dokuwiki/doku.php?id=radio_astronomy_course_description.

Garrett, M. A., Muxlow, T. W. B., Garrington, S. T., Alef, W., Alberdi, A., van Langevelde, H. J., Venturi, T., Polatidis, A. G., Kellermann, K. I., Baan, W. A., Kus, A., Wilkinson, P. N., and Richards, A. M. S. (2001). AGN and starbursts at high redshift: High resolution EVN radio observations of the Hubble Deep Field. *A&A*, 366:L5.

Garrett, M. A., Porcas, R. W., Pedlar, A., Muxlow, T. W. B., and Garrington, S. T. (1999). Wide-field VLBI imaging. *New Astronomy Reviews*, 43:519.

Garrett, M. A., Wrobel, J. M., and Morganti, R. (2005). Deep VLBI Imaging of Faint Radio Sources in the NOAO Bootes Field. *ApJ*, 619:105.

Gendre, M. A., Fenech, D. M., Beswick, R. J., Muxlow, T. W. B., and Argo, M. K. (2013). Flux density variations of radio sources in M82 over the last three decades. *MNRAS*, 431:1107.

Gentile, G., Rodríguez, C., Taylor, G. B., Giovannini, G., Allen, S. W., Lane, W. M., and Kassim, N. E. (2007). Monitoring the Bidirectional Relativistic Jets of the Radio Galaxy 3C 338. *ApJ*, 659:225.

Giacconi, R., Rosati, P., Tozzi, P., Nonino, M., Hasinger, G., Norman, C., Bergeron, J., Borgani, S., Gilli, R., Gilmozzi, R., and Zheng, W. (2001). First Results from the X-Ray and Optical Survey of the Chandra Deep Field South. *ApJ*, 551:624.

Giroletti, M. and Panessa, F. (2009). The Faintest Seyfert Radio Cores Revealed by VLBI. *ApJL*, 706:L260.

Godfrey, L. E. H., Bignall, H., Tingay, S., Harvey-Smith, L., Kramer, M., Burke-Spolaor, S., Miller-Jones, J. C. A., Johnston-Hollitt, M., Ekers, R., and Gulyaev, S. (2012). Science at Very High Angular Resolution with the Square Kilometre Array. *Publications of the Astronomical Society of Australia*, 29:42.

Griga, T., Marulla, A., Grenier, A., and et al. (2011). Supernova 2011dh in M51 = Psn J13303600+4706330. *Central Bureau Electronic Telegrams*, 2736:1.

Haarsma, D. B., Partridge, R. B., Windhorst, R. A., and Richards, E. A. (2000). Faint Radio Sources and Star Formation History. *ApJ*, 544:641.

Hales, C. A., Murphy, T., Curran, J. R., Middelberg, E., Gaensler, B. M., and Norris, R. P. (2012). BLOBCAT: software to catalogue flood-filled blobs in radio images of total intensity and linear polarization. *MNRAS*, 425:979.

Hancock, P. J., Murphy, T., Gaensler, B. M., Hopkins, A., and Curran, J. R. (2012). Compact continuum source finding for next generation radio surveys. *MNRAS*, 422:1812.

Harp, G., Wilcox, B., Arbunich, J., Blair, S., Backus, P. R., Tarter, J. C., Shostak, S., Jordan, J., Kilsdonk, T., Ackermann, R. F., Ross, J., and ATA Team (2010). PiH$_i$ Observations at the ATA, Conventional and Unconventional SETI. In *American Astronomical Society Meeting Abstracts #215*, volume 42 of *Bulletin of the American Astronomical Society*, page 403.06.

Hart, M. H. (1978). The evolution of the atmosphere of the earth. *Icarus*, 33:23.

Hasinger, G., Burg, R., Giacconi, R., Schmidt, M., Trumper, J., and Zamorani, G. (1998). The ROSAT Deep Survey. I. X-ray sources in the Lockman Field. *A&A*, 329:482.

Heywood, I., Blundell, K. M., Klöckner, H.-R., and Beasley, A. J. (2009). The radio remnant of SN1993J: an instrumental explanation for the evolving complex structure. *MNRAS*, 392:855.

Hjellming, R. M. and Rupen, M. P. (1995). Episodic ejection of relativistic jets by the X-ray transient GRO J1655 - 40. *Nature*, 375:464.

Ho, L. C. (2008). Nuclear Activity in Nearby Galaxies. *ARA&A*, 46:475.

Horesh, A., Stockdale, C., Fox, D. B., and et al. (2013). An early and comprehensive millimetre and centimetre wave and X-ray study of SN 2011dh: a non-equipartition blast wave expanding into a massive stellar wind. *MNRAS*, 436:1258.

Imai, H., Oyadomari, M., Chong, S. N., and et al. (2012). Pilot VLBI Survey of SiO v = 3 J = 1→0 Maser Emission around Evolved Stars. *PASJ*, 64:L6.

Jones, D. L. and Preston, R. A. (2001). Fossil Radio Emission Associated with Currently Active Radio Galaxies. *AJ*, 122:2940.

Kaleida, C. and Scowen, P. A. (2010). Mapping the Recent Star Formation History of the Disk of M51. *AJ*, 140:379.

Karachentsev, I. D., Grebel, E. K., Sharina, M. E., Dolphin, A. E., Geisler, D., Guhathakurta, P., Hodge, P. W., Karachentseva, V. E., Sarajedini, A., and Seitzer, P. (2003). Distances to nearby galaxies in Sculptor. *A&A*, 404:93.

Kasting, J. F., Whitmire, D. P., and Reynolds, R. T. (1993). Habitable Zones around Main Sequence Stars. *Icarus*, 101:108.

Kay, S. M. (1998). *Fundamentals of Statistical Signal Processing: Detection Theory*, volume 2. New Jersey: Prentice Hall.

Kellermann, K. I. and Moran, J. M. (2001). The Development of High-Resolution Imaging in Radio Astronomy. *ARA&A*, 39:457.

Kennicutt, Jr., R. C. (1998). Star Formation in Galaxies Along the Hubble Sequence. *ARA&A*, 36:189.

Kettenis, M., Keimpema, A., Small, D., and Marchal, D. (2009). e-VLBI with the SFXC correlator. In *8th International e-VLBI Workshop*.

Kettenis, M., van Langevelde, H. J., Reynolds, C., and Cotton, B. (2006). ParselTongue: AIPS Talking Python. In C. Gabriel, C. Arviset, D. Ponz, & S. Enrique, editor, *Astronomical Data Analysis Software and Systems XV*, volume 351 of *Astronomical Society of the Pacific Conference Series*, page 497.

Kohno, K., Kawabe, R., Tosaki, T., and Okumura, S. K. (1996). Aperture Synthesis CO and HCN Observationsof M51: Dense Molecular Disk around a Low-Luminosity Active Galactic Nucleus. *ApJL*, 461:L29.

Kopparapu, R. K. (2013). A Revised Estimate of the Occurrence Rate of Terrestrial Planets in the Habitable Zones around Kepler M-dwarfs. *ApJL*, 767:L8.

Korpela, E. J., Cobb, J., Lebofsky, M., Siemion, A., von Korff, J., Bankay, R., Werthimer, D., and Anderson, D. (2010). Candidate Identification and Interference Removal in SETI@home. *LPI Contributions*, 1538:5478.

Kowal, C. T. and Sargent, W. L. W. (1971). Supernovae discovered since 1885. *AJ*, 76:756.

Krauss, M. I., Soderberg, A. M., Chomiuk, L., and et al. (2012). Expanded Very Large Array Observations of the Radio Evolution of SN 2011dh. *ApJL*, 750:L40.

Kulkarni, S. R., Frail, D. A., Wieringa, M. H., Ekers, R. D., Sadler, E. M., Wark, R. M., Higdon, J. L., Phinney, E. S., and Bloom, J. S. (1998). Radio emission from the unusual supernova 1998bw and its association with the γ-ray burst of 25 April 1998. *Nature*, 395:663.

Lacey, C., Duric, N., and Goss, W. M. (1997). A Survey of Compact Radio Sources in NGC 6946. *ApJS*, 109:417.

Lacey, C. K., Weiler, K. W., Sramek, R. A., and van Dyk, S. D. (1998). Supernova 1997eg in NGC 5012. *IAU Circ.*, 7068:2.

Lagos, C. d. P., Lacey, C. G., and Baugh, C. M. (2013). A dynamical model of supernova feedback: gas outflows from the interstellar medium. *MNRAS*, 436:1787.

Lazio, T. J. W. and Cordes, J. M. (1998). Hyperstrong Radio-Wave Scattering in the Galactic Center. I. A Survey for Extragalactic Sources Seen through the Galactic Center. *ApJS*, 118:201.

Lehnert, M. D. and Heckman, T. M. (1996). The Nature of Starburst Galaxies. *ApJ*, 472:546.

Lenc, E., Garrett, M. A., Wucknitz, O., Anderson, J. M., and Tingay, S. J. (2008). A Deep, High-Resolution Survey of the Low-Frequency Radio Sky. *ApJ*, 673:78.

Lenc, E. and Tingay, S. J. (2006). The Subparsec-Scale Radio Properties of Southern Starburst Galaxies. I. Supernova Remnants, the Supernova Rate, and the Ionized Medium in the NGC 253 Starburst. *AJ*, 132:1333.

Lenc, E. and Tingay, S. J. (2009). The Sub-Parsec Scale Radio Properties of Southern Starburst Galaxies. II. Supernova Remnants, the Supernova Rate, and the Ionised Medium in the NGC 4945 Starburst. *AJ*, 137:537.

Lien, A., Chakraborty, N., Fields, B. D., and Kemball, A. (2011). Radio Supernovae in the Great Survey Era. *ApJ*, 740:23.

Lobanov, A. P. (2012). *The SKA and "High-Resolution" Science*, page 75.

Lonsdale, C. J., Diamond, P. J., Thrall, H., Smith, H. E., and Lonsdale, C. J. (2006). VLBI Images of 49 Radio Supernovae in Arp 220. *ApJ*, 647:185.

Lu, J.-F. and Zhou, B.-Y. (2005). Observational Evidence of Jet Precession in Galactic Nuclei Caused by Accretion Disks. *ApJL*, 635:L17.

Maccacaro, T., Gioia, I. M., Wolter, A., Zamorani, G., and Stocke, J. T. (1988). The X-ray spectra of the extragalactic sources in the Einstein extended medium sensitivity survey. *ApJ*, 326:680.

Maddox, L. A., Cowan, J. J., Kilgard, R. E., Lacey, C. K., Prestwich, A. H., Stockdale, C. J., and Wolfing, E. (2006). A Study of Compact Radio Sources in Nearby Face-on Spiral Galaxies. I. Long-Term Evolution of M83. *AJ*, 132:310.

Maddox, L. A., Cowan, J. J., Kilgard, R. E., Schinnerer, E., and Stockdale, C. J. (2007). A Study of Compact Radio Sources in Nearby Face-on Spiral Galaxies. II. Multiwavelength Analyses of Sources in M51. *AJ*, 133:2559.

Mainieri, V., Bergeron, J., Hasinger, G., Lehmann, I., Rosati, P., Schmidt, M., Szokoly, G., and Della Ceca, R. (2002). XMM-Newton observation of the Lockman Hole. II. Spectral analysis. *A&A*, 393:425.

Martí-Vidal, I., Tudose, V., Paragi, Z., and et al. (2011). VLBI observations of SN 2011dh: imaging of the youngest radio supernova. *A&A*, 535:L10.

McDonald, A. R., Muxlow, T. W. B., Wills, K. A., Pedlar, A., and Beswick, R. J. (2002). A parsec-scale study of the 5/15-GHz spectral indices of the compact radio sources in M82. *MNRAS*, 334:912.

McHardy, I. M., Gunn, K. F., Newsam, A. M., and et al. (2003). A medium-deep Chandra and Subaru survey of the 13-h XMM/ROSAT deep survey area. *MNRAS*, 342:802.

McMullin, J. P., Waters, B., Schiebel, D., Young, W., and Golap, K. (2007). CASA Architecture and Applications. In Shaw, R. A., Hill, F., and Bell, D. J., editors, *Astronomical Data Analysis Software and Systems XVI*, volume 376 of *Astronomical Society of the Pacific Conference Series*, page 127.

Metcalfe, L., O'Halloran, B., McBreen, B., Delaney, M., Burgdorf, M., Leech, K., Barr, P., Clavel, J., Coia, D., Hanlon, L., Gallais, P., Laureijs, R., and Smith, N. (2005). ISO observations of the interacting galaxy Markarian 297. with the powerful supernova remnant 1982aa. *A&A*, 444:777.

Middelberg, E. and Bach, U. (2008). High resolution radio astronomy using very long baseline interferometry. *Reports on Progress in Physics*, 71(6):066901.

Middelberg, E., Deller, A., Morgan, J., Rottmann, H., Alef, W., Tingay, S., Norris, R., Bach, U., Brisken, W., and Lenc, E. (2011). Wide-field VLBA observations of the Chandra deep field South. *A&A*, 526:A74.

Middelberg, E., Deller, A. T., Norris, R. P., Fotopoulou, S., Salvato, M., Morgan, J. S., Brisken, W., Lutz, D., and Rovilos, E. (2013). Mosaiced wide-field VLBI observations of the Lockman Hole/XMM. *A&A*, 551:A97.

Middelberg, E., Roy, A. L., Nagar, N. M., Krichbaum, T. P., Norris, R. P., Wilson, A. S., Falcke, H., Colbert, E. J. M., Witzel, A., and Fricke, K. J. (2004). Motion and properties of nuclear radio components in Seyfert galaxies seen with VLBI. *A&A*, 417:925.

Miley, G. K. and Rickett, B. J. (1967). Angular Measurements of the Structure of 3C 446 and Other Quasars with High Red-shifts. *Nature*, 216:974.

Milisavljevic, D., Margutti, R., Soderberg, A. M., and et al. (2013). Multi-wavelength Observations of Supernova 2011ei: Time-dependent Classification of Type IIb and Ib Supernovae and Implications for Their Progenitors. *ApJ*, 767:71.

Miller, G. E. and Scalo, J. M. (1979). The initial mass function and stellar birthrate in the solar neighborhood. *ApJS*, 41:513.

Mohan, N. R., Anantharamaiah, K. R., and Goss, W. M. (2002). Very Large Array Detection of Radio Recombination Lines from the Radio Nucleus of NGC 253: Ionization by a Weak Active Galactic Nucleus, an Obscured Super Star Cluster, or a Compact Supernova Remnant? *ApJ*, 574:701.

Mohan, N. R., Goss, W. M., and Anantharamaiah, K. R. (2005). Multi-density model of the ionised gas in NGC 253 using radio recombination lines. *A&A*, 432:1.

Montebugnoli, S., Monari, J., Cattani, A., Maccaferri, A., Maccaferri, G., Mariotti, S., Poloni, M., Scalambra, A., D'Amico, M., Maccone, C., and Cosmovici, C. B. (2001). SETI-Italia. In P. Ehrenfreund, O. Angerer, & B. Battrick, editor, *Exo-/Astro-Biology*, volume 496 of *ESA Special Publication*, page 281.

Montes, M. J., van Dyk, S. D., Weiler, K. W., Sramek, R. A., and Panagia, N. (1997). Radio Detection of SN 1986E in NGC 4302. *ApJL*, 482:L61.

Morgan, J. (2010a). Simulating, planning and analysing multiple-pointing VLBI surveys. In *10th European VLBI Network Symposium and EVN Users Meeting: VLBI and the New Generation of Radio Arrays*.

Morgan, J. S. (2010b). Very long baseline interferometry in italy (doctoral dissertation, università di bologna). retreived from http://www.physics-astronomy.unibo.it/en/teaching/phd-programs/astronomy/theses.

Morgan, J. S., Argo, M. K., Trott, C. M., Macquart, J.-P., Deller, A., Middelberg, E., Miller-Jones, J., and Tingay, S. J. (2013). Wide-field VLBI Observations of M31: A Unique Probe of the Ionized Interstellar Medium of a Nearby Galaxy. *ApJ*, 768:12.

Morgan, J. S., Mantovani, F., Deller, A. T., Brisken, W., Alef, W., Middelberg, E., Nanni, M., and Tingay, S. J. (2011). VLBI imaging throughout the primary beam using accurate UV shifting. *A&A*, 526:A140.

Muendlein, R., Li, W., Yamaoka, H., and Itagaki, K. (2005). Supernova 2005cs in M51. *IAU Circ.*, 8553:1.

Murgia, M., Markevitch, M., Govoni, F., Parma, P., Fanti, R., de Ruiter, H. R., and Mack, K.-H. (2012). Chandra observations of dying radio sources in galaxy clusters. *A&A*, 548:A75.

Mutchler, M., Beckwith, S. V. W., Bond, H., Christian, C., Frattare, L., Hamilton, F., Hamilton, M., Levay, Z., Noll, K., and Royle, T. (2005). Hubble Space Telescope multi-color ACS mosaic of M51, the Whirlpool Galaxy. In *American Astronomical Society Meeting Abstracts #206*, volume 37 of *Bulletin of the American Astronomical Society*, page 452.

Muxlow, T. W. B., Beswick, R. J., Garrington, S. T., Pedlar, A., Fenech, D. M., Argo, M. K., van Eymeren, J., Ward, M., Zezas, A., and Brunthaler, A. (2010). Discovery of an unusual new radio source in the star-forming galaxy M82: faint supernova, supermassive black hole or an extragalactic microquasar? *MNRAS*, 404:L109.

Muxlow, T. W. B., Pedlar, A., Wilkinson, P. N., Axon, D. J., Sanders, E. M., and de Bruyn, A. G. (1994). The Structure of Young Supernova Remnants in M82. *MNRAS*, 266:455.

Nandra, K. and Pounds, K. A. (1994). GINGA Observations of the X-Ray Spectra of Seyfert Galaxies. *MNRAS*, 268:405.

Netzer, H. (2009). Accretion and star formation rates in low-redshift type II active galactic nuclei. *MNRAS*, 399:1907.

Ng, C.-Y., Potter, T. M., Staveley-Smith, L., Tingay, S., Gaensler, B. M., Phillips, C., Tzioumis, A. K., and Zanardo, G. (2011). First VLBI Detection of the Radio Remnant of Supernova 1987A: Evidence for Small-scale Features. *ApJL*, 728:L15.

Ohyama, Y., Taniguchi, Y., Iye, M., Yoshida, M., Sekiguchi, K., Takata, T., Saito, Y., Kawabata, K. S., Kashikawa, N., Aoki, K., Sasaki, T., Kosugi, G., Okita, K., Shimizu, Y., Inata, M., Ebizuka, N., Ozawa, T., Yadoumaru, Y., Taguchi, H., and Asai, R. (2002). Decomposition of the Superwind in M 82. *PASJ*, 54:891.

Ott, J., Weiss, A., Henkel, C., and Walter, F. (2005). The Temperature Distribution of Dense Molecular Gas in the Center of NGC 253. *ApJ*, 629:767.

Paggi, A., Fabbiano, G., Risaliti, G., Wang, J., and Elvis, M. (2013). Two Compton-Thick Active Nuclei in Arp 220? *arXiv:1303.2630*.

Paglione, T. A. D. and Abrahams, R. D. (2012). Properties of nearby Starburst Galaxies Based on their Diffuse Gamma-Ray Emission. *ApJ*, 755:106.

Panessa, F. and Giroletti, M. (2013). Sub-parsec radio cores in nearby Seyfert galaxies. *MNRAS*, 432:1138.

Pannuti, T. G., Duric, N., Lacey, C. K., Ferguson, A. M. N., Magnor, M. A., and Mendelowitz, C. (2002). An X-Ray, Optical, and Radio Search for Supernova Remnants in the Nearby Sculptor Group Sd Galaxy NGC 7793. *ApJ*, 565:966.

Pannuti, T. G., Duric, N., Lacey, C. K., Goss, W. M., Hoopes, C. G., Walterbos, R. A. M., and Magnor, M. A. (2000). An X-Ray, Optical, and Radio Search for Supernova Remnants in the Nearby Sculptor Group Sd Galaxy NGC 300. *ApJ*, 544:780.

Papovich, C., Finkelstein, S. L., Ferguson, H. C., Lotz, J. M., and Giavalisco, M. (2011). The rising star formation histories of distant galaxies and implications for gas accretion with time. *MNRAS*, 412:1123.

Parma, P., Murgia, M., de Ruiter, H. R., Fanti, R., Mack, K.-H., and Govoni, F. (2007). In search of dying radio sources in the local universe. *A&A*, 470:875.

Parra, R., Conway, J. E., Diamond, P. J., Thrall, H., Lonsdale, C. J., Lonsdale, C. J., and Smith, H. E. (2007). The Radio Spectra of the Compact Sources in Arp 220: A Mixed Population of Supernovae and Supernova Remnants. *ApJ*, 659:314.

Pauliny-Toth, I. I. K. and Kellermann, K. I. (1966). Variations in the Radio-Frequency Spectra of 3C 84, 3C 273, 3C 279, and Other Radio Sources. *ApJ*, 146:634.

Pedlar, A., Muxlow, T. W. B., Garrett, M. A., Diamond, P., Wills, K. A., Wilkinson, P. N., and Alef, W. (1999). VLBI observations of supernova remnants in Messier 82. *MNRAS*, 307:761.

Pellegrini, S., Cappi, M., Bassani, L., Malaguti, G., Palumbo, G. G. C., and Persic, M. (2000). The low luminosity AGN in the LINER galaxy M 81: it BeppoSAX discovery of highly ionized gas. *A&A*, 353:447.

Pérez-Torres, M. A., Alberdi, A., Colina, L., Torrelles, J. M., Panagia, N., Wilson, A., Kankare, E., and Mattila, S. (2009). Radio monitoring of NGC 7469: late-time radio evolution of SN 2000ft and the circumnuclear starburst in NGC 7469. *MNRAS*, 399:1641.

Perez-Torres, M. A., Alberdi, A., Romero-Canizales, C., Bondi, M., and Polatidis, A. (2010). Arp 299-A: More than "just" a prolific supernova factory. *ArXiv e-prints*.

Perley, R. A. (1999). Imaging with Non-Coplanar Arrays. In G. B. Taylor, C. L. Carilli, & R. A. Perley, editor, *Synthesis Imaging in Radio Astronomy II*, volume 180 of *Astronomical Society of the Pacific Conference Series*, page 383.

Perley, R. A., Roser, H.-J., and Meisenheimer, K. (1997). The radio galaxy PictorA – a study with the VLA. *A&A*, 328:12.

Perryman, M. A. C., Lindegren, L., Kovalevsky, J., and et al. (1997). The HIPPARCOS Catalogue. *A&A*, 323:L49.

Pooley, D., Lewin, W. H. G., Fox, D. W., and et al. (2002). X-Ray, Optical, and Radio Observations of the Type II Supernovae 1999em and 1998S. *ApJ*, 572:932.

Prialnik, D. (2000). *An Introduction to the Theory of Stellar Structure and Evolution*.

Puckett, T., Armstrong, J., Johnson, W., and et al. (1994). Supernova 1994I in NGC 5194. *IAU Circ.*, 5961:1.

Radovich, M., Kahanpää, J., and Lemke, D. (2001). Far-infrared mapping of the starburst galaxy NGC 253 with ISOPHOT. *A&A*, 377:73.

Rampadarath, H., Garrett, M. A., Józsa, G. I. G., and et al. (2010). Hanny's Voorwerp . Evidence of AGN activity and a nuclear starburst in the central regions of IC 2497. *A&A*, 517:L8.

Rampadarath, H., Garrett, M. A., and Polatidis, A. (2009). Observations of 44 extragalactic radio sources with the VLBA at 92 cm. A list of potential calibrators and targets for LOFAR and RadioAstron. *A&A*, 500:1327.

Rampadarath, H., Morgan, J. S., Lenc, E., and Tingay, S. J. (2014). Multi-epoch Very Long Baseline Interferometric Observations of the Nuclear Starburst Region of NGC 253: Improved Modeling of the Supernova and Star formation Rates. *AJ*, 147:5.

Reines, A. E. and Marcy, G. W. (2002). Optical Search for Extraterrestrial Intelligence: A Spectroscopic Search for Laser Emission from Nearby Stars. *PASP*, 114:416.

Reynolds, J. (1994). *A Revised Flux Scale for the AT Compact Array.* CSIRO, ATNF Technical Memo, 39:040. Retreived from http://www.atnf.csiro.au/observers/memos/index.html.

Rhee, M., Byun, Y., Kim, H. R., Choi, J. W., Yoon, J. W., An, J. E., Kim, H. J., Lee, K. H., and Kan-Ya, Y. (2010). Project SETI KOREA. *LPI Contributions*, 1538:5191.

Rioja, M. J., Porcas, R. W., Garrington, S., Alberdi, A., and Saikia, D. J. (1999). Phase-reference mapping of a weak-cored double-lobed source in the 1636+473 system using MERLIN and Global VLBI. *New Astronomy Reviews*, 43:593.

Romero-Cañizales, C., Mattila, S., Alberdi, A., Pérez-Torres, M. A., Kankare, E., and Ryder, S. D. (2011). The core-collapse supernova rate in Arp 299 revisited. *MNRAS*, 415:2688.

Roming, P. W. A., Pritchard, T. A., Brown, P. J., Holland, S. T., Immler, S., Stockdale, C. J., Weiler, K. W., Panagia, N., Van Dyk, S. D., Hoversten, E. A., Milne, P. A., Oates, S. R., Russell, B., and Vandrevala, C. (2009). Multi-Wavelength Properties of the Type IIb SN 2008ax. *ApJL*, 704:L118.

Rosenberg, M. J. F., van der Werf, P. P., and Israel, F. P. (2012). [FeII] as a tracer of supernova rate in nearby starburst galaxies. *A&A*, 540:A116.

Rosenberg, M. J. F., van der Werf, P. P., and Israel, F. P. (2013). The excitation of near-infrared H_2 emission in NGC 253. *A&A*, 550:A12.

Rovilos, E., Diamond, P. J., Lonsdale, C. J., Smith, H. E., and Lonsdale, C. J. (2005). The 18-cm light curves of the luminous radio supernova candidates in Arp 220. *MNRAS*, 359:827.

Ryder, S., Covarrubias, R., Amy, S., Argo, M., Stockdale, C., van Dyk, S., Immler, S., Weiler, K., and Panagia, N. (2010a). Supernova 2010as in NGC 6000. *Central Bureau Electronic Telegrams*, 2242:1.

Ryder, S. D., Amy, S. W., Stockdale, C. J., Immler, S., Russell, B. R., and Weiler, K. W. (2010b). Radio Non-Detection of the Type IIb Supernova 2009mk in ESO 293-34. *The Astronomer's Telegram*, 2450:1.

Ryder, S. D., Amy, S. W., Stockdale, C. J., Immler, S., Stevens, J., and Weiler, K. W. (2011a). Radio Detection of the Type IIb Supernova 2011cb in ESO 109-21. *The Astronomer's Telegram*, 3370:1.

Ryder, S. D., Sadler, E. M., Subrahmanyan, R., Weiler, K. W., Panagia, N., and Stockdale, C. (2004). Modulations in the radio light curve of the Type IIb supernova 2001ig: evidence for a Wolf-Rayet binary progenitor? *MNRAS*, 349:1093.

Ryder, S. D., Stockdale, C. J., Immler, S., Stevens, J. B., Edwards, P. G., and Weiler, K. W. (2011b). Radio Non-Detection of the Type Ic Supernova 2011hp in NGC 4219. *The Astronomer's Telegram*, 3764:1.

Salas, P., Bauer, F. E., Stockdale, C., and Prieto, J. L. (2013). SN 2007bg: the complex circumstellar medium around one of the most radio-luminous broad-lined Type Ic supernovae. *MNRAS*, 428:1207.

Salpeter, E. E. (1955). The Luminosity Function and Stellar Evolution. *ApJ*, 121:161.

Sanna, A., Moscadelli, L., Cesaroni, R., Tarchi, A., Furuya, R. S., and Goddi, C. (2010). VLBI study of maser kinematics in high-mass star-forming regions. I. G16.59-0.05. *A&A*, 517:A71.

Sault, R. J., Teuben, P. J., and Wright, M. C. H. (1995). A Retrospective View of MIRIAD. In Shaw, R. A., Payne, H. E., and Hayes, J. J. E., editors, *Astronomical Data Analysis Software and Systems IV*, volume 77 of *Astronomical Society of the Pacific Conference Series*, page 433.

Schilizzi, R. T., Dewdney, P. E. F., and Lazio, T. J. W. (2010). The square kilometre array. In *Society of Photo-Optical Instrumentation Engineers (SPIE) Conference Series*, volume 7733 of *Presented at the Society of Photo-Optical Instrumentation Engineers (SPIE) Conference*.

Shepherd, M. C. (1997). Difmap: an Interactive Program for Synthesis Imaging. In G. Hunt & H. Payne, editor, *Astronomical Data Analysis Software and Systems VI*, volume 125 of *Astronomical Society of the Pacific Conference Series*, page 77.

Sholomitsky, G. B. (1965). Variability of the Radio Source CTA-102. *Information Bulletin on Variable Stars*, 83:1.

Shostak, S. (2009). New Strategies for SETI. In K. J. Meech, J. V. Keane, M. J. Mumma, J. L. Siefert, & D. J. Werthimer , editor, *Bioastronomy 2007: Molecules, Microbes and Extraterrestrial Life*, volume 420 of *Astronomical Society of the Pacific Conference Series*, page 403.

Siemion, A., Von Korff, J., McMahon, P., Korpela, E., Werthimer, D., Anderson, D., Bower, G., Cobb, J., Foster, G., Lebofsky, M., van Leeuwen, J., and Wagner, M. (2010). New SETI sky surveys for radio pulses. *Acta Astronautica*, 67:1342.

Siemion, A. P. V., Demorest, P., Korpela, E., and et al. (2013). A 1.1-1.9 GHz SETI Survey of the Kepler Field. I. A Search for Narrow-band Emission from Select Targets. *ApJ*, 767:94.

Sirianni, M., Jee, M. J., Benítez, N., and et al. (2005). The Photometric Performance and Calibration of the Hubble Space Telescope Advanced Camera for Surveys. *PASP*, 117:1049.

Slysh, V. I. (1991). VLBI and Interstellar Scattering Tests for SETI Signals. In J. Heidmann & M. J. Klein, editor, *Bioastronomy: The Search for Extraterrestial Life − The Exploration Broadens*, volume 390 of *Lecture Notes in Physics, Berlin Springer Verlag*, page 270.

Soderberg, A. M., Berger, E., Page, K. L., Schady, P., and et al. (2008). An extremely luminous X-ray outburst at the birth of a supernova. *Nature*, 453:469.

Soderberg, A. M., Brunthaler, A., Nakar, E., Chevalier, R. A., and Bietenholz, M. F. (2010). Radio and X-ray Observations of the Type Ic SN 2007gr Reveal an Ordinary, Non-relativistic Explosion. *ApJ*, 725:922.

Soderberg, A. M., Chevalier, R. A., Kulkarni, S. R., and Frail, D. A. (2006a). The Radio and X-Ray Luminous SN 2003bg and the Circumstellar Density Variations around Radio Supernovae. *ApJ*, 651:1005.

Soderberg, A. M., Kulkarni, S. R., Berger, E., Chevalier, R. A., Frail, D. A., Fox, D. B., and Walker, R. C. (2005). The Radio and X-Ray-Luminous Type Ibc Supernova 2003L. *ApJ*, 621:908.

Soderberg, A. M., Nakar, E., Berger, E., and Kulkarni, S. R. (2006b). Late-Time Radio Observations of 68 Type Ibc Supernovae: Strong Constraints on Off-Axis Gamma-Ray Bursts. *ApJ*, 638:930.

Somerville, R. S. (2008). The Co-Evolution of Galaxies, Black Holes, and AGN in a Hierarchical Universe. In Kodama, T., Yamada, T., and Aoki, K., editors, *Panoramic Views of Galaxy Formation and Evolution*, volume 399 of *Astronomical Society of the Pacific Conference Series*, page 391.

Somerville, R. S., Primack, J. R., and Faber, S. M. (2001). The nature of high-redshift galaxies. *MNRAS*, 320:504.

Sramek, R. A., Panagia, N., and Weiler, K. W. (1984). Radio emission from a type I supernova - SN 1983.51 IN NGC 5236. *ApJL*, 285:L59.

Stappers, B. W., Hessels, J. W. T., Alexov, A., and et al. (2011). Observing pulsars and fast transients with LOFAR. *A&A*, 530:A80.

Stockdale, C. J., Kelley, M., van Dyk, S. D., Sramek, R. A., Weiler, K. W., and Panagia, N. (2005). Supernova 2005cs in NGC 5194 (M51). *IAU Circ.*, 8603:2.

Stockdale, C. J., Williams, C. L., Weiler, K. W., Panagia, N., Sramek, R. A., Van Dyk, S. D., and Kelley, M. T. (2007). The Radio Evolution of SN 2001gd. *ApJ*, 671:689.

Strom, R. (2004). What is the primary beam response of an interferometer with unequal elements? In Bachiller, R., Colomer, F., Desmurs, J.-F., and de Vicente, P., editors, *European VLBI Network on New Developments in VLBI Science and Technology*, page 273.

Symons, G. (1998). *Spectrum Demand for New Telecommunication Services, Final Report*. The Australian Communications and Media Authority, RCC Working Group. Retreived from http://www.acma.gov.au.

Szomoru, A. (2008). EXPReS and the e-EVN. In *The role of VLBI in the Golden Age for Radio Astronomy*.

Takano, S., Hofner, P., Winnewisser, G., Nakai, N., and Kawaguchi, K. (2005). High Angular Resolution Observations of the (J, K) = (1, 1), (2, 2), and (3, 3) Transitions of Ammonia in NGC 253. *PASJ*, 57:549.

Tarter, J. (2001). The Search for Extraterrestrial Intelligence (SETI). *ARA&A*, 39:511.

Tarter, J. C. (2004). Astrobiology and SETI. *New Astronomy Reviews*, 48:1543.

Taylor, G. B., Carilli, C. L., and Perley, R. A., editors (1999). *Synthesis Imaging in Radio Astronomy II*, volume 180 of *Astronomical Society of the Pacific Conference Series*.

Terashima, Y. and Wilson, A. S. (2001). A Chandra Observation of M51: Active Nucleus and Nuclear Outflows. *ApJ*, 560:139.

Terashima, Y. and Wilson, A. S. (2003). Chandra Snapshot Observations of Low-Luminosity Active Galactic Nuclei with a Compact Radio Source. *ApJ*, 583:145.

Thompson, A. R. (1999). Fundamentals of Radio Interferometry. In Taylor, G. B., Carilli, C. L., and Perley, R. A., editors, *Synthesis Imaging in Radio Astronomy II*, volume 180 of *Astronomical Society of the Pacific Conference Series*, page 11.

Thompson, A. R., Moran, J. M., and Swenson, Jr., G. W. (2001). *Interferometry and Synthesis in Radio Astronomy, 2nd Edition*.

Thompson, D. R., Wagstaff, K. L., Brisken, W. F., Deller, A. T., Majid, W. A., Tingay, S. J., and Wayth, R. B. (2011). Detection of Fast Radio Transients with Multiple Stations: A Case Study Using the Very Long Baseline Array. *ApJ*, 735:98.

Tingay, S. J. (2004). A VLBI Study of Free-Free Absorbed Compact Radio Sources in the NGC 253 Starburst. *AJ*, 127:10.

Tingay, S. J., Jauncey, D. L., Preston, R. A., and et al. (1995). Relativistic motion in a nearby bright X-ray source. *Nature*, 374:141.

Tuomi, M. (2011). Bayesian re-analysis of the radial velocities of Gliese 581. Evidence in favour of only four planetary companions. *A&A*, 528:L5.

Turnbull, M. C. and Tarter, J. C. (2003). Target Selection for SETI. I. A Catalog of Nearby Habitable Stellar Systems. *ApJS*, 145:181.

Turner, J. L. and Ho, P. T. P. (1985). The 1 parsec radio core and possible nuclear ejection in NGC 253. *ApJL*, 299:L77.

Turner, J. L. and Ho, P. T. P. (1994). Bright radio continuum emission from star formation in the cores of nearby spiral galaxies. *ApJ*, 421:122.

Ubeda, L, e. a. (2014). *ACS Instrument Handbook Version 13.0*. STScI, Baltimore. Retreived from http://www.stsci.edu/hst/acs/documents/handbooks/current/cover.html.

Udry, S., Bonfils, X., Delfosse, X., Forveille, T., Mayor, M., Perrier, C., Bouchy, F., Lovis, C., Pepe, F., Queloz, D., and Bertaux, J. (2007). The HARPS search for southern extra-solar planets. XI. Super-Earths (5 and 8 $M_{\oplus}$) in a 3-planet system. *A&A*, 469:L43.

Ulvestad, J. S. (2009). Radio Emission from Young Supernovae and Supernova Remnants in Arp 299. *AJ*, 138:1529.

Ulvestad, J. S. and Antonucci, R. R. J. (1991). Second-epoch VLA observations of compact radio sources in NGC 253. *AJ*, 102:875.

Ulvestad, J. S. and Antonucci, R. R. J. (1994). Do the compact radio sources in NGC 253 and M82 fade over time? *ApJL*, 424:L29.

Ulvestad, J. S. and Antonucci, R. R. J. (1997). VLA Observations of NGC 253: Supernova Remnants and H II Regions at 1 Parsec Resolution. *ApJ*, 488:621.

Ulvestad, J. S., Wong, D. S., Taylor, G. B., Gallimore, J. F., and Mundell, C. G. (2005). VLBA Identification of the Milliarcsecond Active Nucleus in the Seyfert Galaxy NGC 4151. *AJ*, 130:936.

van Dyk, S. D., Montes, M. J., Weiler, K. W., Sramek, R. A., and Panagia, N. (1998). Radio Detection of SN 1985L in NGC 5033. *AJ*, 115:1103.

van Dyk, S. D., Sramek, R. A., Weiler, K. W., and Panagia, N. (1993). The radio emission from the type IC supernova SN 1990B. *ApJ*, 409:162.

van Langevelde, H. J., Frail, D. A., Cordes, J. M., and Diamond, P. J. (1992). Interstellar scattering toward the Galactic center as probed OH/IR stars. *ApJ*, 396:686.

Vinkó, J., Takáts, K., Szalai, T., and et al. (2012). Improved distance determination to M 51 from supernovae 2011dh and 2005cs. *A&A*, 540:A93.

Vogt, S. S., Butler, R. P., Rivera, E. J., Haghighipour, N., Henry, G. W., and Williamson, M. H. (2010). The Lick-Carnegie Exoplanet Survey: A 3.1 $M_{\odot}$ Planet in the Habitable Zone of the Nearby M3V Star Gliese 581. *ApJ*, 723:954.

Wayth, R. B., Brisken, W. F., Deller, A. T., Majid, W. A., Thompson, D. R., Tingay, S. J., and Wagstaff, K. L. (2011). V-FASTR: The VLBA Fast Radio Transients Experiment. *ApJ*, 735:97.

Weedman, D. W. (1987). Starburst galaxies. In Lonsdale Persson, C. J., editor, *NASA Conference Publication*, volume 2466 of *NASA Conference Publication*, page 351.

Weiler, K. W., Panagia, N., Montes, M. J., and Sramek, R. A. (2002). Radio Emission from Supernovae and Gamma-Ray Bursters. *ARA&A*, 40:387.

Weiler, K. W., Panagia, N., Sramek, R. A., van der Hulst, J. M., Roberts, M. S., and Nguyen, L. (1989). Radio emission from supernovae. I - One to twelve year old supernovae. *ApJ*, 336:421.

Weiler, K. W., Panagia, N., Stockdale, C., Rupen, M., Sramek, R. A., and Williams, C. L. (2011). Radio Emission from SN 1994I in NGC 5194 (M 51): The Best-studied Type Ib/c Radio Supernova. *ApJ*, 740:79.

Weiler, K. W., Sramek, R. A., Panagia, N., van der Hulst, J. M., and Salvati, M. (1986). Radio supernovae. *ApJ*, 301:790.

Weiler, K. W., Williams, C. L., Panagia, N., and et al. (2007). Long-Term Radio Monitoring of SN 1993J. *ApJ*, 671:1959.

Wellons, S., Soderberg, A. M., and Chevalier, R. A. (2012). Radio Observations Reveal Unusual Circumstellar Environments for Some Type Ibc Supernova Progenitors. *ApJ*, 752:17.

Werthimer, D., Anderson, D., Bowyer, C. S., Cobb, J., Heien, E., Korpela, E. J., Lampton, M. L., Lebofsky, M., Marcy, G. W., McGarry, M., and Treffers, D. (2001). Berkeley radio and optical SETI programs: SETI@home, SERENDIP, and SEVENDIP. In S. A. Kingsley & R. Bhathal, editor, *Society of Photo-Optical Instrumentation Engineers (SPIE) Conference Series*, volume 4273 of

Presented at the Society of Photo-Optical Instrumentation Engineers (SPIE) Conference, page 104.

White, R. L., Becker, R. H., Helfand, D. J., and Gregg, M. D. (1997). A Catalog of 1.4 GHz Radio Sources from the FIRST Survey. *ApJ*, 475:479.

Williams, C. L., Panagia, N., Van Dyk, S. D., Lacey, C. K., Weiler, K. W., and Sramek, R. A. (2002). Radio Emission from SN 1988Z and Very Massive Star Evolution. *ApJ*, 581:396.

Woltjer, L. (1972). Supernova Remnants. *ARA&A*, 10:129.

Wordsworth, R. D., Forget, F., Selsis, F., Madeleine, J.-B., Millour, E., and Eymet, V. (2010). Is Gliese 581d habitable? Some constraints from radiative-convective climate modeling. *A&A*, 522:A22.

Wrobel, J. M. and Walker, R. C. (1999). Sensitivity. In Taylor, G. B., Carilli, C. L., and Perley, R. A., editors, *Synthesis Imaging in Radio Astronomy II*, volume 180 of *Astronomical Society of the Pacific Conference Series*, page 171.

Wucknitz, O. (2010). Efficient wide-field VLBI imaging. In *10th European VLBI Network Symposium and EVN Users Meeting*.

A

Publications

Publications directly resulting from work done in this thesis:

- **H. Rampadarath**, J. S. Morgan, S. J. Tingay & C. M. Trott, The First Very Long Baseline Interferometric SETI Experiment. *The Astronomical Journal, Volume 144, Issue 2, article id. 38, 2011.*

- **H. Rampadarath**, J. S. Morgan, E. Lenc, & S. J. Tingay, Multi-epoch Very Long Baseline Interferometric Observations of the Nuclear Starburst Region of NGC 253: Improved Modeling of the Supernova and Star formation Rates, *The Astronomical Journal, Volume 147, Issue 1, article id. 5, 2014.*

- **H. Rampadarath**, J. S. Morgan, S. J. Tingay, R. Soria, C. Reynolds, M. Argo & G. Dumas, Probing the Compact Radio Source Population of the Whirlpool Galaxy with Wide-Field VLBI, *The Monthly Notices of the Royal Astronomical Society*, in preparation.

Other publications that, while not associated with this thesis, were instrumental in providing the necessary preparations that were required for the research presented in this document:

- Garrett, M. A.; **Rampadarath, H.**; Jozsa, G. I. G.; Muxlow, T. W. B.; Oosterloo, T. A.; Paragi, Z.; Beswick, R.; van Arkel, H.; Schawinski, K.; Keel, W. C. Hanny's Voorwerp: a nuclear starburst in IC2497. *Proceedings of the 10th EVN Symposium in Manchester, Sep. 2010.*

- **H. Rampadarath**; Garrett, M. A.; Józsa, G. I. G.; T. Muxlow; Oosterloo, T. A.; Paragi, Z.; R. Beswick; van Arkel, H.; Lintott, C.; Keel, W. C.;

Schawinski, K.; Edmondson, E. Hanny's Voorwerp . Evidence of AGN activity and a nuclear starburst in the central regions of IC 2497 *Astronomy and Astrophysics, Volume 517, id. L8, 2010*

- **Rampadarath, H.**; Garrett, M. A.; Muxlow, T.; Józsa, G. I. G.; Oosterloo, T. A.; Paragi, Z. Is an obscured AGN at the centre of the disk galaxy IC 2497 responsible for Hanny's Voorwerp? *Proceedings of the 8th International e-VLBI Workshop: the Science and Technology of Long Baseline Real-Time Interferometry, EXPReS09. Madrid, Spain. 2009*

- Józsa, G. I. G.; Garrett, M. A.; Oosterloo, T. A.; **Rampadarath, H.**; Paragi, Z.; van Arkel, H.; Lintott, C.; Keel, W. C.; Schawinski, K.; Edmondson, E. Revealing Hanny's Voorwerp: radio observations of IC 2497 *Astronomy and Astrophysics, Volume 500, Issue 2, 2009, pp.L33-L36.*

- **Rampadarath, H.**; Garrett, M. A.; Polatidis, A. Observations of 44 extragalactic radio sources with the VLBA at 92 cm. A list of potential calibrators and targets for LOFAR and RadioAstron*Astronomy and Astrophysics, Volume 500, Issue 3, pp.1327-1336, 2009.*

- Garrett, M. A.; **Rampadarath, H.**; Lenc, E.; Wucknitz, O. LOFAR, E-LOFAR and a 327 MHz VLBA survey. *Proceedings of the 9th European VLBI Network Symposium on The role of VLBI in the Golden Age for Radio Astronomy and EVN Users Meeting. Bologna, Italy. 2008*